



HAL
open science

Orientation analysis and liquid crystalline behavior of lanthanide-doped nanorods

Jeongmo Kim

► **To cite this version:**

Jeongmo Kim. Orientation analysis and liquid crystalline behavior of lanthanide-doped nanorods. Materials Science [cond-mat.mtrl-sci]. Institut Polytechnique de Paris, 2021. English. NNT : 2021IP-PAX021 . tel-03738033

HAL Id: tel-03738033

<https://theses.hal.science/tel-03738033>

Submitted on 25 Jul 2022

HAL is a multi-disciplinary open access archive for the deposit and dissemination of scientific research documents, whether they are published or not. The documents may come from teaching and research institutions in France or abroad, or from public or private research centers.

L'archive ouverte pluridisciplinaire **HAL**, est destinée au dépôt et à la diffusion de documents scientifiques de niveau recherche, publiés ou non, émanant des établissements d'enseignement et de recherche français ou étrangers, des laboratoires publics ou privés.

Orientation analysis and liquid crystalline behavior of lanthanide-doped nanorods

Thèse de doctorat de l'Institut Polytechnique de Paris
préparée à École Polytechnique

École doctorale n°626 Ecole Doctorale de l'Institut Polytechnique de
Paris (ED IP Paris)
Spécialité de doctorat: Physique

Thèse présentée et soutenue à Palaiseau, le 07 Avril 2021, par

M. Jeongmo Kim

Composition du Jury :

M. Stéphane Parola Professeur, École normale supérieure, Lyon	Président
Mme. Agnès Maître Professeure, Sorbonne Université	Rapporteur
M. Patrick Davidson Directeur de recherche, CNRS-Université Paris-Saclay	Rapporteur
M. Andries Meijerink Professor, Utrecht University	Examineur
M. Daniel Jaque Professor, Universidad Autónoma de Madrid	Examineur
Mme. Sophie Brasselet Directrice de recherche, CNRS-Institut Fresnel, Marseille	Examineur
M. Thierry Gacoin Directeur de recherche, CNRS-École Polytechnique, IP Paris	Directeur de thèse
M. Jongwook Kim Professeur assistant, École Polytechnique, IP Paris	Co-Encadrant
M. Khalid Lahlil Ingénieur de recherche, CNRS-École Polytechnique, IP Paris	Invité

Acknowledgments

First of all, I would like to thank all the jury members for their kind acceptance of reviewing my thesis and their interest in my study, and the many valuable comments suggested during the defense presentation.

I would like to express my deepest gratitude to my thesis supervisor, **Thierry Gacoin**. He always provided insightful advice on my research and asked critical questions that helped my dissertation study get on the right track. I could easily interact with him by knocking on his office door at any time and start a discussion. It was always good times to discuss with him, which I found very precious each time. I would like to express the same gratitude to **Jongwook Kim**, one of my thesis supervisors. He has been the inspiration behind my research. I had the chance to observe and see how he carried out the experiment while experimenting together with him. That way, I could learn how to do the proper scientific investigation. Also, he never stopped helping me and giving me advice, which helped me overcome the difficult times I experienced during my thesis. I would like to thank **Khalid Lahlil**, who helped me in the synthesis and functionalization of particles. Doing chemistry is not always successful. It takes many attempts and fails. His sense of humor and professional knowledge of particle synthesis helped me appreciate chemistry work during the challenging times I've had during the thesis study. Along with his professional knowledge, he has always been a pleasant supervisor. I could learn how to get along with other researchers by watching his interaction with other researchers.

I would like to thank **Patrick Davidson** and **Ivan Dozov** for their collaboration on inorganic particle liquid crystals. It was a precious moment to watch the renowned scientists do their experiments by themselves and introduce me know-hows they accumulated for a long time. I would also like to thank **Reinaldo Chacon**, **Aymeric Leray**, and **Gérard Colas-des-francs** for the collaborative work on the orientation analysis of nanorods. I visited their lab 3-4 times during my thesis study. Whenever I was in their lab, I've brought lots of samples and planned complex and intense experiments with a very tight schedule. Even so, they always welcomed me and ready for any discussion. In addition, I could observe how researchers in the optics field do their work and could watch their passion for building an optical system, which was, in fact the motivation I started to assemble a confocal microscope in PMC. I also would like to thank **Aashutosh Kumar** and **Jochen Fick** for the collaborative work on the optical trapping of the nanorods.

I would like to thank **Eric Larquet**, **Fouad Maroun**, **Sandrine Tusseau-Nenez**, **Melanie Poggi**, **Rabei Mohammedi**, **Lucio Martinelli**, **Claude-Alban Ranély-Vergé-Dépré**, **Jacques Peretti**, and **Alistair Rowe** for their help in training me on various characterization tools (SEM, TEM, XRD, etc.) and in assembling a polarizing confocal microscopy system. I would also like to thank my officemates, **André**

Wack and **Didier Lenoir**, who taught me many French words and their patience in understanding my French. I also appreciate the beautiful tools they made for my experiments.

I would also like to thank **Elodie Chaudan** and **Godefroy Lemenager**, who worked with me on a similar subject. Based on many pieces of knowledge accumulated from their research, I was able to proceed with my thesis study very quickly and efficiently. I would like to thank **Francesca Corbella**, **Naoto Hikawa**, **Lilian Magermans**, and **Zijun Wang**, with whom I had the chance to work together during my thesis study. By working closely with them, I could understand how essential colleagues are to go further in scientific work. I would like to thank also **all the Ph.D. students in PMC and colleagues in the chemistry group**. It was always a great time to work or interact with them, which has helped me enjoy laboratory life over the past four years. I appreciate a lot the beautiful gifts they prepared for me after the thesis defense.

I would like to thank **Hamza Mohsin**. He has been a delightful friend and a brother to me during my stay in France. It was him always next to me and enjoyed together with me the important moments in my stay in France of last six years. It was so lucky to get to know him as a friend. I would like to thank also **Yannis Cheref**. He started an internship as well as a thesis study in PMC in the same year. So, we could exchange many difficulties in the research, and also, he was a good counselor on many different subjects. He was the man who has a similar taste with me, gaming, music, etc. So, I enjoyed having a chat with him, which helped relieve some stress during my thesis study.

I would like to thank my family, **Jungin Kim**, **Hyeja Seo**, and **Sangdon Kim**, who gave me a full support for my stay in France. Thanks to their support, I could be stable in every aspect and only focus on my research work, which helps me successfully finish my thesis study. I want to thank also my girlfriend, **Jiwon Jeong**. She was the one who understood every facet of me and faced me with daily changes during my thesis study. Without her, I don't think I could have finished my thesis study with such great outcomes. Over the past seven years, we have shared many moments of joy and sadness. And I'm happy that I can continue to share parts of my life with her, which would make it much easier for us to overcome many difficult times ahead in the future.

I would like to thank also **Ecole Doctorale of l'Institut Polytechnique de Paris** and **Kwanjeong Educational Foundation** for their financial supports during my thesis study, which helps me fully concentrate on scientific work.

Finally, I would like to thank God for allowing me this incredible journey.

Abstract

Luminescent nanocrystals have been of great interest for their use for many applications such as display devices or biological markers. Among them, nanocrystals doped with lanthanide ions exhibit particular emission features associated with magnetic (MD) or electric dipole (ED) transitions.

The first objective of this thesis was to develop a methodology for the determination of the 3D orientation of nanocrystals by taking advantage of the unique polarization features of MD and ED transitions. As a case example, NaYF₄:Eu nanorods were synthesized, surface-functionalized, and randomly oriented within a rigid polymer film. The possible determination of the 3D orientation of the nanorods with high accuracy is demonstrated using a single-shot spectrogram of the polarized photoluminescence. A second part is devoted to determining the degree of orientation (order parameter) with respect to the global alignment direction of colloidal NaYF₄:Eu nanorods aligned under an electric field in an electro-optical cell.

The second objective of this thesis was to investigate the colloidal liquid crystal behavior of anisotropic nanocrystals. LaPO₄:Eu nanorods were synthesized, stabilized with a surface ligand, and dispersed in an apolar medium where its liquid crystalline (LC) behavior was evidenced. This phenomenon was compared to the previously reported LC behavior of the same nanorods dispersed in polar media. In the second part, the LCs behavior was investigated when the system is confined between two walls. The confined LC showed an unprecedented LC evolution leading to the observation of flower-shaped LC domains. A 3D tomographic mapping of the orientation and order parameter was performed based on the polarized photoluminescence of doped lanthanide ions. This thesis study provides the first example of applying the new spectroscopic orientation analysis technique for the characterization of nanoparticle self-assemblies, opening a way toward even more challenging applications such as the rotational dynamic tracking of nano-objects.

Résumé

Les nanocristaux luminescents ont fait l'objet de nombreux travaux en vue de leurs applications dans de nombreux domaines tels que les dispositifs d'affichage ou comme marqueurs biologiques. Parmi eux, les nanocristaux dopés aux ions lanthanides présentent des caractéristiques d'émission très spécifiques associées à des transitions soit dipolaires magnétiques (MD), soit dipolaires électriques (ED).

Le premier objectif de cette thèse était de développer une méthodologie pour la détermination de l'orientation 3D des nanocristaux en tirant parti des caractéristiques uniques de polarisation des transitions MD et ED. À titre d'exemple, des nanobâtonnets de $\text{NaYF}_4:\text{Eu}$ ont été synthétisés, fonctionnalisés en surface et orientés aléatoirement dans un film de polymère rigide. La détermination avec une grande précision de l'orientation 3D des nanorods est démontrée à l'aide d'un spectrogramme unique de la photoluminescence polarisée. Une deuxième partie est consacrée à la détermination du degré d'orientation (paramètre d'ordre) par rapport à la direction d'alignement global de nanobâtonnets colloïdaux $\text{NaYF}_4:\text{Eu}$ alignés par un champ électrique dans une cellule électro-optique.

Le deuxième objectif de cette thèse était d'étudier le comportement cristal liquide des nanocristaux anisotropes. Des nanobâtonnets de $\text{LaPO}_4:\text{Eu}$ ont été synthétisés, stabilisés avec un ligand de surface et dispersés dans un milieu apolaire où le comportement cristal liquide (CL) a été mis en évidence. Ce phénomène a été comparé au comportement CL précédemment rapporté des mêmes nanobâtonnets dispersés en milieu polaire. Dans une seconde partie, le comportement CL a été étudié dans le cas où le système est confiné entre deux parois. La dispersion confinée a montré une évolution originale de sa structure menant à l'observation de domaines CL en forme de fleur. Une cartographie tomographique 3D de l'orientation et du paramètre d'ordre a été réalisée sur la base de la photoluminescence polarisée des ions lanthanides dopés. Ceci fournit un premier exemple d'application de la technique pour la caractérisation d'assemblages auto-organisés, ouvrant la voie à des applications encore plus complexes comme le suivi de la dynamique rotationnelle de nano-objets.

Table of Contents

Introduction	14
Chapter 1. Orientation Analysis of Single Nanorod	18
1.1. Introduction	19
1.1.1. State-of-the-art methods for orientation analysis	20
1.1.2. Orientation analyses using photoluminescence of rare-earth dopants	23
1.2. Elaboration of NaYF₄:Eu nanorods and their photoluminescence	26
1.2.1. Synthesis and surface functionalization of NaYF ₄ :Eu nanorod	26
1.2.2. Polarized photoluminescence of NaYF ₄ :Eu nanorod	29
1.3. Orientation analysis of NaYF₄:Eu single nanorod	35
1.3.1. Theoretical methodology for orientation analysis	35
1.3.2. Orientation analysis by spectral fitting and area under curve ratiometry	38
1.3.3. Errors in orientation analysis	51
1.4. Conclusion	56
Chapter 2. Order Parameter Analysis of Aligned Nanorods Assembly	58
2.1. Introduction	59
2.1.1. Aligned nanorods assembly	59
2.1.2. State-of-the-art methods for order parameter analysis	61
2.1.3. Order parameter analysis using photoluminescence of rare-earth dopants	63
2.2. In-plane order parameter analysis of NaYF₄:Eu aligned nanorod assembly	65
2.2.1. In-plane alignment using in-plane switching (IPS) electro-optical cell	65
2.2.2. Theoretical methodology for in-plane order parameter analysis	67
2.2.3. In-plane order parameter analysis by spectral fitting	69
2.3. Homeotropic order parameter analysis of NaYF₄:Eu aligned nanorod assembly	72
2.3.1. Theoretical methodology for homeotropic order parameter analysis	72
2.3.2. Homeotropic alignment using homeotropic electro-optical cell	75
2.3.3. Homeotropic order parameter analysis by spectral fitting	76
2.4. Conclusion	81
Chapter 3. Liquid Crystalline Behavior of Nanorod Suspension	84
3.1. Introduction	85
3.1.1. Colloidal dispersion of nanoparticles and their stability	85
3.1.2. Colloidal liquid crystal	88
3.2. Charge-stabilized LaPO₄:Eu nanorods suspension in a polar medium	92
3.2.1. Hydrothermal synthesis and charge-stabilization of nanorods in ethylene glycol	92
3.2.2. Liquid crystalline behavior of charge stabilized nanorods in ethylene glycol	94
3.3. Ligand-stabilized LaPO₄:Eu nanorods suspension in an apolar medium	96
3.3.1. Solvent transfer by surface functionalization	96
3.3.2. Liquid crystalline behavior of ligand-stabilized nanorods suspension in chloroform	102
3.3.3. Phase behavior: liquid crystalline transition and gel formation	108

3.4. Conclusion	116
<i>Chapter 4. 3D Tomography of Liquid Crystalline Nanorod Assembly</i>	118
4.1. Evolution of liquid crystalline phase of LaPO₄:Eu nanorods in confined geometry	119
4.1.1. Evolution of liquid crystalline phase over time in confined geometry	120
4.1.2. A rich diversity of liquid crystalline phase in confined geometry	125
4.1.3. Birefringence pattern study of liquid crystalline phase in confined geometry	127
4.2. 3D tomography of liquid crystalline assembly of LaPO₄:Eu nanorods	131
4.2.1. State-of-the-art method for tomography of liquid crystalline phase	131
4.2.2. Theoretical methodology for tomography of liquid crystalline assembly	132
4.2.3. Fluorescence confocal polarizing microscopy	137
4.2.4. 3D tomography of liquid crystalline nanorod assembly	140
4.3. Conclusion	155
<i>Conclusion and Prospects</i>	158
<i>Experimental details</i>	162
<i>Appendix</i>	166
<i>References</i>	192

Introduction

Nanoparticle systems have greatly attracted the materials science community because nano-sized particles can exhibit novel physical, chemical, optical, and mechanical properties different from the typical properties of materials on a larger scale. Over the past decades, research on nanoparticles has significantly advanced thanks to the remarkable improvements in characterization techniques, making it possible to observe nanoparticles with unprecedented temporal and spatial resolutions. Along with the innovation in characterization techniques, a better understanding of materials chemistry has enabled precise control of the size, shape, composition, and stability of nanoparticles, which helps optimize materials' properties according to various needs. This parallel breakthrough has led to many fascinating applications such as electroluminescent display based on quantum dots, bio-imaging and nano-thermometer based on up-converting nanoparticles, nano-thermotherapy, and sensors based on semiconducting nanoparticles, to name a few.

In the vast field of nanoparticle research, this thesis is devoted to developing fluorescent nanoparticles having an anisotropy in their morphology and their fluorescence. Such anisotropies in nanoparticles open a new research area, taking advantage of new material properties beyond spherical nanoparticles. The first is morphological anisotropy, which offers the possibility to align them under applied fields and use them as building blocks of liquid crystalline assembly, which is the basis for developing new applications such as electro-optical devices, birefringent coatings, and smart windows. The second is polarized fluorescence, which establishes a new methodology to characterize nanoparticles' orientation, which is proved to be a valuable tool for an in-depth examination of the rotational dynamics of various nano- and bio-systems.

As part of these objectives, we studied rod-shaped nanocrystals doped with lanthanide ions as a continuation of a group project.¹⁻³ We have synthesized the lanthanide-doped nanorods and made a directed assembly of them by applying the external electric field. We also developed liquid crystalline self-assemblies of nanorods by controlling the sophisticated surface chemistry. Afterward, the spatial orientation of an as-prepared either individual or assembled lanthanide-doped nanorods is analyzed based on the lanthanide photoluminescence employing the multiple optical dipoles of different nature (magnetic and electric dipole).

In **Chapter 1**, the photo-physics of orientation analysis based on excitation/emission polarization is discussed. Nanorods doped with lanthanide ions are synthesized, and their polarized photoluminescence is studied. The methodology for calculating the three-dimensional (3D) orientation of a single nanorod is developed based on the unique characteristic of lanthanides' emission that employs multiple optical dipoles of different nature - magnetic and electric dipole. The developed methodology is demonstrated

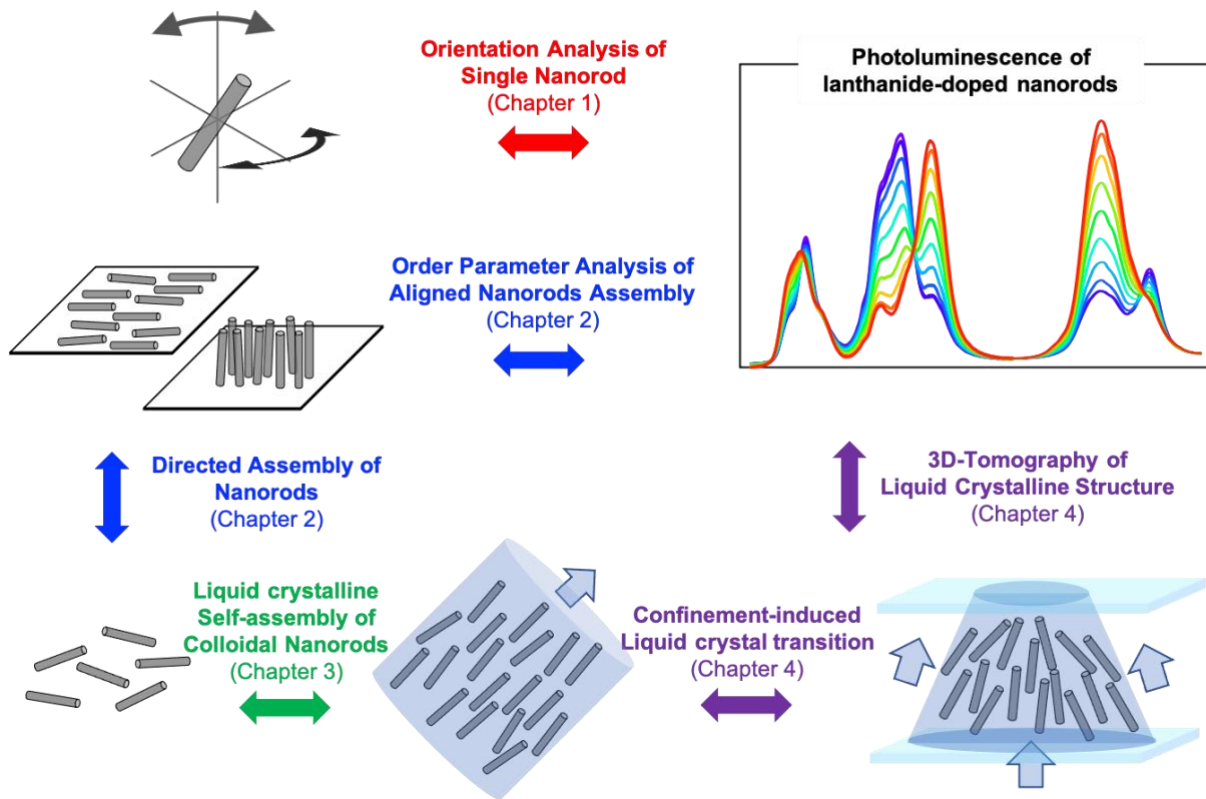
experimentally, and its advantages over other orientation analysis methods using different types of fluorophores are discussed.

In **Chapter 2**, the aligned nanorod assembly and its application are discussed. State-of-the-art methods for measuring the degree of order (order parameter) of aligned assemblies are introduced. The aligned lanthanide-doped nanorod assembly is fabricated by the application of an external electric field. The methodology for calculating the order parameter is developed based on the intrinsic anisotropy in the emission of lanthanides, which allows for following *in situ* the evolution of the order parameter of nanorods assembly as a function of electric field intensity.

In **Chapter 3**, colloidal liquid crystals and their colloidal stability are discussed. A stable charge stabilized LaPO₄ nanorod suspension is prepared in a polar medium, and its LC behavior is studied based on the Onsager's hard rod model. The nanorods are then ligand-stabilized by a surface functionalization and redispersed in apolar media. Its LC behavior in apolar media is then compared with the one in a polar medium. The influences of charges in apolar media on the LC behavior of colloidal LC suspension are discussed.

In **Chapter 4**, the liquid crystal phase transition induced by the confinement effect is discussed. The state-of-the-art method for the tomography of the three-dimensional liquid crystalline structure is discussed. A rich phenomenology of confinement-induced liquid crystalline structure composing of colloidal LaPO₄:Eu nanorods is investigated. The methodology for calculating the orientation of the nematic director \vec{n} and the order parameter S of liquid crystalline (LC) nanorods assembly is developed based on the lanthanide emission employing multiple optical dipoles of different nature. Polarizing fluorescence confocal microscopy is designed and used to perform a 3D tomographic mapping of \vec{n} and S of LC nanorods assembly based on the developed methodology.

Table of Contents Graphic



Chapter 1.

Orientation Analysis of Single Nanorod

Orientation analysis is of great interest because the spatial orientation of many systems (*e.g.*, molecular motors, nanocrystal assembled structure, electro-optical device, smart window, *etc.*) are the key structural changes leading to their functionality. The orientation of nanocrystals can be measured by examining the polarized luminescence of emission dipole inherent in light-emitting compounds such as quantum dots or organic fluorophores. To retrieve a three-dimensional (3D) orientation of such nanocrystals, it has been essential to observe this dipole (single emission dipole) along multiple viewing angles or/and scan the polarized luminescence intensity with a rotating analyzer. However, this method is limited for its practical use as it is subject to various external sources of error and requires a relatively complex optical setup with multiple excitations and emission beam paths.

In this chapter, we propose a fundamentally different approach employing coupled multiple emission dipoles that are inherent in lanthanide-doped phosphors. Simultaneous observation of these coupled dipoles and comparison of their relative intensities allowed to determine the 3D orientation from a single viewing angle. Furthermore, the distinct natures of electric and magnetic dipoles originating in lanthanide luminescence enable an instant orientation analysis with a single-shot emission spectrum. Eu^{3+} -doped NaYF_4 nanorod is considered as a proof-of-concept material to demonstrate this straightforward orientation analysis using a conventional fluorescence microscope. This methodology would find applicability into the study in rotational dynamics of various nano- and biomolecular systems.

Parts of results presented in this chapter were made collaborating with Mr. Reinaldo Chacón, Dr. Aymeric Leray and Prof. Gérard Colas-des-Francis in Laboratoire Interdisciplinaire Carnot de Bourgogne (ICB), Université Bourgogne Franche-Comté, Dijon, France.

Parts of results presented in this chapter are published: “Measuring 3D orientation of nanocrystals via polarized luminescence of rare-earth dopants”, **J. Kim**, R. Chaçon, Z. Wang, E. Larquet, K. Lahlil, A. Leray, G. Colas des Francs, J. -W. Kim, T. Gacoin, *Nature Communications*, 12, 1943 (2021)

1.1. Introduction

Luminescent molecules or nanoparticles are universally used as labels to observe small objects (*e.g.*, bio-macromolecules).⁴⁻²⁶ The position and movement of the target object can be precisely detected and tracked by virtue of the bright light emission of the point luminescent labels. Current super-resolution fluorescence microscopy techniques achieve a nanometer-scale spatial resolution far beyond the light diffraction limit^{4, 5}, and the advanced labels can even signal chemical and biomolecular events by FRET (Förster resonance energy transfer)^{6, 7} or SPR (surface plasmon resonance) effects⁸⁻¹⁰. However, for most microscopic systems of interest, their rotational motions remain largely unexplored while this mechanical degree of freedom is often the key to understand the functionality of the system (*e.g.*, molecular motors¹¹⁻¹³, protein folding²⁷, assembly of anisotropic objects^{28, 29}). Tracking the rotation of a small object with the size below the wavelength of light is a challenging problem independent of tracking the translation. It requires discerning the spatial orientation of a point object without visible shape. Thus, the emitted light must contain the information about its orientation that can be quantitatively analyzed by the observer. **Figure 1.1** shows an example where a quantum rod is tagged to a biological object (myosin V), allowing the rod to follow the orientational behavior of myosin V.¹⁷ The orientational dynamics of myosin molecular motor can thus be characterized by analyzing the orientation of the quantum rod.

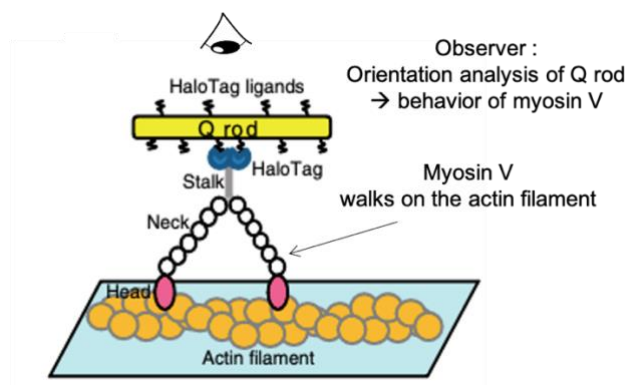


Figure 1.1. Schematic showing how myosin V rotation around its own axis was measured. A quantum rod (Q rod) was bound to the myosin V. The figure is taken from the reference.¹⁷

1.1.1. State-of-the-art methods for orientation analysis

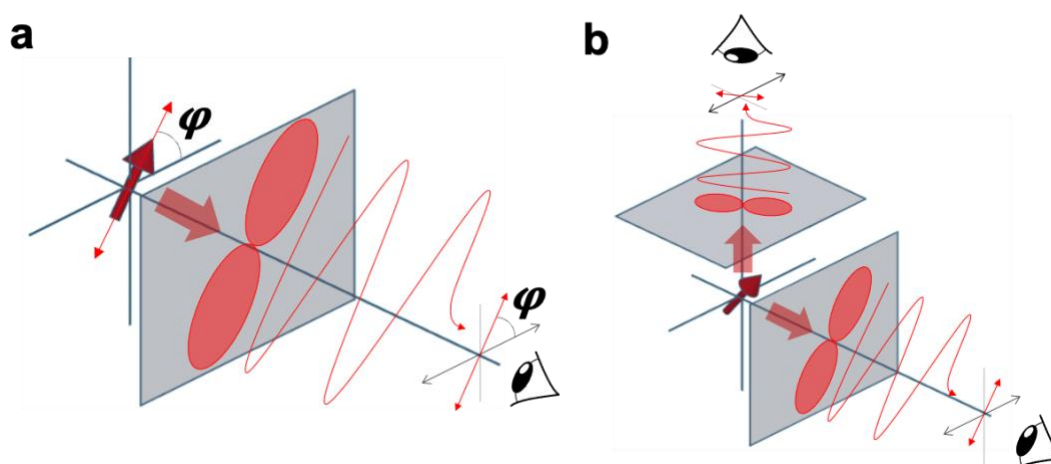


Figure 1.2. Schematic illustrations of the emission dipoles (arrows) and their polar diagrams (dumbbells) indicating the measurable field intensity as a function of the angle of the analyzer on the observation planes (grey plane). Note that observation planes are perpendicular to the light propagating direction. The wavy lines depict the oscillating electric field (red) and magnetic field (blue) polarized along the dipole axis. **(a)** A single electric dipole is oriented parallel to the observation plane. The dipole's in-plane orientation angle can be determined from one polar diagram. **(b)** A single electric dipole with an out-of-plane orientation. The projections of the dipole on two different observation planes render two polar diagrams, from which the three-dimensional (3D) dipole orientation can be determined.

A principal way for discerning the spatial orientation of optical probe is to examine the light polarization of an anisotropic emission distribution in space, which lies in the nature of vector field of optical transition dipoles in luminescent species.^{30, 31} The dipole axis parallel to the polarization is determined by the intrinsic nature of the emitting particle, molecule, or cluster, which can be rigidly tagged with the target object. The orientation of the target can be deduced by taking into account the measured polarization. In this principle, molecular fluorescent dyes¹¹⁻¹⁵, quantum rods¹⁶⁻²⁰, and nanocrystals

exhibiting second-harmonic generation (SHG)²¹⁻²⁴ or up-conversion emission^{25, 26} have been used as optical probes to monitor the rotational dynamics of various nano-objects. A comparison of the existing methods using various types of optical probes can be found in **Appendix Table 1.1**.

Such polarimetry is simple when observing the in-plane (2D) orientation of a probe determined by one variable φ , the angle between the dipole axis and the analyzer (polarizer in front of the detector). The measured intensity of the polarized emission with a rotating polarizer follows a sinusoidal function, illustrated as a dumbbell-shaped polar diagram in **Figure 1.2a**. Note that this schematic dumbbell polar diagram with a rotating polarizing is drawn assuming that the polarized light intensity is measured at the fixed light propagating direction. The φ value can be determined from the experimentally observed polar diagram. However, when regarding the orientation in 3D space, it is necessary to measure the emission polarization from at least two different viewing angles (**Figure 1.2b**). This is because two spherical angles (θ -polar and φ -azimuthal) contribute together to the polarized emission intensity measured from the observer.

Otherwise, two unparallel excitation beams can be used while observing through one viewing angle.³⁰ These, namely, *stereoscopic* methods have been used for studying the rotational dynamics of several systems (*e.g.*, walking motion of myosin V^{17, 32}, rotational diffusion of rod-like particle³³⁻³⁵), but they require optical instrumentation with separate beam paths and multiple detectors and/or excitation sources, which is incompatible with conventional microscopes. Moreover, the accuracy of the orientation analysis can easily deteriorate because the measured signal intensity can vary not only with the dipole orientation but also with many other intrinsic and extrinsic sources such as photo-bleaching^{36, 37} or -blinking³⁸⁻⁴⁰, polydispersity of the emitters⁴¹, experimental errors from the sensitive polarizing optics, and instrumental noise. An alternative approach, fluorescence correlation spectroscopy, monitors the intensity fluctuation of the polarized emission from which the rotational diffusion coefficient is obtained. It is efficient to study the time scale of rotational dynamics but cannot measure the absolute values of θ and φ .³³⁻³⁵

The recent approaches using a microscope objective with a large numerical aperture (NA) have reduced such uncertainties by analyzing the integrative signal from continuous viewing angles over the large NA. Back-focal plane/defocusing imaging⁴²⁻⁴⁶ in this principle let the photons emitted along different directions fall on different regions of the camera detector making a specific image pattern from which the dipole orientation can be deduced. A single-shot image pattern can provide the 3D orientation in this way (**Figure 1.3**). However, the numerical modeling for the pattern analysis is heavy and sensitive to optical parameters (*e.g.*, refractive index, focal depth, aberration)^{16, 47}, which remains as a limitation.

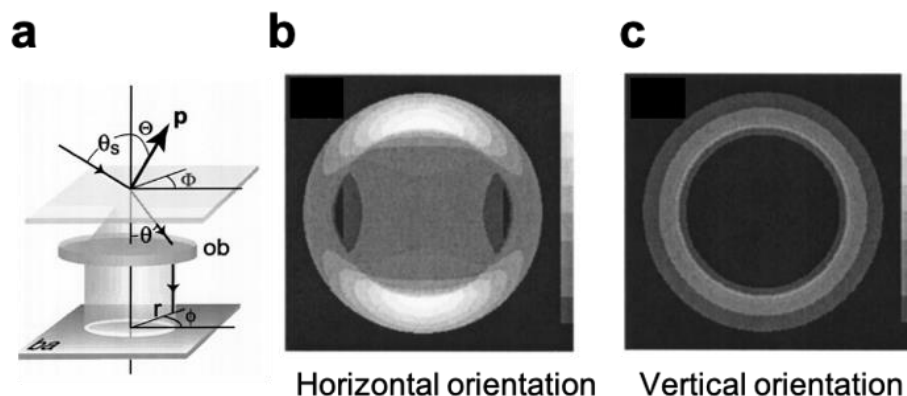


Figure 1.3. (a) Coordinate system used for analysis. P : dipole moment, ob : the objective lens, ba : the back aperture of the objective. Emission pattern of (b) horizontal dipole and (c) vertical dipole. The figure is taken from the reference.⁴²

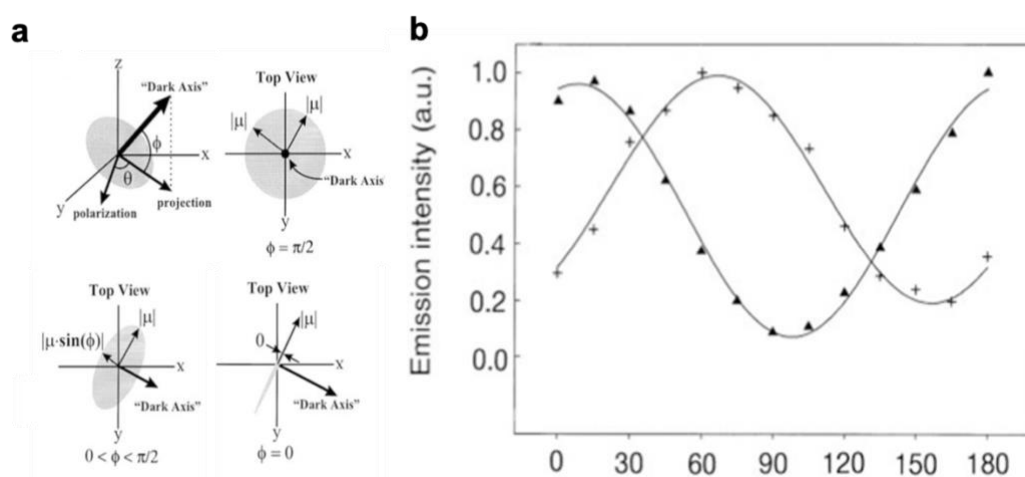


Figure 1.4. (a) 'Dark axis' coordinate system with light propagation along the z-axis. The shaded disk represents the planar, degenerate transition dipole oriented normal to the 'dark axis'. Top views depict the projection of the dipole onto the sample (x-y) plane at three different values of ϕ , corresponding to the polarization distribution observed by the detection system. Also included are the magnitudes of two orthogonal dipole projections, as well as the projection of the 'dark axis' onto the sample plane at each angle. (b) Normalized emission intensity of two single nanocrystals as a function of polarization angle with fit. The strength of dark axis is equal to $(1 - \cos^2\theta \cdot \cos^2\phi)$ and I_{\max} is equal to $|\mu|^2$ and I_{\min} is equal to $|\mu|^2 \cdot \sin^2\phi$. By rotating the analyzer, one can determine $|\mu|^2$ from the maximum intensity, which allows to determine $\sin^2\phi$ from the minimum intensity. Figures and the legends were taken from the reference.²⁰

An alternative method without pattern analysis while measuring at one viewing angle is to use certain highly symmetric single chromophores involving degenerate 2D dipoles.^{16, 20} The orientation analysis based on such degenerate dipoles is successfully demonstrated using CdSe quantum dots.^{16, 20} In this case, measuring the 3D orientation requires a precise scanning of the emission intensity profile with non-zero minimum while rotating the analyzer in many steps until the maximum and minimum intensity is determined (**Figure 1.4**). This method is thus not suitable when observing unstable or dynamically

rotating systems. Moreover, quantum dots generally have a degree of polarization (DOP) that varies in different morphology of nanocrystals, which hinders precise orientation analysis of the polydisperse system.⁴¹

As discussed above, it is still challenging to establish a straightforward method to instantly and accurately measure the orientation of microscopic emitters. In the following sections, we propose a fundamentally different approach employing coupled multiple emission dipoles inherent in rare-earth doped phosphors. This approach allows determining the 3D orientation from a single viewing angle with a single emission spectrum.

1.1.2. Orientation analyses using photoluminescence of rare-earth dopants

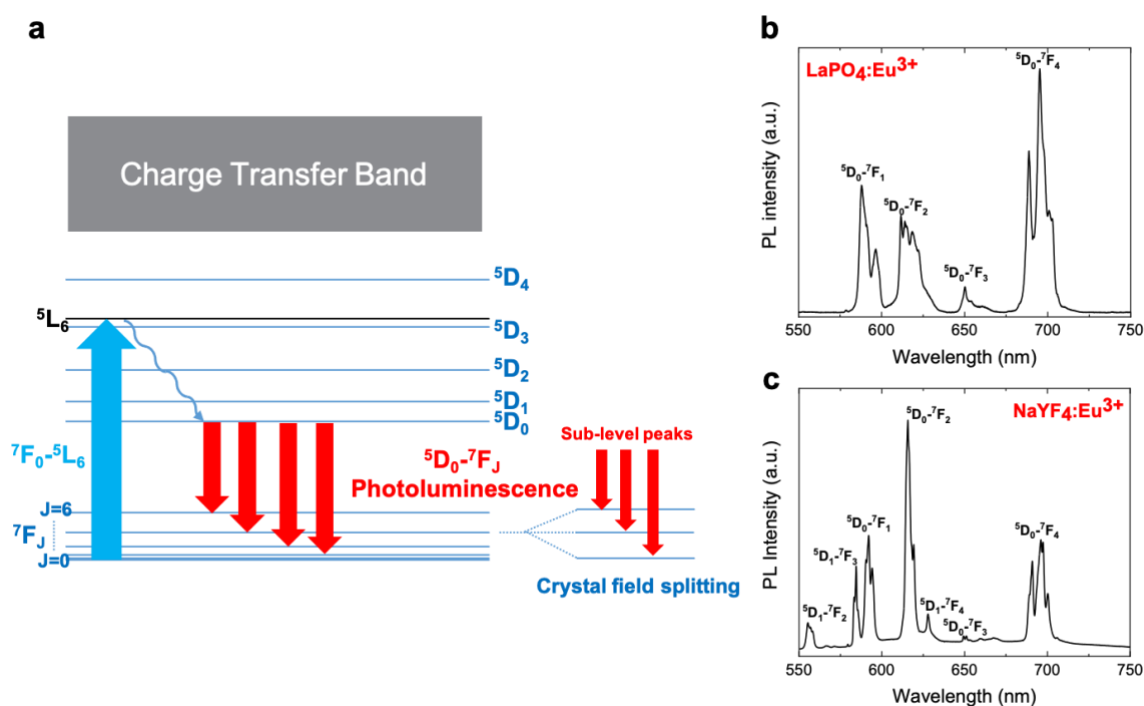


Figure 1.5. (a) Energy level scheme of Europium (Eu^{3+}) ion. Photoluminescence spectra of Eu^{3+} doped (b) LaPO_4 and (c) NaYF_4 nanoparticle. Corresponding transition level is noted for each group peak.

When lanthanide ions are doped in the crystalline host particle, each energy level of lanthanide ion in the $4f^n$ configuration is split into several sublevels by the crystal field. **Figure 1.5a** shows the energy level of one of the lanthanide ions, trivalent Europium (Eu^{3+}) ion. The electrons in such ions can be excited by absorbing energy (blue arrow) and relax back to the low energy levels by the radiative transitions (red arrows) emitting a photon. These transitions appear as a group peak with many narrow emissions peaks in the spectrum (**Figure 1.5b-c**) and are related to a specific type of transition dipole – magnetic (MD) and electric dipole (ED) – according to selection rule⁴⁸. For example, in the case of Eu^{3+}

ions, ${}^5D_0\text{-}{}^7F_1$ transition exhibit a MD nature and ${}^5D_0\text{-}{}^7F_2$, ${}^5D_0\text{-}{}^7F_3$ and ${}^5D_0\text{-}{}^7F_4$ have an ED nature and each of their sublevel peaks feature the same type of dipole.

These ED and MD inherent in rare-earth dopants exhibit mutually different polarization natures. Simultaneous consideration of this different polarization behavior can deliver the information on the 3D orientation through a single viewing angle (**Figure 1.6**, detailed in the following sections). Different natures of polarization of sublevel emission dipoles (ED, MD) can be observed simultaneously using a spectrometer in separated wavelength ranges and manifested as a varying line shape of the photoluminescence spectrum as a function of the angle of the analyzer (**Chapter 1.2.2**). Only a single spectrogram is sufficient to determine θ and φ because ED and MD offer two simultaneous equations (**Chapter 1.3**). Moreover, the dipole orientation with respect to the crystal axis of the host particle depends exclusively on the local site symmetry of the lanthanide dopant.⁴⁹ This provides a crucial advantage that the size and morphology of nanocrystals do not influence the spectral profile of the emission spectrum.⁴⁹ Hence, the emission spectra obtained from a sample with a known orientation are valid as a reference for other particles with the same crystal structure (**Chapter 1.3.2**). This is not the case for other types of emitters such as quantum dots whose emission polarization sensitively varies with the particle size and shape.⁴¹

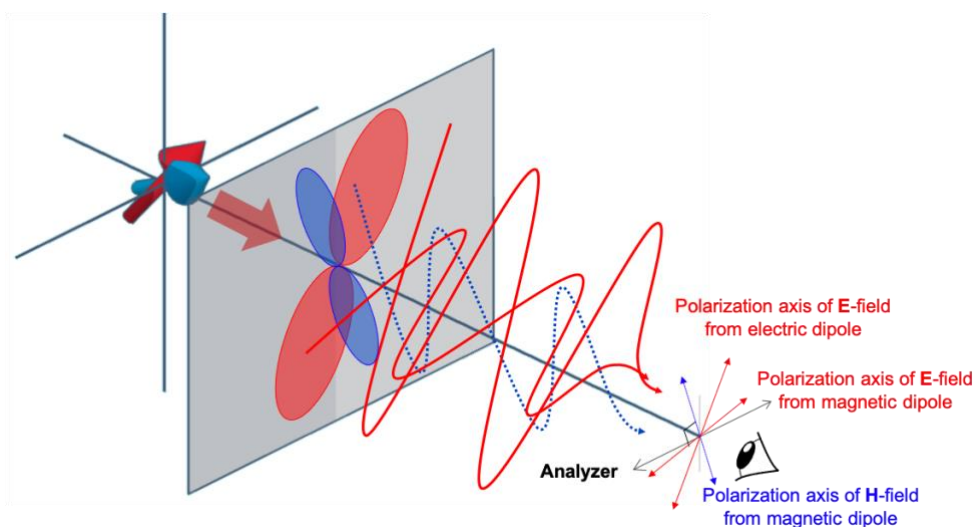


Figure 1.6. Two dipoles with electric (red arrow) and magnetic (blue arrow) dipolar natures are oriented out-of-plane while they are coupled with an arbitrary fixed angle with respect to each other. Each dipole renders a distinct polar diagram (blue dumbbell – magnetic polar diagram / red dumbbell – electric polar diagram) on the same observation plane, from which the 3D orientation of the coupled dipoles can be determined. Polar diagrams (dumbbells) indicate the measurable field intensity as a function of the angle of the analyzer on the observation planes (grey plane). Note that the observation plane is perpendicular to the light propagating direction.

Choice of the material

As a proof of concept of the proposed method, we investigated the 3D orientation of monocrystalline sodium yttrium fluoride (NaYF₄) nanorods doped with trivalent europium (Eu³⁺) ions. NaYF₄ is an efficient crystalline matrix for lanthanide doping and is widely studied for applications in up-conversion probes⁵⁰⁻⁵³ and nano-thermometry^{54, 55}. Among many common emitting rare-earth ions, Eu³⁺ ion is selected as a dopant as it shows sharp and well-defined emission peaks thanks to the non-degenerate upper level of its main emission (⁵D₀→⁷F_J) which is ideal for the spectroscopic orientation analysis intended in this work (**Figure 1.5b-c**). Nanocrystals of NaYF₄:Eu could be synthesized with good control of shape up to micrometer length³, which allowed us to compare the orientation directly seen by the optical microscope with the spectroscopically calculated value.

Summary of Chapter 1.1

Although many analytical methods using different fluorophores have been proposed to calculate the 3D orientation of nanocrystals, there are still many limitations. For example, it requires measurements at multiple viewing angles or polarizations, otherwise, it requires sophisticated image analysis. There are also limitations arising from the fluorophores themselves exploited for the analysis. For example, in the case of quantum dots, it shows different polarization behavior depending on their morphology and exhibit photo-blinking and -bleaching. Therefore, there is a pressing need to develop a robust and straightforward method for calculating the 3D orientation of nanocrystals.

1.2. Elaboration of NaYF₄:Eu nanorods and their photoluminescence

1.2.1. Synthesis and surface functionalization of NaYF₄:Eu nanorod

Synthesis of NaYF₄:Eu nanorod

The synthesis protocol of NaYF₄ nanocrystal doped with rare-earth ions has been optimized previously in the group by adapting protocol from the reference.^{3, 56-58} The synthesis is made by a solvothermal method and yields rod-shaped nanocrystals (nanorod) of which size is dependent on the experimental parameters, principally, reacting temperature (bigger size in higher reaction temperature), reacting time (bigger size in longer reaction) and the percentage of doping ratio (bigger size in lower doping percentage).³ The synthesis protocol is optimized to produce rather big nanorods (micrometer in length) for this work to enable direct comparison of the orientation of nanorod calculated by *spectroscopic* orientation analysis and by direct imaging from the optical microscope. Optimized synthesis protocol (**Experimental details**) produced a straight rod-like morphology of the NaYF₄:Eu nanocrystals (**Figure 1.7a**). Their sizes are quite polydisperse (length = 1184 ± 430 nm, width = 117 ± 24 nm), which is a typical feature of solvothermal synthesized nanorods as shown in the size distribution histogram presented in **Figure 1.7b**. The high-resolution TEM and its fast Fourier transformation (FFT) (**Figure 1.7c-d**) confirmed their single-crystalline nature.

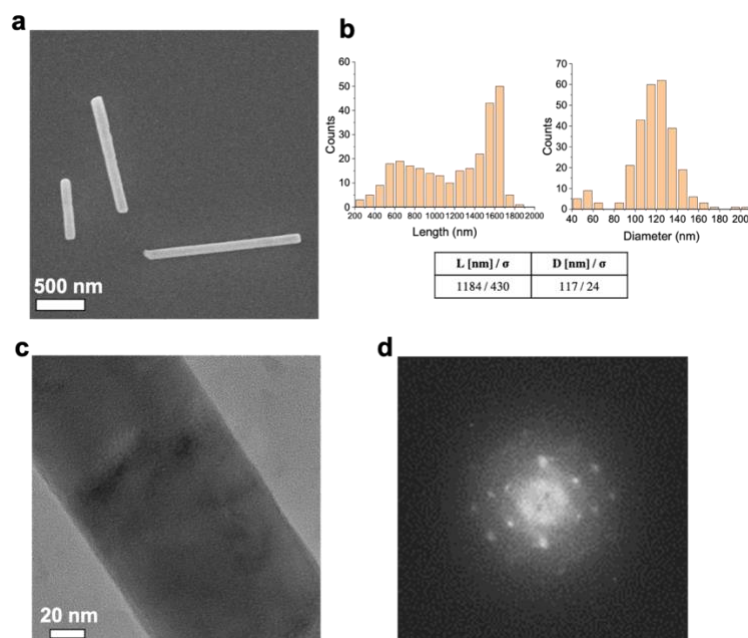


Figure 1.7. (a) Scanning electron microscopy (SEM) image of NaYF₄:Eu nanorods. (b) Measured length and diameter distributions of NaYF₄:Eu nanorods. 276 rods were counted from SEM images. The inset table shows averaged length and diameter of NaYF₄:Eu nanorods with their standard deviation (σ). (c) High-resolution transmission electron microscopy (HR-TEM) image with (d) fast Fourier transformation of NaYF₄:Eu nanorods.

Surface-functionalization of NaYF₄:Eu nanorod by ligand exchange

The resulting particles at the end of synthesis are capped with oleic acid (OA) that is used to prevent aggregation during the solvothermal synthesis process (**Figure 1.8-left**). OA is a fatty acid that grafts to the surface of NaYF₄ crystal, making a particle's surface hydrophobic by the presence of long alkyl chains projecting outward. In this state, synthesized NaYF₄:Eu³⁺ crystals are only soluble in a non-polar organic solvent such as toluene. A ligand exchange was performed to disperse nanoparticles in polar solvents by exchanging native OA ligands with citrate ions that possess large surface charges (**Figure 1.8-right**). Citrate-functionalized nanorods are then stable in a polar solvent by a strong electrostatic repulsion and used to prepare optical samples. Dispersing particles in a polar medium was necessary to produce optical samples with homogeneously deposited individual nanorods by spin-coating.

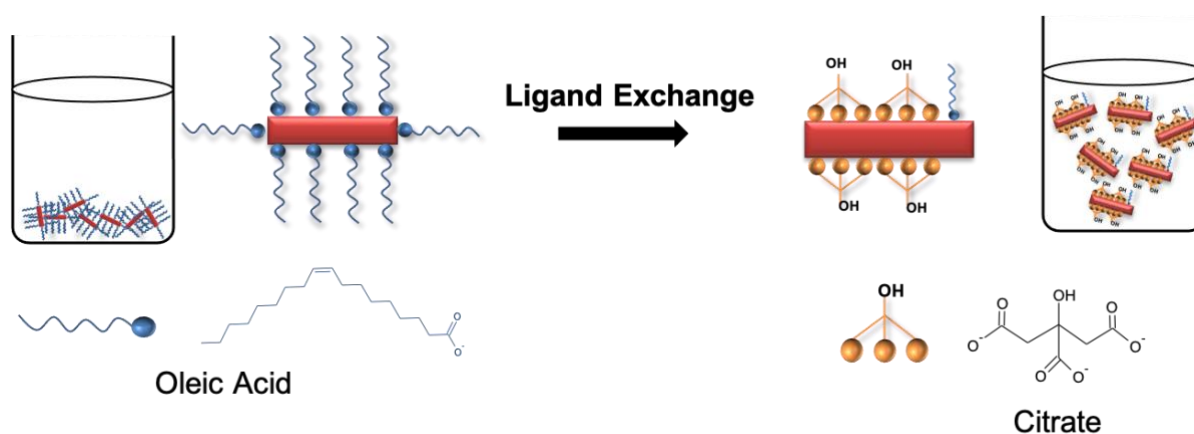


Figure 1.8. Schematic illustration of ligand exchange process from oleic acid (OA) capped nanorod to citrate-functionalized nanorod. The figure is adapted from the reference.³

Removal of NaF particles by-products

At the end of the synthesis, the resulting nanoparticles are a mixture of cubic phased NaF particles and hexagonal phase β -NaYF₄ nanorods (**Figure 1.9a**). After several times of washing process (centrifugation, removing the supernatant, redisperse pellet) during ligand exchange, NaF cubic particles were washed away as they remain in the supernatant owing to their relatively smaller size (requires faster centrifugation speed than the particle having a higher mass to collect as a pellet). At the end of the washing steps, the only citrate functionalized β -NaYF₄ nanorods were collected as pellets and redispersed in a polar solvent. This purification is first confirmed in the SEM images (**Figure 1.9b**) that show only β -NaYF₄ nanorods without cubic NaF particles. Subsequent XRD analysis also confirmed the absence of NaF particles as the peak corresponding to NaF particles disappears after the ligand exchange process (See asterisk sign in **Figure 1.9c**). Such prepared citrate-functionalized β -

NaYF₄ nanorods were stable for years without any sign of aggregation in water or ethylene glycol (EG), as shown in **Figure 1.9d-e**.

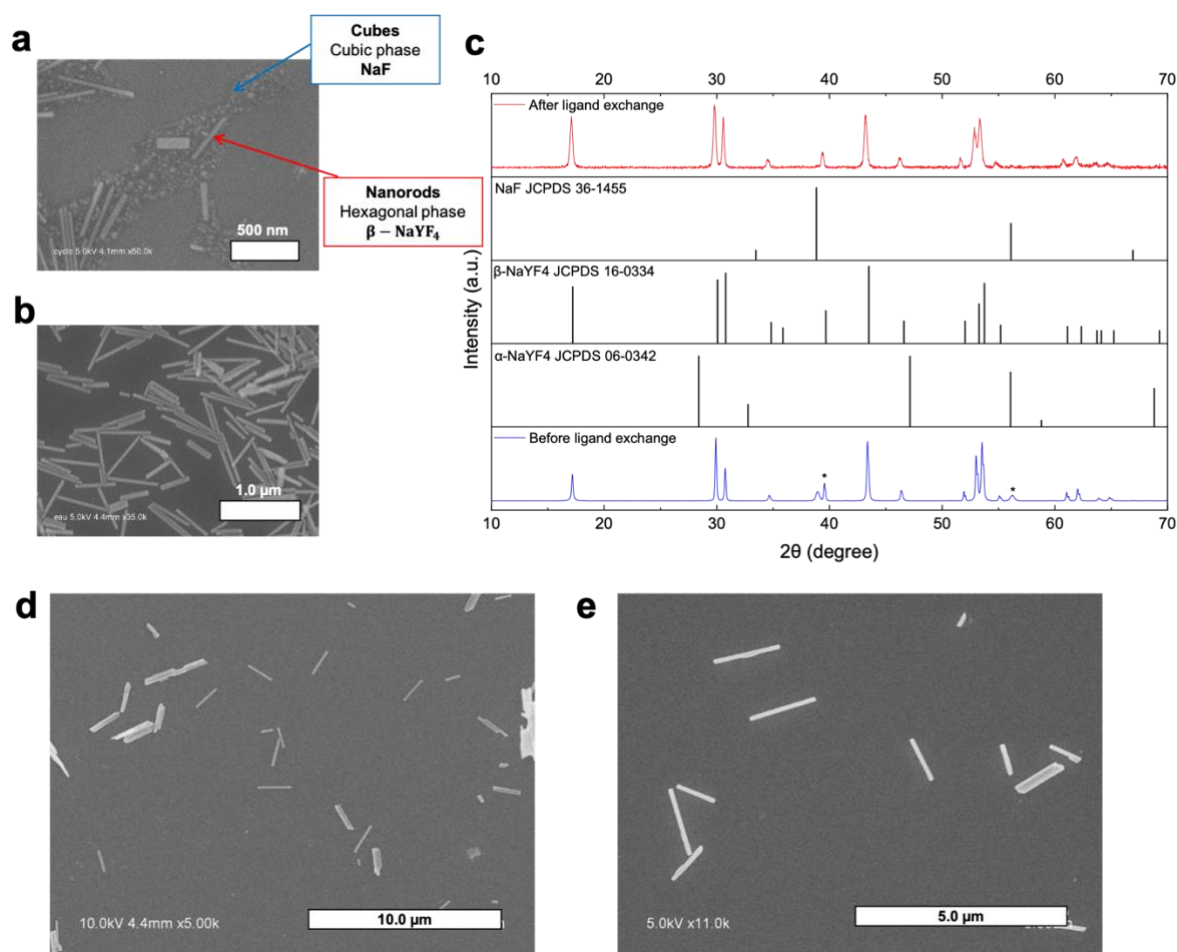


Figure 1.9. Scanning electron microscopy (SEM) image of NaYF₄ nanoparticles **(a)** before and **(b)** after the ligand exchange process. **(c)** XRD pattern of NaYF₄ nanoparticles before (blue line) and after (red line) the ligand exchange process. Reference XRD peaks of cubic NaF (JCPDS 36-1455), hexagonal β-NaYF₄ (JCPDS 16-0334), and cubic α-NaYF₄ (JCPDS 06-0342) are displayed in black line. SEM image of the same batch of surface-functionalized NaYF₄ nanoparticles pictured **(e)** 1.5 years later than the time of **(d)**.

Preparation of optical samples for spectroscopy

As-prepared citrate-functionalized NaYF₄:Eu³⁺ nanorods dispersed in water were then spin-coated on quartz or glass substrates to produce an optical sample where nanorods were spread and lying on the substrate. Quartz substrate gave a relatively less auto-fluorescence intensity than a glass substrate when they were excited by a UV-laser used to excite Eu³⁺ ions doped in NaYF₄ particles. Prior UV-Ozone treatment or plasma treatment to the substrate was essential to enhance the wetting property of substrates

occupation of Y^{3+} sites by Eu^{3+} with a well-controlled doping percentage (here, doping percentage is 5%).^{3, 56}

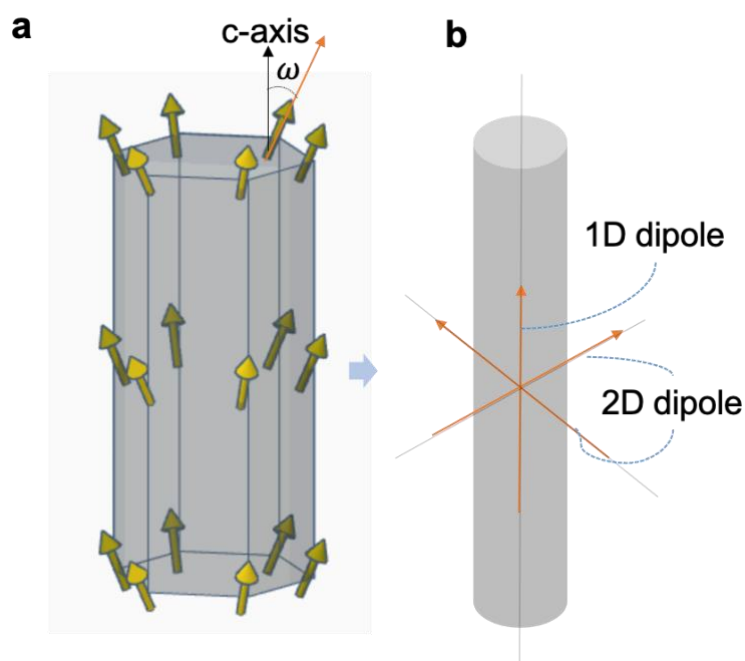


Figure 1.11. Schematic illustration of one kind of emission dipoles at Eu^{3+} ion sites oriented with a certain polar angle (ω) with respect to the c-axis. c-axis is parallel to the geometrical axis of the nanorod. The site symmetry determines ω , and the crystal symmetry induces the hexagonal arrangement of the dipoles. The ensemble of the tilted dipoles in different sites performs a hexagonal symmetry on average, which can be decomposed as an axial component (1D dipole) and a radial component (2D dipole), which are parallel and perpendicular to the c-axis, respectively.

One transition dipole of Eu^{3+} is assumed to have a certain polar angle (ω) with respect to the c-axis of the crystal that is parallel to the geometrical axis of the nanorod (**Figure 1.11**). The symmetry and group theory predicts either purely axial or purely radial dipole for sublevel emission for the C_{3h} symmetry group of the Y site.⁵⁹⁻⁶¹ However, symmetry breaking occurs to a lower C_s site symmetry because of the larger ionic radius of Eu^{3+} in comparison to Y^{3+} .⁶² Most of the few reported experimental observations, including $NaYF_4:Eu$ of our case, show the superposition of the two components manifested as varying degrees of polarization for different sublevel peaks.⁶³⁻⁶⁵ We ascribe this to the tilting of dipoles ($0^\circ < \omega < 90^\circ$) as schematized in **Figure 1.11a** which is probable with low site symmetry.^{62, 66, 67} Further verification of the angle of Eu^{3+} dipole at one site could be made by polarization spectroscopy associated with super-resolution microscopy, which remains as a future work at this state. Also, it would be highly interesting to investigate the degree of polarization (DOP) of emissions of lanthanide ions lightly doped in a single crystal, for which the breakdown of crystallographic site symmetry probably is negligible. Studying the polarized emission of Ho^{3+} doped nanocrystal would also be a good subject as the Ho^{3+} ions have a similar ionic radius to Y^{3+} .

The ensemble of the tilted dipoles in different sites performs a hexagonal symmetry on average, which can be decomposed as an axial component and a radial component (parallel and perpendicular to the c -axis, respectively) (**Figure 1.11b**). The axial component has a 1D nature, whereas the radial component has a degenerate 2D nature due to the in-plane distribution of individual dipoles. Here, the degenerate nature of the radial component is expressed as two orthogonal dipoles off-axis to the rod c -axis.

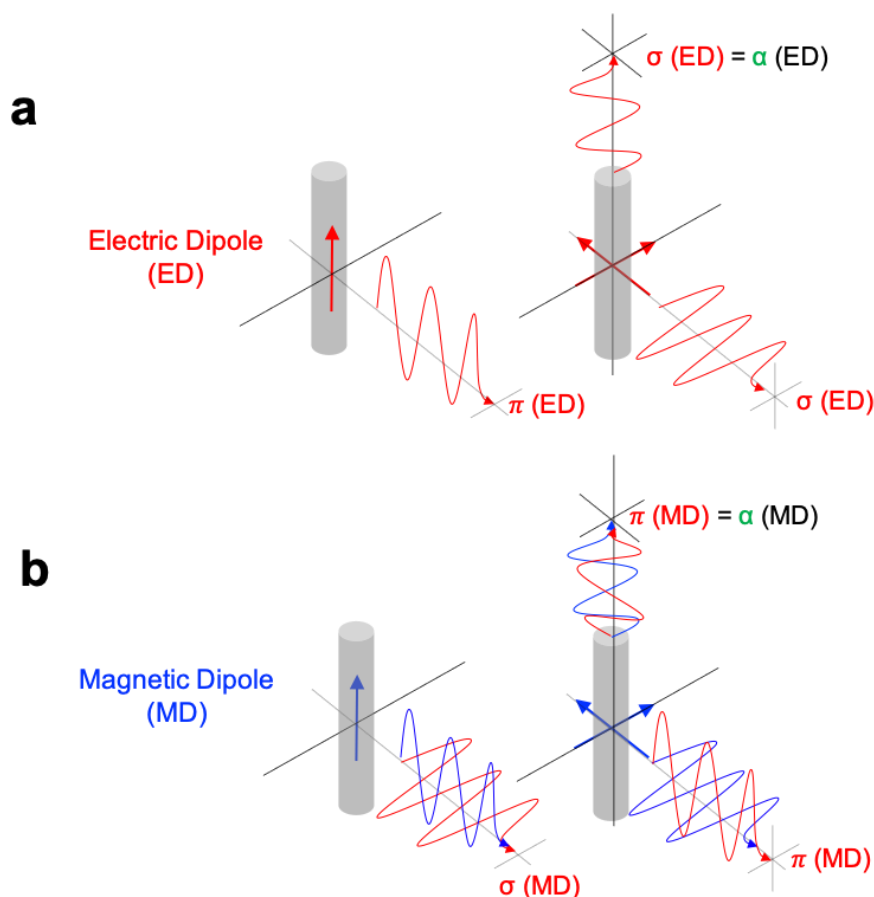


Figure 1.12. Schematic illustrations of the symmetric ensemble of ω -angled dipoles decomposed to two orthogonal components: a 1D dipole parallel to the c -axis and a 2D dipole parallel to the basal plane. For electric dipole (ED), the 1D dipole contributes to the π -polarization and the 2D dipole contributes to the σ -polarization equal to the α -configuration. This relation is inverted for magnetic dipole (MD) as its 1D dipole contributes to the σ -polarization and its 2D dipole contributes to the π -polarization equal to the α -configuration. α -configuration denotes a light propagating along with the rod c -axis, originating from the 2D degenerate dipoles.

In the case of ED (**Figure 1.12a**), where the electric field oscillates along the dipole axis, the light radiated from the axial component is polarized parallel (π) to the c -axis and the light from the radial component is polarized perpendicular (σ) to the c -axis. In the case of MD (**Figure 1.12b**), by contrast, as the electric field is perpendicular to the magnetic field oscillating along the dipole, the light from the axial and radial components are σ - and π -polarized respectively. For both ED and MD, the light propagating along the c -axis (α) is unpolarized as it originates from the 2D nature of the radial components (the unpolarized feature of the α -configuration is shown in **Figure 1.13c**). Note that the

light from 1D dipole parallel to the rod c-axis is not propagating along the rod c-axis. As α -configuration originates from the radial components, α -configuration is identical to the π -configuration for the MD and to the σ -configuration for the ED.

Polarized photoluminescence of NaYF₄:Eu nanorod

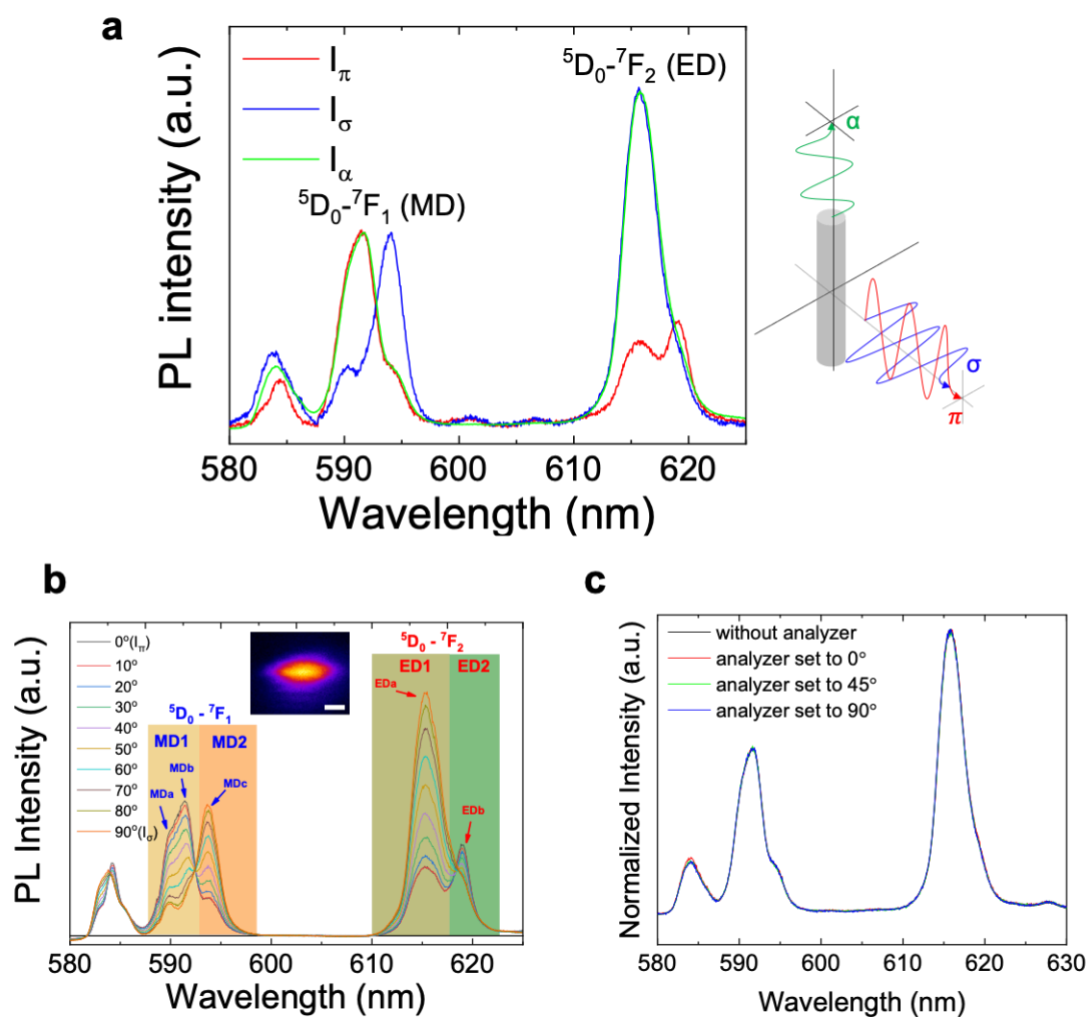


Figure 1.13. (a) Polarized photoluminescence (PL) spectra in π , σ , and α configurations of NaYF₄:Eu nanorods under the excitation at 394 nm (${}^7F_0 \rightarrow {}^5L_6$). These spectra were obtained from a colloidal solution in which the nanorods were uniformly aligned by an external electric field (see **Chapter 2** for detailed experiments). (b) Polarized PL spectra of a single NaYF₄:Eu nanorod lying on a plane substrate with varied analyzer angles. The blue and red arrows indicate the three main peaks (MDa-c) in the ${}^5D_0 \rightarrow {}^7F_1$ transition and the two main peaks (EDa-b) in the ${}^5D_0 \rightarrow {}^7F_2$ transition. The selected wavelength ranges (MD1, MD2, ED1, and ED2) to perform the area under curve ratiometry are highlighted in different colors. The inset is an image of the nanorod obtained by scanning the PL signal using a piezo-stage (scale bar: 1 μm). (c) Emission spectrum of α configuration measured without analyzer and with a rotating analyzer (0°, 45°, 90°).

Figure 1.13a shows the polarized photoluminescence emission spectra of NaYF₄:Eu nanorods in three main configurations (π , σ , and α). These spectra were obtained from aligned colloidal nanorods under an externally applied electric field. Briefly, in-plane aligned nanorods were used to obtain the emission spectra of π and σ configurations by putting the analyzer parallel and perpendicular to the rods' alignment direction, respectively. Vertically aligned nanorods were used to obtain the emission spectrum of α configuration. The experimental detail about the electro-switching experiment are described in **Chapter 2**.^{68, 69} The intense group of peaks at 587~597 nm corresponds to the $^5D_0 \rightarrow ^7F_1$ transition of Eu³⁺ which originates from MDs, and the one at 610~622 nm corresponds to the $^5D_0 \rightarrow ^7F_2$ transition from EDs. Each narrow peak (partially overlapping with the adjacent peaks) corresponds to one sublevel transition split by the crystal field.⁵⁹ One can see that the π and σ spectra are dramatically different to each other and the α spectrum is identical to the π spectrum for the MD transition ($^5D_0 \rightarrow ^7F_1$) and to the σ spectrum for the ED transition ($^5D_0 \rightarrow ^7F_2$). This unique polarization behavior confirms the above-described axial/radial and ED/MD dipolar nature (**Figure 1.12**), which is the basis of the orientation analysis throughout this thesis study. Consequently, π , σ and α spectra are all different from each other considering the whole spectral range. Thus, a spectrum observed from an arbitrary viewing angle would be a weighted sum of the three reference spectra depending on the viewing angle (*i.e.* rod orientation with respect to the observer).

An isolated single NaYF₄:Eu nanorod shows the same π and σ spectra and the continuous line shape variation between them when the analyzer was rotated every 10° with respect to the rod axis lying on a plane substrate (**Figure 1.13b**). The degree of polarization (DOP) for each peak is defined as:

$$\text{DOP} = (I_{\pi} - I_{\sigma}) / (I_{\pi} + I_{\sigma}) \quad (1.1)$$

where I_{π} and I_{σ} stand for the relative intensities of π and σ configurations. The three main peaks within $^5D_0 \rightarrow ^7F_1$ transition (MDa: 589.9 nm, MDb: 591.4 nm, and MDc: 593.7 nm) have DOPs of 0.53, 0.56, and -0.56 respectively, and the two main peaks in $^5D_0 \rightarrow ^7F_2$ transition (EDa: 615.3 nm and EDb: 619.0 nm) have DOPs of -0.56 and 0.21. Therefore, in both MD and ED transitions, there exist at least two peaks with high DOPs, which ensures a precise ratiometric analysis.

The well-defined three peaks in the $^5D_0 \rightarrow ^7F_1$ transition confirm that the 7F_1 level is split into three sublevels by the crystal field in a low symmetry (C_s) of Eu³⁺ sites.⁷⁰ As the low symmetry would split the $^5D_0 \rightarrow ^7F_2$ level into five sublevels,⁷⁰ the broad EDa peak seems to be indeed several sublevels that are merged. When regarding, for simplicity, each of EDa and EDb as one dipole, the positive DOP of EDa ($I_{\pi} > I_{\sigma}$) indicates the dipole axis close to the c -axis ($\omega < 45^\circ$) and the negative DOP of EDb indicates the dipole lying close to the basal plane ($\omega > 45^\circ$). This relation is inversed for MD peaks due to the orthogonality of electric and magnetic fields (*i.e.*, positive DOP of MD indicates its dipole axis close to the basal plane).

In the following sections, the analytical method is provided to determine the 3D orientation of a nanorod based on the intrinsic emission polarization property of NaYF₄:Eu described above.

Summary of Chapter 1.2

Europium doped NaYF₄ nanorods with a micrometer size are solvothermally synthesized and surface functionalized to prepare samples for optical spectroscopy. Lanthanide doped nanorods exhibit a different nature of polarization depending on the different nature of the transitions - magnetic (MD) or electric dipole (ED). When the europium ions are inserted in crystalline sites of the host crystal having a hexagonal symmetry, the tilted emission dipoles perform a symmetry on average. As a result, it exhibits a unique relationship between polarized spectra collected with analyzer either parallel (I_{π}) or perpendicular (I_{σ}) to the main axis of nanorod and reference spectrum collected along the main axis (I_{α}): $I_{\pi} = I_{\alpha}$ in MD transition, and $I_{\sigma} = I_{\alpha}$ in ED transition. This relationship is the basis of the orientation analysis throughout this thesis study.

1.3. Orientation analysis of NaYF₄:Eu single nanorod

1.3.1. Theoretical methodology for orientation analysis

For a nanorod with arbitrary orientation in the laboratory frame by polar and azimuthal angles (θ , φ) (**Figure 1.14a**), the emission intensities collected at two orthogonal polarization angles, I_{zx} and I_{zy} (first and second subscripts refer to the axes of propagation and polarization respectively), have contributions of the π , σ and α configurations as their projections on the measurement axis. Note that the equations described below were written under the assumption where the emission is collected along a certain viewing angle with a numerical aperture (N.A.) near zero. In real experiments, microscope objectives have certain values of N.A. and the equations should spatially integrate the emission over the N.A. We have compared the orientation analyses with the integrated calculation and with the following equations assuming zero-N.A. using the reference π , σ and α spectra obtained with a given microscope objective, and we found that the results of the two are very similar within the experimental error range.⁶⁷ This confirms that the method of calculation presented below is a valid approximation when using conventional microscopes with different objectives.

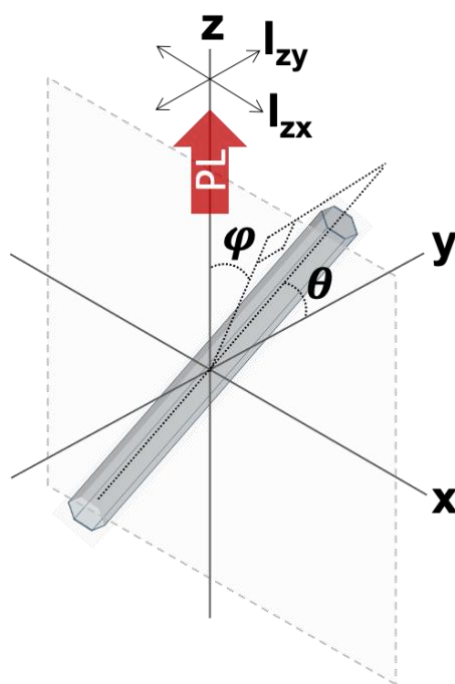


Figure 1.14. (a-b) Schematic illustration of a hexagonal crystalline NaYF₄:Eu nanorod with an arbitrary 3D orientation denoted by the spherical angles (θ , φ) when the polar axis is y-axis. The observation plane is fixed as xy-plane.

For a given wavelength (λ):

$$I_{zx}(\lambda) = I_{\pi}(\lambda) \cdot \sin^2\theta \cdot \sin^2\varphi + I_{\sigma}(\lambda) \cdot \cos^2\theta + I_{\alpha}(\lambda) \cdot \sin^2\theta \cdot \cos^2\varphi \quad (1.2)$$

$$I_{zy}(\lambda) = I_{\pi}(\lambda) \cdot \cos^2\theta + I_{\sigma}(\lambda) \cdot \sin^2\theta \cdot \sin^2\varphi + I_{\alpha}(\lambda) \cdot \sin^2\theta \cdot \cos^2\varphi \quad (1.3)$$

where I_{π} , I_{σ} , and I_{α} indicate the relative intensities of the π , σ and α configurations.

As the α spectrum is identical to the σ spectrum for ED and to the π spectrum for MD (**Figure 1.13a**), the above equations can be rewritten separately as functions of only I_{π} and I_{σ} as (see also **Appendix Note 1.1** for more details about the origin of the below-written equations):

for ED transition,

$$I_{zx,ED}(\lambda) = I_{\pi,ED}(\lambda) \cdot \sin^2\theta \cdot \sin^2\varphi + I_{\sigma,ED}(\lambda) \cdot (\cos^2\theta \cdot \sin^2\varphi + \cos^2\varphi) \quad (1.4)$$

$$I_{zy,ED}(\lambda) = I_{\pi,ED}(\lambda) \cdot \cos^2\theta + I_{\sigma,ED}(\lambda) \cdot \sin^2\theta \quad (1.5)$$

and for MD transition,

$$I_{zx,MD}(\lambda) = I_{\sigma,MD}(\lambda) \cdot \cos^2\theta + I_{\pi,MD}(\lambda) \cdot \sin^2\theta \quad (1.6)$$

$$I_{zy,MD}(\lambda) = I_{\sigma,MD}(\lambda) \cdot \sin^2\theta \cdot \sin^2\varphi + I_{\pi,MD}(\lambda) \cdot (\cos^2\theta \cdot \sin^2\varphi + \cos^2\varphi) \quad (1.7)$$

Hence, one can choose a single polarization axis (for either I_{zx} or I_{zy}) to get two simultaneous equations on ED and MD from which the unknown θ and φ values can be calculated. As the ED and MD transitions occur simultaneously in lanthanides, a single emission spectrum is sufficient to determine the 3D orientation (θ , φ) of a nanorod. It is also apparently possible to choose one transition (either ED or MD) at two polarization axes (see **Appendix Figure 1.1** and **Appendix Table 1.2-3**). The choice of two equations among the four above can indeed be made as preferred considering the material property such as the DOP of the transition and the experimental condition such as the type, number, and spectral resolution of the detectors.

Conversion of the coordinates

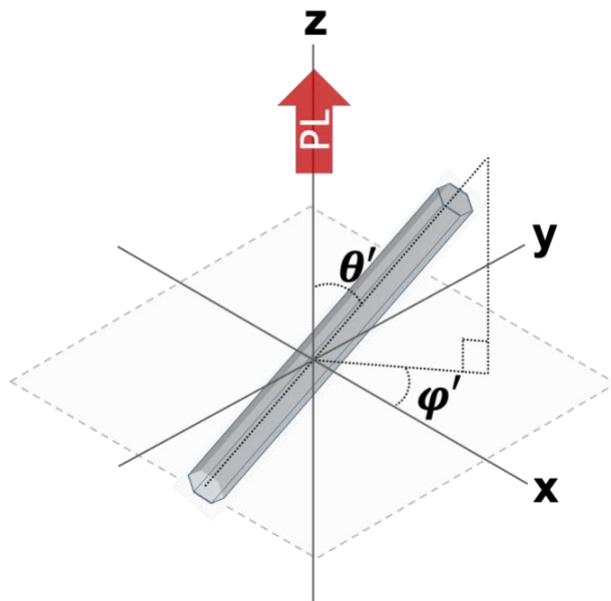


Figure 1.15. Schematic illustration of a hexagonal crystalline NaYF₄:Eu nanorod with an arbitrary 3D orientation denoted by the spherical angles (θ' , φ') when the polar axis is z-axis respectively. The observation plane is fixed as xy-plane.

The y-axis in the laboratory frame was chosen as the polar axis related to the (θ , φ) angles (**Figure 1.14**), which simplifies **Equations 1.4-7**. A transformation of (θ , φ) into a new spherical coordinate with the z-axis as its polar axis (**Figure 1.15**) can be made by the following equations. Spherical coordinates (1 , θ , φ) of a nanorod can be expressed in cartesian coordinates system (x , y , z) (**Figure 1.14-15**) as:

$$x \text{ coordinate} = \sin\theta \cdot \sin\varphi = \sin\theta' \cdot \cos\varphi' \quad (1.8)$$

$$y \text{ coordinate} = \cos\theta = \sin\theta' \cdot \sin\varphi' \quad (1.9)$$

$$z \text{ coordinate} = \sin\theta \cdot \cos\varphi = \cos\theta' \quad (1.10)$$

Now, out-of-plane angle θ' can be calculated from determined angle set (θ , φ) using **Equations 1.10**, and the in-plane angle φ' can be calculated by using **Equation 1.8-9** as summarized in **Equation 1.11-12**.

$$\theta' = \cos^{-1}(\sin\theta \cdot \cos\varphi) \quad (1.11)$$

$$\varphi' = \sin^{-1} \left(\frac{\cos\theta}{\sin\theta'} \right) = \sin^{-1} \left(\frac{\cos\theta}{\sqrt{1 - \cos^2\theta'}} \right) = \sin^{-1} \left(\frac{\cos\theta}{\sqrt{1 - \sin^2\theta \cdot \cos^2\varphi}} \right) \quad (1.12)$$

where (θ', φ') are the polar and azimuthal angles in the new coordinate which is more intuitive for the observer: φ' and θ' correspond to the in-plane and out-of-plane orientation angles with respect to the observation plane (**Figure 1.15**).

1.3.2. Orientation analysis by spectral fitting and area under curve ratiometry

Optical experiment

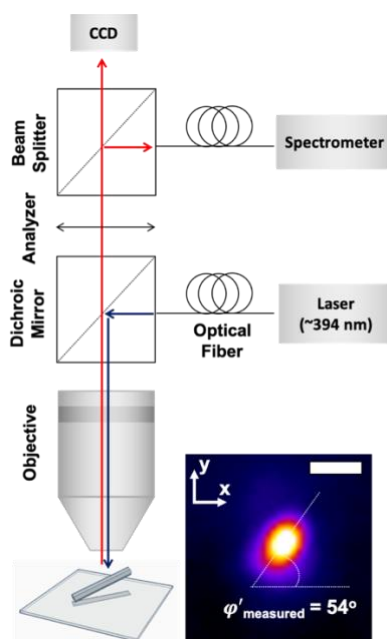


Figure 1.16. A scheme of the optical microscopy setup used to conduct the orientation analysis. The inset is a photograph of the photoluminescence (PL) of a single nanorod captured by the CCD camera (scale bar: 1 μm). The in-plane angle (φ') of the nanorod was found as the long axis of the ellipsoidal shape of this image.

In order to test the discussed methodology, we have prepared $\text{NaYF}_4:\text{Eu}$ nanorods that are embedded in a thick polymer film with random orientation, as discussed above. The individual dispersion of the nanorods was achieved by mixing citrate-functionalized nanorods with an aqueous solution of polyvinyl alcohol (PVA) at very low rod-concentration, which was then drop-casted on a glass coverslip. The refractive index of PVA is ~ 1.5 , close to ~ 1.52 for a standard glass coverslip. The optical environment surrounding the $\text{NaYF}_4:\text{Eu}$ nanorods can thus be regarded as homogeneous and not significantly distorting the emission dipoles even near the polymer-glass interface. Photoluminescence

measurements and nanorod observations were carried out using a conventional optical microscope equipped with a fiber-coupled excitation laser ($\lambda_{\text{ex}} = 394 \text{ nm}$, matching with the ${}^7\text{F}_0 \rightarrow {}^5\text{L}_6$ transition line), a spectrometer, and a CCD camera (**Figure 1.16**).

A photograph of photoluminescence (PL) emitting nanorod captured by the CCD camera (**Figure 1.16-inset**) shows a slightly elliptical shape of the spot due to the out-of-plane tilt of the embedded nanorod (length $\sim 1 \mu\text{m}$). The in-plane projection of the nanorod length in this case is close to the spatial resolution of the optical microscope. The long axis of the ellipsoid provides the azimuthal orientation ϕ' of the nanorod. Its measured value of 54° will be compared below with the calculated one from the polarized emission spectra. Only the in-plane projection of the 3D orientation of the nanorod is barely discernible even though the rod size was controlled to be relatively large. Particles smaller than the spatial resolution of the microscope or in a vertical orientation ($\theta' \sim 0^\circ$) will appear in a circular shape on such images.

Orientation analysis by spectral fitting

The polarized photoluminescence emission spectra were collected using a rotating analyzer in front of the spectrometer (**Figure 1.17a-d**). As discussed above, the line shape of each spectrum on both ED and MD ranges contains information on the 3D orientation of the nanorod. By fitting one of these spectra (I_{zx} or I_{zy}) separately in ED and MD wavelength ranges with the reference π - and σ -polarized spectra (I_π , I_σ), the (θ, φ) values were obtained using **Equations 1.4-7**, which were then converted to (θ', φ') using **Equations 1.11-12**. Reference π - and σ -polarized spectra (I_π , I_σ) used for the orientation analysis are obtained from a single NaYF₄:Eu nanorod lying on the substrate by putting a polarizer parallel or perpendicular to the main axis of the nanorod. It can be seen in **Figure 1.17** that the fitting curves (magenta lines) as weighted sums of the I_π , I_σ curves (red and blue lines) match well with the observed I_{zx} and I_{zy} spectra (black lines). The two sets of $(\cos^2\theta, \sin^2\varphi, \text{ and } \theta', \varphi')$ values calculated from the two polarizations (I_{zx}, I_{zy}) are presented in the same figure. The φ' values calculated from I_{zx} and I_{zy} using both MD and ED (**Figure 1.17a-b**) are 59° and 52° and the φ' values calculated from ED and MD using both I_{zx} and I_{zy} (**Figure 1.17c-d**) are 57° and 54° respectively while the measurement on the CCD-captured image was 54° . The several degrees of error and discrepancy between different selections of the analyzer angle are ascribed to be due to the experimental errors such as the alignment of the analyzer and the polarization-dependent fluctuation of the background offset on the spectrograms. Errors in orientation analysis are discussed more in detail in **Chapter 1.3.3**. We conducted the same orientation analysis repeatedly on 33 randomly oriented single nanorods in the polymer film and the mean absolute error (average of the difference between the angle determined by direct PL imaging and

by spectroscopic orientation analysis) for φ' was 4.6° (**Appendix Table 1.4**). The out-of-plane angle (θ') remains incomparable as CCD images a projection. The deviation in (θ' , φ') values were less than 4° on average compared with the values calculated either using a different polarization (I_{zx} or I_{zy} using both MD and ED transition) or using a different dipole transition (MD or ED emission using both I_{zx} and I_{zy} polarizations) (**Appendix Table 1.2-4**), confirming wide applicability of the proposed method to various materials and experimental conditions.

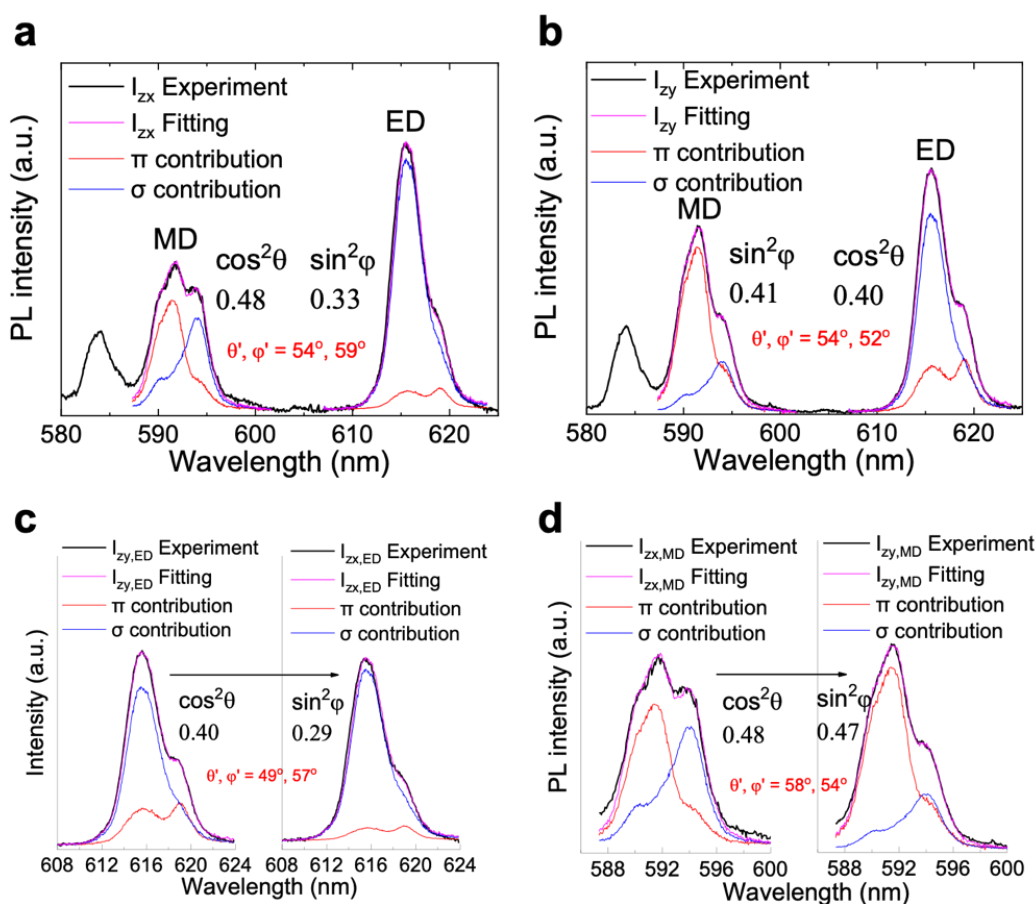


Figure.1.17. (a-b) Spectral fitting analysis using a polarized PL spectrum I_{zx} or I_{zy} obtained with the analyzer (a) parallel to the x-axis or (b) parallel to the y-axis. Each analysis considers both ED and MD transitions in order to determine θ and φ from a single spectrum. (c-d) Spectral fitting orientation analysis on single dipole of (c) ED and (d) MD using two orthogonal polarizations (I_{zx} , I_{zy}). The calculated values of the trigonometric functions of (θ , φ) and the absolute values of (θ' , φ') are presented in the figure. The results of the same analysis for different particles are shown in **Appendix Figure 1.1** and **Appendix Table 1.2-3**.

The same orientation analysis is also conducted on 21 different nanorods directly deposited on the substrate without polymer: $\theta' = 90^\circ$ (**Appendix Table 1.3**). In this case, the mean absolute errors for θ' and φ' were 13.1° and 3.2° (**Appendix Table 1.4**). We found that the mean errors for θ' and φ' can vary depending on their absolute values because they are calculated from sinusoidal curves. The errors are relatively large when θ' or φ' is close to 0° or 90° (i.e., when the rods are oriented parallel or perpendicular to the analyzer or the substrate). This is why the mean error for θ' is larger than that of

φ' for the rods lying on the substrate ($\theta' = 90^\circ$). At this specific orientation condition of the nanorod, a small experimental error in the spectral fitting may cause the analysis to fail. Errors in orientation analysis are discussed in **Section 1.3.3**.

Orientation analysis by area under curve ratiometry

The spectral fitting analysis minimizes the error in calculating (θ' , φ') values. This requires spectra recorded with a spectrometer. Other types of detectors such as photomultiplier tube (PMT), avalanche photodiode (APD), or electron multiplying CCD are often preferred when higher photosensitivity or spatially resolved photography is desired. In such cases, the photons emitted in four different spectral ranges can be separately collected using a combination of dichroic mirrors and optical bandpass filters. The detected signal intensities are then proportional to the integrated areas under the spectrum curve in the selected ranges. The ratiometry between the signal intensities in different ranges can be used to calculate (θ' , φ') angles instead of the spectral fitting analysis.

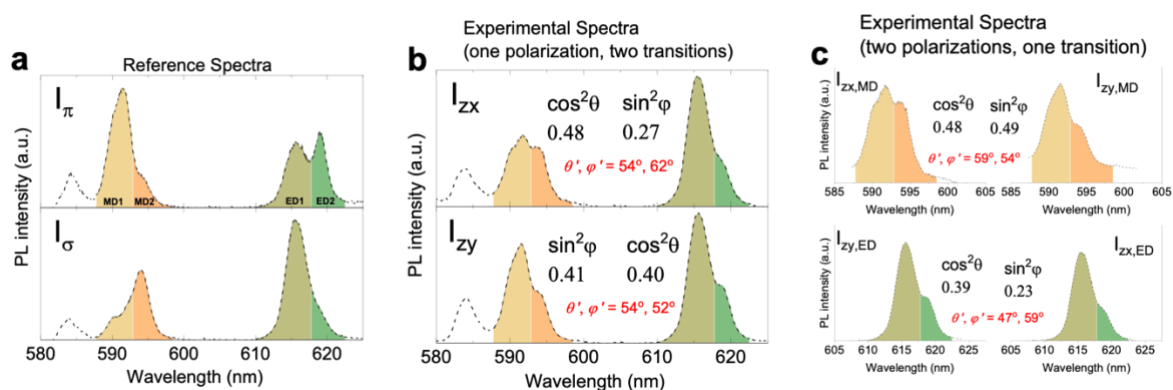


Figure 1.18. (a) Reference emission spectra of the photoluminescence (PL) of a NaYF₄:Eu nanorod polarized parallel (I_π) and perpendicular (I_σ) to the rod axis. Experimental spectra using (b) one polarization (I_{zx} or I_{zy}) with two transitions (MD and ED) or (c) two polarizations (I_{zx} and I_{zy}) using one transition (MD or ED) of the nanorod shown in **Figure 1.17**. The selected wavelength ranges (MD1, MD2, ED1, and ED2) used for the area under curve ratiometry (AUCR) are highlighted in different colors, from which the values of the trigonometric functions of (θ , φ) and the absolute values of (θ' , φ') were calculated using **Equations 1.13-16** and **Equations 1.11-12**. The results of the same AUCR analysis for different particles are shown in **Appendix Table 1.2-3**.

Theoretical methodology for orientation analysis by area under curve ratiometry

The **Equations 1.4-7**, with the intensities as continuous functions of wavelength, can be rewritten with the integrated intensities for divided ranges referred to as ED1, ED2, MD1, and MD2 (**Figure 1.18a-c**), from which the $\cos^2\theta$ and $\sin^2\varphi$ can be expressed as:

for ED transition,

$$\cos^2\theta = \frac{k_{zy,ED} \cdot I_{\sigma,ED2} - I_{\sigma,ED1}}{k_{zy,ED} \cdot (I_{\sigma,ED2} - I_{\pi,ED2}) - (I_{\sigma,ED1} - I_{\pi,ED1})} \quad (1.13)$$

$$\sin^2\varphi = \frac{k_{zx,ED} \cdot I_{\sigma,ED2} - I_{\sigma,ED1}}{(1 - \cos^2\theta) \cdot [(I_{\pi,ED1} - I_{\sigma,ED1}) - k_{zx,ED} \cdot (I_{\pi,ED2} - I_{\sigma,ED2})]} \quad (1.14)$$

where $I_{\pi,EDn}$ and $I_{\sigma,EDn}$ ($n = 1$ or 2) indicate the relative area under curve of the π and σ spectra (**Figure 1.18a**) and $k_{zy,ED}$ and $k_{zx,ED}$ stand for the measured intensity ratios $I_{zy,ED1}/I_{zy,ED2}$ and $I_{zx,ED1}/I_{zx,ED2}$, respectively (**Figure 1.18b-c**).

And for MD transition,

$$\cos^2\theta = \frac{k_{zx,MD} \cdot I_{\pi,MD2} - I_{\pi,MD1}}{k_{zx,MD} \cdot (I_{\pi,MD2} - I_{\sigma,MD2}) - (I_{\pi,MD1} - I_{\sigma,MD1})} \quad (1.15)$$

$$\sin^2\varphi = \frac{k_{zy,MD} \cdot I_{\pi,MD2} - I_{\pi,MD1}}{(1 - \cos^2\theta) \cdot [(I_{\sigma,MD1} - I_{\pi,MD1}) - k_{zy,MD} \cdot (I_{\sigma,MD2} - I_{\pi,MD2})]} \quad (1.16)$$

where $I_{\pi,MDn}$ and $I_{\sigma,MDn}$ ($n = 1$ or 2) indicate the relative area under curve of the π and σ spectra (**Figure 1.18a**) and $k_{zx,MD}$ and $k_{zy,MD}$ stand for $I_{zx,MD1}/I_{zx,MD2}$ and $I_{zy,MD1}/I_{zy,MD2}$, respectively (**Figure 1.18b-c**). The orientation determination proceeds similar with the spectral fitting analysis. One can choose one polarization axis (I_{zx} or I_{zy}) and use both ED and MD transitions or one can choose one transition (ED or MD) and use two polarizations (I_{zx} and I_{zy}). Once a set of two k values among $k_{zx,ED}$, $k_{zx,MD}$, $k_{zy,ED}$, and $k_{zy,MD}$, calculation of (θ, φ) values using a set of two equations among **Equation 1.13-16** can be performed.

This ratiometric analysis was performed on the same polarized photoluminescence spectra used for the fitting analysis to compare the accuracy of the two methods. The reference areas under curve ($I_{\pi,MD1}$, $I_{\pi,MD2}$, $I_{\pi,ED1}$, $I_{\pi,ED2}$ and $I_{\sigma,MD1}$, $I_{\sigma,MD2}$, $I_{\sigma,ED1}$, $I_{\sigma,ED2}$) were measured on the reference π and σ spectra (**Figure 1.18a**). The areas under curve on the experimental spectra ($I_{zx,MD1}$, $I_{zx,MD2}$, $I_{zx,ED1}$, $I_{zx,ED2}$ and $I_{zy,MD1}$, $I_{zy,MD2}$, $I_{zy,ED1}$, $I_{zy,ED2}$) were measured for the same spectral ranges (**Figure 1.18b-c**), from which

the k values ($k_{zx,MD}$, $k_{zx,ED}$, $k_{zy,MD}$, and $k_{zy,ED}$) were obtained and the (θ, φ) and finally (θ', φ') values were calculated using **Equations 1.13-16** and **Equations 1.11-12**. The deviation in (θ', φ') values for a number of tested nanorod samples were less than 2° on average compared with the values calculated by the spectral fitting analysis (**Appendix Table 1.2-3**). The mean absolute error is also similar to that of the spectral fitting analysis. (**Appendix Table 1.4**). The area under curve ratiometry is thus a good alternative method of spectral fitting analysis, almost maintaining the accuracy of orientation measurement. Examples of the optical filter that can be used for ratiometric orientation calculation of NaYF₄:Eu or LaPO₄:Eu nanoparticles are shown in **Appendix Figure 1.2** and **Appendix Figure 1.3**.

How to obtain the best precision of orientation analysis through ratiometry approach

The best precision of the ratiometry approach can be achieved by adequately selecting the wavelength ranges (ED1, ED2, MD1, and MD2) to have the highest DOP in each range. As highlighted in the diagram of the series of reference spectra for varied analyzer angles (**Figure 1.13b**), the similarly polarized neighboring sublevel peaks were grouped in one range.

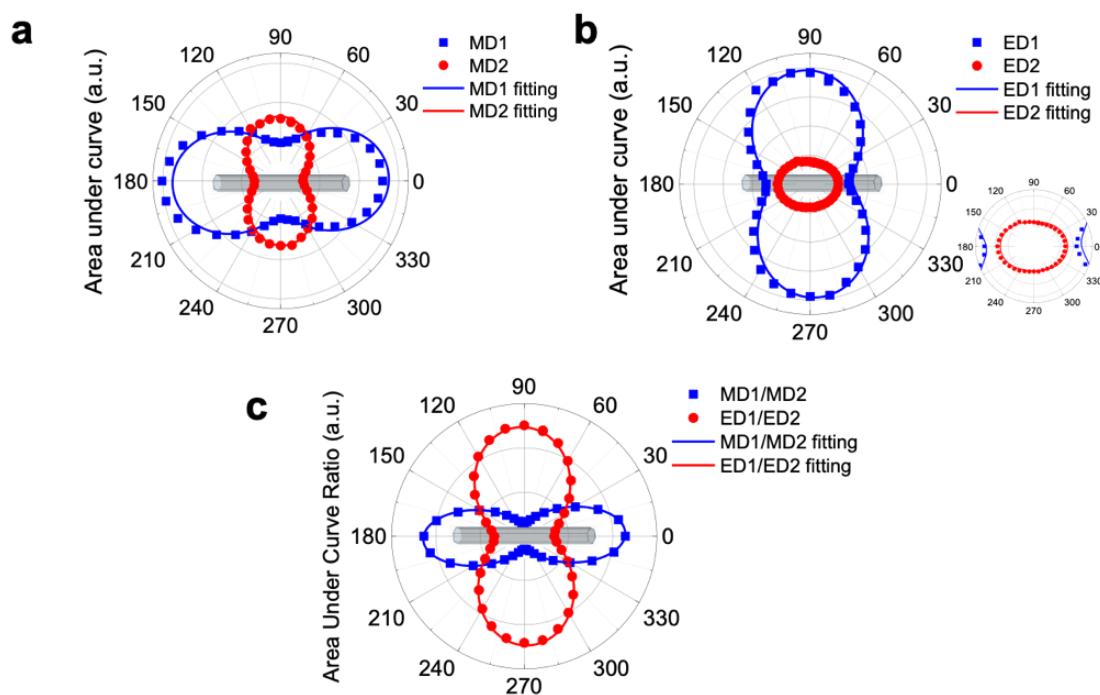


Figure 1.19. (a-b) Polar diagrams and fitting curves of the selected areas under curve for (a) MD1 and MD2, (b) ED1 and ED2, and (c) their ratios MD1/MD2 and ED1/ED2.

For example, the MDa (589.9 nm) and MDb (591.4 nm) peaks were grouped as MD1 and the MDc (593.7 nm) peak was defined as MD2. **Figure 1.19a-b** shows polar diagrams of the in-planned oriented nanorod plotted for the varied areas under curve as a function of the analyzer angle (χ). The data points

should in principle fit with a simple trigonometric equation (**Equation 1.17**) implying a sum of the projections of the π and σ components:

$$I_{\chi} = I_{\pi} \cdot \cos^2(\chi) + I_{\sigma} \cdot \sin^2(\chi) \quad (1.17)$$

However, the experimental points are not perfectly matching with the fitting lines for the **Equation 1.17**. This typical mismatch is caused by signal fluctuation during scanning over χ -angles or by the beam distortion along the optical setup. The points for $\chi = 120^\circ$ in **Figure 1.19b** markedly deviate from the fitting line presumably due to the fluctuation of the excitation source. And the asymmetry of the polar diagram for MD1 in **Figure 1.19a** (left arc is larger than the right) seems to be due to a slight distortion of the emission beam path when rotating the analyzer. Nevertheless, the ratiometric polar diagrams of the k -values (**Figure 1.19c**) consistently match the fitting curves by virtue of the simultaneous measurements of the emission peaks in different wavelength ranges. Such a high precision of the k -polar diagrams was preserved even when the overall emission intensity was largely varied during scanning χ from 0° to 360° . **Figure 1.20** shows one extreme example where the global intensity variation is much higher. The k -polar diagram nevertheless fits perfectly with theoretical estimation (**Figure 1.20d**).

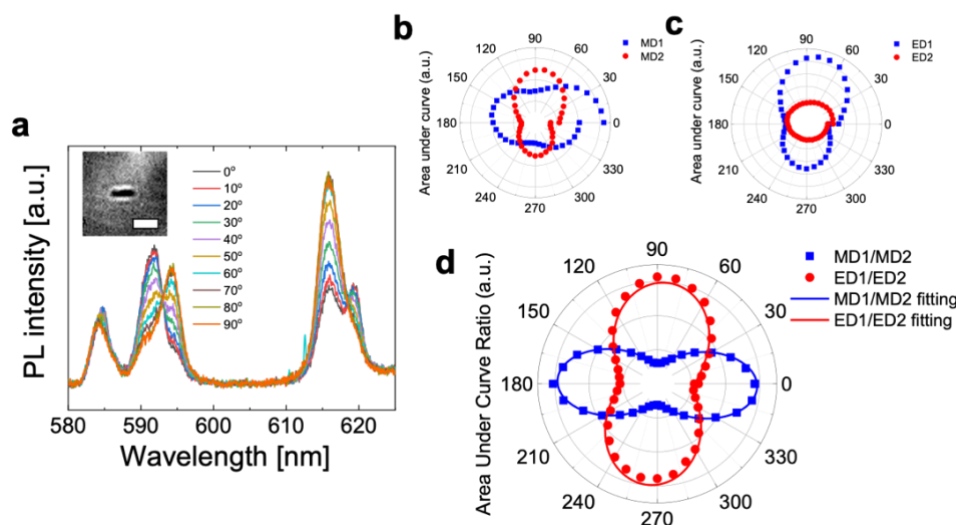


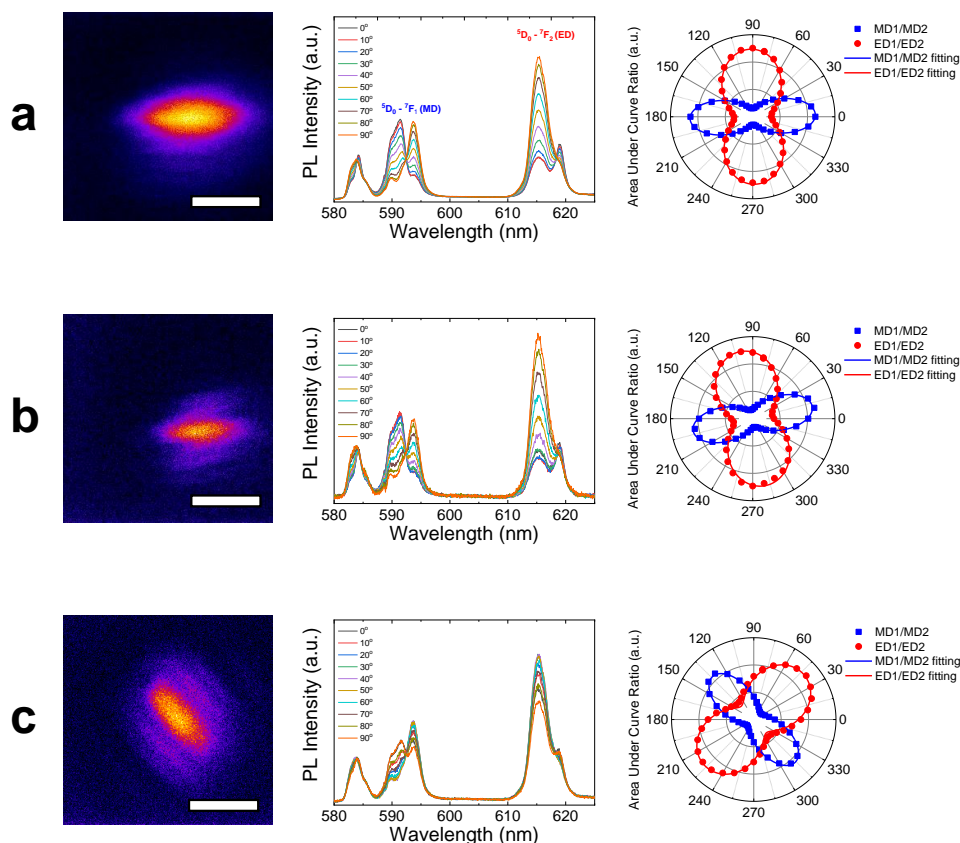
Figure 1.20. (a) Polarized PL spectra of a single $\text{NaYF}_4:\text{Eu}$ nanorod lying on a plane substrate with varied analyzer angles. The inset is an image of CCD captured nanorod by white-light illumination (scale bar = $3 \mu\text{m}$). (b-d) Polar diagrams of the selected areas under curve for (b) MD1 and MD2, (c) ED1 and ED2, and (d) their ratios MD1/MD2 and ED1/ED2. The selected wavelength ranges (MD1, MD2, ED1, and ED2) to perform the area under curve ratiometry are highlighted in **Figure 1.13b**.

This feature represents the outstanding accuracy of our *spectroscopic* orientation analysis by both the spectral fitting and area under curve ratiometry methods. Moreover, the k -polar diagrams (**Figure 1.19c**) are narrower in the cervical region due to the combination of the DOPs for different wavelength ranges. The DOP values for MD1/MD2 and ED1/ED2 are 0.77 and -0.57, respectively (for $\text{NA} = 0.6$), higher

than the DOPs of each peak. This also assures a higher accuracy to determine (θ', φ') values compared to an analysis based on measuring the variation of an absolute intensity of a single emission peak.

DOP analysis of polarized photoluminescence of NaYF₄:Eu particles in different sizes

We checked that the DOPs of five randomly selected nanorods with different sizes are all the same (**Figure 1.21, Table 1.1**), confirming that the lanthanide emission is independent of the particle morphology and that the orientation analysis is robust against polydisperse systems. This is thanks to that the orientation of each dipole axis within the crystal is determined exclusively by the crystal structure and the local site symmetry of the lanthanide dopants, as discussed in the introduction. Plotted polar diagram of area under curve ratio (MD1/MD2 and ED1/ED2) showed no noticeable difference for different nanorods (**Figure 1.21-third column**). DOP value obtained from particles of different sizes shows negligible deviation (less than 5%), as shown in **Table 1.1**. The small but existing deviation is due to the experimental errors: instrument noise, baseline, slight peak shift, *etc.*



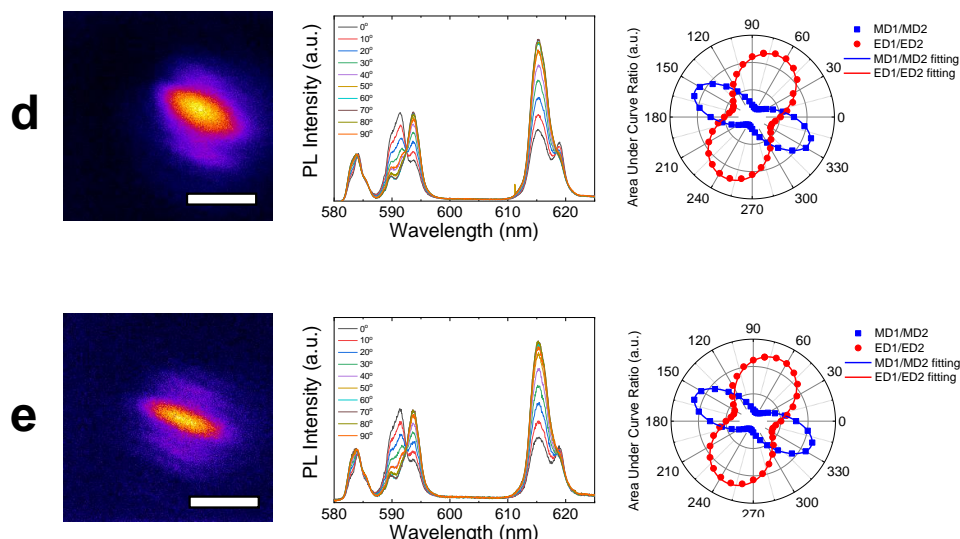


Figure 1.21. (a-e) Polarized photoluminescence of five randomly selected NaYF₄:Eu nanorods with different sizes. First column shows an image of the nanorod obtained by scanning the PL signal using a piezo-stage (scale bar: 2 μ m). Second column shows polarized PL spectra of corresponding NaYF₄:Eu nanorod lying on a plane substrate with varied analyzer angles. Third column shows polar diagrams of the selected areas under curve for the ratios of MD1/MD2 and ED1/ED2. The selected wavelength ranges (MD1, MD2, ED1, and ED2) to perform the area under curve ratiometry are highlighted in **Figure 1.13b**. Calculated DOPs of these ratios are presented in **Table 1.1**.

Table 1.1. Calculated DOPs of area under curve ratio (MD1/MD2 and ED1/ED2) of polarized PL spectra of NaYF₄:Eu nanorods with different sizes (**Figure 1.21**). DOP is calculated according to **Equation 1.1**.

		I_{π}	I_{σ}	DOP		I_{π}	I_{σ}	DOP
Figure 1.21a	MD1/MD2	4.57	0.60	0.77	ED1/ED2	1.34	4.94	-0.57
Figure 1.21b		4.43	0.64	0.75		1.34	4.99	-0.58
Figure 1.21c		4.35	0.66	0.74		1.34	4.92	-0.57
Figure 1.21d		4.58	0.64	0.75		1.34	4.88	-0.57
Figure 1.21e		4.59	0.63	0.76		1.34	4.91	-0.57

DOP analysis of polarized photoluminescence of NaYF₄:Eu particles using a different numerical aperture of objective

The measured DOPs decrease as the NA of the microscope objective increases because the emission towards a wider solid angle is averaged (**Figure 1.22, Table 1.2**). There is a tradeoff between the spatial resolution – for which large NA is favored – and the accuracy of orientation analysis – for which high DOPs by small NA are favored. An optimal NA is to be selected considering the specific experimental requirements.

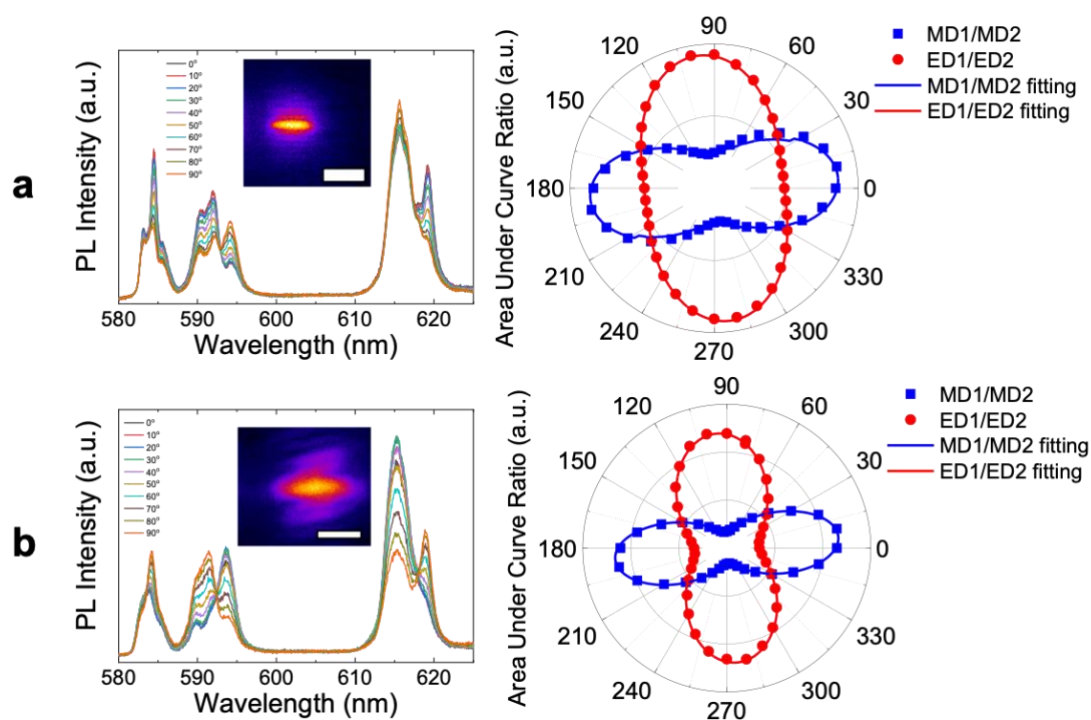


Figure 1.22. (a,b) Polarized photoluminescence spectra of NaYF₄:Eu nanorod measured using an objective numerical aperture of (a) 1.49 and (b) 0.6. First column shows the polarized PL spectra of a single NaYF₄:Eu nanorod lying on a plane substrate with varied analyzer angles. The inset is an image of the nanorod obtained by scanning the PL signal using a piezo-stage (scale bar: 2 μ m). Second column shows a polar diagram of the selected areas under curve for the ratios of MD1/MD2 and ED1/ED2. The selected wavelength ranges (MD1, MD2, ED1, and ED2) to perform the area under curve ratiometry are highlighted in **Figure 1.13b**. Calculated DOPs of these ratios are presented in **Table 1.2**.

The detected line shape of polarized photoluminescence varies depending on the numerical aperture (NA) of objective, as shown in **Figure 1.22** and **Table 1.2**. Spectra are measured separately using a different particle that has a different size. As morphology does not affect the polarization behavior (**Figure 1.21, Table 1.1**), the difference of line shape and calculated DOP is purely due to the NA of the objective. Besides, DOP can also be affected by other environmental and experimental factors such as spectral efficiency of the analyzer, the optical properties of the medium surrounding the emitter, and the doping concentration of rare-earth ions in the host crystal.^{71, 72} The reference spectra (I_r , I_o) and the

experimental spectra (I_{zx} , I_{zy}) should therefore be collected in the same condition for the correct orientation analysis.

Table 1.2. Calculated DOPs of area under curve ratio (MD1/MD2 and ED1/ED2) of polarized PL spectra of NaYF₄:Eu nanorods measured using different numerical aperture (NA) of objective (**Figure 1.22**). DOP is calculated according to **Equation 1.1**.

		I_{π}	I_{σ}	DOP		I_{π}	I_{σ}	DOP
NA 1.49 (Figure 1.22a)	MD1/M D2	3.45	0.95	0.57	ED1/ED2	1.93	3.70	-0.31
NA 0.6 (Figure 1.22b)		4.67	0.66	0.75		1.34	4.79	-0.56

Discriminating mirror orientation

Because the above equations provide the values of trigonometric functions, the θ' and φ' are indistinguishable from $-\theta'$ and $-\varphi'$ creating four-fold mirror orientations. The in-plane mirror angle ($-\varphi'$) can be discriminated by measuring a spectrum at one supplementary analyzer angle between x- and y- axis (for example, I_{z45°). The reference k-polar diagram can be plotted based on **Figure 1.19c** at the different analyzer angles (k_{zx} , k_{zy} and k_{z45°) as a function of φ' , which can serve to establish a boundary condition to distinguish φ' and $-\varphi'$. A detailed procedure is described as follows.

Once in-plane angle φ' is determined, mirror angle can be discriminated by a boundary condition established using reference k-polar diagram shown in **Figure 1.23a-b**. Boundary condition can be written considering absolute value of k as:

for MD transition (**Figure 1.23a**),

$$\text{if } 0^\circ < \varphi' < 22.5^\circ : \text{ if } k_{z45^\circ, \text{MD}} - k_{zy, \text{MD}} < 0.94, \text{ then } \varphi' > 0^\circ, \text{ if } 0.94 < k_{z45^\circ, \text{MD}} - k_{zy, \text{MD}}, \text{ then } \rightarrow \varphi' < 0^\circ$$

$$\text{if } 22.5^\circ < \varphi' < 67.5^\circ : \text{ if } k_{z45^\circ, \text{MD}} - k_{zx, \text{MD}} < 0, \text{ then } \varphi' > 0^\circ, \text{ if } 0 < k_{z45^\circ, \text{MD}} - k_{zx, \text{MD}}, \text{ then } \varphi' < 0^\circ$$

$$\text{if } 67.5^\circ < \varphi' < 90^\circ : \text{ if } k_{z45^\circ, \text{MD}} - k_{zx, \text{MD}} < 0.92, \text{ then } \varphi' > 0^\circ, \text{ if } 0.92 < k_{z45^\circ, \text{MD}} - k_{zx, \text{MD}}, \text{ then } \varphi' < 0^\circ$$

for ED transition (**Figure 1.23b**),

$$\text{if } 0^\circ < \varphi' < 22.5^\circ : \text{ if } k_{zy, \text{ED}} - k_{z45^\circ, \text{ED}} < 1.8, \text{ then } \varphi' > 0^\circ, \text{ if } 1.8 < k_{z45^\circ, \text{ED}} - k_{zy, \text{ED}}, \text{ then } \varphi' < 0^\circ$$

if $22.5^\circ < \varphi' < 67.5^\circ$, if $0 < k_{z45^\circ,ED} - k_{zx,ED}$, then $\varphi' > 0^\circ$, if $k_{z45^\circ,ED} - k_{zx,ED} < 0$, then $\varphi' < 0^\circ$

if $67.5^\circ < \varphi' < 90^\circ$, if $k_{z45^\circ,ED} - k_{zx,ED} < 2.0$, then $\varphi' > 0^\circ$, if $2.0 < k_{z45^\circ,ED} - k_{zx,ED}$, then $\varphi' < 0^\circ$

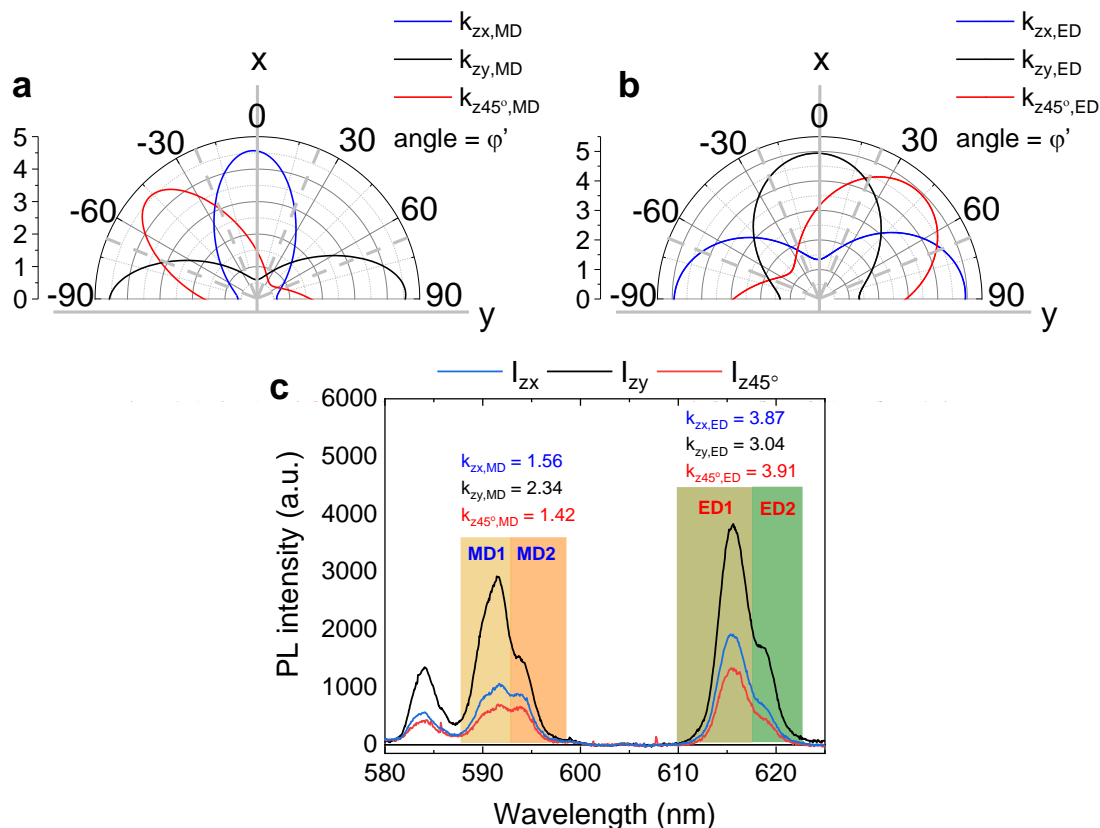


Figure 1.23. The reference k-polar diagram plotted based on **Figure 1.19c** at different analyzer angles (k_{zx} , k_{zy} and k_{z45°) within wavelength ranges of **(a)** MD and **(b)** ED as a function of in-plane angle φ' . **(c)** Polarized photoluminescence of a randomly oriented NaYF₄:Eu single nanorod measured at different analyzer angles (I_{zx} , I_{zy} , I_{z45°). The selected wavelength ranges (MD1, MD2, ED1, and ED2) used for the area under curve ratiometry are highlighted in different colors. Measured area under curve ratio for MD and ED at different analyzer angle ($k_{zx,MD}$, $k_{zy,MD}$, $k_{z45^\circ,MD}$, $k_{zx,ED}$, $k_{zy,ED}$, $k_{z45^\circ,ED}$) are presented in the figure.

In the analyzed orientation shown in **Figure 1.17a-b**, in-plane angle φ' is determined to 59° from I_{zx} polarization and 52° from I_{zy} polarization, which are both the case of ($22.5^\circ < \varphi' < 67.5^\circ$). Measured k value at different analyzer angle ($k_{zx,MD}$, $k_{zy,MD}$, $k_{z45^\circ,MD}$, $k_{zx,ED}$, $k_{zy,ED}$, $k_{z45^\circ,ED}$) shown in **Figure 1.23c** is thus to be served to decide whether the in-plane angle φ' is positive or negative, considering boundary condition written above. As $k_{z45^\circ,MD} - k_{zx,MD}$ is negative and $k_{z45^\circ,ED} - k_{zx,ED}$ is positive, in-plane angle φ' is determined to positive, which is consistent with CCD captured PL image (**Figure 1.16-inset**). If the absolute value of in-plane angle φ' is close to the boundary (*e.g.*, 0° , 22.5° , 67.5° , and 90°), a small error in the measured area under curve ratio k can result in wrong determination. Finally, discriminating the mirror orientation of θ' is also technically possible if a measurement can be done on another viewing

angle adopting the previous stereoscopic method (e.g., by tilting the sample or using a large N.A objective with a diaphragm at different positions).

Applicability of other lanthanide ions to the proposed method

Table 1.3. Summary of the transition of common lanthanide ions for spectroscopy (Tb^{3+} , Ho^{3+} , Er^{3+} and Tm^{3+}). The energy level of the transition, the wavelength of the transition and the nature of the transition are summarized. The nature of the transition is estimated according to the selection rule.⁴⁸ The magnetic dipole (MD) transition is blue, and the electric dipole (ED) transition is red.

Lanthanide ions	Transitions					
Eu^{3+}	$^5D_0-^7F_1$ (580 nm, MD)	$^5D_0-^7F_2$ (620 nm, ED)	$^5D_0-^7F_3$ (650 nm, ED)	$^5D_0-^7F_4$ (700 nm, ED)		
Tb^{3+}	$^5D_4-^7F_6$ (480 nm, ED)	$^5D_4-^7F_5$ (540 nm, MD)	$^5D_4-^7F_4$ (580 nm, MD)	$^5D_4-^7F_3$ (620 nm, MD)		
Ho^{3+}	$^5F_4/^5S_2-^5I_8$ (540 nm, ED)	$^5F_5-^5I_8$ (650 nm, ED)	$^5F_5-^5I_6$ (1487 nm, MD)	$^5I_6-^5I_8$ (1200 nm, ED)	$^5I_7-^5I_8$ (2000 nm, MD)	
Er^{3+}	$^2H_{11/2}-^4I_{15/2}$ (520 nm, ED)	$^4S_{3/2}-^4I_{15/2}$ (540 nm, ED)	$^4F_{9/2}-^4I_{15/2}$ (660 nm, ED)	$^4I_{11/2}-^4I_{15/2}$ (980 nm, ED)	$^4I_{13/2}-^4I_{15/2}$ (1520 nm, MD)	
Tm^{3+}	$^1I_6-^3H_6$ (290 nm, MD)	$^1I_6-^3F_4$ (340 nm, ED)	$^1D_2-^3H_6$ (360 nm, ED)	$^1D_2-^3F_4$ (450 nm, ED)	$^1G_4-^3H_6$ (475 nm, ED)	$^1G_4-^3F_4$ (640 nm, MD)
	$^3F_3-^3H_6$ (695 nm, ED)	$^1D_2-^3F_3$ (740 nm, MD)	$^1G_4-^3H_5$ (770 nm, MD)	$^3H_4-^3H_6$ (790 nm, ED)	$^1G_4-^3H_4$ (1170 nm, MD)	$^3H_4-^3F_4$ (1470 nm, MD)
			$^3F_4-^3H_6$ (1800 nm, ED)			

Table 1.3 summarizes the ED and MD transition levels of different lanthanide ions commonly used for spectroscopy (Tb^{3+} , Ho^{3+} , Er^{3+} , and Tm^{3+}). The nature of the transition is estimated according to the selection rule.⁴⁸ We have shown that the 3D orientation of nanocrystals can be calculated by simultaneously taking into account the transition of MD and ED with a single viewing angle. According to **Table 1.3**, the same analysis can be performed using other commonly used lanthanide ions because

they also show a transition of both MD and ED. For example, when considering Tb^{3+} , one can choose the transition of ${}^5\text{D}_4\text{-}{}^7\text{F}_6$ for ED emission and the transition of ${}^5\text{D}_4\text{-}{}^7\text{F}_5$ for MD emission for the orientation analysis. As these two transitions appear at adjacent wavelength ranges (480 nm for the ${}^5\text{D}_4\text{-}{}^7\text{F}_6$ transition and 540 nm for ${}^5\text{D}_4\text{-}{}^7\text{F}_5$), the emission can thus be collected in a single spectrogram with a fine spectral resolution. It requires measuring the degree of polarization (DOP) to select the transition having the highest DOP for best accuracy. Note that DOP can be improved even for the same transition when the crystal structure of the host matrix is optimized. For example, in the previous study of the group, the DOP was found to be much higher for monazite $\text{LaPO}_4\text{:Eu}$ nanocrystal than rhabdophane $\text{LaPO}_4\text{:Eu}$ nanocrystal.⁶⁶ When considering the use of Er^{3+} , although it exhibits a transition from both MD and ED, the MD emission appears only in the infrared range, away from ED emission. If the emissions are not adjacent in wavelength, it would be difficult to see both emissions on one spectrogram with good resolution. If only one type of dipoles is available (either ED or MD) in such cases, one can still measure the 3D orientation from two spectra obtained with two different analyzer angles, which still benefits from the accuracy of ratiometry and opens a diversified choice for probes even beyond lanthanide-doped species. Finally, it should be noted that different transitions must be well-separated to consider the different polarization nature of each.

1.3.3. Errors in orientation analysis

Figure 1.24 discusses experimental errors that could deteriorate the accuracy of orientation analysis and its propagation to orientation determination. Orientation analysis can be degraded primarily for two reasons. The first reason is the background offset. **Figure 1.24a** shows the varying background offset for the reference spectrum (red, blue line) and the experimental spectrum (black line). The difference in background offset can be attributed to the optical anisotropy of spectrometer gratings, different emission beam distortion as a function of analyzer angle, different focus of excitation to the sample, spectral efficiency of the analyzer, *etc.* When the excitation/emission is not perfectly aligned/focused on the center of the emitters, the emission beam may also be distorted due to the abrupt change in refractive index or wave-guiding effect, causing the background offset to be tilted as shown in **Figure 1.24b**. The collection of autofluorescence from the substrate or any other surrounding components (due to UV-laser used for Eu^{3+} ions excitation) can be significant if the emission intensity of lanthanide ions is low. All of these sources affecting the background offset may degrade the precision of the orientation analysis. These backgrounds offset should be corrected by subtracting them, as shown in **Figure 1.24c**. In this study, the baselines of the experimental spectra were taken as a flat line at the averaged intensity between 600 nm and 608 nm where Eu^{3+} luminescence is not present, which is an approximation that may have caused certain errors. Other wavelengths can be chosen as preferred in their experimental availability. It is also interesting to note that the effect of autofluorescence on the background offset can

be technically minimized by using higher wavelength excitation (*e.g.*, 464 nm for Eu^{3+} ions excitation instead of 394 nm used in this study) or using a time-gated collection (decay of autofluorescence is on the scale of $\sim\mu\text{s}$ and the decay of lanthanide ions is on the scale of $\sim\text{ms}$). The second possible reason is the peak shift. **Figure 1.24d** represents an example of peak shift between the reference spectra (red, blue line) and an experimental spectrum (black line). Such small peak shifts can occur when the spectrometer grating was moved in the meantime. Although the shift is small, it may affect the spectroscopic/ratiometric orientation analysis significantly. Therefore, the reference and experimental spectra should be collected under the same condition to avoid this source of errors.

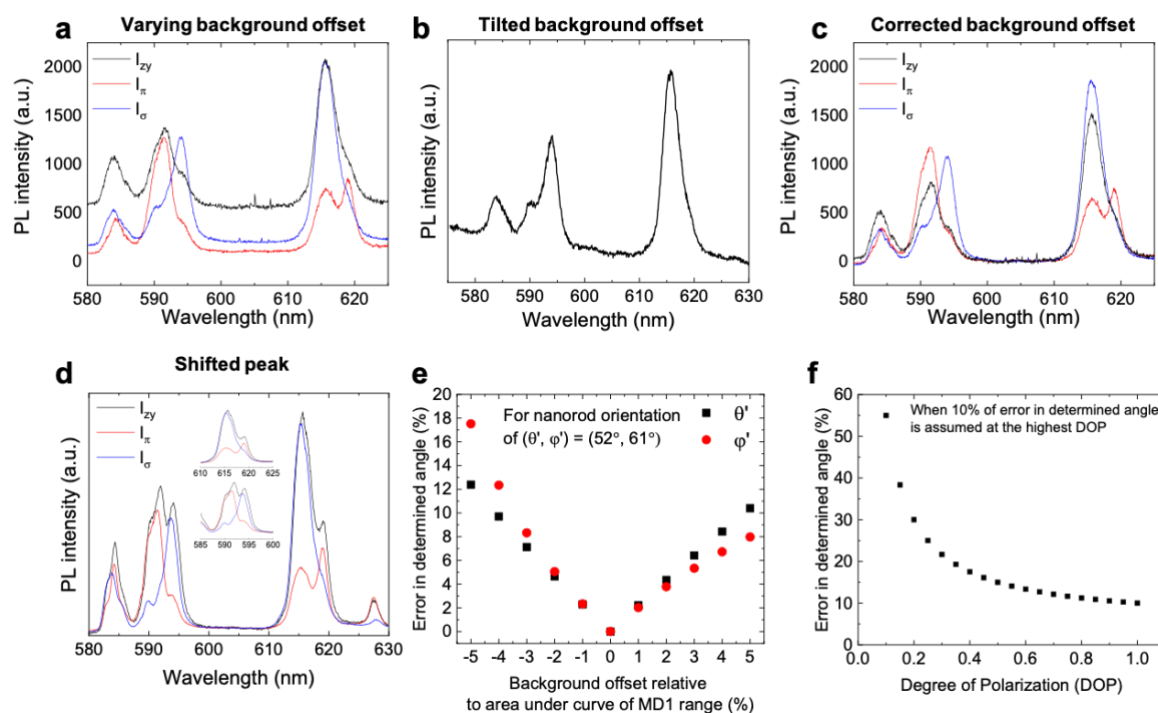


Figure 1.24. Examples of experimental errors in background treatment: **(a)** varying background offset where the background offset of experimental and reference spectrum is not subtracted correctly, **(b)** tilted background offset where the significant background signal from an external source is added. **(c)** Corrected background for orientation analysis. **(d)** Example of experimental peak shift error where the wavelength of intensity peak of the experimental and reference spectrum does not match. **(e)** Simulated error in determining angle (θ' , ϕ') as a function of the amount of background offset relative to the area under curve of MD1 range. Simulation is made using the dataset of a certain orientation of a nanorod (θ' , ϕ') = (52° , 61°). **(f)** Simulated error in determining angle as a function of the degree of polarization (DOP). The Error in the determined angle is assumed to have a 10 % when the DOP is highest (DOP = 1.0).

As noted above, if the background offset is not handled correctly, it could degrade the accuracy of the orientation analysis. **Figure 1.24e** shows the simulated error in (θ' , ϕ') as a function of the amount of background offset relative to the area under curve of MD1 range. The simulation is done using the dataset of a certain orientation of a nanorod which shows the calculated angle of (θ' , ϕ') = (52° , 61°) when the background offset is subtracted correctly. When the 5% of background offset relative to the

area under curve of MD1 range is subtracted less or more than necessary, the determined angle shows a deviation of 10~12 % for θ' and 8~18 % for φ' comparing to values calculated with the appropriate background treatment. However, note that these values of angle deviation cannot be considered as general values because the amount of error varies also depending on the absolute values of (θ' , φ'). The errors are relatively large when θ' or φ' is close to 0° or to 90° (*i.e.*, when the rods are oriented parallel or perpendicular to the analyzer or the substrate) (see the discussion in **Figure 1.25-26**).

Finally, the effect of degree of polarization (DOP) on the determination of the orientation is simulated (**Figure 1.24f**). The accuracy of the orientation analysis depends on the DOP of the peaks considered for the analysis. It can be seen that when 10 % error in angle is assumed to occur when the DOP is highest (DOP = 1, perfect polarization), the error in determining angle increases to 15% when DOP is 0.5 and to 30% when DOP is 0.2. This result shows a quantitative relation between the DOP and the accuracy of angular measurement. Finding a host crystal structure giving a higher DOP of emission is therefore essential to improve the accuracy of the proposed method.⁶⁶

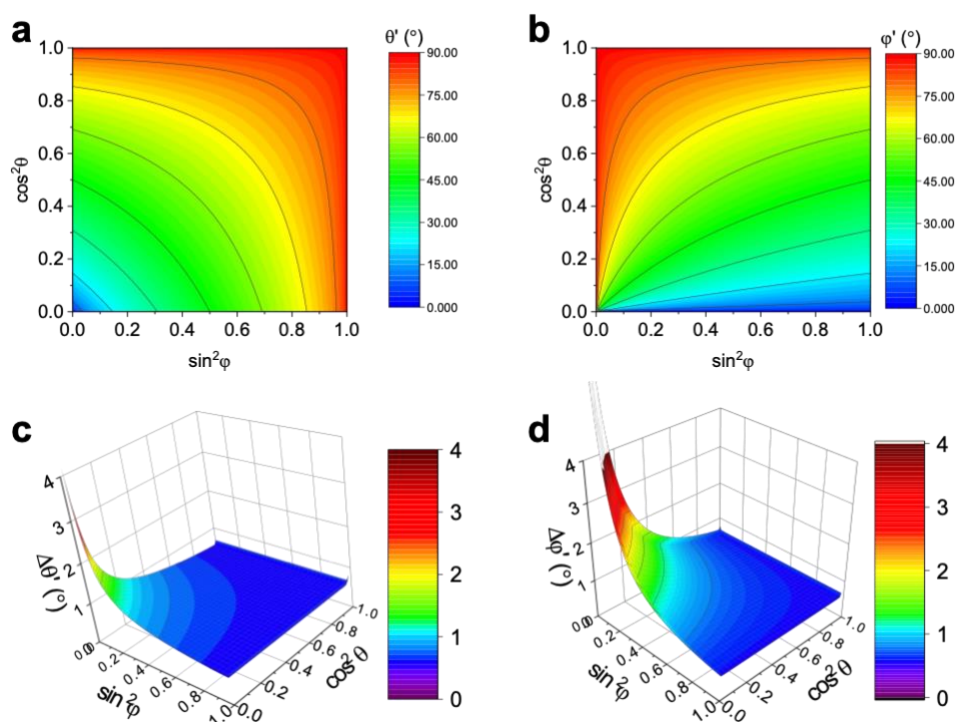


Figure 1.25. Simulated (a) out-of-plane angle θ' and (b) in-plane angle φ' as a function of $\sin^2\varphi$ and $\cos^2\theta$ based on **Equations 1.11-12**. Simulated error Δ in (c) out-of-plane angle θ' and (d) in-plane angle φ' as a function of $\sin^2\varphi$ and $\cos^2\theta$. $\Delta\theta' = \sqrt{\Delta_{\sin^2\varphi}\theta' \times \Delta_{\cos^2\theta}\theta'}$ where $\Delta_{\sin^2\varphi}\theta'$ and $\Delta_{\cos^2\theta}\theta'$ are the deviated angle of θ' when $\sin^2\varphi$ and $\cos^2\theta$ deviates 0.02, respectively. $\Delta\varphi' = \sqrt{\Delta_{\sin^2\varphi}\varphi' \times \Delta_{\cos^2\theta}\varphi'}$ where $\Delta_{\sin^2\varphi}\varphi'$ and $\Delta_{\cos^2\theta}\varphi'$ are the deviated angle of φ' when $\sin^2\varphi$ and $\cos^2\theta$ deviates 0.02, respectively.

Figure 1.25 shows the set of angles (θ' , φ') calculated from the set of angles ($\cos^2\theta$, $\sin^2\varphi$) based on the **Equations 1.11-12**. Any experimental error in fitting analysis or area under curve ratiometry leads to the error in determining the set of angles ($\cos^2\theta$, $\sin^2\varphi$), which is the basis of conversion to (θ' , φ'). Assuming that the experimental error in the determined set of angles ($\Delta\cos^2\theta$, $\Delta\sin^2\varphi$) is equal to 0.02, the error in the out-of-plane angle θ' ($\Delta\theta'$) and in-plane angle φ' ($\Delta\varphi'$) can be estimated, as shown in **Figure 1.25c-d**. According to the simulated profile, it is more likely to have a larger error during the angle conversion when the rods are oriented close to normal to the measurement plane ($\theta'=0^\circ$). This can be explained by the fact that the line shape of polarized spectrum will not change much because the spectrum is dominated by α configuration which is an isotropic configuration (**Figure 1.13c**). The large error is also expected when rods are lying on the measurement plane ($\theta'=90^\circ$) or oriented parallel or perpendicular to the analyzer angle ($\varphi'=0^\circ, 90^\circ$). This error is due to the shape of the square sinusoidal function which has a pole at 0° and 90° . In particular, at this extreme condition, even for the very small error in determined angle (e.g. $\Delta\cos^2\theta = \Delta\sin^2\varphi = 10^{-3}$) the correct analysis could not be carried out because the calculated $\cos^2\theta$, $\sin^2\varphi$ can be off sinusoidal function range (e.g. $\cos^2\theta = \Delta\sin^2\varphi = 1+10^{-3}$).

Error of orientation analysis by area under curve ratiometry

The same error simulation illustrated in **Figure 1.25** can be performed directly in the orientation analysis using an area under curve ratiometry approach. When one considers only the MD emission, one can calculate a set of angles (θ' , φ') based on the area under curve ratio ($k_{zx,MD}$, $k_{zy,MD}$) of the polarized spectrum obtained at from two orthogonal polarizations according to **Equations 11-12,15-16** (**Figure 1.26a-b**). Any error in obtaining ($k_{zx,MD}$, $k_{zy,MD}$) result in an error in determined angle. When the error in area under curve ratio ($\Delta k_{zx,MD}$, $\Delta k_{zy,MD}$) is assumed equal to 0.02, the error of calculated angle ($\Delta\theta'$, $\Delta\varphi'$) can be simulated, as shown in **Figure 1.26c-d**. According to the simulated profile, the errors are relatively larger when θ' is close to 0° or to 90° , which is consistent with the discussion made in **Figure 1.25**. As discussed above, even for the very small error in determining angle due to the error in the obtained area under curve ratio, the correct analysis could not be performed because the calculated $\cos^2\theta$, $\sin^2\varphi$ can be out of the sinusoidal function range.

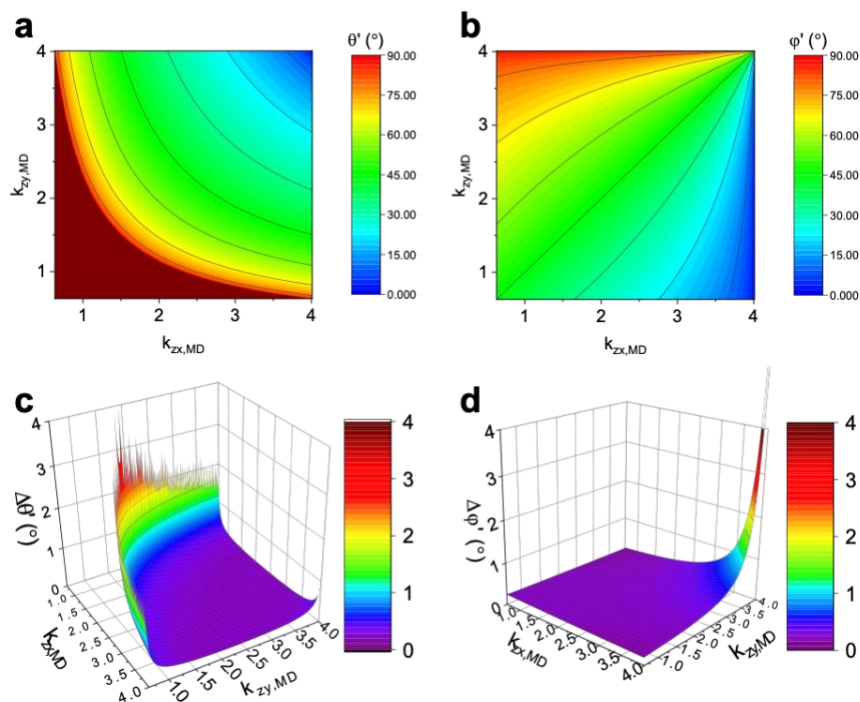


Figure 1.26. Simulated (a) out-of-plane angle θ' and (b) in-plane angle φ' based on Equation 11-12,15-16 as a function of area under curve ratio ($k_{zx,MD}$, $k_{zy,MD}$). Simulated error Δ in (c) out-of-plane angle θ' and (d) in-plane angle φ' as a function of ($k_{zx,MD}$, $k_{zy,MD}$). $\Delta\theta' = \sqrt{\Delta_{k_{zx,MD}}\theta' \times \Delta_{k_{zy,MD}}\theta'}$ where $\Delta_{k_{zx,MD}}\theta'$ and $\Delta_{k_{zy,MD}}\theta'$ are the deviated angle of θ' when $k_{zx,MD}$ and $k_{zy,MD}$ deviates 0.02, respectively. $\Delta\varphi' = \sqrt{\Delta_{k_{zx,MD}}\varphi' \times \Delta_{k_{zy,MD}}\varphi'}$ where $\Delta_{k_{zx,MD}}\varphi'$ and $\Delta_{k_{zy,MD}}\varphi'$ are the deviated angle of φ' when $k_{zx,MD}$ and $k_{zy,MD}$ deviates 0.02.

Summary of Chapter 1.3

The unique relationship in lanthanide emission ($I_{\pi} = I_q$ in MD transition, and $I_{\sigma} = I_q$ in ED transition) enabled the calculation of 3D orientation of nanocrystals using a single polarized photoluminescence spectrogram. The method is demonstrated via two approaches: spectral fitting analysis, area under curve ratiometry. The degree of polarization of lanthanide emission was the same regardless of the morphology of the host crystals, which makes the method robust to the polydisperse system. The presented method applies not only to the Eu^{3+} ions used in this study but also to other lanthanide ions. Higher error in orientation determination is expected when the observed rods are oriented parallel or perpendicular to the analyzer or the substrate.

1.4. Conclusion

We have demonstrated, in this chapter, a straightforward spectroscopic method to measure the three-dimensional orientation of nanocrystalline probes. We show that the large measurement uncertainty of previous methods using a single dipole emitter can be eliminated via ratiometric analysis of multiple transition dipoles inherent in lanthanide phosphors. The spectral line shape (*i.e.*, relative probabilities of different emission dipoles) of lanthanides doped in a crystal structure is independent of the particle size, shape, and surface chemistry that are major factors governing other types of nano-emitters, which is a great advantage to analyze the absolute angles of orientation with high accuracy.

We used NaYF₄:Eu nanorod as a model system, but any probe material with different dopants, composition, and structure (*e.g.*, β -NaYF₄:Er³⁺,Yb³⁺ upconverting nanoparticles⁷³) exhibiting simultaneous ED and MD transitions (**Table 1.3**) can be used to measure the 3D orientation from a single-shot spectrum obtained with a fixed analyzer. Organometallic lanthanide chelates are also one of the potential orientation probes that are smaller and compatible with biomolecular targets.

Depending on such measurement conditions, the presented principle of analysis can be easily adapted to conventional microscopy setups with various designs and detector types. The measurement precision can be further improved by using a host crystal structure providing higher degree of polarization (DOP).⁶⁶ Such an analytical performance combined with the versatility in the choice of emitter material and optical instrument is promising for studying the orientation and rotational dynamics of a wide variety of biological, chemical, and colloidal systems.

Nevertheless, there exist several intrinsic drawbacks of lanthanides to overcome. The long lifetime of lanthanide luminescence in the millisecond scale and their relatively small absorption cross-section may cause low signal-to-noise ratio and spatiotemporal resolution. It is thus necessary to optimize the excitation power, acquisition time, and crystal size. Such limitation is critical for specific applications. For instance, when characterizing the dynamics of small biomolecules, large nanocrystal sizes chosen for high signal intensity may hinder the movement of target. It is thus interesting to develop fundamental solutions to increase luminescence efficiency by co-doping with sensitizing lanthanides or by plasmonic enhancement.

Chapter 2.

Order Parameter Analysis of Aligned Nanorods Assembly

In the previous chapter, we have shown that one of the anisotropic material properties, polarized photoluminescence, can be used to calculate the spatial orientation of nanorods in 3D space. Many other anisotropic material properties involving polarized plasmons⁷⁴, optical retardation^{68,75}, ferro -electricity, and -magnetism⁷⁶⁻⁷⁹ are also fundamentally interesting and promising for their practical use in functional devices. However, it is challenging to investigate and manipulate such properties because of the limited signal-to-noise ratio for individual nanorods and the random orientation of nanorods in an ensemble. Achieving significant intensities of response signals while getting access to the anisotropic properties inherent in individual particles becomes possible when considering aligned particles by self-assembly^{69, 80-82} or directed assembly^{68, 69, 75, 80, 81, 83-94}.

Description of the assembled nanorods involves an analysis of the degree of orientation, represented quantitatively by the order parameter S . Instantaneous measurement of the order parameter S of assemblies in dynamic states can allow further optimization of the assembly process and the device performance. Although many techniques (*e.g.*, birefringence measurement^{68, 95-97}, SAXS analysis^{94, 98, 99}, high-resolution microscopy^{29, 87, 90, 100, 101}) have been proposed to characterize S , these do not yet meet the essential criteria such as for rapid, *in situ* and non-destructive analyses.

In this chapter, we propose an approach of measuring S , employing a unique polarization behavior of lanthanide-doped crystalline nanorods discussed in **Chapter 1**. We demonstrate a rapid *in-situ* determination of S of Eu^{3+} -doped NaYF_4 nanorods of which the orientation is controlled under an external electric field. This methodology would provide a more in-depth examination of various assembled nanostructures and the collective dynamics of their building blocks.

Parts of results presented in this chapter are published: “Measuring the Order Parameter of Vertically Aligned Nanorods Assembly”, **J. Kim**, K. Lahlil, T. Gacoin, J. -W. Kim, *Nanoscale*, 13, 7630-7637 (2021)

2.1. Introduction

2.1.1. Aligned nanorods assembly

Two main fabrication methods for aligned nanorod assembly are self-assembly¹⁰² and directed assembly^{68, 69, 75, 80, 81, 83-94}. Self-assembly can be achieved by controlling the sophisticated surface chemistry of colloidal nanorods, allowing the nanorods to be assembled into a specific structure.¹⁰² One of the self-assembly processes of anisotropic nanoparticles is the liquid crystalline (LC) behavior where the main axis of nanorods is aligned in one direction while having the ability to flow like a liquid (detailed discussion about LC is made in **Chapter 3**). Taking advantage of this LC property, anisotropic properties inherent in individual particles or molecules have been observed in many different works in the LC state.^{69, 80-82} Directed assemblies are made by exerting external forces, for instance, capillary forces during solvent drying⁸³⁻⁸⁶ (**Figure 2.1a**), shear stress under flow^{75, 80, 87, 88} (**Figure 2.1b**), and externally applied electric^{68, 69, 81, 89-91}, or magnetic fields⁹²⁻⁹⁴ (**Figure 2.1c**). These approaches enabled the active control of the order parameter and allowed to obtain the alignment much longer than what is attainable with self-assembled LC. A combination of these approaches has been useful to prepare active devices modulating strong anisotropic properties by reversibly controlling the director of organized particles with external fields (*e.g.*, electro-optical device^{69, 81, 91}).

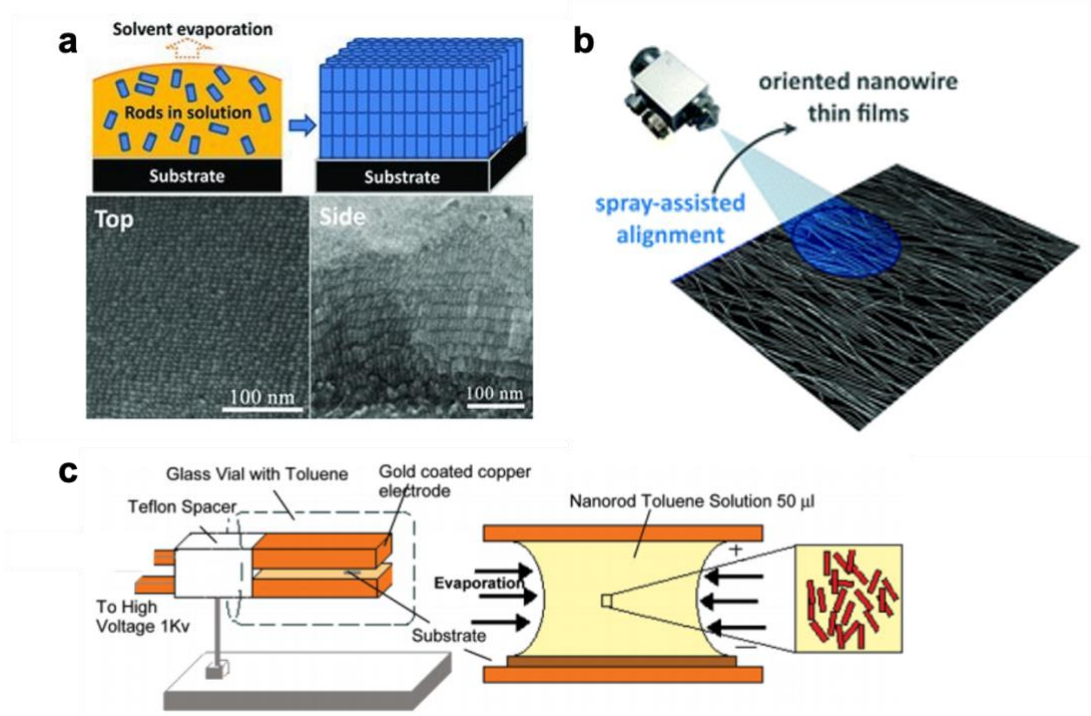


Figure 2.1. (a) Drop casting of highly concentrated solutions of nanorods in high boiling point solvents, followed by slow solvent evaporation, leads to the formation of multilayers of vertically aligned rods. (b) Thin film of oriented nanowire by spray-assisted shear force. (c) Schematic of electrode assembly for nanorod alignment. Figures were taken from the reference.^{84, 87, 89}

Order parameter

Description of the assembled nanorods involves an analysis of the degree of orientation, represented quantitatively by the order parameter S as:

$$S = (3 \cdot \langle \cos^2 \theta \rangle - 1) / 2 \quad (2.1)$$

where θ is the angle of the long axis of an individual nanorod with respect to the director \vec{n} of the ensemble (Figure 2.2a). The angle brackets indicate a temporal and spatial average in nanorods' ensemble residing in the measured volume. According to Equation 2.1, the order parameter S in the three-dimensional space is 1 for a system perfectly aligned along the reference axis, 0 for a random ensemble (Figure 2.2), and -1/2 for rods lying in-plane vertical to the reference axis.

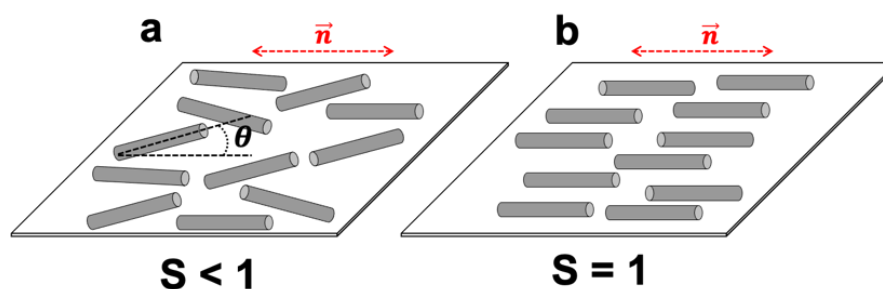


Figure 2.2. Schematic illustration of nanorods assembly with the alignment director \vec{n} parallel to the substrate (**b**) with order parameter $S < 1$ and (**c**) with $S = 1$ (perfect alignment). θ indicates the angle of an individual nanorod's long axis with respect to the director \vec{n} of the ensemble.

2.1.2. State-of-the-art methods for order parameter analysis

Birefringence

A widely used technique for analyzing assembled structures and determining S is to measure the optical birefringence. The aligned nanorods assembly results in birefringence, a contrast in refractive indices Δn along axes parallel and perpendicular to the director \vec{n} . When such a birefringent medium is placed between crossed polarizers, the intensity of transmitted light reflects the amount of optical retardation induced by Δn , a basis of calculating S . One can quantify the amount of optical retardation by observing the light intensity with a full rotation of assembly in-plane with respect to the polarizer. However, in practice, determining the absolute value of S is a complex problem often requiring a sophisticated intrinsic- and form- birefringence modeling that relates to the structure of assembly and the intrinsic optical constants of the building blocks and surrounding medium.^{68, 95-97} Moreover, birefringence measurement is only useful for simple configurations where the assembly is unidirectional and \vec{n} is parallel to the measurement plane (*i.e.*, perpendicular to the light propagation) (**Figure 2.3a**). When the assembly has an out-of-plane component of \vec{n} (ω), S cannot be deduced unless ω is known. (**Figure 2.3b**). **Figure 2.3c** shows the schematics of vertically aligned nanorod assembly (homeotropic alignment) where \vec{n} is perpendicular to the measurement plane (*i.e.*, parallel to the propagation of light). Because homeotropic alignment is not optically anisotropic ($\Delta n \cong 0$), the optical retardation is not produced. Therefore, it is impossible to deduce order parameter S using a birefringence technique for homeotropic assembly.

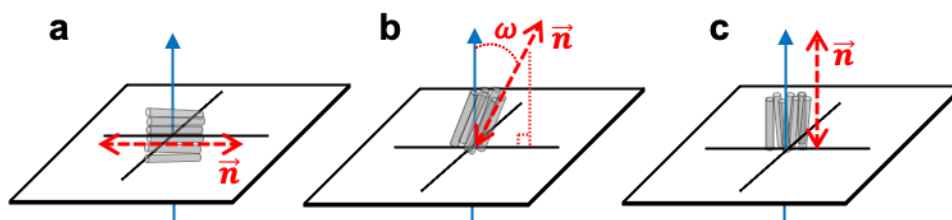


Figure 2.3. Schematic illustration of nanorods assembly with the alignment director (a) \vec{n} parallel to the substrate (measurement plane), (b) \vec{n} with out-of-plane angle (ω) and (c) \vec{n} perpendicular to the substrate. The blue line indicates the direction of light propagation for measurement.

Small-angle x-ray scattering (SAXS) and High-resolution microscopy

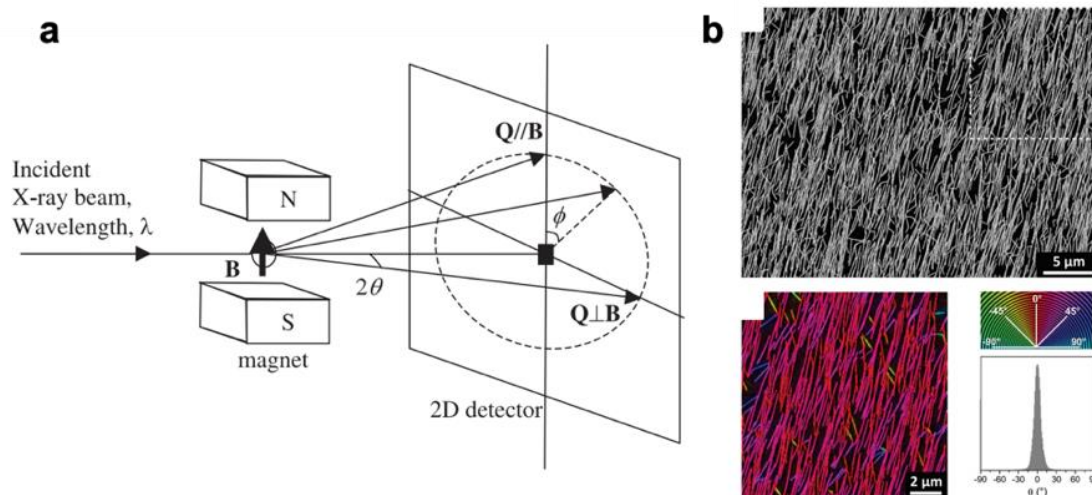


Figure 2.4. (a) The X-ray scattering experiment from samples with an applied magnetic field. (b) SEM picture of a silver nanowire aligned layer. Nanowires are color-coded according to their orientation and the distribution of the nanowire angle θ relative to the global alignment direction. Figures were taken from the reference.^{87, 98}

Another method to measure the order parameter of assembled structures is based on SAXS (small-angle x-ray scattering) analysis that measures the intensities of X-rays scattered by the assembly as a function of the scattering angle (**Figure 2.4a**). It offers a non-destructive method to characterize S and detailed information such as superlattice structure and inter-particle spacing.^{94, 98, 99} However, a sophisticated scattering pattern analysis is essential to quantify S , which is highly sensitive to the experimental and materials parameters. The typical focal resolution of the SAXS beam is hundreds of micrometers, limiting the observable domain size to be larger. Moreover, SAXS instruments are heavy, costly, and not easily accessible.

Measuring S has sometimes been made by direct observation of assembled nanorods by electron (*e.g.*, cryo, transmission, scanning) or optical microscopy (*e.g.*, confocal) (**Figure 2.4b**).^{29, 87, 90, 100, 101}

However, electron microscopy is destructive and cannot be made *in situ* in most cases, while the optical microscopy imaging is only applicable when the size of particles is larger than the optical resolution. Furthermore, the determination of \mathbf{S} and \vec{n} from image data is not straightforward.

2.1.3. Order parameter analysis using photoluminescence of rare-earth dopants

As discussed above, even the current state-of-the-art methods for measuring \mathbf{S} have not yet met the essential criteria such as rapid, *in situ*, and non-destructive analyses. The purpose of the study presented in this chapter is to develop a rapid, high-resolution, non-destructive, and *in-situ* method to measure \mathbf{S} . We achieved such an analytic method using photoluminescence of rare-earth dopants. The method relies on the same basis discussed in **Chapter 1**, employing the mutually different polarization nature of multiple emission dipoles of different nature, MD and ED, inherent in lanthanide emission. In **Chapter 1**, a single polarized photoluminescence spectrogram of a nanorod enabled the calculation of the 3D orientation (θ, φ) of the nanorod. Similarly, the emission spectra obtained from an ensemble of nanorods have the information of temporal and spatial average of (θ, φ) of all nanorods within the measured volume and time. With a known direction of \vec{n} that is determined by the direction of the applied electric field, such an averaged orientation of nanorods can be directly applied to **Equation 2.1**, which allows the direct calculation of order parameter \mathbf{S} of aligned nanorod assembly.

In this work, as a proof-of-concept system to apply the developed methodology, we prepared an electro-optical (E/O) cell in which a colloidal suspension of Eu^{3+} -doped monocrystalline sodium yttrium fluoride ($\text{NaYF}_4:\text{Eu}$) nanorods is inserted. An AC (alternating current) electric field (E-field) applied between two electrodes could align nanorod in parallel to E-field direction, which could be reversibly controlled by adjusting E-field intensity. NaYF_4 was selected as it is known as an efficient host crystal for doping lanthanide ions^{103, 104}, the same nanocrystal discussed in **Chapter 1**. Note that the method is not limited to $\text{NaYF}_4:\text{Eu}$ nanocrystals. The applicability of the presented method is discussed in **Chapter 1.3.2**. Micrometer-long $\text{NaYF}_4:\text{Eu}$ nanorods were synthesized by a wet-chemical method⁵⁸, surface-functionalized with citrate molecules¹⁰⁵, and stably dispersed in ethylene glycol (EG). EG is used instead of water as a dispersing medium due to the higher threshold to the electrolysis during the electro-optical switching experiment. E-field showed an ability that effectively tunes the assemblies' order parameter as a function of E-field strength. The PL signal was collected simultaneously with the applied E-field intensity to determine \mathbf{S} at each moment quantitatively.

We considered two different types of aligned assembly - in-plane and homeotropic - achieved by two different types of E/O cell geometry. In-plane alignment is achieved using a lab-made in-plane switching (IPS) E/O cell where two electrodes are deposited on the same plane, generating an in-plane

E-field in the middle of two electrodes (**Figure 2.5a**). Vertical alignment is achieved using a commercially available homeotropic E/O cell where two electrodes are deposited on top and bottom substrate, generating a vertical electric field (**Figure 2.5b**).

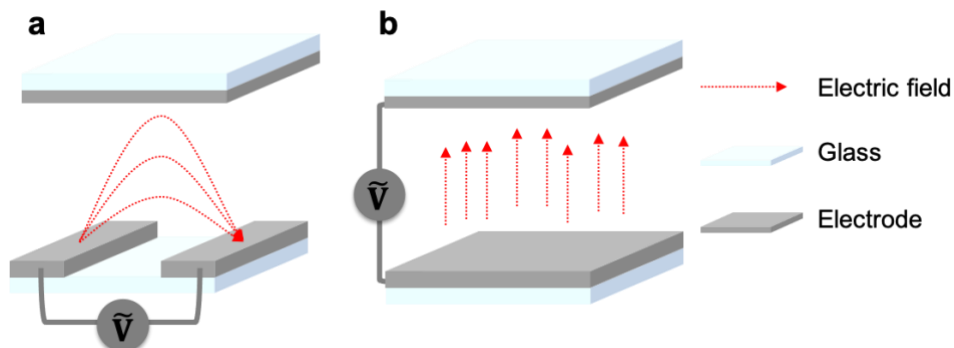


Figure 2.5. (a,b) Schematic illustrations of electro-optical cells with two geometries: (a) in-plane switching (IPS) and (b) homeotropic. Dashed arrows indicate the direction of the electric field.

Summary of Chapter 2.1

Analyzing the order parameter of the aligned nanorod assembly allows optimization of many different functional devices based on the nanorod's anisotropic material properties. Although there have been many approaches to analyze the order parameter of the aligned nanorod assembly (*e.g.*, birefringence, SAXS, high-resolution microscopy), these still do not meet essential criteria such as rapid, in situ, and non-destructive analysis. We have prepared a nanorod assembly aligned in-plane or homeotropic by applying an external electric field. In this case, the direction of alignment of the assembly is known because the electric field's direction determines it. The order parameter of the aligned nanorod assembly of these two geometries will be examined based on the photoluminescence of the lanthanide ions doped in the nanorod, a building block of the assembly.

2.2. In-plane order parameter analysis of NaYF₄:Eu aligned nanorod assembly

2.2.1. In-plane alignment using in-plane switching (IPS) electro-optical cell

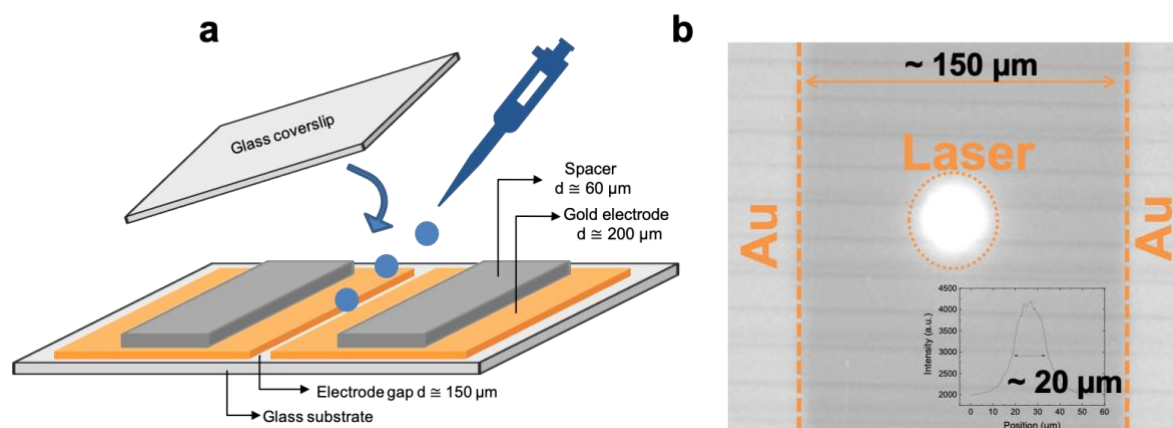


Figure 2.6. (a) Illustration of preparation of lab-made in-plane switching (IPS) electro-optical cell and switching experiment (b) CCD captured image of lab-made IPS electro-optical cell. Inset: intensity profile of laser excitation area with a full-width-half-max (FWHM) of $\sim 20 \mu\text{m}$.

Figure 2.6a shows the schematics of lab-made in-plane switching (IPS) cell. Gold thin film is firstly sputtered to the glass substrate with a thickness of $\sim 200 \text{ nm}$. A gap ($\sim 150 \mu\text{m}$) is made in the middle of a gold film by scratching the film using a razor blade. Subsequently, commercially available scotch tape (thickness $\sim 60 \mu\text{m}$) is used as a spacer. Afterward, around $20 \mu\text{L}$ of NaYF₄:Eu colloidal nanorods dispersed in ethylene glycol (EG) is deposited in the gap between electrodes and covered by a glass coverslip. **Figure 2.6b** shows the CCD-captured image of the lab-made IPS cell. The bright circle in the middle of electrodes is where the NaYF₄:Eu nanorods are excited by UV-laser ($\lambda \sim 394 \text{ nm}$). As the E-field \vec{n} of IPS cell is transverse only at the middle of electrodes, it is crucial to collect PL signals at the center of two electrodes from the smallest possible region. **Figure 2.6b-inset** shows the measured intensity profile of the excited area, showing around $20 \mu\text{m}$ of full-width-half-max (FWHM).

Nanorods submitted in such in-plane E-field begin to align parallel to field direction \vec{n} and in-plane order parameter $S_{\text{in-plane}}$ increases as schematized in **Figure 2.7a**. When there is no applied E-field, the measured spectrum at two orthogonal polarization shows negligible changes as nanorods are randomly oriented (**Figure 2.7b**). When E-field controls the nanorod's orientation, the observed line shape of the PL signal is different when measured with a polarizer set to parallel (I_{\parallel}) and perpendicular (I_{\perp}) to \vec{n} (**Figure 2.7c-e**).

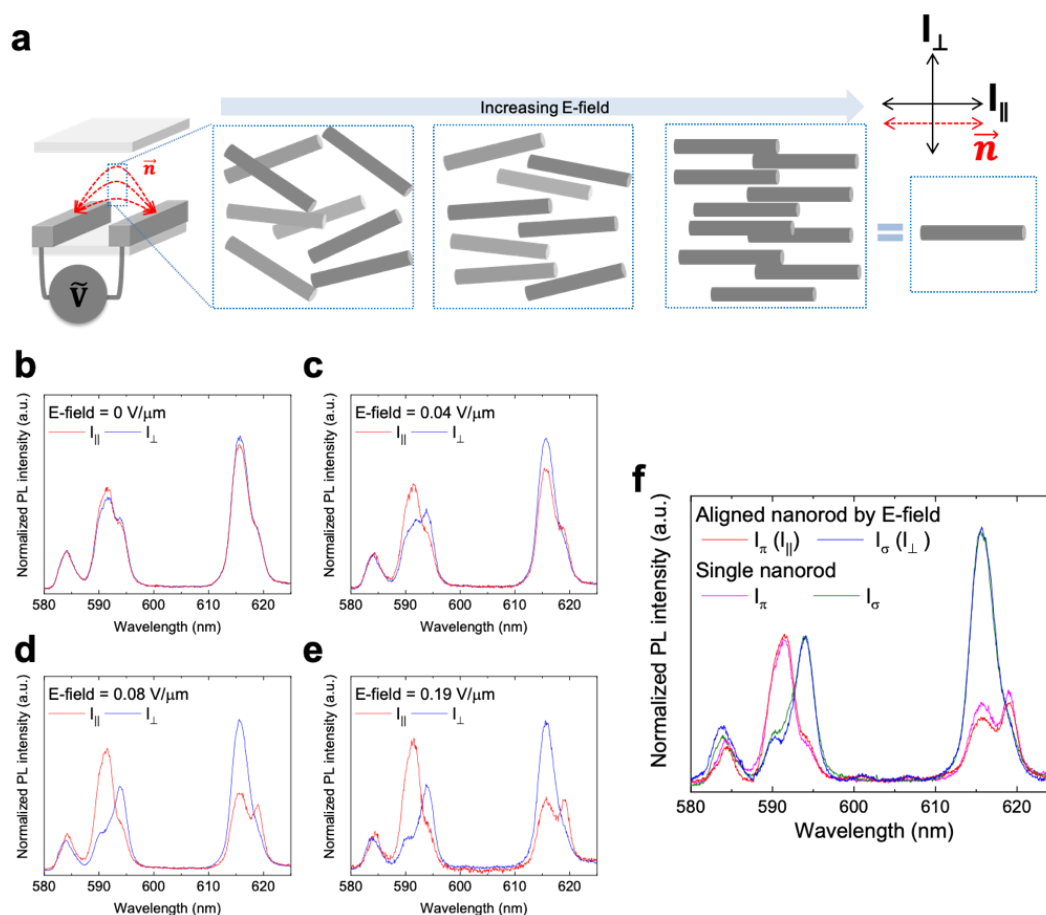


Figure 2.7. (a) Schematic illustration of IPS electro-optical (E/O) cell with aligning nanorods as increasing E-field. Red dashed line stands for the direction of E-field \vec{n} . At the middle of two electrodes, E-field direction \vec{n} is transverse where polarized photoluminescence (PL) spectra of aligned NaYF₄:Eu nanorods are measured. Polarized photoluminescence spectra of orientation-controlled NaYF₄:Eu nanorods measured at different E-field intensity of (b) 0 (c) 0.04 (d) 0.08 and (e) 0.19 V/ μm ($f = 1$ kHz) with the polarizer set to parallel (I_{\parallel} , red line) and perpendicular (I_{\perp} , blue line) to the direction of E-field direction \vec{n} (f) Reference spectra (I_{π} , I_{σ}) were obtained from aligned nanorods under the E-field (at saturated voltage, $E \sim 0.47$ V/ μm) and from the single nanorod.

When increasing the E-field intensity, the line shape of the I_{\parallel} spectrum becomes similar to the line shape of the I_{π} spectrum obtained from the single rod. In the 5D_0 - 7F_1 transition (MD) of I_{\parallel} spectrum, the relative peak intensity at 590.0 nm increases comparing to the intensity at 593.7 nm. In the 5D_0 - 7F_2 transition (ED) of I_{\parallel} spectrum, the relative peak intensity at 619.0 nm increases comparing to the intensity at 615.3 nm. Contrarily, the line shape of I_{\perp} spectrum becomes similar to the line shape of the I_{σ} spectrum obtained from the single rod. In the 5D_0 - 7F_1 transition (MD) of I_{\perp} spectrum, the relative peak intensity at 590.0 nm decreases compared to the intensity at 593.7 nm. In the 5D_0 - 7F_2 transition (ED) of I_{\perp} spectrum, the relative peak intensity at 619.0 nm decreases compared to the intensity at 615.3 nm. When E-field intensity is higher than ~ 0.47 V/ μm , line shape showed no longer changes. At this saturating E-field intensity, the line shape of π signal obtained from I_{\parallel} (red line) and the σ signal obtained from I_{\perp} (blue line) is identical to those obtained from the single nanorod (magenta and olive line), indicating

alignment of nanorods by E-field is close to perfect in-plane alignment ($S_{\text{in-plane}} \sim 1$) (Figure 2.7f). It is interesting to note that applying E-field to the randomly oriented colloidal nanorods does not always make a perfect alignment even at a very high E-field due to the randomization by thermal effect.¹ In this study using micrometer-sized NaYF₄:Eu nanorods, the thermal motion is relatively weak due to the large size, while the E-field is still efficient to align the rods. This seems to be the reason for the high order parameter ($S \sim 1$) achieved. Further study is necessary to confirm this hypothesis.

2.2.2. Theoretical methodology for in-plane order parameter analysis

Using as-established reference signals (I_{π} , I_{σ}), in-plane order parameter $S_{\text{in-plane}}$ can be calculated. The observed polarized emission spectra from a local area (I_{\parallel} , I_{\perp}) is an averaged sum of the emissions from all the nanorods in the observed focal volume (Figure 2.8a). Nanorods in such measured volume have a certain orientation distribution in θ and φ with respect to global alignment direction \vec{n} (parallel to the E-field direction) (Figure 2.8b).

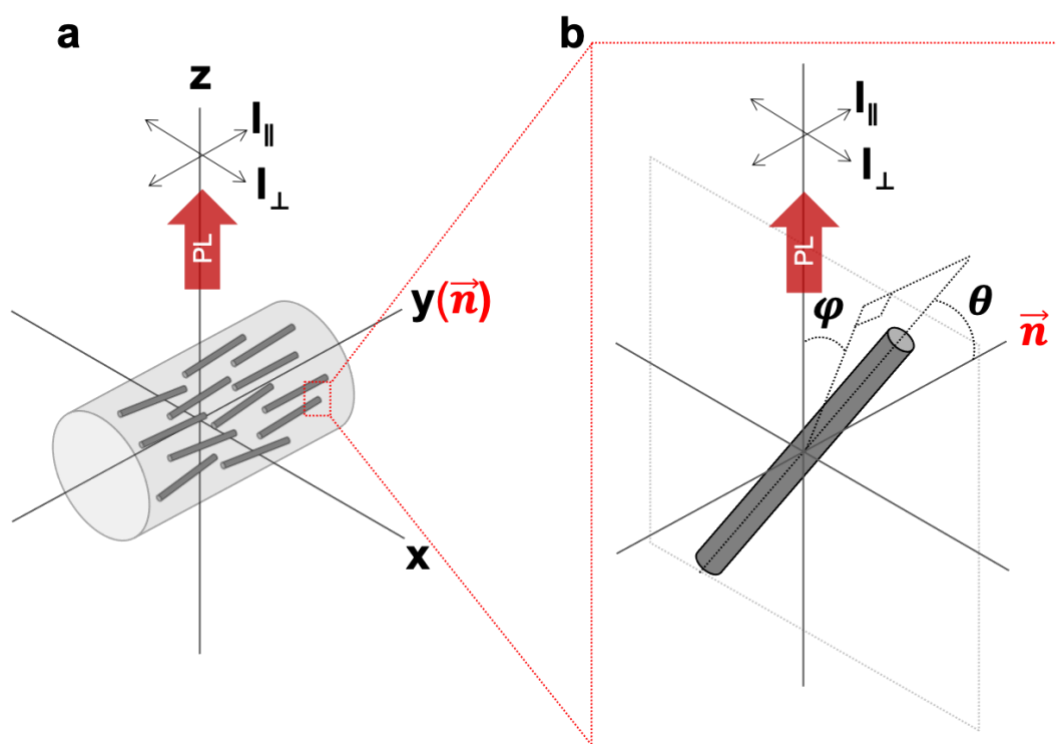


Figure 2.8. (a) Schematic illustration of aligned nanorod assembly to the alignment direction \vec{n} , parallel to the y-axis. Two polarization I_{\parallel} , I_{\perp} represent two polarization components parallel and perpendicular to the director \vec{n} . (b) Schematic illustration of a single nanorod in the aligned assembly, having an orientation distribution respect to \vec{n} with spherical angles (θ , φ).

When the polar axis (y-axis) in the lab-coordinates system (**Figure 2.8a**) is assumed parallel to the alignment axis \vec{n} (parallel to the E-field direction), two polarization components parallel (I_{\parallel}) and perpendicular (I_{\perp}) to the E-field direction \vec{n} can be expressed as:

For a given wavelength (λ) for both MD and ED transition lines:

$$I_{\parallel}(\lambda) = \langle I_{\pi}(\lambda) \cdot \cos^2\theta + I_{\sigma}(\lambda) \cdot \sin^2\theta \cdot \sin^2\varphi + I_{\alpha}(\lambda) \cdot \sin^2\theta \cdot \cos^2\varphi \rangle \quad (2.2)$$

$$I_{\perp}(\lambda) = \langle I_{\pi}(\lambda) \cdot \sin^2\theta \cdot \sin^2\varphi + I_{\sigma}(\lambda) \cdot \cos^2\theta + I_{\alpha}(\lambda) \cdot \sin^2\theta \cdot \cos^2\varphi \rangle \quad (2.3)$$

where the sign $\langle \rangle$ stands for the average over all the nanorods contributing to the signal. When the nanorods possess a cylindrical symmetry of their crystal structure, the α -spectrum - the emission along the rod axis - is isotropic and its line shape is identical to the π -spectrum for 5D_0 - 7F_1 (MD) transition and σ -spectrum for 5D_0 - 7F_2 (ED) transition^{80, 106}, as discussed in **Chapter 1 (Figure 1.13a)**. Therefore, the above equations can be rewritten separately as functions of only I_{π} and I_{σ} as:

For electric dipole (ED) transition,

$$I_{\parallel,ED}(\lambda) = \langle I_{\pi,ED}(\lambda) \cdot \cos^2\theta + I_{\sigma,ED}(\lambda) \cdot \sin^2\theta \rangle \quad (2.4)$$

$$I_{\perp,ED}(\lambda) = \langle I_{\pi,ED}(\lambda) \cdot \sin^2\theta \cdot \sin^2\varphi + I_{\sigma,ED}(\lambda) \cdot (\cos^2\theta \cdot \sin^2\varphi + \cos^2\varphi) \rangle \quad (2.5)$$

For magnetic dipole (MD) transition,

$$I_{\parallel,MD}(\lambda) = \langle I_{\sigma,MD}(\lambda) \cdot \sin^2\theta \cdot \sin^2\varphi + I_{\pi,MD}(\lambda) \cdot (\cos^2\theta \cdot \sin^2\varphi + \cos^2\varphi) \rangle \quad (2.6)$$

$$I_{\perp,MD}(\lambda) = \langle I_{\sigma,MD}(\lambda) \cdot \cos^2\theta + I_{\pi,MD}(\lambda) \cdot \sin^2\theta \rangle \quad (2.7)$$

Since nanorods' orientation distribution with respect to \vec{n} has cylindrical symmetry, $\langle \sin^2\varphi \rangle$ and $\langle \cos^2\varphi \rangle$ become $\frac{1}{2}$. Therefore, **Equations 2.4-7** can be rewritten as:

For electric dipole (ED) transition,

$$I_{\parallel,ED}(\lambda) = I_{\pi,ED}(\lambda) \cdot \langle \cos^2\theta \rangle + I_{\sigma,ED}(\lambda) \cdot (1 - \langle \cos^2\theta \rangle) \quad (2.8)$$

$$I_{\perp,ED}(\lambda) = \frac{I_{\pi,ED}(\lambda)}{2} \cdot (1 - \langle \cos^2\theta \rangle) + \frac{I_{\sigma,ED}(\lambda)}{2} \cdot (1 + \langle \cos^2\theta \rangle) \quad (2.9)$$

For magnetic dipole (MD) transition,

$$I_{\parallel,MD}(\lambda) = \frac{I_{\sigma,MD}(\lambda)}{2} \cdot (1 - \langle \cos^2\theta \rangle) + \frac{I_{\pi,MD}(\lambda)}{2} \cdot (1 + \langle \cos^2\theta \rangle) \quad (2.10)$$

$$I_{\perp,MD}(\lambda) = I_{\sigma,MD}(\lambda) \cdot \langle \cos^2\theta \rangle + I_{\pi,MD}(\lambda) \cdot (1 - \langle \cos^2\theta \rangle) \quad (2.11)$$

where θ is an average polar angle of all nanorods residing in the volume to field direction \vec{n} . Since reference spectra (I_{π} , I_{σ}) are already established (**Figure 2.7f**), one can perform spectral fitting analysis and can determine $\langle \cos^2\theta \rangle$ from the coefficients obtained. Once $\langle \cos^2\theta \rangle$ is decided, the order parameter can be calculated according to **Equation 2.1**.

2.2.3. In-plane order parameter analysis by spectral fitting

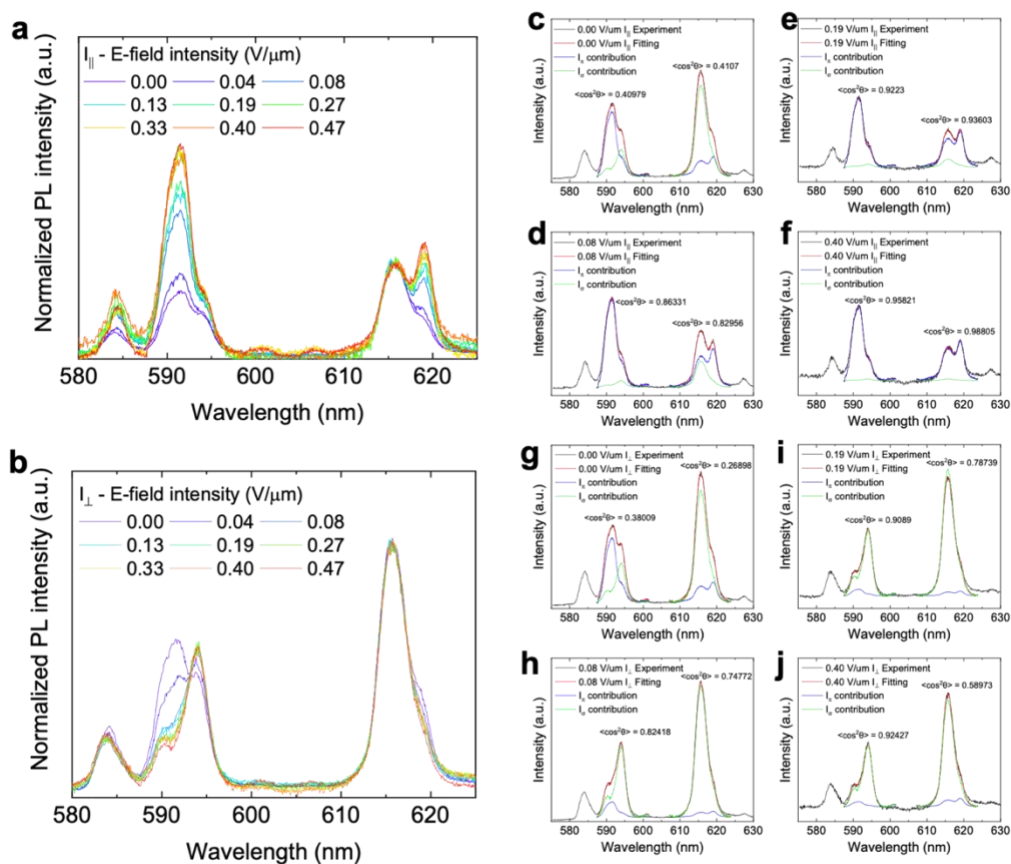


Figure 2.9. Polarized photoluminescence spectra of NaYF₄:Eu nanorods in-plane aligned assembly measured as a function of E-field intensity ($f = 1$ kHz) in IPS E/O cell with the analyzer set to **(a, c-f)** parallel (I_{\parallel}) or **(b, g-j)** perpendicular (I_{\perp}) to the direction of E-field \vec{n} . All spectra are normalized to the intensity at peak $\lambda \sim 615$ nm. Spectral fitting $S_{in-plane}$ analysis of spectra obtained at E-field intensity of **(c,g)** 0, **(d,h)** 0.08, **(e,i)** 0.19, **(f,j)** 0.40 V/ μ m. At spectra obtained at different E-field strength, two wavelength ranges - MD emission (5D_0 - 7F_1 transition), ED emission (5D_0 - 7F_2 transition) - at two orthogonal polarization state - I_{\parallel} and I_{\perp} - are used for extracting $\langle \cos^2\theta \rangle$ by spectral fitting. Extracted value of $\langle \cos^2\theta \rangle$ is written in the Figure.

Figure 2.9a-b shows the polarized photoluminescence spectra measured with an analyzer set parallel to \vec{n} (I_{\parallel}) and perpendicular to \vec{n} (I_{\perp}) as a function of E-field intensity, respectively. The optical setup used for collecting polarized photoluminescence is presented in **Figure 1.16**. **Figure 2.9c-j** shows the result of spectral fitting $S_{\text{in-plane}}$ analysis according to **Equations 2.8-11**. For each line shape of the experimental spectrum (black line), two different wavelength ranges (MD or ED transition) are separately fitted using as-established reference signals (I_{π} – blue line, I_{σ} – green line) and the coefficient obtained from best fit (red line) directly provided the value of $\langle \cos^2\theta \rangle$ as presented in each Figure. As shown in **Figure 2.9c-j**, the fitting line (red) overlaps almost perfectly with the experimental line (black), indicating a successful fitting analysis. In-plane order parameter $S_{\text{in-plane}}$ is then calculated according to **Equation 2.1**.

Figure 2.10 summarizes calculated in-plane order parameter $S_{\text{in-plane}}$ by spectra fitting analysis. At one given electric field intensity, four different value of order parameter S could be obtained from the different polarization (I_{\parallel} , I_{\perp}) or different dipole emission (ED, MD), notably from $I_{\parallel,MD}$, $I_{\parallel,ED}$, $I_{\perp,MD}$ and $I_{\perp,ED}$. Calculated in-plane order parameter $S_{\text{in-plane}}$ from $I_{\parallel,MD}$, $I_{\parallel,ED}$ and $I_{\perp,MD}$ spectrum lines showed the tendency where $S_{\text{in-plane}}$ increases upon increasing E-field, increasing from isotropic orientation ($S_{\text{in-plane}} \sim 0.1$) to close to perfect alignment ($S_{\text{in-plane}} \sim 1$). The difference of $S_{\text{in-plane}}$ obtained from different spectral ranges or polarizations seems to originate from the error in the fitting analysis due to the peak shift or non-stable baseline treatment, as discussed in **Chapter 1.3.3**. Calculated $S_{\text{in-plane}}$ from $I_{\perp,ED}$ spectrum is an outlier where the calculated order parameter is decreased even at a higher electric field. This error seems to be due to the small intensity and very low degree of polarization (DOP) of the peak at 619 nm (DOP ~ 0.2) comparing to the other peaks (DOP ~ 0.5), for which the accuracy of analysis is not sufficient. Obviously, the line shape change in the ED emission of the I_{\perp} signal is much smaller than other transitions or/and polarization, as shown in **Figure 2.9b**.

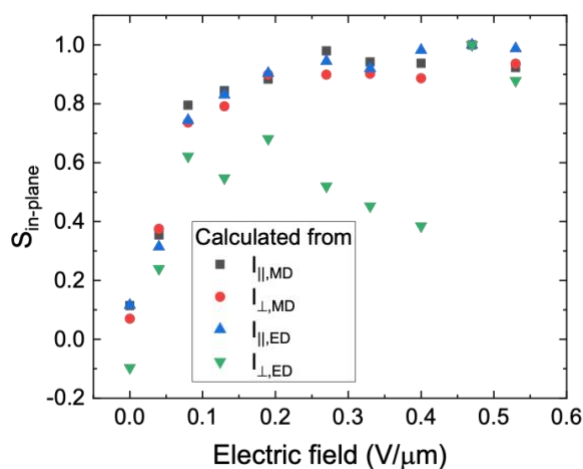


Figure 2.10. In-plane order parameter $S_{\text{in-plane}}$ calculated by spectral fitting analysis as a function of E-field intensity. For each E-field intensity, $S_{\text{in-plane}}$ is calculated from 2 different polarization at 2 different transition ($I_{\parallel,MD}$, $I_{\parallel,ED}$, $I_{\perp,MD}$ and $I_{\perp,ED}$).

Summary of Chapter 2.2

A methodology for calculating the *in-plane* order parameter of the aligned nanorod assembly with a known global alignment orientation is presented. The method is based on the mutually different polarization nature of several emission dipoles of different nature (MD, ED) inherent to lanthanides' emission, as discussed in **Chapter 1**. As a proof-of-concept system, NaYF₄:Eu nanorods are aligned *in-plane* by applying an electric field. The evolution of the *in-plane* order parameter is then followed *in situ* as a function of the electric field intensity. The order parameter could be calculated based on a single polarized photoluminescence spectrogram in a non-destructive manner.

2.3. Homeotropic order parameter analysis of NaYF₄:Eu aligned nanorod assembly

Vertically aligned (homeotropic) nanorod assembly

In recent years, vertically aligned (homeotropic) assembly (**Figure 2.3c**) has gained particular attention as they are useful in various applications. For instance, homeotropic assemblies of semiconducting nanorods are promising for energy and sensor devices due to their improved light absorption, large surface-to-volume ratio, and increased carrier collection efficiency.¹⁰⁷⁻¹¹¹ Homeotropic assemblies of plasmonic nanorods improve the performance of surface-enhanced Raman scattering (SERS) substrates thanks to their ability to enhance local electromagnetic fields with better uniformity and reproducibility.^{112, 113} Vertically aligned nanorods assembly can be fabricated in many different approaches, involving a seeded growth^{112, 114} (**Figure 2.11**), a lithographic template technique¹¹³, by evaporation⁸³⁻⁸⁶, *etc.* Measuring the order parameter of homeotropic alignment (S_{homeo}) is a key to optimize the structure and performance of such systems, which is however challenging using the currently existing techniques, as discussed above.

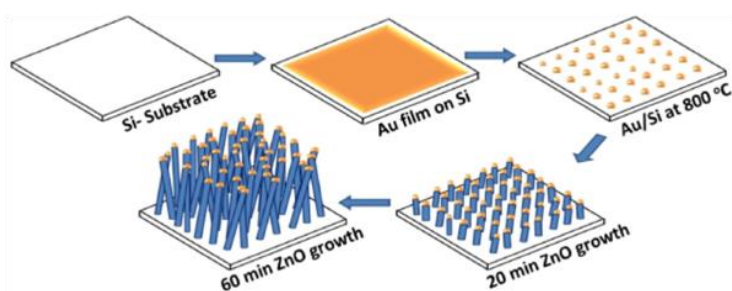


Figure 2.11. The schematic growth mechanism of ZnO nanorods by vapor liquid solid (VLS) process. The Figure is taken from the reference.¹¹⁵

2.3.1. Theoretical methodology for homeotropic order parameter analysis

In the previous chapters, we have shown that the orientation of individual or ensemble of Eu³⁺-doped nanorods can be analyzed based on the peculiar characteristic of π -, σ -, and α - spectra from “polarization” resolved observation of their photoluminescence. Here, we show that the homeotropic order parameter S_{homeo} of vertically aligned nanorods assembly can be analyzed even without using any polarization optics nevertheless it relies on the same basis. The methodology allows a facile and robust analysis of S_{homeo} eliminating measurement errors and complexity due to the polarizing optics. This is an excellent advantage because various optical components easily perturb the polarization state (*e.g.*, mirrors, filters, gratings, detector arrays, diffusing media, *etc.*).

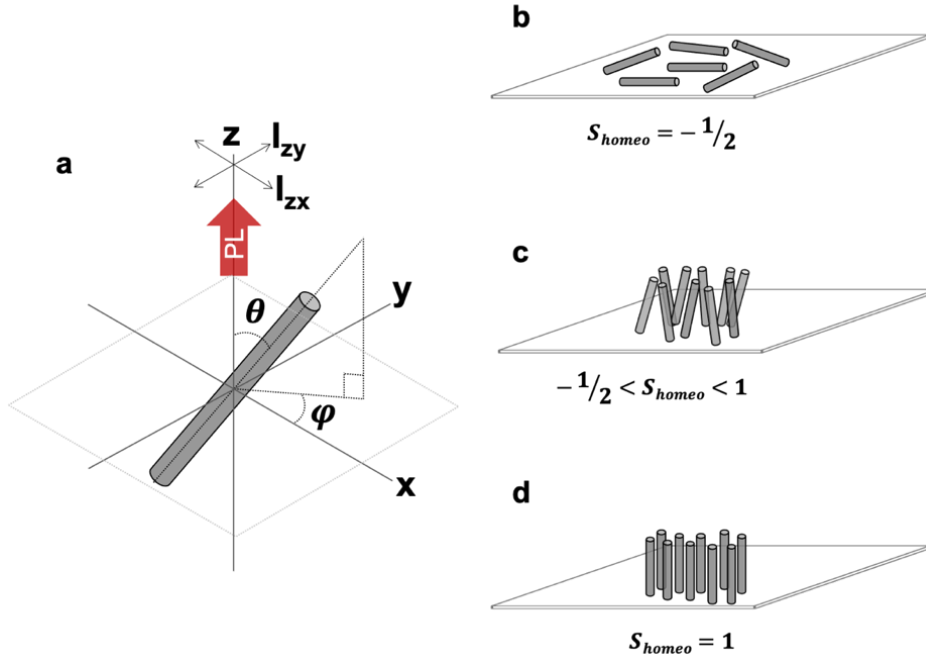


Figure 2.12. (a) Schematic illustration of a single nanorod in laboratory frame with an arbitrary orientation - polar and azimuthal angles (θ , φ) with respect to the measurement axis (z-axis). The PL signal measured along the z-axis is a projected sum of π and σ signals. Schematic illustration of nanorods assembly (b) lying on the substrate (normal to the measurement axis) and (d) standing normal to the substrate (parallel to the measurement axis). (c) shows an intermediate state where the nanorods are partially oriented normal to the substrate. The value or the range of the homeotropic order parameter S_{homeo} for each state is noted.

When a single Eu^{3+} doped nanorod is considered in 3D space with arbitrary spherical angles (θ -polar and φ -azimuthal) with respect to the measurement axis (z-axis) (**Figure 2.12a**), its PL intensities collected at two orthogonal analyzer angles (I_{zx} , I_{zy} – the two indices indicate the measurement axis and the analyzer axes respectively) are projected sums of π , σ , and α components. Note that the axis used for the polar angle is different from what is used to calculate a single nanorod orientation presented in **Chapter 1 (Figure 1.14a)**. The two spherical angles (θ , φ) of single nanorod in the laboratory coordinates (**Figure 2.12a**) can be calculated using the following equations.

At whole wavelength (λ) for both MD and ED transition lines:

$$I_{zy}(\lambda) = I_{\pi}(\lambda) \cdot \sin^2\theta \cdot \sin^2\varphi + I_{\sigma}(\lambda) \cdot \sin^2\theta \cdot \cos^2\varphi + I_{\alpha}(\lambda) \cdot \cos^2\theta \quad (2.12)$$

$$I_{zx}(\lambda) = I_{\pi}(\lambda) \cdot \sin^2\theta \cdot \cos^2\varphi + I_{\sigma}(\lambda) \cdot \sin^2\theta \cdot \sin^2\varphi + I_{\alpha}(\lambda) \cdot \cos^2\theta \quad (2.13)$$

The PL collected in the measurement axis (I_z) without an analyzer is the sum of the two orthogonal polarizations (I_{zx} and I_{zy}). Therefore, **Equations 2.12-13** can be rewritten as:

$$I_z(\lambda) = I_{zx}(\lambda) + I_{zy}(\lambda) = \sin^2\theta \cdot (I_{\pi}(\lambda) + I_{\sigma}(\lambda)) + 2\cos^2\theta \cdot I_{\alpha}(\lambda) \quad (2.14)$$

When considering an assembly of multiple nanorods, the collected PL emission is a sum of the contributions by all the nanorods residing in the measured volume. Hence, $\cos^2\theta$ can be replaced by $\langle \cos^2\theta \rangle$, indicating the spatial and temporal average for the nanorods residing in the focal volume during the time of measurement. In the case of homeotropic assembly (*i.e.* \vec{n} is vertical to the substrate plane and parallel to the measurement axis, **Figure 2.3c**), $\langle \cos^2\theta \rangle$ corresponds to the mean distribution of the polar angles with respect to the director of the alignment \vec{n} . Therefore, **Equation 2.14** can be rewritten using **Equation 2.1** as:

$$\frac{3}{2}I_z(\lambda) = (1 - S_{\text{homeo}}) \cdot I_{\pi+\sigma}(\lambda) + (1 + 2 \cdot S_{\text{homeo}}) \cdot I_{\alpha}(\lambda) \quad (2.15)$$

where $I_{\pi+\sigma}(\lambda)$ is a sum of $I_{\pi}(\lambda)$ and $I_{\sigma}(\lambda)$. Therefore, the PL collected with the measurement axis (I_z) is a simple function of the homeotropic order parameter (S_{homeo}) and the reference emission intensities ($I_{\pi+\sigma}$ and I_{α}). Hence, once $I_{\pi+\sigma}(\lambda)$ and $I_{\alpha}(\lambda)$ are known, S_{homeo} can be obtained by a simple measurement of the unpolarized emission spectrum ($I_z(\lambda)$).

The value of S_{homeo} is 1 for a perfect homeotropic alignment (**Figure 2.12d**). S_{homeo} can be $-1/2$ when all the nanorods are lying on the substrate plane normal to the measurement axis (**Figure 2.12b**). In this case, $\langle \cos^2\theta \rangle$ is zero, and thus I_z is equal to $I_{\pi+\sigma}$ without the contribution of I_{α} . So, the reference spectrum, $I_{\pi+\sigma}(\lambda)$, can easily be collected without using an analyzer from a sample of nanorods lying on a substrate. By a separate experiment observing electrically in-plane-aligned nanorods with an analyzer (**Figure 2.7f**), it was confirmed that the sum of the two orthogonally polarized π - and σ -spectra ($I_{\pi}(\lambda) + I_{\sigma}(\lambda)$) is identical to the $I_{\pi+\sigma}(\lambda)$ spectrum of randomly deposited nanorods (**Figure 2.13**).

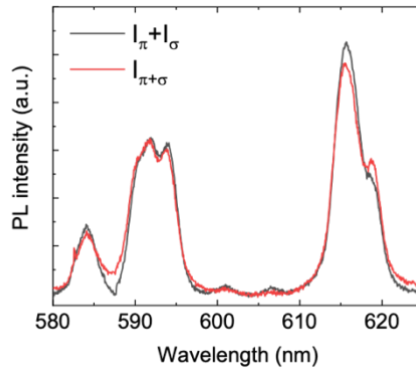


Figure 2.13. Sum of separately measured emission spectra of π and σ configuration ($I_{\pi}+I_{\sigma}$) from the electrically aligned $\text{NaYF}_4:\text{Eu}$ nanorod assembly and the emission spectrum of randomly deposited $\text{NaYF}_4:\text{Eu}$ nanorods lying on the substrate ($I_{\pi+\sigma}$).

The other reference spectrum, $I_{\alpha}(\lambda)$, can also be obtained without an analyzer from a sample with perfect vertical alignment as $I_z = 2I_{\alpha}$ for $S_{\text{homeo}} = 1$ (**Figure 2.12d**). As the experimental spectrum ($I_z(\lambda)$) and the two reference spectra ($I_{\pi+\sigma}(\lambda)$ and $I_{\alpha}(\lambda)$) can be obtained without an analyzer, this method does not

require consideration of polarization during measurement. Nevertheless, it relies on the intrinsic anisotropy of PL emission from lanthanide-doped nanorods. It is also worth noting that this methodology is free from considering the structural factors other than S_{homeo} such as volume fraction of the nanorods, sample thickness, and other intrinsic material properties.

2.3.2. Homeotropic alignment using homeotropic electro-optical cell

When nanorods are submitted in the vertical E-field \vec{n} , nanorods begin to orient parallel to E-field \vec{n} and the PL signal is simultaneously collected at the axis parallel to \vec{n} (I_z). The optical setup used for the PL collection is presented in **Figure 1.16** but without an analyzer. Subsequently, the PL signal is collected as a function E-Field intensity (**Figure 2.14**). The line shape of the collected PL spectrum is analyzed based on **Equation 2.15** of which S_{homeo} is extracted by spectral fitting. The S_{homeo} analysis requires a preset of reference spectra ($I_{\pi+\sigma}$ and I_α), as discussed above.

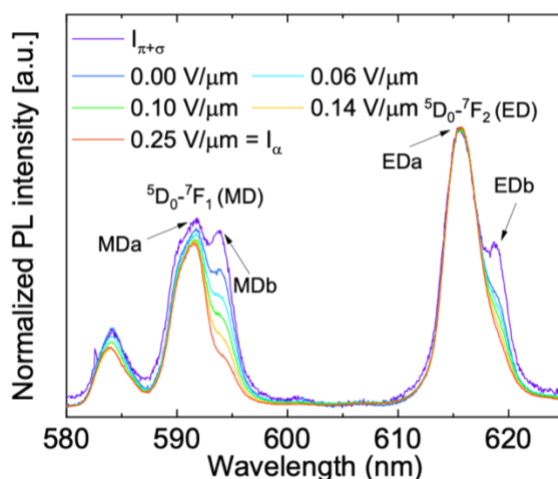


Figure 2.14. The collected PL emission spectra with gradually increased E-field strength (E). $I_{\pi+\sigma}$ indicates a reference spectrum taken with randomly deposited nanorods lying on the substrate. All the spectra were collected without polarizer and normalized to the peak with the highest intensity at $\lambda \sim 615$ nm.

Spin-coated NaYF₄:Eu nanorods dispersion on the glass substrate followed by an annealing process is used to collect $I_{\pi+\sigma}(\lambda)$ signal (**Figure 2.13**, **Figure 2.14**). Subsequently, the I_α signal was collected from perfectly vertically aligned nanorods assembly under a strong E-field ($E > 0.25$ V/ μ m) saturating the increase of S_{homeo} (**Figure 2.14**). The PL spectra collected with varied E-field intensity show a clear line shape change (**Figure 2.14**). As the E-field strength increases, in the 5D_0 - 7F_1 (MD) transition range, the relative intensity of the MDb peak at 593.7 nm decreases compared to the almost constant intensity of the MDa peak at 591.4 nm. While in the 5D_0 - 7F_2 (ED) transition range, the relative intensity of the EDb peak at 619.0 nm decreases compared to the constant intensity of the EDa peak at 615.3 nm. When the

E-field strength was increased higher than $0.25 \text{ V}/\mu\text{m}$, spectral line shape change was no longer observed. The PL emission spectrum observed at this saturation level was identical to the π spectrum in the ${}^5\text{D}_0\text{-}{}^7\text{F}_1$ (MD) transition range and to the σ -spectrum in the ${}^5\text{D}_0\text{-}{}^7\text{F}_2$ (ED) transition range (**Figure 1.13a**), which is equal to the α -spectrum and confirms that S_{homeo} is close to 1 at this state. Compared to the typical organic liquid crystals used for electro-optical devices, $0.25 \text{ V}/\mu\text{m}$ is about one order of magnitude lower E-field strength required to fully control their orientations. Such an efficient control with a moderate E-field may be useful for further device application using colloidal nanorod systems.

2.3.3. Homeotropic order parameter analysis by spectral fitting

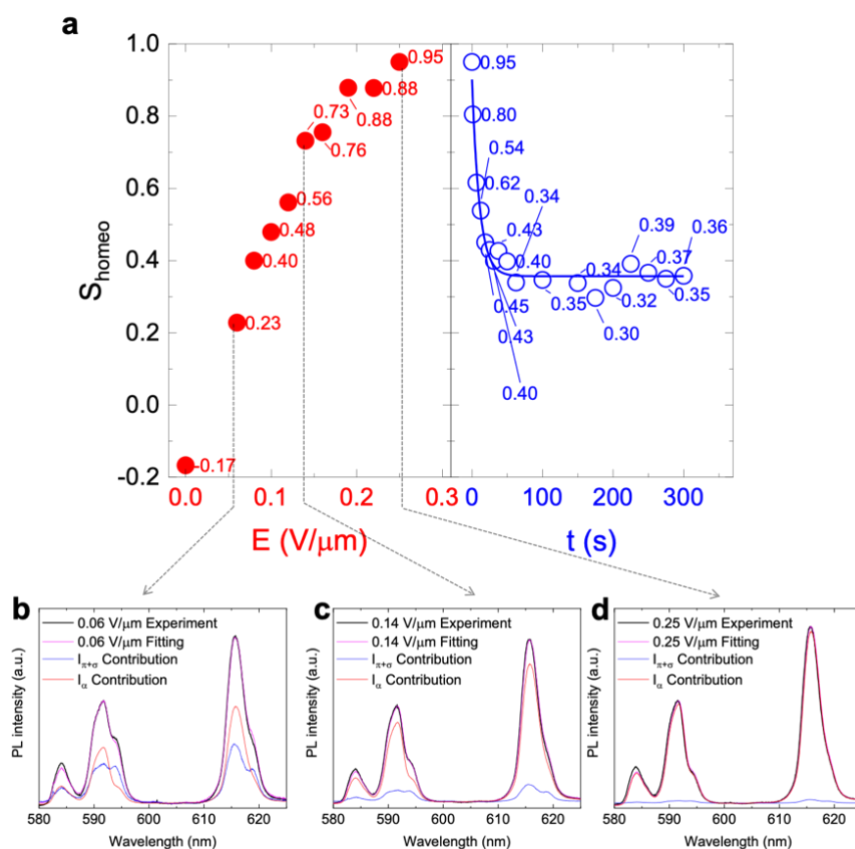


Figure 2.15. (a) A plot of the calculated homeotropic order parameter S_{homeo} as a function of E (red, left panel) and of the relaxation time (t) after saturation at $E = 0.25 \text{ V}/\mu\text{m}$ and turning off the E-field (blue, right panel). The spectral fitting of the emission spectra for different E-field intensities of (b) 0.06 , (c) 0.14 , and (d) $0.25 \text{ V}/\mu\text{m}$ with the reference spectra ($I_{\pi+\sigma}$ and I_{α}) providing the value of S_{homeo} according to the **Equation 2.15**.

By fitting the reference spectra ($I_{\pi+\sigma}$ and I_{α}) on the experimental spectra using **Equation 2.15**, the S_{homeo} values were calculated and plotted as a function of E-field strength (**Figure 2.15a**, left panel). When $E = 0 \text{ V}/\mu\text{m}$, the calculated S_{homeo} was -0.17 , lower than 0 for perfectly random orientation. This seems to

be due to the in-plane capillary force that induces partial orientation of nanorods parallel to the substrate plane when injecting them into the thin gap (20 μm) of the E/O cell. The S_{homeo} value gradually increases as a function of the E-field strength. **Figure 2.15b-d** are examples of the fitting analysis showing that the contribution of I_{α} (red lines) compared to $I_{\pi+\sigma}$ (blue lines) increases when increasing the E-field strength. When $E = 0.25 \text{ V}/\mu\text{m}$, the contribution of $I_{\pi+\sigma}$ is almost negligible and I_{α} occupies most of the emission spectrum, providing $S_{\text{homeo}} = 0.95$ (**Figure 2.15d**).

The PL spectrum was also continuously observed after turning off the E-field to examine the relaxation behavior of the aligned nanorods. Without E-field, nanorods are subject to randomization of their orientation due to the Brownian motion. The calculated S_{homeo} values as a function of time after turning off the E-field are shown in **Figure 2.15a, right panel**. The corresponding PL spectra are shown in **Figure 2.16**, and the spectral fitting analysis result is shown in **Figure 2.17**.

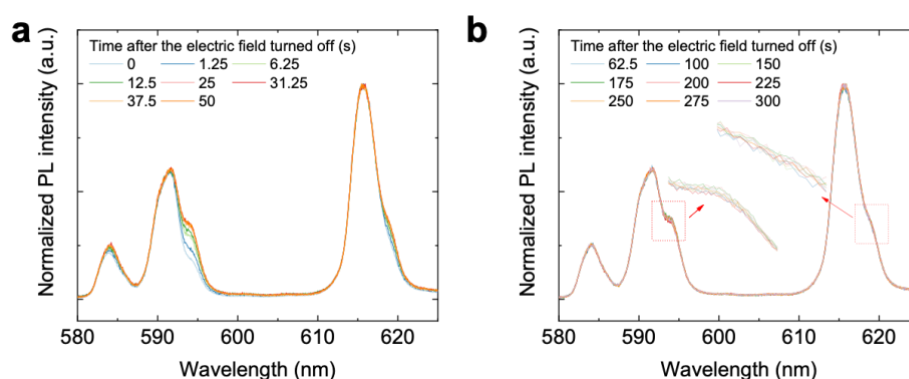


Figure 2.16. Photoluminescence spectra of $\text{NaYF}_4:\text{Eu}$ nanorods collected as a function of relaxation time after the E-field turned off from the saturating E-field. All spectra are normalized to the intensity at peak $\lambda \sim 615 \text{ nm}$.

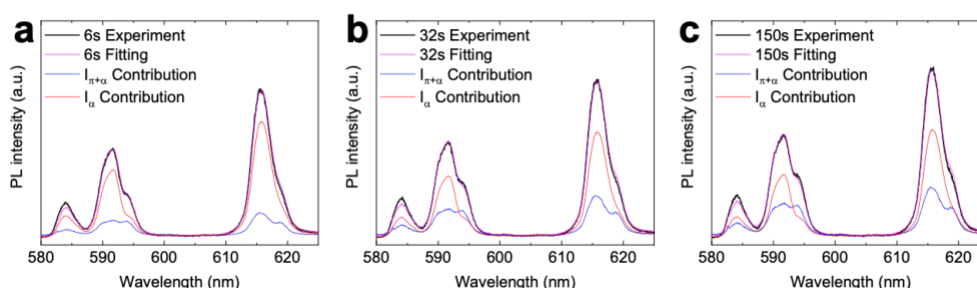


Figure 2.17. Analyzed emission spectrum measured as a function of relaxation time after the E-field turned off from the saturating E-field : (a) 6, (b) 32, and (c) 150 seconds. The spectral fitting analysis is made according to **Equation 2.15**.

These experimental points fit with an exponential decay curve ($y = A \cdot \exp(-x/t_1) + y_0$) with a relatively long decay time ($\tau = 7.4 \text{ s}$). We attribute this slow orientation relaxation of the nanorods to their relatively large size ($1184 \pm 430 \text{ nm}$ in length and $117 \pm 24 \text{ nm}$ in diameter) and the large viscosity of

ethylene glycol ($1.61 \cdot 10^{-2}$ Pa·s) as a dispersion medium. The theoretical rotational diffusion coefficient is given as:

$$\Omega = \frac{3k_b T}{16\pi\eta_0 a^3} \left(-1 + 2 \ln \frac{2a}{b} \right) \quad (2.16)$$

where k_b is Boltzmann constant, η_0 is solvent viscosity, a and b are respectively the half-length and equatorial radius of the ellipsoidal particle.¹¹⁶ The Ω calculated for our NaYF₄:Eu nanorods dispersed in ethylene glycol is 0.37 s^{-1} , which is in good accordance with the experimentally obtained relaxation time of 7.4 s ($\cong 0.14 \text{ s}^{-1}$) regarding that Ω is highly sensitive to the particle size while our nanorods have a certain polydispersity. Interestingly, the relaxation of S_{homeo} showed saturation at around 0.35, meaning that the orientation of nanorods was not completely randomized, and there was a memory effect maintaining partially the orientation along the previously applied E-field. It is presumably due to some portion of nanorods that were dragged by the E-field and vertically stuck on the electrode surface losing their mobility. This effect may have affected the calculated Ω value. Further study is required to explain and control this phenomenon. It is also worth noting that there exists fluctuation of S_{homeo} from 0.30 to 0.39 when measured at different moments even after the saturation without E-field. Thus, there seems to be a continuous thermal agitation, and the presented method is quite sensitive to these small changes (see also **Figure 2.16b**).

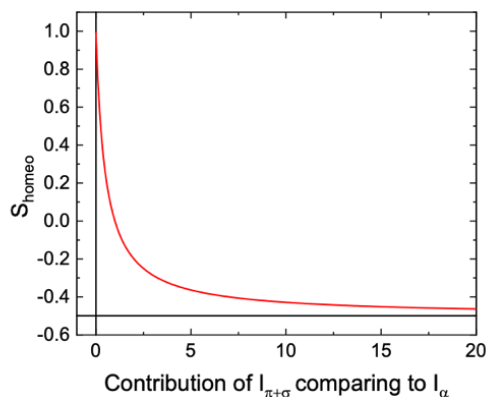


Figure 2.18. Simulated homeotropic order parameter S_{homeo} as a function of $I_{\pi+\sigma}$ contribution comparing to I_{α} . Simulation is made according to **Equation 2.15**.

The accuracy of the calculation of S_{homeo} according to **Equation 2.15** can be evaluated from its simulated profile as a function of relative contributions of $I_{\pi+\sigma}$ and I_{α} (**Figure 2.18**). One can expect that the accuracy would be less good at the extremities where S_{homeo} is near 1 or $-1/2$. This implies that there might be some error on the calculated value of $S_{\text{homeo}} = 0.95$ near saturation ($E = 0.25 \text{ V}/\mu\text{m}$). To minimize errors, stable and good spectral resolution and correct baseline treatment of the measured spectra are necessary, as discussed in **Chapter 1**. Instead of spectral fitting analysis, S_{homeo} can also be calculated as a function of wavelength, as discussed in **Appendix Figure 2.1**.

Out-of-plane angle analysis of a single nanorod without polarization measurement

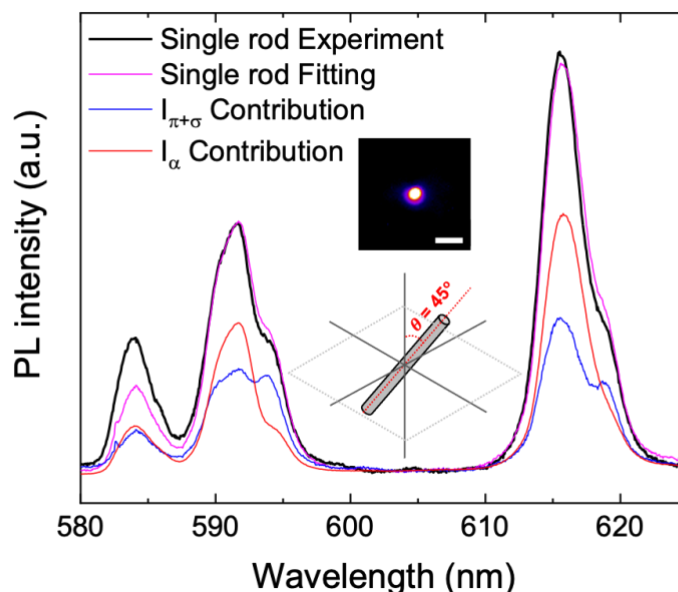


Figure 2.19. The emission spectrum of a single NaYF₄:Eu nanorod embedded in a polymer film with an arbitrary orientation (black line) and its fitting analysis with the reference spectra determining the polar angle θ of the nanorod. The inset picture is a photograph of the PL emission of the single nanorod captured with a CCD camera (scale bar: 2 μm). The inset scheme indicates the out-of-plane angle of a nanorod in the coordinates with a calculated value.

The same method can be applied to measure the out-of-plane orientation (θ) of a single NaYF₄:Eu nanorod (**Figure 2.19, inset scheme**). Individually dispersed and randomly oriented nanorods were immobilized in a $\sim 8 \mu\text{m}$ thick PVA (polyvinyl alcohol) polymer film in the same way presented in **Chapter 1**. The PL image of a nanorod captured by a CCD camera (**Figure 2.19, inset picture**) shows an almost circular shape due to the nanorod size smaller than the camera's spatial resolution. So, any information about the nanorod orientation cannot be retrieved from the image. However, the line shape of the emission spectrum from the same nanorod enables calculating a polar angle (θ) of the nanorod orientation with respect to the measurement axis according to **Equation 2.14**. The calculated value of θ is 45° , as noted in the Figure. Calculating azimuthal angle φ from the line shape of photoluminescence is also possible if the polarization of the emission spectrum is measured, as discussed in **Chapter 1**. The calculated values of θ of a single nanorod using unpolarized spectrum and a polarized signal are compared in **Appendix Table 2.2**.

Summary of Chapter 2.3

A methodology to calculate the *homeotropic* order parameter of an aligned nanorod assembly with a known global alignment orientation is presented. The method enables an instant determination of the *homeotropic* order parameter of an aligned lanthanide-doped nanorod assembly from a single photoluminescence spectrogram of lanthanide emission. The method is demonstrated without any polarization measurements, although it relies on the polarization behavior of the lanthanide emission. As a proof-of-concept system, NaYF₄:Eu nanorods are vertically aligned by applying an electric field. The evolution of the *homeotropic* order parameter is then followed *in situ* as a function of the electric field intensity in a non-destructive way. The same method is applied to the measurement of the out-of-plane orientation of a single nanorod without considering polarization.

2.4. Conclusion

This chapter has shown that varying degrees of orientation (order parameter S) in nanorods assembly under externally applied electric field (in-plane and homeotropic) could be investigated in real-time by a spectroscopic analysis of the photoluminescence emission of rare-earth dopants. The presented method is based on the optical anisotropy, mutually different polarization behavior of MD and ED, inherent in lanthanide luminescence resulting in the variation of the emission spectral line shape as a function of S , as also extensively discussed in **Chapter 1** for the case of the single nanorod.

We have also shown that a precise measurement of S of dynamically modulated assembly can be performed using a conventional microscope and a single emission spectrum, which is much more straightforward, facile, and cost-effective compared to classical methods for measuring S such as birefringence, SAXS, and high-resolution microscope. Another crucial advantage of the presented method is that the measurement domain can be controlled. It can be as small as the focal volume of optical microscopy ($< 0.1 \mu\text{m}^3$) or can be larger according to various needs, which has not been achieved by other techniques to assess the order parameter S . Furthermore, a rapid *in-situ* analysis can be realized in a non-destructive way by this spectroscopic method. It is thus promising for investigations of various collective dynamics of nano-scale materials (*e.g.*, self-assembly, directed assembly, liquid crystalline behavior, thermal motions, vertical anisotropic growth, *etc.*) with a closer look into a micro- and nano-scale domain.

Chapter 3.

Liquid Crystalline Behavior of Nanorod Suspension

In the previous chapters, we discussed the anisotropic properties of nanorods in their luminescence and their use to calculate orientation or order parameter. This chapter discusses another important characteristic of colloidal anisotropic nanomaterials: liquid crystalline (LC) behavior, a spontaneous transition from disordered phase (isotropic) to orientationally/positionally ordered nematic/smectic phase. Onsager's hard rod theory describes the isotropic-nematic transition threshold concentration ($\Phi_{\text{ISO-NEM}}$) as a function of the length/diameter (aspect) ratio of the rods. This Onsager's hard rod theory explains that the long-range repulsive force between the rods stabilized by the surface charge can significantly increase their effective diameter D_{eff} , resulting in decreased $\Phi_{\text{ISO-NEM}}$ compared to sterically stabilized rods.

In this chapter, we considered highly charged $\text{LaPO}_4:\text{Eu}$ nanorods in ethylene glycol and showed that the behavior of the LC is in good agreement with Onsager's hard rod theory. Subsequently, we prepared the ligand stabilized $\text{LaPO}_4:\text{Eu}$ nanorods (sterically stabilized) dispersed in chloroform by the phase transfer surface functionalization, and their LC behavior is compared to LC stabilized with a long-range electrostatic repulsive force. Interestingly, the ligand stabilized LC suspension showed a counterintuitive phenomenon that the transition to the nematic phase occurs at an extremely low $\Phi_{\text{ISO-NEM}}$. Furthermore, $\Phi_{\text{ISO-NEM}}$ was found to vary with the amount of excess ligands dissolved in the solvent in a manner similar to polar media where the increase in ionic strength led to surface charge screening. Under gravity, this diluted nematic suspension left to age in a capillary tube showed a macroscopic separation where the biphasic LC transition and gel formation seem induced in the same suspension. We discuss the unique characteristic of charges in the apolar solvent (far-reaching interaction but weak) and the resultant sophisticated LC behaviors. This fundamental understanding would help prepare a new type of colloidal LC in an apolar medium stabilized by steric and electrostatic repulsion.

Parts of the results presented in this chapter were made collaborating with Dr. Ivan Dozov and Prof. Patrick Davidson in Laboratoire de Physique des Solides (LPS), Université Paris-Sud, Orsay, France.

Parts of the results presented in this chapter are under the publication process: "Liquid crystalline behavior of charged nanorods in apolar media", *to be submitted*

3.1. Introduction

3.1.1. Colloidal dispersion of nanoparticles and their stability

A colloidal dispersion is a system where particles are homogeneously distributed in the dispersing medium. The size of particles ranges very broadly (from a few nanometers to micrometers) and can also be shaped in a very wide variety such as spheres, discs, cubes, plates, and rods. When such particles are dispersed in the medium, they exhibit a thermal diffusion phenomenon known as Brownian motion. This diffusion rate is associated with various parameters such as temperature, the solvent's viscosity, and particles' size. When the particles' size is sufficiently small, the diffusion rate is fast enough to compensate for gravitational force. Thus particles are homogeneously distributing in the medium and do not settle down (**Figure 3.1a**).^{117, 118} However, when particles' size is increased due to aggregation, the diffusion rate rapidly decreases, resulting in sedimentation by gravitational force (**Figure 3.1b**). Therefore, preventing aggregation is an essential factor for good colloidal stability.

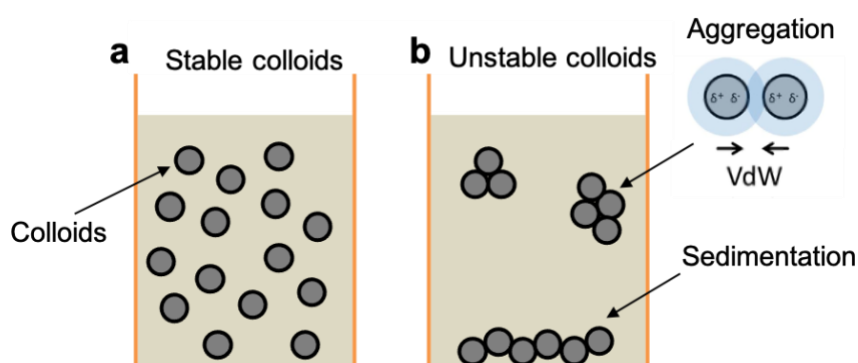


Figure 3.1. Schematic illustration of (a) stable or (b) unstable colloids dispersed in the liquid medium. The scheme of aggregation is taken from the reference.¹¹⁹

Aggregates are known to be formed by an interaction between particles, called Van der Waals (VdW) force (**Figure 3.1b**). VdW force is an attractive interparticle force originating from a distance-dependent instant electron density polarization. The interaction energy, VdW force, for two spherical particles dispersed in the dielectric medium can be estimated using Hamaker's approximation as ^{120, 121} :

$$V_{VdW} \approx -\frac{A_H \cdot R}{12 \cdot D} \quad (3.1)$$

where A_H is the Hamaker constant, R is the particle's radius, and D is the distance between particles. This VdW force quickly vanishes when two particles are far from each other. However, when the distance between particles is small (*e.g.*, at the event of particle collision), strong VdW force leads to a permanent aggregation of particles, which is typically irreversible. VdW force itself can also be reduced. However, it has a very small modulation window because Hamaker constant A_H depends on the bulk material properties such as dielectric constant or refractive index. Thus, the most common method of preventing aggregation is preventing particles come close to each other by giving a repulsive force to the particles. If this repulsive force is higher than the attractive VdW force, particles can be dispersed homogeneously in the medium, guaranteeing long-term colloidal stability. There are two common methods imparting a repulsive force to the particle surface, which involves the electrostatic repulsion and the steric repulsion/hindrance (**Figure 3.2**).

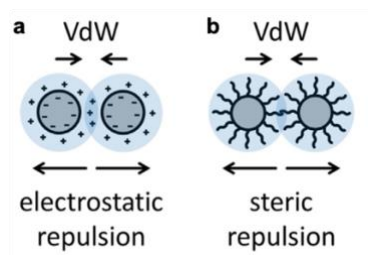


Figure 3.2. Schematic illustration of particles stabilization (a) with repulsive electrostatic (b) and repulsive steric interactions. Figures were taken from the reference.¹¹⁹

Electrostatic repulsion

When particles are dispersed in a polar medium, particles can be charged due to the presence of certain acidic or basic groups in the medium, dissociation of the surface molecules, and selective or preferential adsorption of ions present in the medium. These surface charges form an inner layer and attract counter ions from the medium through a Coulomb force, generating an extended outer layer called the "electric double layer". When particles are close to each other, this layer exerts a repulsive electrostatic force (**Figure 3.2a**). Electrostatic repulsion can be mathematically expressed as¹²²:

$$V_{electric} \approx 2\pi\epsilon\epsilon_0 R \cdot \psi_0^2 \cdot e^{-\frac{D}{\lambda_D}} \quad (3.2)$$

where R is particle radius, ψ_0 is surface potential, D is the distance between particles, λ_D is Debye length. According to **Equation 3.2**, there are two main parameters that influence electrostatic repulsion: surface potential ψ_0 and Debye length λ_D .¹²² Surface potential defines the repulsion strength based on surface

charge density, and Debye length defines the range of inter-particle interaction (*i.e.*, screening length). Surface potential can be controlled by changing the ligand attached to the particle surface or/and by tuning the pH of the dispersing medium. For example, a strongly charged ligand on the particle surface can increase the surface potential (*e.g.*, charge-rich citrate ion grafted to the surface of NaYF₄:Eu nanorods shown in **Chapter 1**). Debye length λ_D can be expressed as¹²²:

$$\lambda_D = \sqrt{\frac{\epsilon\epsilon_0 k_B T}{e^2 N_A 2I}} \quad (3.3)$$

where ϵ is the dielectric constant, T is the solvent temperature, and I is the ionic strength of the medium.

DLVO theory

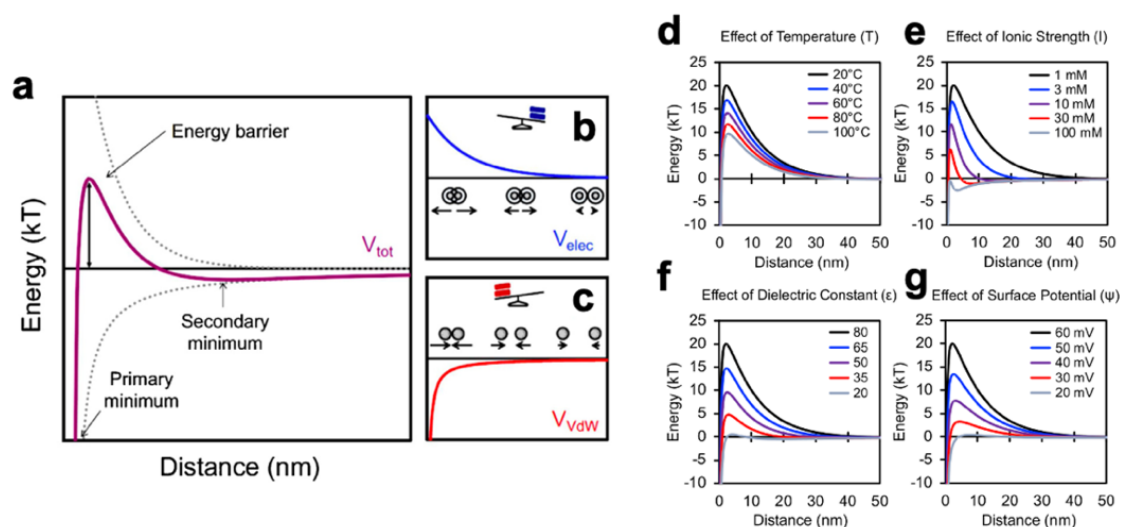


Figure 3.3. (a) Schematic DLVO interaction energy diagram composed of (b) electrostatic repulsion (c) and VdW interactions. Computed DLVO interaction potentials of two spherical particles with a variation of (d) temperature, (e) ionic strength, (f) dielectric constant, and (g) surface potential. The figures are taken from the reference.¹¹⁹

The DLVO theory quantitatively describes the total energy as a function of inter-particle distance, taking into account the effect of attractive VdW force and electrostatic repulsive force^{119, 123} (**Figure 3.3**). As shown in **Figure 3.3b-c**, VdW attractive force and electrostatic repulsive force show a different decay profile as a function of the distance between particles. When the electrostatic repulsion is introduced in the total interaction profiles, a high energy barrier forms by the balance between VdW force and electrostatic repulsion force (**Figure 3.3a**). The thermal energy of particles cannot overcome this high-energy barrier. Therefore, particles do not fall into the primary minimum potential well but stay away from each other around the distance of secondary minimum potential. The colloidal system

having a higher energy barrier shows better colloidal stability. This energy barrier can be controlled by various experimental parameters such as temperature (**Figure 3.3d**), ionic strength (**Figure 3.3e**), dielectric constant (**Figure 3.3f**), and surface potential (**Figure 3.3g**).

Steric repulsion/hindrance

The above-mentioned electrostatic charge stabilization is expected to be inconsequential in nanoparticles dispersed in an apolar solvent. It is because that the introduction of electric charge costs much higher energy than thermal energy $k_B T$ due to a low permittivity of apolar solvent (typically, $\epsilon_{\text{apolar}} < 15$ and $\epsilon_{\text{water}} \sim 80$). In this case, the steric repulsive force can be used for stabilizing colloids, provided by long-chain molecules that are anchored to the particle surface, which physically hinders particles come close to each other (**Figure 3.2b**). The steric repulsion approach is also interesting for nanoparticles dispersed in a polar medium with a very high ionic strength. The thickness of the electric double layer (*i.e.*, Debye length) of nanoparticles in such medium is very low. Thus the electrostatic repulsive force is very weak (**Equation 3.3**). For instance, biochemists often use PEG (polyethylene glycol) polymer with a high molecular weight as a grafting agent for stabilizing particles dispersed in a physiological medium where a huge amount of ions are dissolved in water.

3.1.2. Colloidal liquid crystal

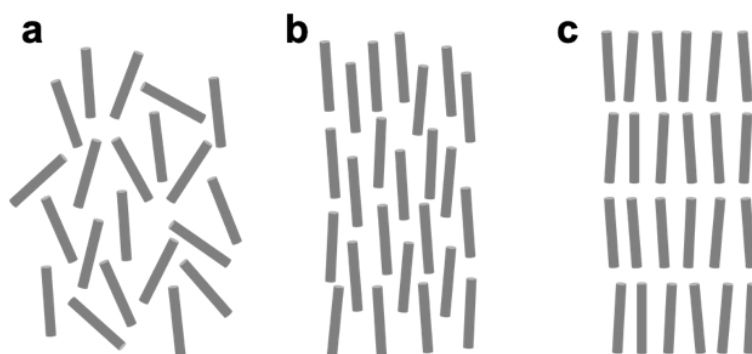


Figure 3.4. Schematic diagrams of the liquid crystalline phases: (a) isotropic, (b) nematic, and (c) smectic.

Liquid crystal (LC) is a state of matter that exhibits orientational order (nematic, **Figure 3.4b**) or both orientational and positional order (smectic, **Figure 3.4c**). LC's structure is similar to a solid crystal but can flow like a liquid. Liquid crystal is an interesting state of matter as it has the capability of spontaneously changing the phase from a disordered phase (isotropic, **Figure 3.4a**) to nematic or smectic phase at different temperatures (thermotropic) or different concentrations (lyotropic). When

ordered phases are viewed between a crossed polarizer, a specific texture is observed as a result of the birefringence of the oriented domains (**Figure 3.5**).

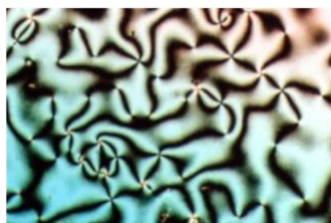


Figure 3.5. Typical Schlieren texture of liquid crystal nematic phase. The image is taken from Wikipedia (link: en.wikipedia.org/wiki/Liquid_crystal).

The phenomenon of liquid crystals is observed in both organic and inorganic materials. Organic LC is a relatively mature scientific field and successfully commercialized, especially with liquid crystal display (LCD) that is now easily found in our daily lives. LC composed of inorganic particles is often referred to as mineral LC or colloidal LC, the main topic of this chapter. Since the first discovery of colloidal LC in the early 20th century by Zocher using rod-like V_2O_5 ¹²⁴, the various mesophases - the nematic, lamellar and columnar phases – have been found in different colloidal LC system such as Rutile (TiO_2)¹²⁵, Goethite ($\alpha-FeOOH$)^{92, 126-128}, graphene oxide¹²⁹, quantum dots ($CdS/CdSe$)¹³⁰, tobacco mosaic virus (TMV)^{131, 132} and clays^{126, 133, 134}, to name a few. Recent work relating to colloidal LC focuses on the understanding of effects of particle polydispersity, gelation, and surface property to the control of LC behavior and on imparting anisotropic physical properties of mineral compounds (*e.g.*, large refractive index^{68, 75}, ferro-electricity and -magnetism⁷⁶⁻⁷⁹, polarized -photoluminescence and -plasmonics^{66, 74, 80, 106}, *etc.*) to LC phase.

Onsager's hard rod model

Onsager's hard rod model gives a simple yet powerful insight into the LC behavior of the colloidal hard rod.¹³⁵ Under the assumption that hard rod does not interact with each other, the theory considers two entropy terms (orientational and packing entropy) to estimate a volume fraction ($\Phi_{ISO-NEM}$) where the transition from isotropic to nematic ordering can be induced. In the case of an isotropic state, it has high orientational entropy because it has a random orientation. And a large volume around a rod is excluded ($V_{ex} = 2 \cdot D \cdot L^2$), which decreases the packing entropy. On the contrary, in the nematic phase where the hard rods are oriented parallel to each other, the orientational entropy decreases. And the excluded volume of hard rods in the nematic phase becomes smaller ($V_{ex} = \pi \cdot D^2 \cdot L$) than that of isotropic state, increasing the packing entropy. Then, the $\Phi_{ISO-NEM}$ is determined by the rods' spatial density based on the balance of these two entropic terms. Onsager's hard rod model is expressed as a simple mathematical equation¹³⁵:

$$\Phi_{\text{ISO-NEM}} \cong 4D/L. \quad (3.4)$$

However, the real colloidal system is much more complex as it has to consider several factors such as particle interaction (attractive or repulsive force), polydispersity, *etc.* In the extended Onsager hard rod model, the intrinsic diameter (D) is replaced by an effective diameter (D_{eff}), taking into account the enlarged diameter of the hard rod by the effect of the electrostatic repulsive force and/or steric hindrance (**Figure 3.6**). The extended Onsager model can be expressed¹³⁵:

$$\Phi_{\text{ISO-NEM}} \cong 5.1 / (L^2 \cdot D_{\text{eff}}) \quad (3.5)$$

From an understanding of **Equation 3.5**, an increase in D_{eff} effectively reduces the critical transition concentration $\Phi_{\text{ISO-NEM}}$. The long-range electrostatic repulsive interaction effectively increases the effective particle diameter D_{eff} because it claims a larger volume for a particle than what it actually occupies. For example, the screening length κ^{-1} of charged colloids can be extended up to 0.3 μm in a polar solvent and up to 7.0 μm in the apolar solvent.¹³⁶⁻¹³⁸ On the contrary, in the case of steric hindrance, D_{eff} remains almost the same with the bare particle because it is governed by a ligand tail that offers relatively short interparticle interaction. For example, the hydrodynamic radius of PEG polymer (molecular weight = 40,000 kDa) commonly used for steric hindrance is known to be 3.95 nm.¹³⁹ Therefore, the charge-based colloidal suspension is expected to have a lower $\Phi_{\text{ISO-NEM}}$ than the steric ligand stabilized suspension. In the case of charge stabilized colloids, the presence of salts dissolved in the same medium can further alter the D_{eff} by adjusting the Debye screen length (**Equation 3.2-3**), functioning as another factor to control $\Phi_{\text{ISO-NEM}}$.

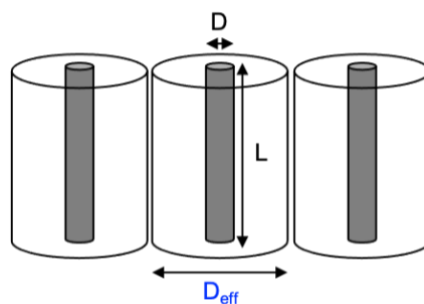


Figure 3.6. Schematic of nanorods with electrostatic repulsion. The diameter of bare nanorods (D) is extended to effective diameter (D_{eff}), claiming a bigger volume than what the bare nanorod actually occupies.

Summary of Chapter 3.1

Colloidal stability of nanoparticles is an important issue and can be achieved by imparting electrostatic or steric repulsive force to the dispersed particles. Depending on the various experimental conditions (*e.g.*, the polarity of the dispersing medium, ionic strength of the dispersing medium, *etc.*), strategies can be developed by choosing an appropriate stabilization method. Well-stabilized suspension of nanorods can exhibit liquid crystalline (LC) behavior where the nanorods are structured like a solid crystal while they can flow like a liquid. Onsager's hard rod theory describes the isotropic-nematic transition threshold concentration ($\Phi_{\text{ISO-NEM}}$) as a function of the length/diameter (aspect) ratio of the rods. This Onsager's hard rod theory explains that the long-range electrostatic repulsive force between nanorods can significantly increase their effective diameter, resulting in a significant decrease of $\Phi_{\text{ISO-NEM}}$. On the contrary, in the case of short-range sterically stabilized rods, $\Phi_{\text{ISO-NEM}}$ should remain almost the same as the one expected from the real dimension of the rods.

3.2. Charge-stabilized LaPO₄:Eu nanorods suspension in a polar medium

This section briefly presents the preparation of charge stabilized LaPO₄:Eu nanorods in a polar medium. The hydrothermal synthesis method of LaPO₄:Eu nanorods is optimized previously in the group.^{1, 69} Such nanorods stabilized by surface-charges in polar medium show exceptional colloidal stability without aggregation for years and exhibit spontaneous LC behavior, of which the LC phase can be controlled by volume fraction Φ and ionic strength. In a previous study, we have shown that such a stable nanorod LC suspension with good controllability of their LC phase can be used for the development of a new type of optical coating and the electro-optical device based on the mineral compound^{69, 75}.

The applicability of such colloidal LC suspension can be even broader by transferring the colloidal particles into different solvents as they can provide a new physical and chemical environment. For example, colloidal particles stabilized in volatile organic solvents can be attractive for the development of closely packed structures since they can self-assemble on the solvent's evaporation.^{140, 141} The efficiency of field-directed nanorods' alignment may be possible to be controlled depending on the dielectric characteristics of dispersing medium. Despite its advantages, stabilizing LC suspension in various solvents with a suitable surfactant is still a complex problem. It requires a thorough understanding of the relationship between the LC behavior of colloidal particles and the interparticle interaction associated with the effect of surface charge and attached ligand.

Here, we have developed the optimized protocol for stabilizing as-prepared LaPO₄:Eu nanorods in the apolar solvent, using an amphiphilic ligand molecule that provides a steric hindrance (**Chapter 3.3.1**). Then, the LC behavior of LaPO₄:Eu nanorods ligand-stabilized in the apolar medium is compared to the LaPO₄:Eu nanorods charge-stabilized in polar medium (**Chapter 3.3.2**). We discuss the effect of the stabilization method on the LC behavior of colloids and propose the use of charges to enrich the LC behaviors of colloids dispersed in the apolar medium.

3.2.1. Hydrothermal synthesis and charge-stabilization of nanorods in ethylene glycol

LaPO₄ nanorods doped with 20% of Eu³⁺ ions are synthesized by the solvothermal method. The stoichiometric concentration of the precursors – La(NO₃)₃, Eu(NO₃)₃, (NH₄)₂HPO₄ – are dissolved in MilliQ water (pH7) and cooled to 0 °C by storing the solutions in the bucket filled with ice. The aqueous solutions of precursors are then mixed, and seed particles are generated instantly, which gives the mixed solution a milky appearance. Aggregation of seed particles is minimized by lowering the temperature before mixing. The solutions are then transferred to a glass tube and flame sealed and heated in an oven

at 170 °C for 3 hours (**Figure 3.7b**). The anisotropic growth of the seed particles generates rod-shaped $\text{LaPO}_4:\text{Eu}$ nanoparticles. After the hydrothermal reaction, the suspension contains residual ions which have not reacted during the reaction. These ions increase the ionic strength of the dispersing medium, making nanorods aggregate and sediment within hours. Therefore, an additional purification step is necessary. The nanorods are then collected by centrifugation and re-dispersed in water adjusted to pH2 using HNO_3 and dialyzed for 2 to 3 days in the same water used as dispersion medium (**Figure 3.7c**). The amount of the residual ions in the nanorod suspension decreases during dialysis, contributing to improving the colloidal stability. The surface of particles is then positively charged in the acidic condition (pH2), providing a strong electrostatic repulsion between particles. Afterward, these charge-stabilized nanorods are transferred to ethylene glycol (EG) by distillation using a rotary evaporator, which has shown better colloidal stability than the one dispersed in pH2 water. The improved colloidal stability is likely due to the complexation of EG molecules to the particles, configuring a cloud that provides steric hindrance in addition to the electrostatic repulsive force.¹ **Figure 3.7e** shows spin-coated nanorods on the substrate, showing individually separated nanorods with no sign of aggregation.

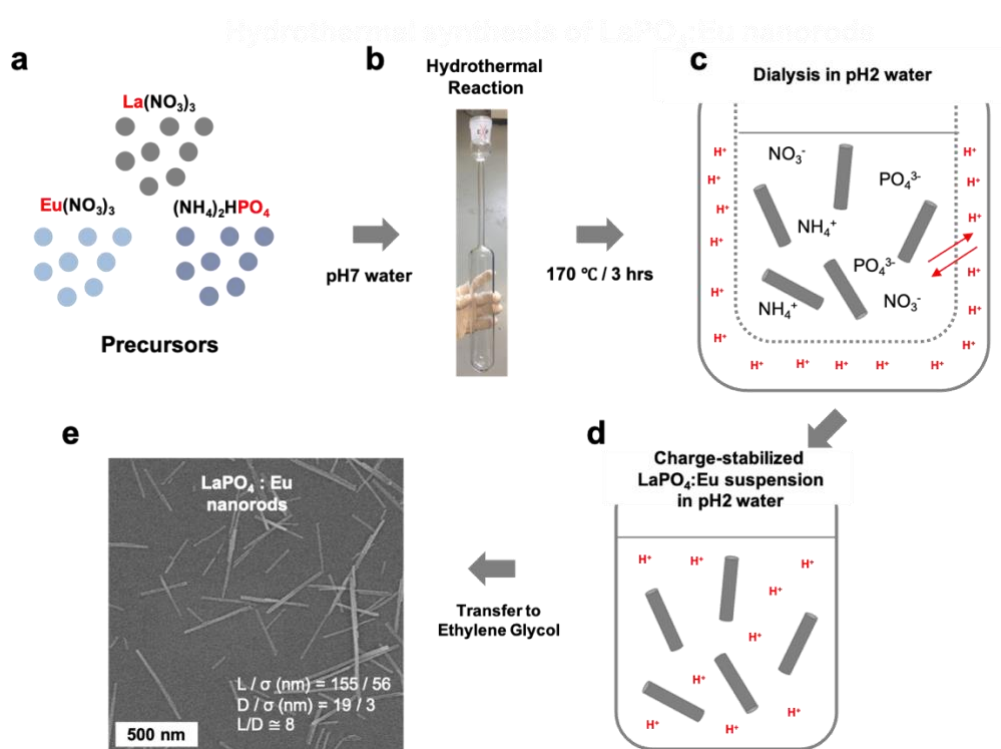


Figure 3.7. Schematics illustration of the hydrothermal synthesis and charge-stabilization process for Eu^{3+} ion doped LaPO_4 nanorods suspension in the polar medium. The process is optimized previously in the group.^{1, 69}

3.2.2. Liquid crystalline behavior of charge stabilized nanorods in ethylene glycol

As-prepared charge-stabilized $\text{LaPO}_4:\text{Eu}$ nanorods exhibit a spontaneous liquid crystalline behavior whose phase changes as a function of the volume fraction Φ (**Figure 3.8**). When diluted, a dark isotropic liquid phase without birefringence is observed (**Figure 3.8a**). By increasing Φ , the biphasic isotropic (ISO)-nematic (NEM) LC appears. **Figure 3.8b** shows positive tactoids where an isotropic phase surrounds the nematic droplet. The specific shape of tactoid (spindle, prolate) results from the balance between the splay and bend elastic constants of the nematic droplets.¹⁴² **Figure 3.8c** shows negative tactoids where the nematic phase surrounds the isotropic droplet. At higher Φ , the typical Schlieren texture of the nematic phase (**Figure 3.8d**) and columnar mesophase (**Figure 3.8e**) are formed.

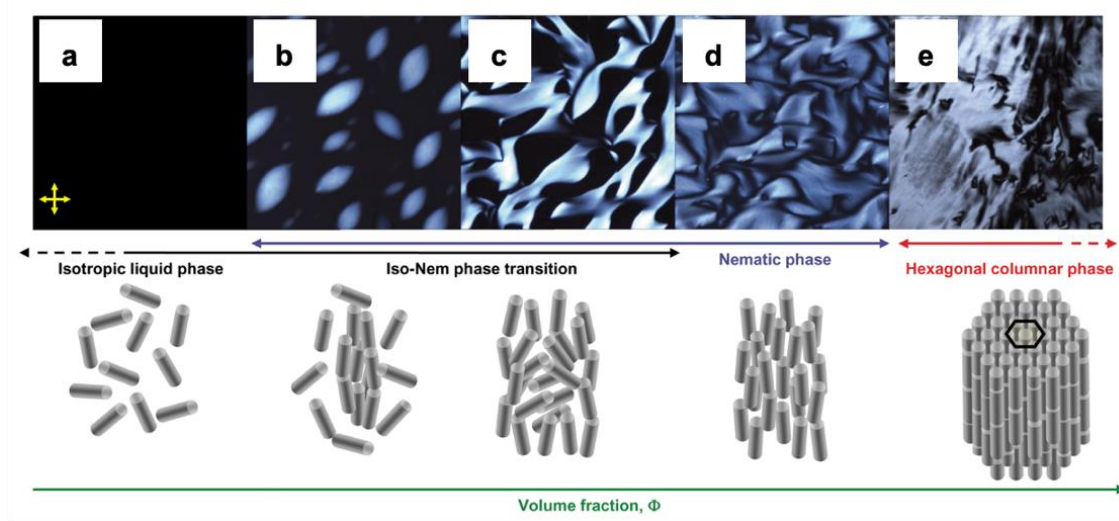


Figure 3.8. Optical texture observed by polarizing microscopy of the different liquid crystalline phases of LaPO_4 nanorod suspensions when increasing the nanorod volume fraction. Birefringence images of (a) isotropic liquid phase (b-c) biphasic LC phase where isotropic and nematic LC phase coexists (d) nematic LC phase (e) hexagonal columnar phase. Schematic rod organization is shown. Figures are taken from the reference.⁶⁹

A phase diagram can be plotted as a function of ionic strength and volume fraction Φ , as shown in **Figure 3.9**. According to the constructed phase diagram, $\Phi_{\text{ISO-NEM}}$ is much lower than the theoretical value ($\Phi_{\text{ISO-NEM}} \sim 17\%$) based on the Onsager's hard rod model under the assumption where the charge effect is absent. This confirms that the colloids are highly charged, and the charges contribute to increasing the effective diameter (D_{eff}), effectively decreasing $\Phi_{\text{ISO-NEM}}$ of the LC system. The presence of charge can also be demonstrated by the fact that $\Phi_{\text{ISO-NEM}}$ increases when the ionic strength of the dispersing medium increases, controlled by dialysis and the amount of HNO_3 . According to **Equation 3.3**, the Debye length decreases in a dispersing medium with a higher ionic strength, which influences the effective diameter D_{eff} , leading to an increase in $\Phi_{\text{ISO-NEM}}$. At very high ionic strength, the electrostatic repulsion is screened, which can no longer compensate for the attractive VdW force, and a transition from a sol state to a gel state is induced. This LC and sol-gel behavior of LaPO_4 nanorods

in polar medium (ethylene glycol) will be compared to the same nanorods ligand-stabilized in apolar medium (chloroform) in the next section.

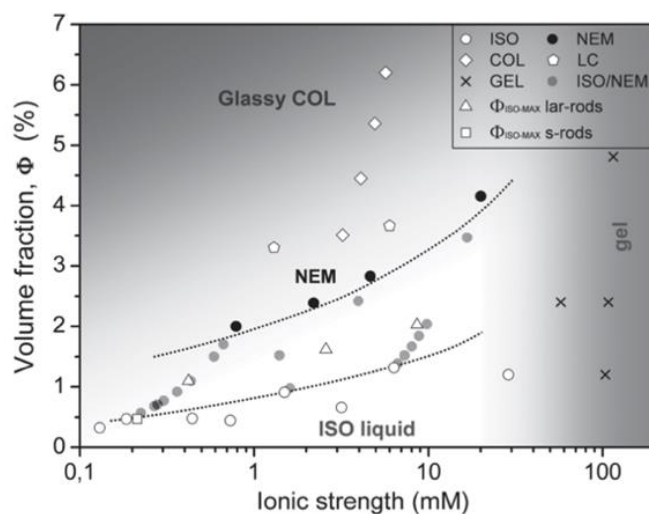


Figure 3.9. Phase diagram of LaPO_4 nanorod colloidal suspension in ethylene glycol as a function of volume fraction and ionic strength. The Figure is taken from the reference.⁶⁹

Summary of Chapter 3.2

LaPO_4 nanorods are hydrothermally synthesized and charge-stabilized in ethylene glycol. The stable nanorods exhibited LC behavior, which is possible to control as a function of nanorods' concentration and the ionic strength of the dispersion medium. The plotted LC phase diagram showed good agreement with the understanding of Onsager's hard rod model. The low $\Phi_{\text{ISO-NEM}}$ of the LC system confirms that colloids are highly charged, and the charges contribute to increasing the effective diameter.

3.3. Ligand-stabilized LaPO₄:Eu nanorods suspension in an apolar medium

3.3.1. Solvent transfer by surface functionalization

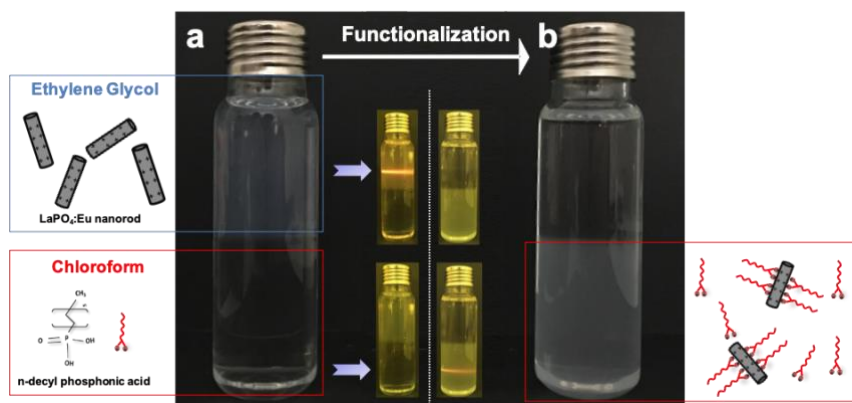


Figure 3.10. Pictures of a biphasic mixture of (top) LaPO₄:Eu nanorod colloidal suspension in ethylene glycol (EG) and (bottom) n-decyl phosphonic acid (n-DPA) in chloroform (a) before and (b) after phase transfer of nanorod into the chloroform. Inset pictures: Red emission of Eu³⁺ ions doped in LaPO₄ nanorod under the excitation of wavelength ~ 394 nm. Arrow indicates the position of the excitation laser. A long-pass optical filter ($\lambda \sim 510$ nm) was put in front of the camera to enhance the visibility of red emission.

It is crucial to maintain the same nanorod morphology (aspect ratio) to accurately compare the LC behavior of colloids stabilized in different methods (electrostatic repulsion, steric repulsion) because the morphology can have a significant impact on LC behavior as understood by the Onsager's hard rod model. In this section, the previously developed charge-stabilized LaPO₄:Eu nanorods are surface functionalized by the solvent transfer technique. And the resultant LC behavior is compared to that of LC stabilized with a long-range electrostatic repulsion force.

As-prepared LaPO₄:Eu nanorods do not have ligands attached to the particle surface. They are directly used for surface functionalization by the solvent transfer technique.^{143, 144} As discussed above, as-prepared LaPO₄:Eu nanorods dispersed in ethylene glycol (EG) are likely to be complexed by EG molecules. Still, they could be directly used for the subsequent functionalization process.¹ **Figure 3.10a** shows the photograph of the biphasic mixture of LaPO₄:Eu nanorod suspension in ethylene glycol (top) and n-decyl phosphonic acid (n-DPA) molecules dissolved in chloroform (bottom). Phosphonic acid is chosen as the surface functionalizing ligand because it has shown a good affinity for the LaPO₄ surface in the previous work of the group and is well known to form a stable complex with metal ions.¹⁴⁵ While stirring, at the interface of two immiscible media, phosphonic acid complexes nanorods' surface and the long alkyl chains project outwards, making the surface of nanorods hydrophobic.

Surface-hydrophobized nanorods by n-DPA relocate from the polar medium (ethylene glycol) to the apolar medium (chloroform). The particles' relocation by the surface modification was followed by the

red photoluminescence of the Eu^{3+} ions doped in LaPO_4 nanorods under the laser excitation $\lambda \sim 394$ nm (inset picture, **Figure 3.10a-b**). After stirring overnight, the red emission is no longer observed in ethylene glycol, but only appears in the chloroform, confirming that LaPO_4 nanorods are functionalized and transferred into chloroform. A similar method is reported which uses photoluminescence intensity to calculate the functionalization kinetics quantitatively.¹⁴⁶ Nanorod relocation can also be seen by a slightly cloudy appearance of the suspension, originating from a scattered light by the nanoparticles.

Optimization of the phase-transfer surface functionalization process

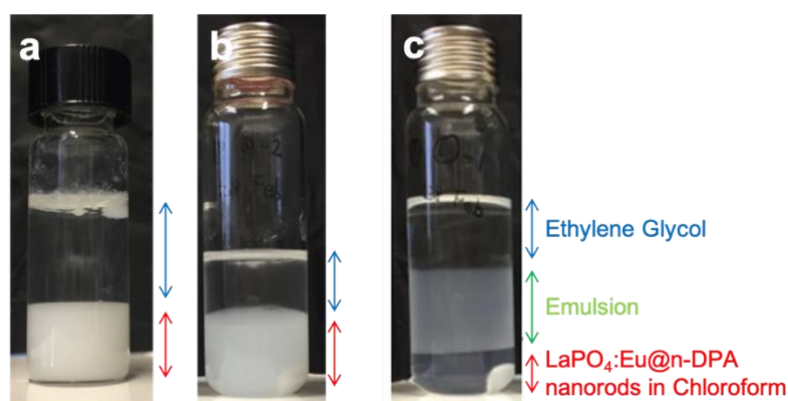


Figure 3.11. Pictures showing test vials after the completion of functionalization. $\text{LaPO}_4:\text{Eu}$ nanorods were initially dispersed in (a) pH2 water (adjusted using HNO_3), (b) in a mixture of ethylene glycol and pH2 water (1:1 v/v), and (c) in ethylene glycol.

There were two essential points for successful surface-functionalization with minimized aggregation. The first was the choice of the appropriate solvent. Among the solvents tested as a dispersing medium for bare $\text{LaPO}_4:\text{Eu}$ nanorod, ethylene glycol results in the least aggregation (**Figure 3.11c**). Otherwise, it showed a severe irreversible aggregation making the surface-functionalized nanorod in chloroform having a milky aspect, typical optical appearance of unstable colloidal dispersion (**Figure 3.11a-b**). However, even for the ethylene glycol as a dispersing medium (**Figure 3.11c**), a huge amount of functionalized nanorods was found to be captured in the emulsion formed between ethylene glycol and chloroform. This is because n-DPA is an amphiphilic molecule that functions as a surfactant like a soap. Emulsion formation can be prevented by controlling the amount of $\text{LaPO}_4:\text{Eu}$ nanorods and the relative amount of n-DPA molecules used for functionalization. Under the best-optimized condition, where 0.01 vol% of $\text{LaPO}_4:\text{Eu}$ nanorods (1eq in Mole) is dispersed in ethylene glycol, and 0.25 eq (in Mole) of n-DPA is dissolved in chloroform, the emulsion did not form at least visually (**Figure 3.12c**).

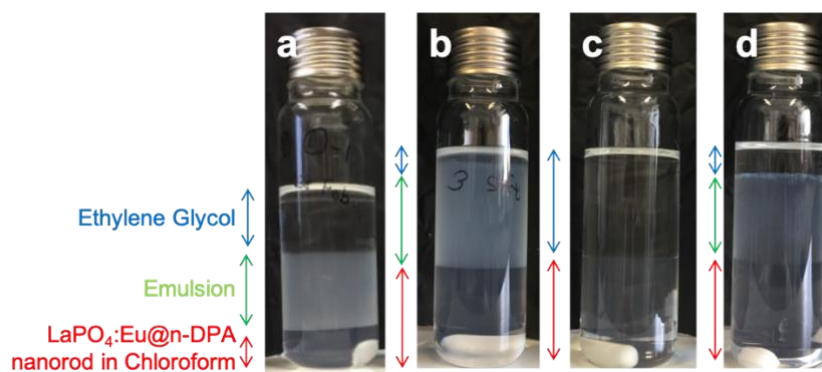


Figure 3.12. Pictures showing test vials after the completion of functionalization. The volume fraction of $\text{LaPO}_4:\text{Eu}$ nanorods in ethylene glycol and relative amount of n-DPA in chloroform is controlled. (a) 0.1 vol% of nanorods with 0.25 eq of n-DPA, (b) 0.01 vol% of nanorods with 0.5 eq of n-DPA, (c) 0.01 vol% of nanorods with 0.25 eq of n-DPA, (d) 0.01 vol% of nanorods with 0.125 eq of n-DPA. 1eq stands for the mole number of nanorods in ethylene glycol.

Morphology of functionalized $\text{LaPO}_4:\text{Eu}$ nanorods

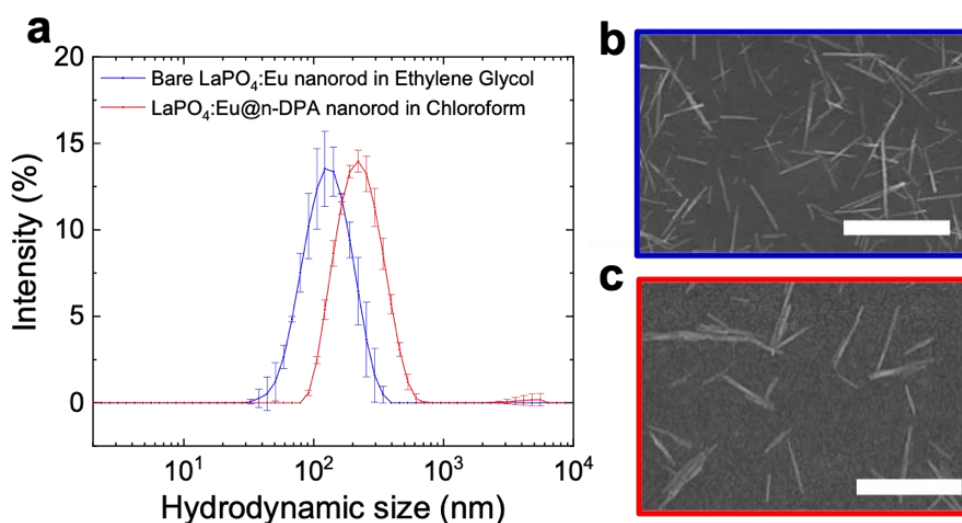


Figure 3.13. (a) Intensity plot as a function of the hydrodynamic size of bare $\text{LaPO}_4:\text{Eu}$ nanorod dispersed in ethylene glycol and functionalized $\text{LaPO}_4:\text{Eu}@n\text{-DPA}$ nanorod dispersed in chloroform measured using dynamic light scattering (DLS). Scanning electron microscope (SEM) images of spin-coated (b) bare $\text{LaPO}_4:\text{Eu}$ nanorod and (c) $\text{LaPO}_4:\text{Eu}@n\text{-DPA}$ nanorods. Scale bar: 1.0 μm .

Subsequently, the DLS is measured to check the hydrodynamic size of nanorods before and after surface functionalization. DLS measurement showed the shift of the hydrodynamic size peak from 122 nm to 220 nm after the functionalization process (Figure 3.13a), indicating a slight aggregation. Nevertheless, this aggregation appears to be formed preferentially by parallel attachments of nanorods, conserving the individuals' anisotropic morphology (Figure 3.13b-c). The morphology measured from SEM images shows that both length and diameter are nearly doubled after the surface functionalization

(Figure 3.14). Note that permanent aggregates are considered as one nanorods for the size measurement. The aspect ratio of measured nanorods remains practically unchanged, implying that $\Phi_{\text{ISO-NEM}}$ should not change significantly compared to LC suspension composing of bare $\text{LaPO}_4:\text{Eu}$ nanorods.

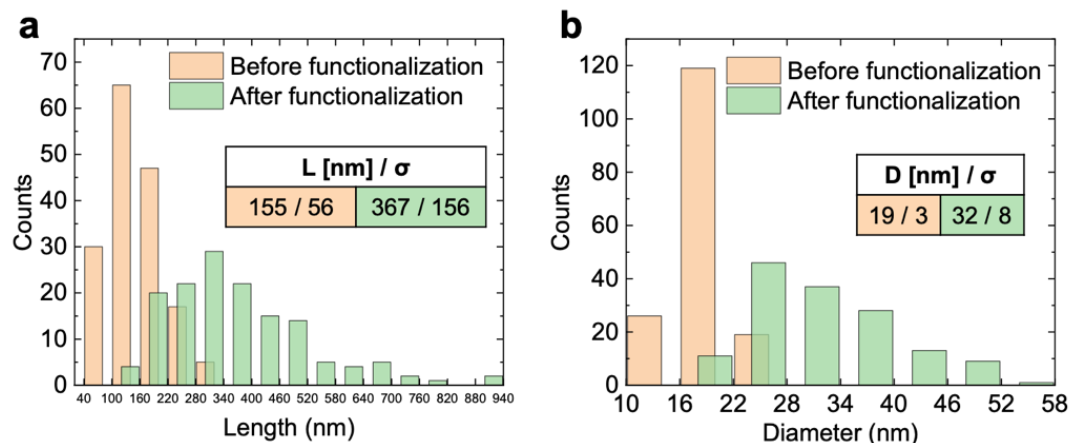


Figure 3.14. Measured (a) length and (b) diameter distributions of $\text{LaPO}_4:\text{Eu}$ nanorod before and after surface-functionalization from SEM images. The inset table shows averaged length and diameter of $\text{LaPO}_4:\text{Eu}$ nanorods with their standard deviations (σ).

Presence of n-DPA molecule on the surface of functionalized $\text{LaPO}_4:\text{Eu}$ nanorods

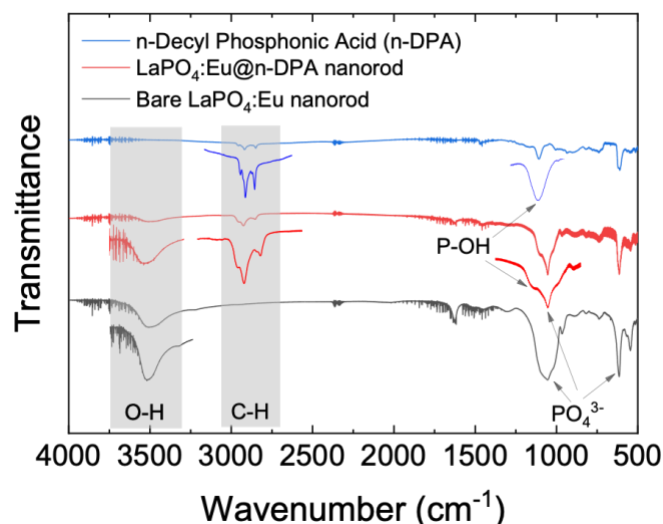


Figure 3.15. Fourier transform infrared microscopy (FTIR) spectra of n-DPA ligand molecules, functionalized $\text{LaPO}_4:\text{Eu}@n\text{-DPA}$ nanorod and bare $\text{LaPO}_4:\text{Eu}$ nanorod deposited on Si substrate.

The surface functionalization by n-DPA ligand molecule is further confirmed by Fourier transform infrared microscopy (FTIR) measurement (Figure 3.15). The spectra obtained with the free molecule of n-DPA (blue line) showed three peaks representative of the C-H stretching vibration of ordered alkyl

chains at $\sim 2850\text{ cm}^{-1}$, $\sim 2918\text{ cm}^{-1}$, and $\sim 2957\text{ cm}^{-1}$.¹⁴⁷ Subsequent FTIR measurement of functionalized nanorod (red line) showed C-H vibration peaks of alkyl chain at a similar wavenumber ($\sim 2855\text{ cm}^{-1}$, $\sim 2926\text{ cm}^{-1}$ and $\sim 2956\text{ cm}^{-1}$), confirming the presence of alkyl chain on the nanorods' surface. Shifting the peak of C-H stretching vibration to a higher wavenumber indicates that the alkyl chains on the particle surface are disordered.¹⁴⁸ The peak attributing to P-OH ($\sim 1108\text{ cm}^{-1}$) also evidences the presence of PA on the particle surface.

Effect of excess n-DPA ligand to the colloidal stability

As-prepared functionalized nanorods are then washed and re-dispersed in pure chloroform or in chloroform with a controlled amount of excess of n-DPA ligand to examine the effect of excess n-DPA ligand to colloidal stability. **Figure 3.16** shows the hydrodynamic size increment of as-prepared suspensions measured over time using DLS. The aggregation rate of nanorods dispersed in pure chloroform appears to be remarkably high comparing to the others (**Figure 3.16**, see **Appendix Figure 3.1** for full DLS dataset). This rapid rate of aggregation seems due to a weak complexation of the n-DPA ligand to the particle surface and the following surface exchange equilibrium between complexed ligands and free ligands in the solvent. On the contrary, the aggregation rate appears to be reduced when the nanorods are dispersed with an excess of n-DPA ligand molecules (**Figure 3.16**, **Appendix Figure 3.1**). This seems due to the shifted surface exchange equilibrium by the presence of numerous free ligands in the solvent, which helps complexed ligands stay complex to the particle surface for the long term. It seems that colloids become stable if excess ligand molecules exist in the medium regardless of its concentration. Note that dissolved n-DPA in chloroform recrystallize at a concentration above approximately 150 mM, which would be the maximum concentration of excess ligand molecules that can be present in the suspension. Such a nanorod suspension prepared with an excess of n-DPA can be stored semi-permanently with occasional sonication (**Appendix Figure 3.1**). In contrast, the nanorods in pure chloroform showed a severe aggregation during sonication due to accelerated surface exchange (**Appendix Figure 3.1**). Therefore, excess ligand molecule was essential to guarantee the long-term colloidal stability in the apolar medium. Similar observations are also reported in other works (*e.g.*, CdSe quantum dots and ZnO nanoparticles dispersed in toluene).^{146, 149}

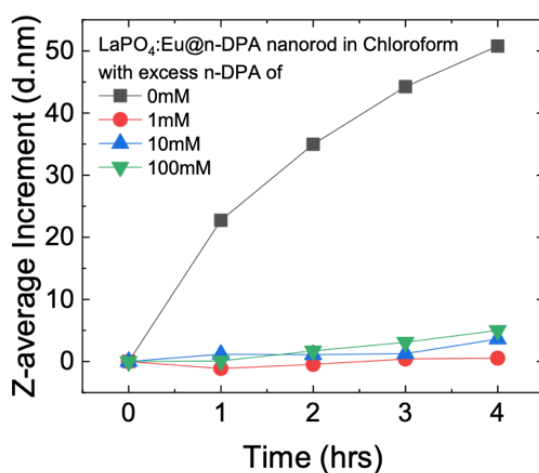


Figure 3.16. Z-average size increment of functionalized $\text{LaPO}_4:\text{Eu}@n\text{-DPA}$ nanorod dispersed in pure chloroform (0 mM) or with excess n-DPA of 1, 10, and 100 mM in chloroform, measured as a function of time after sample preparation using DLS.

While stirring, as-prepared rod-shaped colloidal particles dispersed with excess ligands showed a behavior of alignment by a shear force. The aligned nanorods induce an optical birefringence, exhibiting an optical texture when viewed between crossed polarizers (**Figure 3.17**). This flow birefringence confirms the good colloidal stability of the as-prepared suspension where rod-shaped colloidal particles are free to move individually without aggregating to adjacent particles.

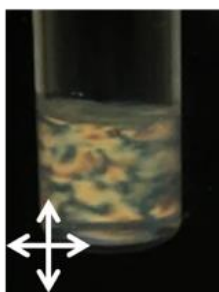


Figure 3.17. Flow birefringence of functionalized $\text{LaPO}_4:\text{Eu}@n\text{-DPA}$ nanorod in chloroform observed between crossed polarizers.

3.3.2. Liquid crystalline behavior of ligand-stabilized nanorods suspension in chloroform

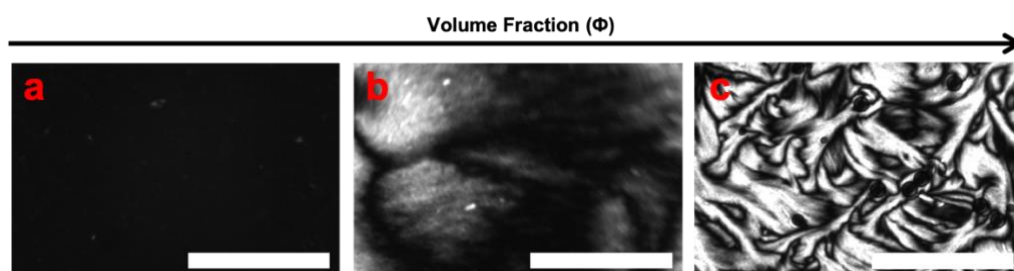


Figure 3.18. Optical texture of functionalized $\text{LaPO}_4:\text{Eu}@n\text{-DPA}$ nanorod colloidal suspension in chloroform observed between crossed polarizer : (a) Isotropic liquid phase ($\Phi = 0.55$ vol%) showing dark image, (b) Birefringent nematic clouds ($\Phi = 0.92$ vol%) and (c) typical nematic schlieren texture ($\Phi = 2.76$ vol%). Scale bar: 200 μm .

Subsequently, functionalized nanorods in chloroform are slowly concentrated by slowly evaporating the solvent. Concentrated dispersions were then inserted into the cell by capillary force, and its birefringence optical textures were directly observed using polarizing microscopy. The cell used for the study is closed except for a small entrance where the suspensions can be injected, which was afterward sealed with UV glue to prevent further evaporation of the dispersing solvent during the observation. The initial dilute suspension (**Figure 3.18a**, $\Phi = 0.55$ vol%) showed dark transmittance between crossed polarizers, indicating an isotropic liquid phase (ISO). Some bright spots attribute to some large aggregates. As increasing nanorod concentration in the dispersion (Φ), birefringent nematic (NEM) cloud-like domains appear (**Figure 3.18b**, $\Phi = 0.92$ vol%). At this state, the optical retardation of NEM domains was not strong and barely stood out with the ISO phase, indicating particle density or/and the order parameter of NEM domains remains low. In the case of such a biphasic state, it is known that NEM domains can coalesce and forms eventual spindle-shaped nematic tactoid droplet as a result of the balance between splay and bend elastic constants of the nematic droplets in the isotropic phase, as also shown above in the case of LaPO_4 nanorods in polar medium (**Chapter 3.2.2**).^{69, 142, 150} However, for ligand-stabilized $\text{LaPO}_4:\text{Eu}@n\text{-DPA}$ nanorods in chloroform, the tactoid formation was not observed. A hypothesis for the absence of tactoid formation can be made from the fact that Debye length λ_D of charged particles suspended in an apolar medium is an order of magnitude larger than one in polar media.¹³⁶⁻¹³⁸ In this state, the effective diameter D_{eff} thus, the effective volume V_{eff} of suspended particles can be very large. Therefore, the threshold concentration to configure a 'repulsive glass' can be very low, and the concentration of observed LC suspension ($\Phi = 0.92$ vol%) is probably already above such threshold concentration. Thus, Isotropic-Nematic phase separation (forming biphasic state) may not be preferential at least in a short time scale as there would not be a considerable difference between the concentration for nematic phase (Φ_{NEM}) and isotropic phase (Φ_{ISO}). Instead, all nanorods may start to orient slightly due to the weak repulsive force. The orientation becomes prominent when increasing concentration, which configures typical NEM Schlieren optical texture (**Figure 3.18c**, Φ

=2.76 vol%). Still, the exact reason for the absence of tactoid formation is unclear at this stage and requires further study to validate the above hypothesis.

The phase diagram in **Figure 3.19** summarizes the observed LC phase of the functionalized $\text{LaPO}_4:\text{Eu}@n\text{-DPA}$ nanorod suspension as a function of the volume fraction (Φ , vol%) and the excess of n-DPA ligand molecule concentration (mM) suspended in the medium (see **Appendix Figure 3.2** for optical texture images supporting **Figure 3.19**). The successive dilution of the concentrated dispersions until all the NEM domains disappear makes it possible to estimate $\Phi_{\text{ISO-NEM}}$. Note that $\Phi_{\text{ISO-NEM}}$ here is defined as a concentration where NEM cloud-like domains start to appear.

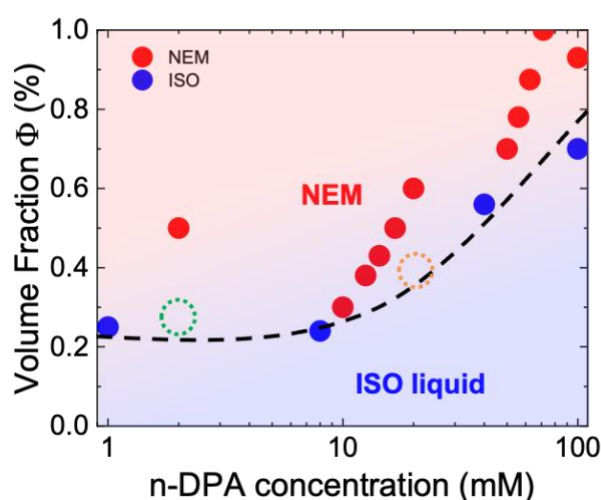


Figure 3.19. Liquid crystal phase diagram of functionalized $\text{LaPO}_4:\text{Eu}@n\text{-DPA}$ nanorod colloidal suspension in chloroform as a function of nanorod volume fraction (Φ , vol%) and excess n-DPA ligand concentration (mM). All optical texture images supporting the Figure are shown in **Appendix Figure 3.2**. Dashed circle in green and orange color indicates $\Phi_{\text{ISO-NEM}}$ obtained from the optical capillary experiment discussed in **Figure 3.22**.

Firstly, we observed that $\Phi_{\text{ISO-NEM}}$ is shifted toward smaller volume fractions at a lower concentration of n-DPA molecule, similar to the typical role of salts in LC suspension in polar media.^{69, 132} We attribute this observation to the decreased surface Z-potential at a higher ligand concentration, as shown in **Figure 3.20**. This indicates that n-DPA ligand molecules dissolved in the medium can act as a charge balancing agent, and the charge screening near the particles can impact the effective diameter D_{eff} of nanorods, which effectively increases $\Phi_{\text{ISO-NEM}}$. It is also interesting to note that the measured Z potential is higher than the standard Z potential values expected in aqueous dispersion (from around -50 mV to 50 mV). The low effective particle charge and nonetheless such a high surface potential are typical characteristics of particles in nonpolar media when the particles are charged.^{136, 138, 151, 152} It is also interesting to note that in some cases of charged particles in the low permittivity solvent such as chloroform used as a dispersing medium in this study, a small number of surface charges can cause a

high surface potential of particles.^{136, 153, 154} For instance, Espinosa et al. showed that PMMA particles in hexane solutions of nonionic sorbitan oleate (Span) surfactants are charged by no more than a few tens of elementary charges per particle for the measured Z-potential between 50 mV and 120 mV.¹³⁶

Secondly, we observed that NEM cloud-like domains appear at very low concentrations (0.2 ~ 0.7 vol%) in whole n-DPA concentration. Since the theoretically estimated $\Phi_{\text{ISO-NEM}}$ for uncharged bare nanorods of similar morphology was about 17 vol%, such a low $\Phi_{\text{ISO-NEM}}$ suggests ligand-stabilized nanorods in the apolar medium were stabilized not simply by short-range steric hindrance provided by surface-ligands but dominantly by the presence of long-range electrostatic repulsion. Indeed, $\Phi_{\text{ISO-NEM}}$ is reported to be almost two orders of magnitude higher for particles of similar morphology when the particles are only sterically stabilized - boehmite ($\gamma\text{-AlO}(\text{OH})$) of similar morphology ($L = 180 \text{ nm}$, $L/D = 18$) dispersed in cyclohexane exhibit $\Phi_{\text{ISO-NEM}}$ at ~ 12 vol%.¹⁵⁵ Another interesting point is that $\Phi_{\text{ISO-NEM}}$ of ligand-stabilized nanorods in chloroform is even lower than that of the same nanorods stabilized by surface charges in ethylene glycol discussed in **Figure 3.9**. This implies that the Debye screening length of suspended particles charged in the low polarity of the medium (frequently called apolar medium) can be much longer than that of the polar medium.

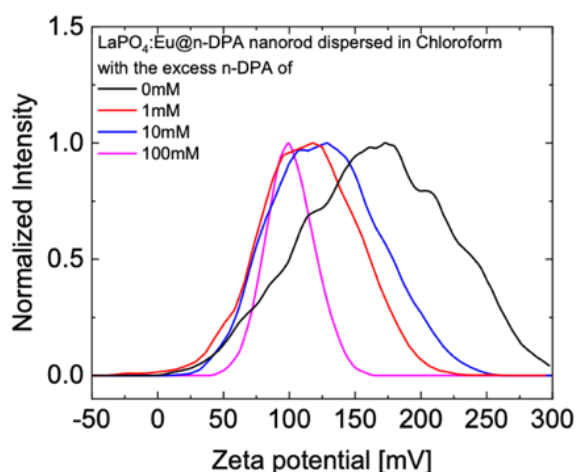


Figure 3.20. Measured Z-potential of surface-functionalized $\text{LaPO}_4:\text{Eu}$ nanorods dispersed in chloroform with/without an excess of n-DPA ligands.

Charged particles in an apolar medium

In the introduction, we presumed that electrostatic charge stabilization is expected to be inconsequential in the case of particles dispersed in an apolar solvent due to the low permittivity of the media. Contrary to common expectations, recent observations have demonstrated that even ligand-stabilized colloidal particles dispersed in apolar solvents can be charged under the influence of suspended macromolecules in the medium.^{136-138, 156} For example, Hsu *et al.* demonstrated that PMMA particles grafted with a poly-

(12-hydroxy-steric acid) (PHSA), providing a steric stabilization, dispersed in dodecane with AOT (sodium di-2-ethyl-hexyl sulfosuccinate) can be charged (**Figure 3.21a**).¹³⁶ Espinosa *et al.* have shown that macromolecules behave in the same manner as salts in the polar medium where the surface Z-potential of particles is lower in higher concentration (**Figure 3.21b**).¹³⁶ Sophisticated analysis revealed that the charged particles suspended in the apolar solvent exhibit a screening length of approximately an order of magnitude longer than those attainable in water but with a much lower charge density. (**Figure 3.21c**).¹³⁶⁻¹³⁸

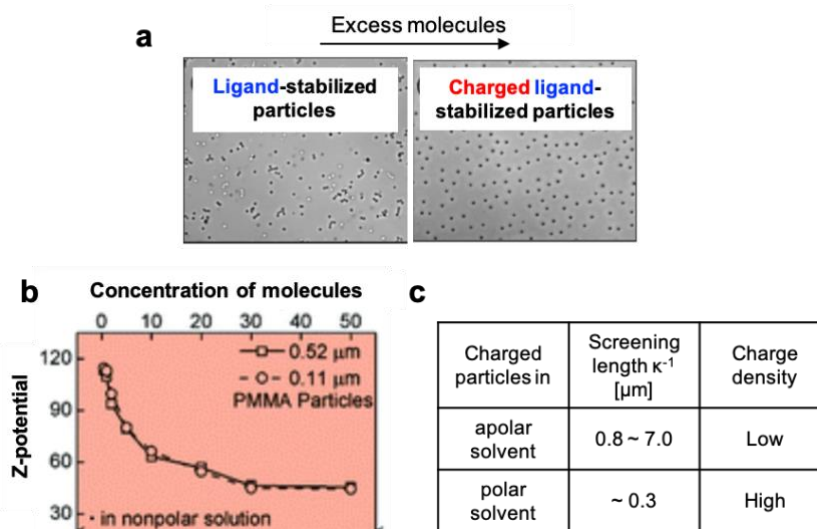


Figure 3.21. (a) Charge stabilization of a nonpolar suspension: optical micrographs of PMMA particles (left) in pure dodecane and (right) with 12 mM AOT (sodium di-2-ethylhexylsulfosuccinate). The Figure is taken from the reference.¹³⁶ (b) Measured Z-potential of charged PMMA particles in nonpolar solution as a function of excess macromolecules. The Figure is taken from the reference.¹³⁶ (c) Comparison of charged particles in an apolar and polar solvent. The values are taken from the reference.¹³⁶⁻¹³⁸

If we relate these results with the Onsager's hard rod model, it suggests that (i) a ligand stabilized LC suspension in an apolar medium can be much more stable thanks to the steric hindrance highly protective from aggregation in addition to the electrostatic repulsion (ii) $\Phi_{\text{ISO-NEM}}$ of apolar LC suspension can be controlled by suspending a different number of molecules to tune the Z-potential (iii) Very low $\Phi_{\text{ISO-NEM}}$ can be achieved with apolar LC suspension, compared to the ones in the polar media due to the extended Debye screen length, and thus increased effective diameter (D_{eff}). These suggestions show good agreement with the above-described observation with ligand-stabilized $\text{LaPO}_4:\text{Eu}$ nanorods with excess n-DPA molecules.

Charging mechanism of particles in an apolar medium

The mechanism of charge formation in nanoparticles dispersed in polar media is a well-documented subject. However, the mechanism of charge formation of particles dispersed in apolar media is still under the subject of discussion. In many individual works that have demonstrated charged particles in apolar media, additional surfactants have been added in the media for stabilizing particles or facilitating the charge formation or both. It is known that amphiphilic ionic surfactants can form reverse micelles in apolar media and early discussions suggested that these micelles play an important role in charging suspended particles in apolar media.¹⁵⁶⁻¹⁵⁹ Some explanations on the mechanism were made as follows.¹⁵¹ First is that a small fraction of micelles can be positively or negatively charged due to thermal fluctuations in the equilibrium.^{157, 158} Suspended particles can then be charged by the preferential adsorption of such charged micelles, molecular ions, or surfactant aggregates onto the particle surface.^{151, 157} Second is that micelles are adsorbed onto the particle surface and complexes particles. Then, the complexed micelles can be charged by dissociation of surface groups and following transfer of molecular ions into the core of the micelles or by exchanging the molecular ions into not-complexed micelles (**Figure 3.22**).^{138, 152 136}

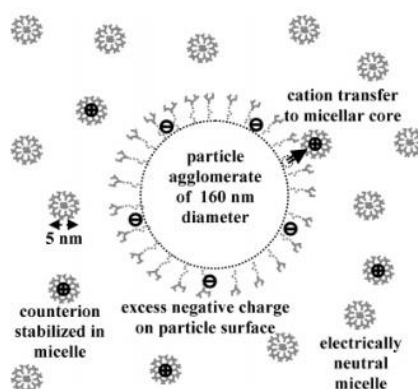


Figure 3.22. Schematic representation of negatively charged particles in the presence of charged and uncharged micelles in the large double layer. The Figure is taken from the reference.¹⁵⁹

Meanwhile, other works counterintuitive to the above explanation are also reported. They have demonstrated that colloids can be charged via nonionic surfactants suspended in a very low concentration even below the critical micelle concentration.^{136, 158} In this case, the authors suggested that the acid-base interactions between the surfactants and the particle surface or increased conductivity of the solvent due to the presence of surfactant could be the reason for the particle charging.¹⁶⁰

In this work, micelle formation of amphiphilic molecules (n-DPA) in chloroform was not observed on the DLS measurement, although the same ligand molecules are known to form a disk-like micelle in an aqueous solution.¹⁶¹ Also, the increased conductivity of the dispersing medium by the presence of n-DPA ligand molecules was not practically evidenced on the Z-potential DLS measurement even at a

very high concentration of excess ligand molecules. Therefore, none of the above-explained mechanisms seem to apply to this work. We, therefore, estimate that the surface charge of particles in this LC system originates from the residual charge of initially highly charged particles that are not fully consumed by the functionalization of the ligands. Another hypothesis is that a small portion of the EG molecules is transferred into chloroform during the functionalization process. The n-DPA molecules are then protonated in a medium close to EG and perform an acid-base interaction with the particles. The exact charging mechanism is unclear at this stage and requires further study to validate the above hypothesis.

Effect of Depletion force

It is also interesting to note that small molecules suspended in the same medium with particles, such as the n-DPA molecules, are known to induce an attractive depletion force acting between the particles by osmotic pressure. This force has also been practically demonstrated to enrich the LC behavior by controlling $\Phi_{\text{ISO-NEM}}$ depending on suspended molecules' concentration.^{82, 162-165} In the case of LC enriched by this attractive depletion force, $\Phi_{\text{ISO-NEM}}$ tends to tilt toward smaller volume fraction at higher concentration of suspended molecules. In the case of LC controlled by the repulsive electrostatic force, $\Phi_{\text{ISO-NEM}}$ tends to tilt toward higher volume fraction at higher concentration of salts, which gives an opposite effect to the control of $\Phi_{\text{ISO-NEM}}$ with the attractive depletion force. In summary, (i) Depletant solutes \uparrow (higher attractive force between nanorods) $\rightarrow \Phi_{\text{ISO-NEM}}\downarrow$, (ii) Salts \uparrow (a screened charge, the shorter effective diameter of nanorods) $\rightarrow \Phi_{\text{ISO-NEM}}\uparrow$. Therefore, the charge effect appears to be dominant in the present case as $\Phi_{\text{ISO-NEM}}$ appears to reduce at a lower n-DPA concentration.

3.3.3. Phase behavior: liquid crystalline transition and gel formation

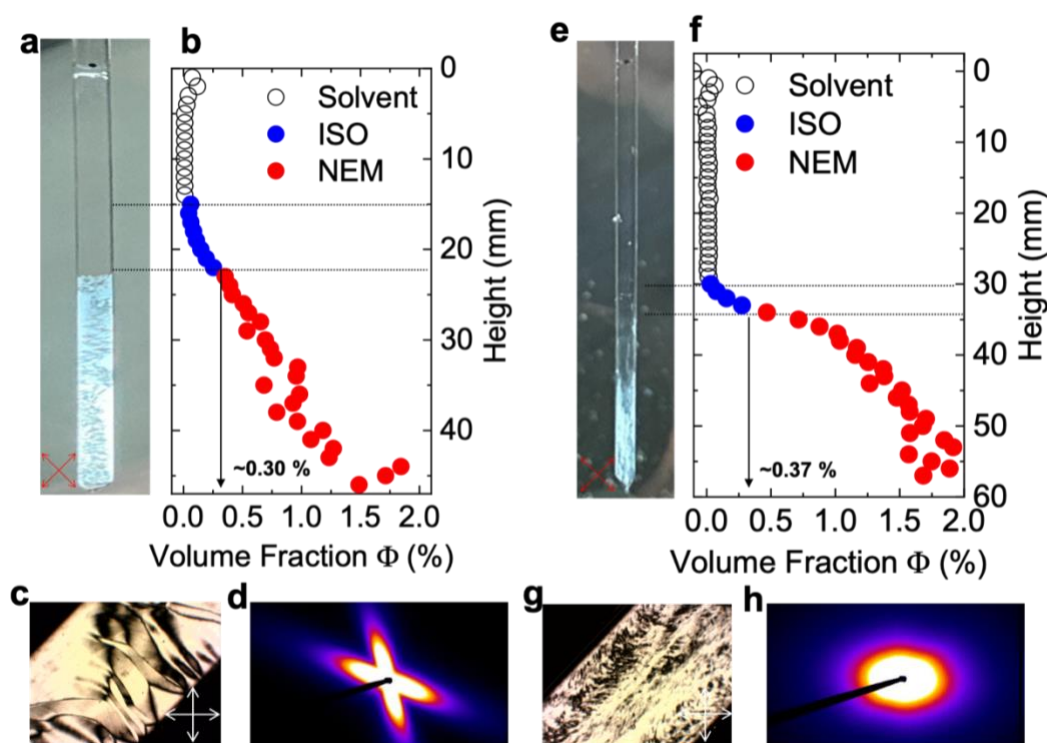


Figure 3.23. Functionalized $\text{LaPO}_4:\text{Eu}@n\text{-DPA}$ nanorod in chloroform with (a-d) Φ (in average) of 0.5 vol% and 2.0 mM of n-DPA molecules, (e-h) Φ (in average) of 0.6 vol% and 20.0 mM of n-DPA molecules aged in a flat optical capillary. Suspension in the capillary is separated into three parts: pure solvent (Solvent), isotropic phase (ISO), and nematic phase (NEM), as indicated in the Figure. (a,e) photograph of the optical capillary taken between the crossed polarizers. (b,f) volume fraction (Φ) profile along with the height of capillary. The volume fraction is calculated based on the fluorescence intensity of Eu^{3+} ions doped in LaPO_4 nanorods (see **Appendix Figure 3.3** for emission spectrum). (c,g) microscopic image of NEM phase taken between crossed polarizers and (d,h) diffraction pattern of NEM phase by SAXS imaging.

As-prepared $\text{LaPO}_4:\text{Eu}@n\text{-DPA}$ apolar LC suspensions are inserted in a flat optical capillary by mild centrifugation and stored upright in the darkroom to study the LC transition under perfectly sealed conditions. **Figure 3.23a** and **Figure 3.23e** show capillaries filled with a similar nanorod concentration but with a different amount of excess n-DPA molecules: (**Figure 3.23a-d**) $\Phi = 0.5$ vol% / n-DPA = 2.0 mM, (**Figure 3.23e-h**) $\Phi = 0.6$ vol% / n-DPA = 20.0 mM. When the suspension in the capillary no longer shows any evolution (after about two months of storage), the suspensions showed a macroscopic phase separation into two parts where the upper part shows no birefringence whereas the lower part shows a strong birefringence due to the nematic alignment of nanorods (NEM) when viewed between crossed polarizers (**Figure 3.23a,e**). Afterward, the profile of volume fraction (Φ) of nanorods along the vertical height of the capillary was measured by observing the emission intensity of Eu^{3+} ions doped in the nanorods using a fluorescence microscope (**Appendix Figure 3.3**). This allows further identification of the non-birefringent upper part in two sub-parts (**Figure 3.23b,f**): a pure solvent part where no nanorods are present and a typical isotropic (ISO) phase. As a result, the suspensions showed

a macroscopic phase separation into three parts along with the capillary height: Solvent, ISO, and NEM part, as presented in the Figure.

Subsequently, microscopic images of the macroscopically separated NEM phase were pictured between crossed polarizers. The suspension with a relatively low n-DPA ligand molecule concentration (2.0 mM) showed a Schlieren optical texture (**Figure 3.23c**), typical of NEM domains. The NEM domain size appears to be relatively large, and its size increases over time probably due to the gravitational force and the progressive coalescence with adjacent NEM domains. The diffraction pattern obtained by SAXS at the NEM phase (**Figure 3.23d**) showed a strong anisotropic pattern in two directions, indicating that there are at least two nematic directors with a high order parameter. On the other hand, the suspension with a relatively high n-DPA ligand molecule concentration (20.0 mM) showed gel-like birefringent NEM domains in the microscopic images taken between crossed polarizers (**Figure 3.23g**). The corresponding SAXS diffraction pattern (**Figure 3.23h**) showed an ellipsoidal shape, which indicates that there are multiple directions of nematic director with one main direction having the highest anisotropy in the measurement volume. From these observations, the different macroscopic separation mechanisms can be applied for different samples, which is discussed in the following sections.

Gravitational length

Before discussing the mechanism, it is also interesting to examine the gravitational length estimated from the volume fraction (Φ) profile along with the capillary height. It is known that suspended particles can sediment and make a gradual concentration change along with the height of capillary by the balance between buoyancy, gravitational force, and the interaction of colloids. When the particles are in a very low volume fraction in the suspension or when the particles' surface charges are perfectly screened, particles can be considered as non-interacting species in the dispersion. In this case, the sedimentation profile of the concentration is expected to be barometric in the equilibrium state. One can then measure the gravitational length that is a decay constant of exponential sedimentation profile. For example, Royall et al. measured the sedimentation profile of screen-charged poly-methyl methacrylate (PMMA) particles (size of around 2 μm) in a solvent mixture of cis-decalin and cyclohexyl bromide. They extracted the gravitational length of about 20 μm .¹⁶⁶

However, in charged particles with a high enough concentration in the suspension, interactions between the colloidal particles become important. In this case, the sedimentation profile can be extended due to a spontaneously formed strong macroscopic electric field that repels particles from one to another.¹⁶⁶

¹⁶⁷ For example, Philipse et al. measured the gravitational length of charged silica particles (size of around 90 nm) in ethanol can be up to a few hundreds of micrometers.¹⁶⁸

In the case of our observed capillary, the gravitational length could be measured from the sample having relatively low n-DPA molecules (n-DPA 2.0 mM) shown an exponential sedimentation profile (**Figure 3.23a-d**). Other samples are not fitted to the exponential curve. A fitting analysis is performed on the whole height of the optical capillary and about 20 mm of gravitational length could be determined. Although the direct comparisons cannot be made due to different sizes/mass of the particle, dispersing medium, *etc.*, the gravitational length that is at least two orders of magnitude longer than the reported values is noteworthy. We attribute the reason for the extended gravitational length to the far-reaching interaction of charges in the apolar media, as discussed throughout this chapter.

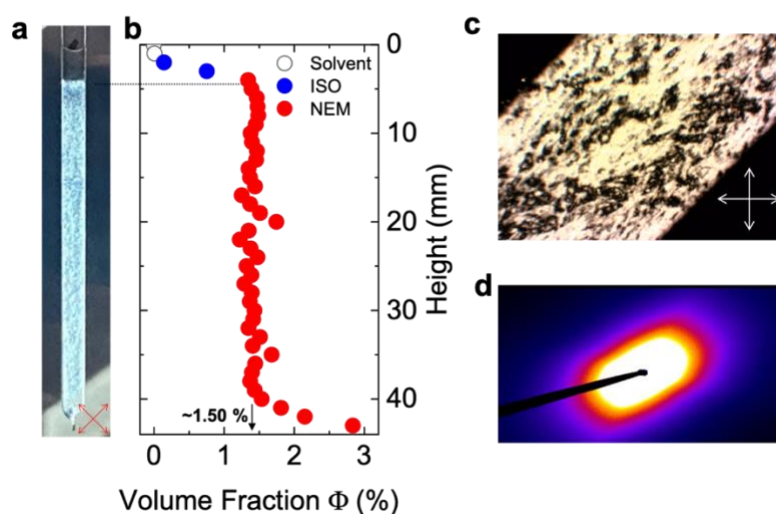


Figure 3.24. Functionalized $\text{LaPO}_4:\text{Eu}@n\text{-DPA}$ nanorod in chloroform aged in a flat optical capillary (Φ of 1.4 vol% and 100.0 mM of n-DPA molecules). (a) photograph of the optical capillary taken between the crossed polarizers. (b) volume fraction (Φ) profile along with the height of capillary. The volume fraction is calculated based on the fluorescence intensity of Eu^{3+} ions doped in nanorods. The volume fraction is calculated based on the fluorescence intensity of Eu^{3+} ions doped in nanorods (see **Appendix Figure 3.3** for emission spectrum). (c) microscopic image of NEM phase taken between crossed polarizers and (d) diffraction pattern of NEM phase by SAXS imaging.

Both suspensions shown in **Figure 3.23** showed an exponential sedimentation profile in the ISO part, which is the typical aspect of the stable colloids system.¹⁶⁶ However, the sedimentation in the NEM part showed a very different profile depending on the samples (**Figure 3.23b,f**). For example, the suspension with a lower amount of n-DPA (**Figure 3.23b**) showed an exponential curve. In contrast, the suspension with a high amount of n-DPA (**Figure 3.23f**) showed a curve similar to a logarithmic decay curve. The suspension at a very high nanorod concentration showed a constant sedimentation profile in the NEM part (**Figure 3.24**). Therefore, it seems that sedimentation by gravity can be strongly disturbed by the gelation process, making an anchored network of particles, which makes the sedimentation profile relatively flat. Further study is necessary to interpret this observation precisely.

Mechanism of macroscopic phase separation into Solvent/ISO/NEM

From all the observations discussed above, there seem to exist at least two possible mechanisms that can be attributed to the macroscopic phase separation into Solvent/Iso/Nem that are presented in the observed capillary (**Figure 3.23**). The first mechanism can be made under the assumption where the colloids are perfectly dispersed and exhibit the sedimentation induced by gravity without aggregation. In this case, if the height of the observed capillary is much longer than the characteristic gravitational length of the investigated colloids system, the colloids will have a gradual concentration change but with a negligible amount of colloids at the top, configuring solvent part in the height of optical capillary (**Figure 3.25a-b**). Afterward, at the height where the concentration reaches $\Phi_{\text{ISO-NEM}}$ in the gradually changed concentration Φ profile, the phase separation occurs, from ISO phase (top) to NEM phase (bottom) (**Figure 3.25c**). This mechanism seems to apply for both suspensions in **Figure 3.23**. As a proof, the values of $\Phi_{\text{ISO-NEM}}$ obtained in the concentration profile along the capillary height (**Figure 3.23b,f**) are in good agreement with the 2D phase diagram presented in **Figure 3.19**: $\Phi_{\text{ISO-NEM}} \sim 0.30$ vol% for the suspension with averaged Φ of 0.5 vol% and 2.0 mM of n-DPA molecule (green colored dashed circle in **Figure 3.19**) and $\Phi_{\text{ISO-NEM}} \sim 0.37$ vol% for the suspension with averaged Φ of 0.6 vol% and 20.0 mM of n-DPA molecule (orange-colored dashed circle in **Figure 3.19**).

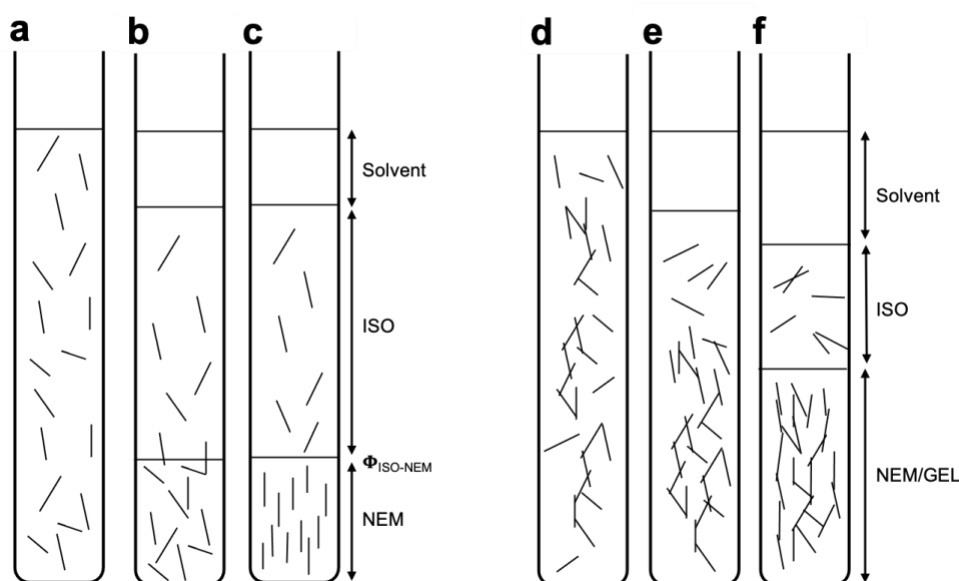


Figure 3.25. Schematic illustration of the mechanism proposed for the macroscopic phase separation into (a-c) Solvent/ISO/NEM or into (d-f) Solvent/ISOs/Gel-like NEM

Second mechanisms can be made under the assumption where the colloids are experiencing an attractive gelation force, which forms aggregated interlocking networks that settle down by gravity (**Figure 3.25d-e**). The system then configures the solvent part in the optical capillary height due to the expelled solvent by syneresis during a gel domain formation or a higher density of particles in the gel domains

(**Figure 3.25d-e**). Then, softly aggregated networks can align to each other, configuring a gel-like birefringent NEM phase and settle to the bottom (**Figure 3.25f**). Residual non-aggregated or lightly aggregated nanorods are then floating, configuring the Solvent/Iso/Nem interface at the optical capillary height. In this case, the NEM domain is expected to be composed of small grains that are not growing at a short time scale due to the interlocked networks. Note that some small reconstructions may occur depending on the interparticle attractive force, and domain growth can be observed but not in a short time scale. However, for the above-presented mechanism, it is expected that the size of NEM domain can grow as floated nanorods in ISO phase can easily merge into NEM domains by the gravitational force or NEM domains can coalesce with adjacent NEM domains.

From the observation made in **Figure 3.23**, it seems that the LC phase separation observed from the LC suspension with a small amount of excess ligand molecule (n-DPA 2.0 mM) (**Figure 3.23a-d**) is made from the first mechanism as it showed a clean Schlieren optical texture of which their domain size is growing over time. Contrarily, LC phase separation observed from the LC suspension with a higher amount of excess ligand molecule (n-DPA 20.0 mM) (**Figure 3.23e-h**) seems to be associated with both mechanisms as it follows the expected $\Phi_{\text{ISO-NEM}}$ in the 2D phase diagram (**Figure 3.19**) but showed gel-like birefringent NEM domains of which small grains are fixed in size and position over time. Indeed, it is known that the gel can be formed in the suspension with a higher ionic strength due to a screened surface charges, as also discussed in **Figure 3.9**.^{155, 169}

Finally, it is also interesting to discuss the relative portion occupied by the pure solvent in the capillary height. As one can see in **Figure 3.23b** and **Figure 3.23f**, the relative portion occupied by the pure solvent in the capillary height is much higher for the suspension with a higher concentration of n-DPA molecule even though the averaged nanorod concentration is almost the same for both suspensions. This observation indicates that relatively dense NEM gels are preferentially formed and expelled more of the solvent in the suspension with a higher concentration of n-DPA molecule (**Figure 3.23f**). This implies that there might be a zone for the GEL phase also at the right side of the phase diagram in **Figure 3.19**, similar to the phase diagram in the polar solvent in **Figure 3.9**, which supports our hypothesis considering the analogy between the polar and apolar media for the charge balance of colloids.

Electric field switching

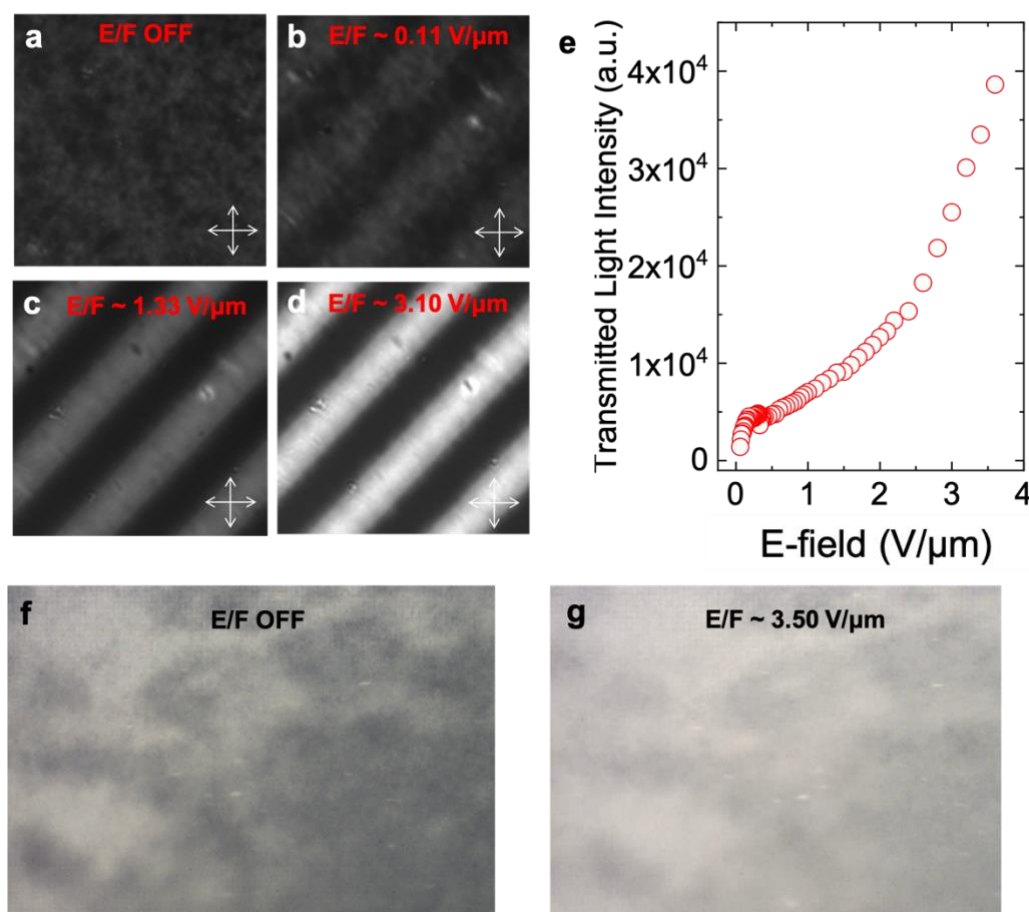


Figure 3.26. (a-d) Optical microscopy images of the functionalized $\text{LaPO}_4:\text{Eu}$ nanorod colloidal liquid crystalline suspensions ($\Phi = 1.4$ vol% with 100 mM of n-DPA concentration) inserted in in-plane-switching (IPS) electro-optical cell. (a) Before applying the electric field (E/F), the samples exhibit birefringent NEM clouds. The application of a sinusoidal electric field at a frequency of 100 kHz with different intensity (b) ~ 0.11 V/ μm (c) ~ 1.33 V/ μm (d) ~ 3.10 V/ μm . Aligned nanorods within the electrode gap exhibit stronger birefringence at a higher intensity of applied E-field due to increased order parameter. (e) Transmitted light intensity as a function of the intensity of applied E-field. Microscopic images of macroscopically separated nematic phase of the suspension - Φ (in average) of 0.6 vol% and 20.0 mM of n-DPA - taken between crossed polarizers (f) before applying an electric field (E/F) and (g) after applying E/F (~ 3.50 V/ μm).

Subsequently, we tested the response of LC suspension to the externally applied electric field (E-field) under the hypothesis where the fluidic NEM domain such as the one in **Figure 3.23b** can be aligned by the application of E-field whereas gel-like NEM domain such as the one **Figure 3.23f** cannot be aligned due to the gelation force. As a first test, the concentrated LC suspension (averaged $\Phi = 1.4$ vol% with 100 mM of n-DPA concentration) that exhibit nematic alignment is directly inserted into the commercially available in-plane electro-optical (E/O) cell and sealed with UV-gel to prevent solvent evaporation during the manipulation. We found that the amount of birefringence increases as a function of E-field intensity, indicating that the randomly oriented director for each NEM domain can be aligned

into one direction under the E-Field (**Figure 3.26a-e**).⁶⁸ Afterwards, we applied the E-field directly to the macroscopically separated NEM phase at the bottom of the optical capillary to assess whether the macroscopically separated NEM phases can also be oriented with an application of E-field. Contrary to the observation that E-field can align NEM domains before the macroscopic separation, all the macroscopically separated NEM phases are found not to align to the E-field, although there was a slight increase in the amount of birefringence under the high intensity of E-field (**Figure 3.26f-g**). This observation indicates that all the macroscopically separated NEM phases formed at the bottom of the capillary have a substantial gelation force which disturbs the alignment of nanorods by E-field. However, this result is counterintuitive to the above discussion where fluidic NEM phase shown in **Figure 3.23a-d** is stable without or with negligible gelation force. The electric field intensity was probably not enough to align the nanorods inside the optical capillary as the electric energy can be consumed by the glass capillary. Or it can be because LC suspensions slowly aggregate over time, and an electric field switching experiment was performed after a few months after preparing the sample when the LC suspensions are too much aged. Further investigations with a fresh sample are necessary to explain this counterintuitive observation.

Summary of Chapter 3.3

LaPO₄ nanorods are stabilized by an amphiphilic molecule (n-DPA) and dispersed in chloroform with an excess of n-DPA molecules. Ligand-stabilized LaPO₄ nanorods dispersed in apolar media have shown a counterintuitive phenomenon that nematic assembly occurs at an extremely low $\Phi_{\text{ISO-NEM}}$ of about 0.5 vol% even lower than the charge-stabilized nanorods that show $\Phi_{\text{ISO-NEM}}$ of about 2.0 vol% in polar media. Furthermore, $\Phi_{\text{ISO-NEM}}$ was found to vary with the addition of excess ligands in a manner similar to the systems in polar media where the increase in ionic strength led to surface charge screening. These observations suggest that the ligand-functionalized surface of LaPO₄ nanorods is charged in apolar medium and that the Debye length (governing the effective radius of the rods) is largely extended. Under gravity, this LC suspension left for aging in a capillary tube shows soft sedimentation. This leads to a vertical gradient of rod concentration where the isotropic/nematic interface appears in the middle with the solvent on the top. The balance between gravity and weak but far-reaching electrostatic repulsive forces seems to provoke LC transition and/or gel formation when repulsive forces are limited by a screening effect associated with an excess surface ligand.

3.4. Conclusion

In this chapter, we have prepared colloidal liquid crystals composed of LaPO₄:Eu nanorods in a polar solvent by charge stabilization and an apolar solvent by ligand stabilization and compared their liquid crystalline behaviors. Contrary to the common expectation where ligand stabilized colloidal LC has a relatively high $\Phi_{\text{ISO-NEM}}$ due to short ligand tail, we found that the ligand stabilized colloidal LC can have an exceptionally low $\Phi_{\text{ISO-NEM}}$ thanks to the far-reaching charges in apolar media. A reduced $\Phi_{\text{ISO-NEM}}$ can provide an enlarged window of concentration for observing LC behavior of nanorods before the concentration of the nanorod system reaches the threshold percolation density ($\Phi_{\text{percolation}} \sim 0.7D/L$).¹⁷⁰ So far, the depletion force provided by the non-absorbent polymer suspended in the suspension is considered a major asset for controlling the LC behavior of colloidal particles suspended in apolar media. Here, we have shown that the LC behavior of colloids in apolar media can also be governed by the charges in low permittivity medium. The fundamental understanding and discussion presented in this chapter would provide in-depth information on preparing colloidal LC stabilized by both steric and electrostatic repulsion in various solvents and how to control their LC behavior.

Chapter 4.

3D Tomography of Liquid Crystalline Nanorod Assembly

In **Chapter 1** and **Chapter 2**, the methodology using the photoluminescence signal of rare-earth dopants as indicative probes of the orientation and order parameter is developed. Such a methodology allowed the characterization of the 3D spatial orientation of a single nanorod and the order parameter of aligned nanorod assembly with a “known” orientation of director \vec{n} . This chapter presents the methodology merging two previously presented concepts, allowing the analysis of the orientation and the order parameter of aligned nanorod assembly with an “unknown” orientation of director \vec{n} . **Chapter 3** discussed the liquid crystalline (LC) assembly of nanorods in which nanorods are aligned with arbitrary orientation and the order parameter. In this chapter, the developed methodology is applied to such LC assembly as a proof-of-concept to perform a 3D tomographic mapping of the orientation profile of nanorods, a building block of LC assembly.

Another essential part of this chapter involves presenting a new class of LC structures formed through the confinement of the LC domains between chemically active surfaces. We found that colloidal LC phases of LaPO₄:Eu nanorods confined between two hard walls exhibit a sequential transition from typical “tactoid” nematic droplets to complex “flower-shaped” domains through an intermediate state with “fingerprint-shaped” patterns. Observation of these mysterious LC transitions and structures have not yet been understood completely. The orientation analysis method developed above was applied to reveal the mechanism of this new LC behavior and the precise structure of the new LC domains. We found that these newly observed LC domains have a complex three-dimensional assembly structure, which could not be precisely characterized by a typical technique observing two-dimensional birefringence patterns. Using a newly developed confocal polarizing fluorescence microscope, we performed a tomographic mapping of this confinement-induced LC structure and characterized the structural information, including the density and orientation profiles of nanorod building blocks.

Parts of results presented in this chapter were made collaborating with Mr. Reinaldo Chacón, Dr. Aymeric Leray and Prof. Gérard Colas-des-Francis in Laboratoire Interdisciplinaire Carnot de Bourgogne (ICB), Université Bourgogne Franche-Comté, Dijon, France.

4.1. Evolution of liquid crystalline phase of $\text{LaPO}_4:\text{Eu}$ nanorods in confined geometry

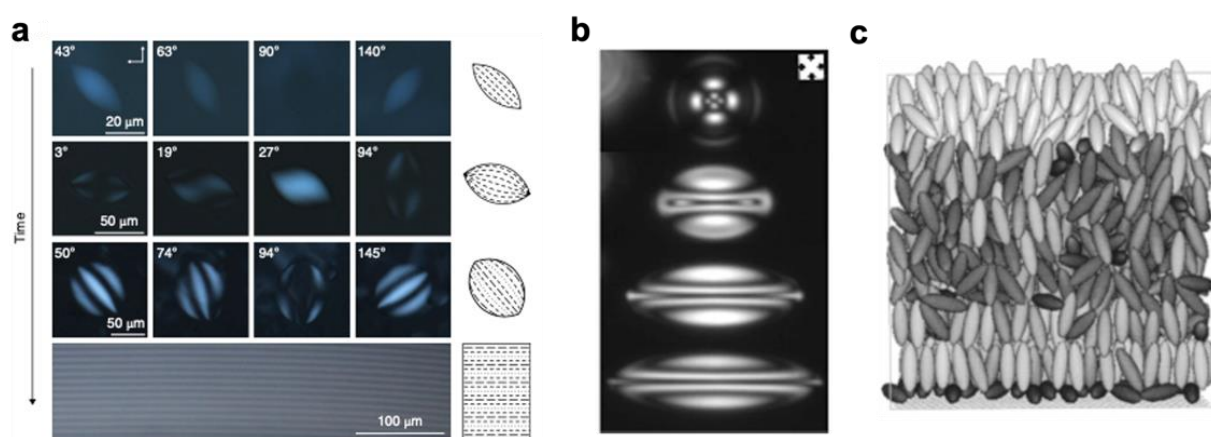


Figure 4.1. Examples of liquid crystalline transition in confined geometry. **(a)** nematic and cholesteric phases of amyloid fibrils observed by rotating the sample in the plane between crossed polarizers. As time goes by, tactoids convert to a bipolar nematic orientation, to a cholesteric ordering and finally a bulk cholesteric phase. The figure is taken from reference.¹⁷¹ **(b)** Birefringence image of Smectic-A LC phase in a different aspect ratio of prolate spheroid cell. The figure is taken from the reference.¹⁷² **(c)** Configuration of LC adsorbed to the substrate, exhibiting the homeotropic orientation near the substrate. The figure is taken from the reference.¹⁷³

Liquid crystal (LC) is a soft state of matter where the disordered isotropic phase transforms into the ordered nematic or smectic phase in a pure entropic regime. When such ordered LC phase is confined in nanoscale geometries, it can transform into a new kind of spatial LC defects/patterns through interactions associated with entropic effects, interparticle forces, and surface adsorption.^{171, 172, 174-178} For example, **Figure 4.1a** shows the amyloid fibrils that exhibit a confinement-induced LC transition to a bulk cholesteric phase from the tactoid nematic droplet.¹⁷¹ **Figure 4.1b** shows the topological defect changes from the point to line defect when the smectic LC is confined in the different geometry of prolate spheroids.¹⁷² **Figure 4.1c** shows the LC molecules adsorbed to the substrate by the strong attractive interaction, inducing the LC molecules to be vertically aligned near the substrate.¹⁷³ Such LC transition caused by the confinement effect is of prime importance due to their interesting phenomenology and the possibility to use them as a template for novel functional devices. Confinement

induced LC transition is understood by some theoretical studies and have been practically observed in a few organic and biological LC molecules.^{171, 172, 174-178}

Such a confinement-induced LC behavior has not yet fully understood in LCs composed of colloidal particles. This is presumably due to the large size of colloidal particles, typically 1-to-3 orders of magnitude larger than LC molecules' size. Thus, the chemical or charge-mediated interaction of colloids at the interface may be too weak to rearrange their organization unless it is deliberately adjusted efficiently. Moreover, particles composing of colloidal LCs have a greater variety than the organic LC molecule in their shape, composition, size, and interparticle interactions, making it difficult to fine-tune the property of the material to observe such a transition. Also, preparing perfectly aggregation-free colloidal LCs is always a difficult task.

This chapter presents the confinement-induced LC transition of colloidal LC, using a previously developed charge-stabilized LaPO₄:Eu colloidal LC suspension having outstanding colloidal stability. We observed such confinement-induced LC transition when LaPO₄:Eu LC suspension in biphasic regime (controlled by volume fraction and ionic strength) is confined between two hard walls. The confinement-induced LC transition led to a formation of flower-shaped nematic domains transiting from fingerprint-like nematic domains and typical nematic tactoid droplets. The surface property of hard walls and the thickness of the cell spacer are found to have a strong influence on the fate of confinement-induced LC structure.

4.1.1. Evolution of liquid crystalline phase over time in confined geometry

Preparation of confined colloidal LCs

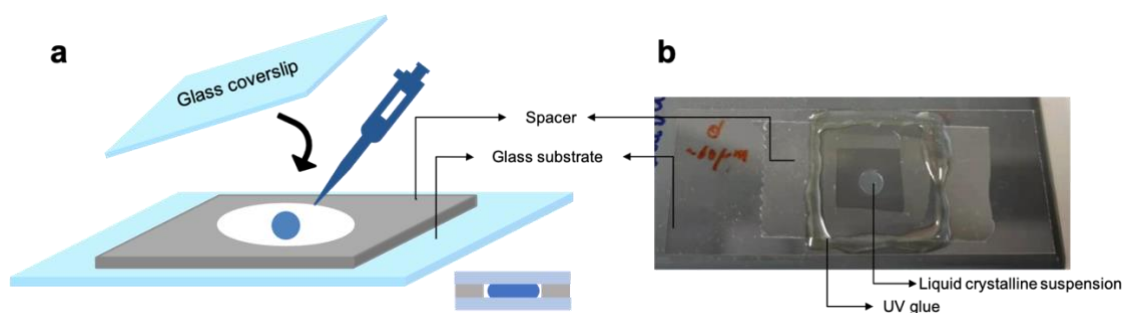


Figure 4.2. (a) Schematic illustration of the preparation of confined colloidal LCs. LC suspension is sandwiched between two hard walls with a gap provided by a spacer. (b) Photograph of confined colloidal LC.

Previously-developed charge-stabilized LaPO₄:Eu nanorods dispersed in ethylene glycol (Eu doping = 5 %, $\Phi = 5.1$ vol%, no dialysis in ethylene glycol, biphasic) was used to observe confinement-induced

LC transition. When such prepared suspension is stored upright in the vial, it showed macroscopic LC separation into the upper isotropic part and bottom nematic phase two months after the preparation.^{1,69} Such suspension is then strongly vortexed to remix completely and homogenize the separated LC phases. Homogenized LC suspension is then deposited on the cell and sandwiched between two hard walls of which the gap between walls is controlled by the spacer thickness ($\sim 60 \mu\text{m}$) (**Figure 4.2a**). The glass substrate and coverslip are cleaned using a detergent, ethanol, and water by rubbing the surface with a gentle mechanical force before depositing the suspension. Afterward, the cell filled with a LC suspension is sealed using UV glue to minimize solvent evaporation during the LC transition. Subsequently, the cell is stored in the ambient condition, and the confinement-induced LC transition is observed between crossed polarizers over time. **Figure 4.2b** shows the photograph of the prepared typical confined cell.

Evolution of LC phase in the cell of spacer thickness $\sim 60 \mu\text{m}$

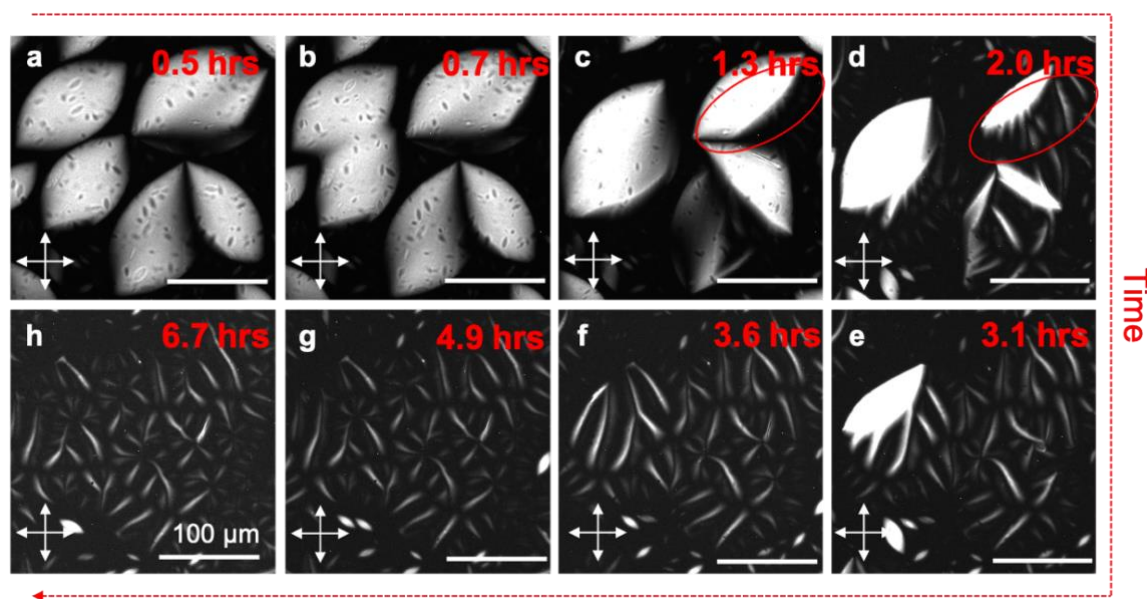


Figure 4.3. The confinement-induced liquid crystalline transition of $\text{LaPO}_4:\text{Eu}$ nanorods observed between crossed polarizers over time. scale bar = $100 \mu\text{m}$. The thickness of the cell spacer is $\sim 60 \mu\text{m}$.

The trajectories of LC transition followed by the growth, nucleation, final structure of LC domains can vary depending on the thickness of the cell spacer (**Figure 4.3-4**) and cell surface properties (**Figure 4.5**). **Figure 4.3** shows the evolution of LC transition confined in the cell having a spacer thickness of about $60 \mu\text{m}$. The LC transition is observed over time between crossed polarizers. The phase development follows a typical Isotropic-Nematic phase separation behavior where small birefringent nematic tactoids form in the isotropic phase medium (**Figure 4.3a**) and increase in size by coalescing with adjacent tactoids (**Figure 4.3b**).¹⁴² Typically, this size growth of the tactoids is the only evolution

process observed with this kind of colloidal LCs. However, in the confinement effect inside the cell, a complete modification of the birefringent pattern was observed (**Figure 4.3c-h**).

When the size of tactoids reaches a certain threshold, it seems that tactoids begin to interact and anchors to the bottom substrate. Anchoring induces the formation of linear defects preferentially at the lateral side of the tactoids (see ellipsoid in **Figure 4.3c-d**), which seems to disrupt the balance between the elastic energy and the free energy of the nematic tactoid droplets. Adjacent tactoids having contact with these defects also form defects (**Figure 4.3e-f**). These metastable linear defects transform again into flower-shaped domains by generating a number of point defects where the rearranged linear defects merge and form flower-shaped domains. (**Figure 4.3g-h**).

Evolution of LC phase in the cell of spacer thickness $\sim 120 \mu\text{m}$

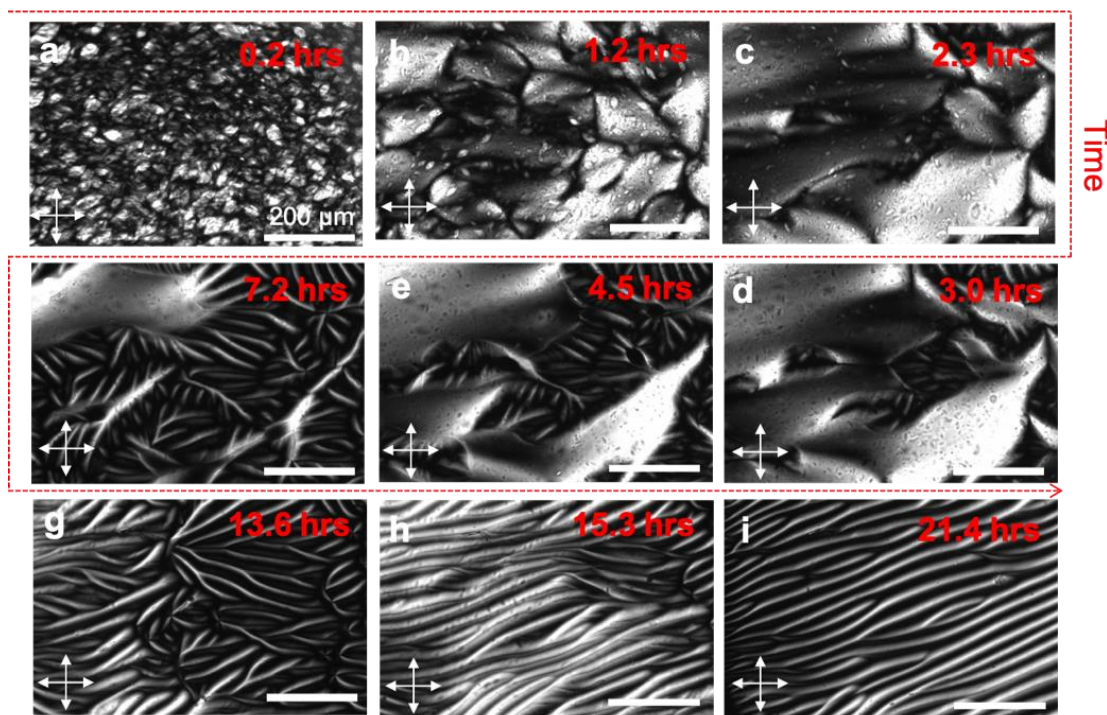


Figure 4.4. The confinement-induced liquid crystalline transition of $\text{LaPO}_4:\text{Eu}$ nanorods observed between crossed polarizers over time. scale bar = $200 \mu\text{m}$. The thickness of the cell spacer is $\sim 120 \mu\text{m}$.

Figure 4.4 shows the confinement-induced LC transition in the cell with a doubled spacer thickness of $\sim 120 \mu\text{m}$. In this case, the nematic tactoid droplets grew much bigger by continuously merging with the adjacent tactoids, and finally a large nematic filled the whole area of the view (**Figure 4.4a-c**) unlike the case with a thinner gap ($\sim 60 \mu\text{m}$) where the isotropic and nematic domains coexisted (**Figure 4.3a-c**). Afterward, linear defects were generated inside the nematic domain (**Figure 4.4d-g**). Instead of evolution into flower-shaped domains increasing the number of point defects shown in the thinner gap

($\sim 60 \mu\text{m}$), the randomly generated linear defects rearranged to form long and parallel linear patterns minimizing the number of point defects. The final LC pattern with only linear defects is similar to the fingerprint-like patterns that are often observed in organic LCs (**Figure 4.4h-i**). Even after long time, further transition to a flower-shaped domains is not observed for this cell. Thus, it seems that the thickness of the cell gap has an important role in determining the stabilized LC domain structure when it is evolving in the confined geometry.

Evolution of LC phase in the surface-treated cell

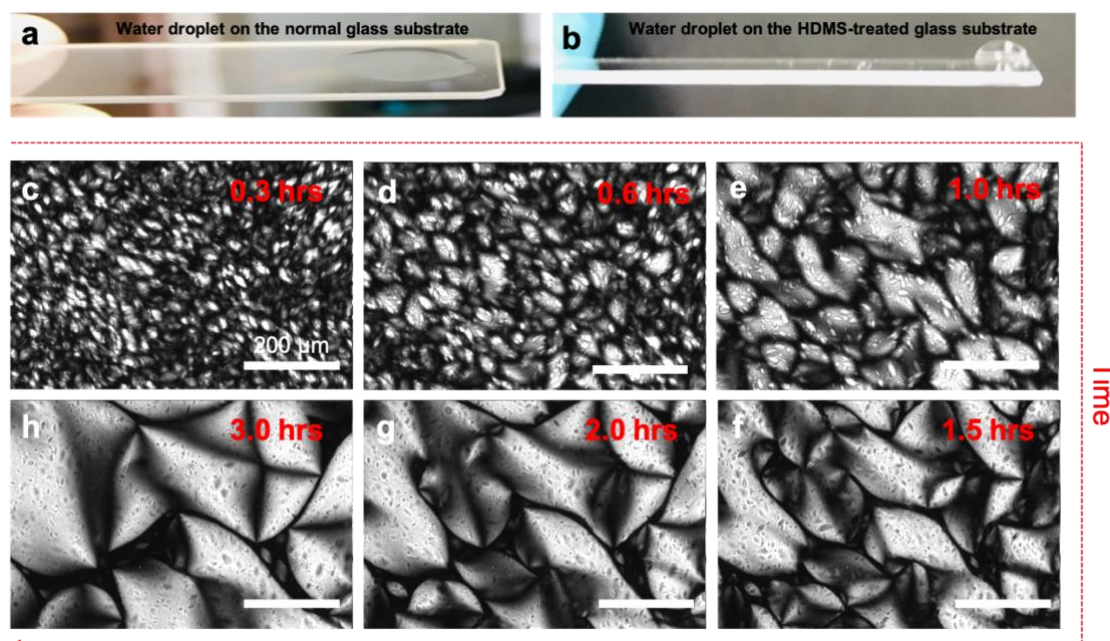


Figure 4.5. Photograph of a water droplet on (a) non-treated and (b) hexamethyldisilazane (HMDS) treated glass substrate.¹⁷⁹ (c-h) Confinement-induced liquid crystalline transition of LaPO₄:Eu³⁺ nanorods observed between crossed polarizers over time. scale bar = 200 μm . The surface of the cell substrate is treated with hexamethyldisilazane (HMDS). The thickness of the cell spacer is $\sim 60 \mu\text{m}$.

As it appears that there is a specific interaction between the LC domain and the substrate, inducing the domain evolution, we designed a study to see if the chemical surface property of the substrate influences the LC transition. We modified the cell surface hydrophilicity by treating the cell surface using a vapor-phase hexamethyldisilazane (HDMS).¹⁷⁹ The HDMS treated cell surface showed a high hydrophobicity, as can be seen in the high contact angle of a water droplet (**Figure 4.5b**) as opposed to the relatively low contact angle on the quasi-hydrophilic surface of the untreated glass substrate (**Figure 4.5a**). The LC suspension confined in such a hydrophobic cell showed the typical growth of tactoids but not the transition into fingerprint-like LC or flower-shaped domains (**Figure 4.5c-h**). Because ethylene glycol (EG) used as a dispersing medium is a hydrophilic molecule, the LC suspensions do not seem to interact

and anchor the HDMS treated hydrophobic substrate. On the contrary, UV-ozone treated confined cells (increase the hydrophilicity) showed the same LC transition shown in **Figure 4.3**, confirming that the confinement-induced LC domain evolution is favored on the hydrophilic surface.

We have shown above that the confinement-induced LC transition of colloidal LC can be controlled by several experimental factors such as the spacer thickness and surface property of the cell. It is interesting to note that some theoretical works based on the organic LC molecule also suggested that LC transition in confined geometry can be controlled by changing the surface property and the thickness of slab geometry.^{176, 177} Based on the observations described above, a hypothetical scenario of colloidal LC evolution in confined geometry could be suggested. The key mechanism of LC evolution seems the interaction between colloidal LC and the substrate, making the particles in LC anchor to the substrate. This anchoring disrupts the balance between the elastic energy and the free energy of the nematic tactoid droplet and generates a defect inside the nematic tactoid droplet. Then, an entropically non-favored coexistence of a new kind of nematic alignment (made by defects) and the surrounding nematic director is restabilized by rearranging into a new type of LC domains. And the configuration of this rearrangement may depend on the gap distance. Further theoretical consideration of the exact mechanism of the confinement-induced evolution of colloidal LCs remains as future work. In this chapter, we focus on the experimental observation revealing the orientation and order parameter profiles of these new LC domains utilizing the previously described optical methods based on the simultaneous consideration of MD and ED emissions of lanthanide dopants.

4.1.2. A rich diversity of liquid crystalline phase in confined geometry

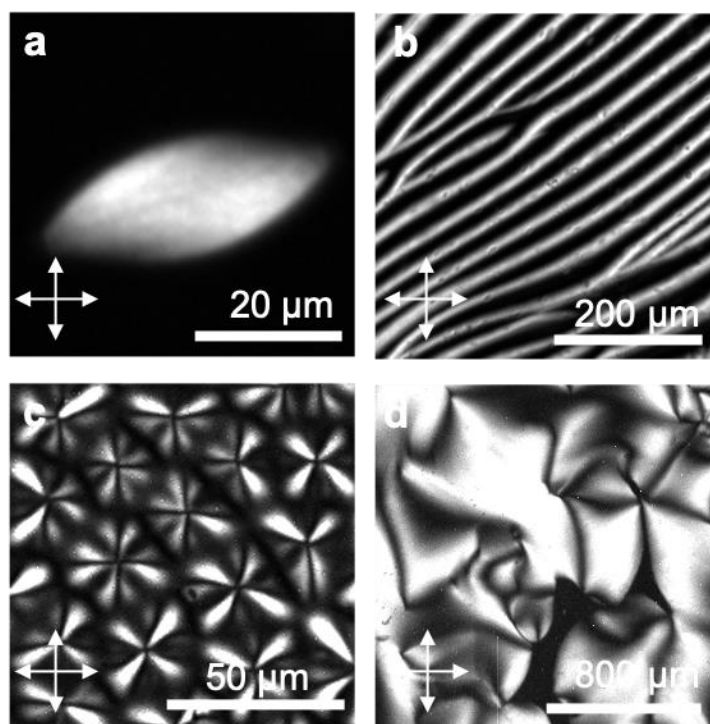


Figure 4.6. Representative confinement-induced liquid crystalline structure of $\text{LaPO}_4:\text{Eu}$ LC suspension observed between crossed polarizers. (a) Nematic tactoid droplet surrounded by isotropic phase, (b) fingerprint-like nematic domains, (c) flower-shaped nematic domains, and (d) nematic domain with point defects.

As discussed in the previous section, the LC suspension composed of $\text{LaPO}_4:\text{Eu}$ nanorods shows a rich variety of LC domains. **Figure 4.6** summarizes the representative LC structures observed in the cell having different gap thickness or different hydrophilicity of the substrate surface. We have often observed that the fate of the final LC domains varies depending on the position in the cell, as summarized in **Figure 4.7**. These LC structures remained the same as an intermediate state without further transition to the final structure.

Some of the prepared cells showed unexpected nucleation and growth of the LC structure aligned in one direction (**Figure 4.8**). This alignment is probably due to the micro-scratches on the substrate, which seem to be created during the substrate cleaning. This observation implies that it might be possible to control such mesostructured LC domains and their patterns by an artificial treatment of the substrate, which is indeed a common method to pre-align molecular LCs. Further studies are necessary to fully understand this phenomenon and develop strategies.

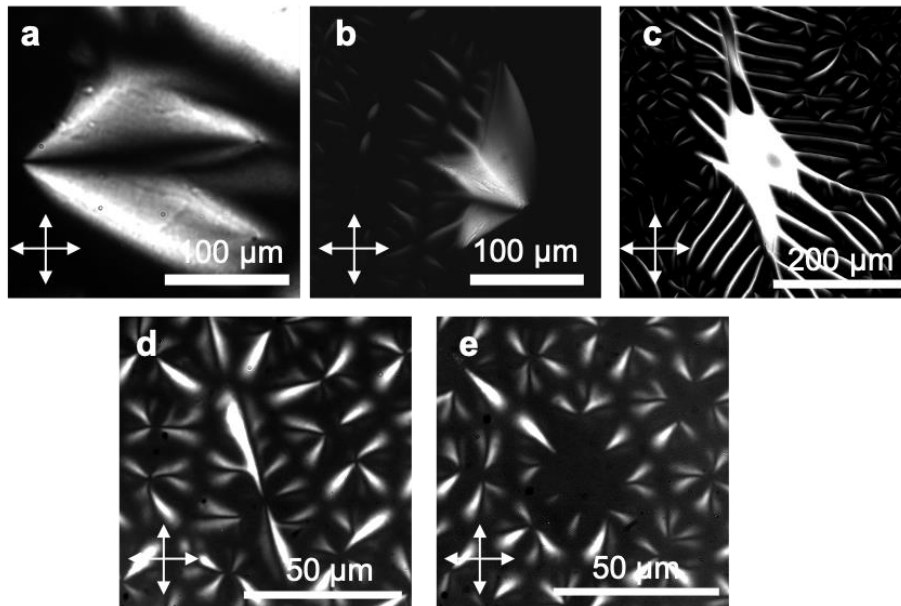


Figure 4.7. The metastable liquid crystalline phase of $\text{LaPO}_4:\text{Eu}$ nanorods suspension found at a different position in the cell. Images are taken between crossed polarizers. (a) Nematic tactoid droplet with point defect (b) Nematic tactoid droplet with linear defect (c) Nematic domain with linear defect and flower-like nematic patterns (d) Connected flower-like nematic pattern with linear defect (e) Boundary between isotropic and flower-like nematic domain.

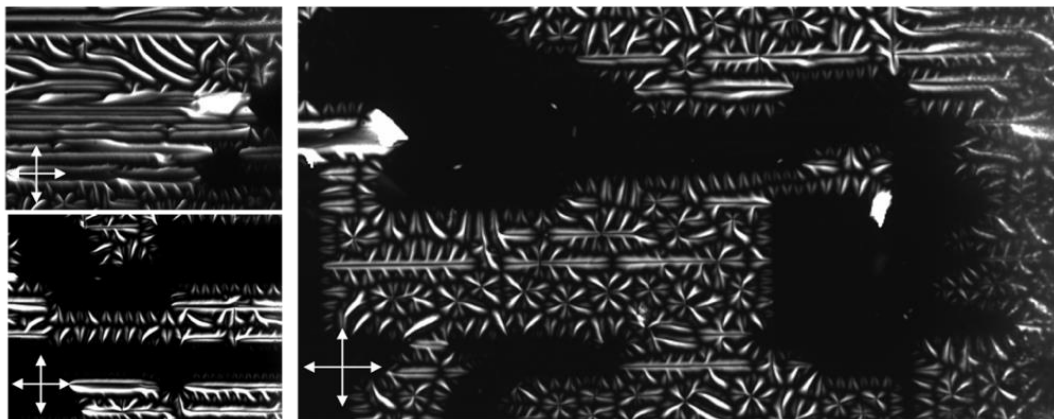


Figure 4.8. Confinement-induced LC domains aligned in one direction.

4.1.3. Birefringence pattern study of liquid crystalline phase in confined geometry

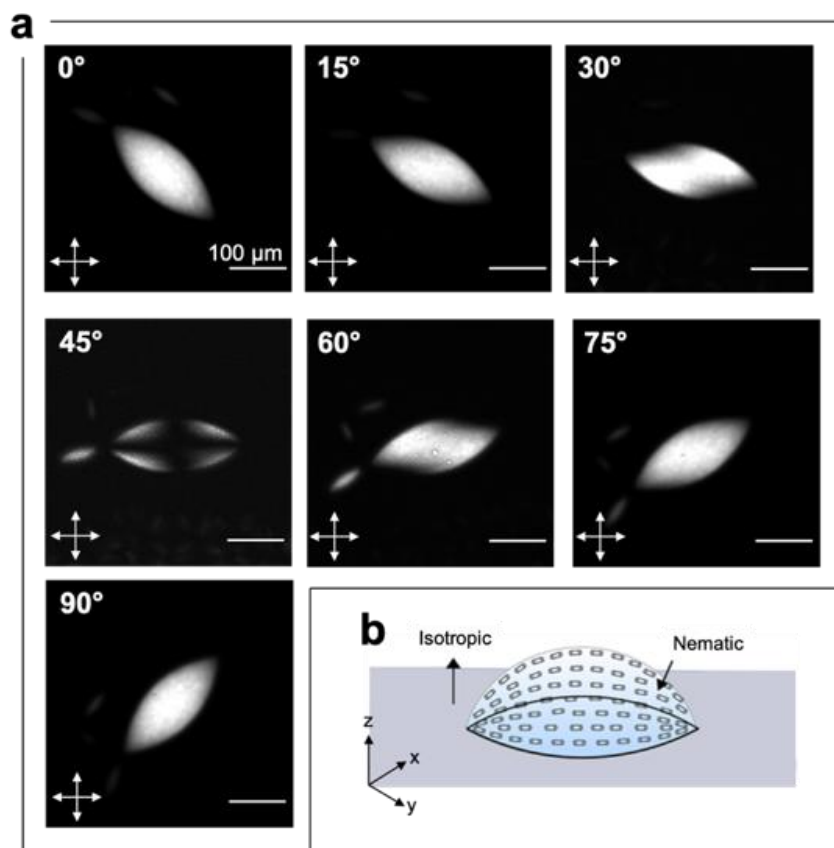


Figure 4.9. (a) Tactoid nematic droplet observed by rotating the sample in the plane between crossed polarizers. Scale bar = 100 μm . (b) Illustration of nanorod orientation in the tactoid nematic droplet. The illustration is taken from the reference.¹⁸⁰

The representative LC structures presented in **Figure 4.6** were investigated by a birefringence technique. When viewed between crossed polarizers by rotating the sample, the orientation of nematic director with respect to the angle of the polarizer and the order parameter of LC structure can be roughly estimated. However, the exact information cannot be obtained because the birefringence signal represents a 2D projection of the LC orientation integrated across the thickness of the sample.

Figure 4.9a shows a nematic tactoid droplet observed by rotating the sample between the crossed polarizers. The measured light intensity I for a birefringence measurement can be expressed as $I = I_0 \cdot \cos^2(\theta) \cdot \sin^2(\theta) \cdot \Delta n \cdot t$ where I_0 is the initial light intensity, θ is the angle between the orientation of the nematic director and the polarizer and Δn is the amount of the birefringence, and t is the thickness of the sample. The amount of birefringence Δn is zero in the isotropic phase due to the random orientation of the nanorods. Therefore, the light intensity measured for the isotropic phase is dark. For example, the outer part of the spindle-shaped tactoid is dark in **Figure 4.9a**. On the contrary, the birefringence Δn inside the nematic droplet is non-zero and its amount of birefringence is proportionally

related to the order parameter S . The measured light intensity I is also a function of θ , the angle between the orientation of nematic director \vec{n} and the polarizer, which is the minimum when $\theta = n\pi$ ($n=0, 1/2, 3/2, \dots$) and the maximum when $\theta = n\pi + \pi/2$ ($n=1/4, 3/4, \dots$). Based on the intensity patterns obtained with rotating samples, it was roughly understood that the studied tactoid nematic droplet had a typical bipolar orientation surrounded by an isotropic phase and the nematic director \vec{n} is tangential to the isotropic-nematic interface¹⁴², as illustrated in **Figure 4.9b**.¹⁸⁰ However, the exact information of order parameter and the orientation of nematic director each unit volume cannot be obtained using a birefringence technique. The methodology for calculating the value of order parameter S and the orientation of nematic director \vec{n} based on the polarized PL of rare-earth dopants is discussed in **Chapter 4.2**.

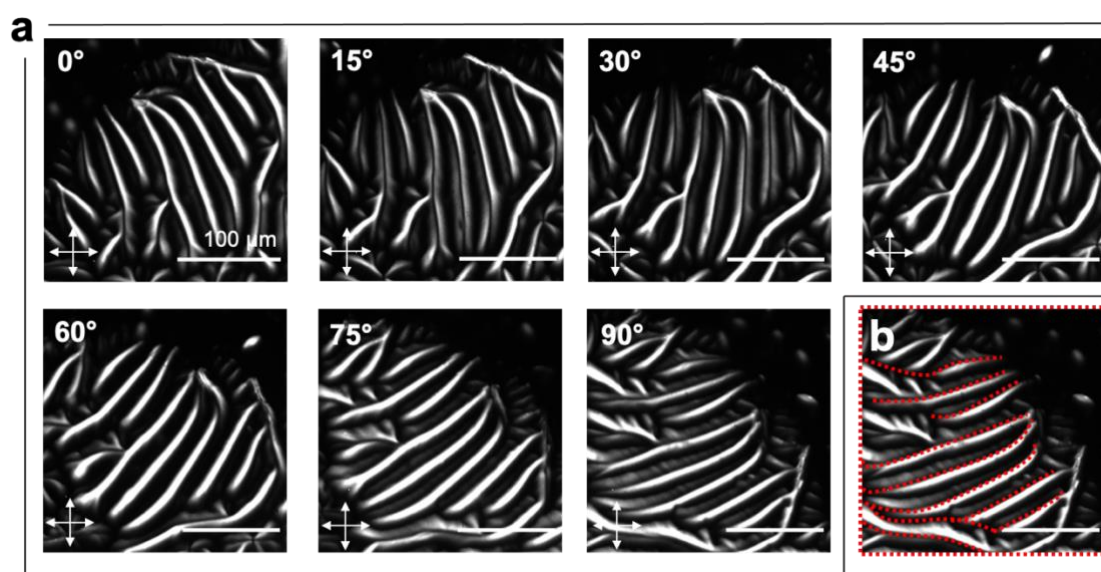


Figure 4.10. (a) Fingerprint-like nematic LC domains observed by rotating the sample in the plane between crossed polarizers. Scale bar = 100 μm . (b) Regions that show dark image when rotating the sample are indicated as a red dashed line.

Figure 4.10a shows fingerprint-shaped nematic LC domains observed by rotating the sample between the crossed polarizers. Comparing to the nematic tactoid droplet having a relatively simple structure, it is difficult to estimate the structure for the fingerprint-shaped LC domains using birefringence images. **Figure 4.10b** show red dashed line that indicates regions always showing dark image when the sample is rotated. Having darkness in the birefringence image implies that this narrow region has nanorods that are either randomly oriented (isotropic) or vertically aligned to the substrate because the amount of birefringence Δn is zero for these two cases.

Figure 4.11a shows the flower-shaped LC domains observed by rotating the sample between the crossed polarizers. Similar to the fingerprint-shaped LC, it is difficult to estimate the structure due to the intricate birefringence patterns. The regions showing a dark image when rotating the sample are also shown in **Figure 4.11b**. Interestingly, the outline and center of a flower-like pattern always appear

dark, meaning that these regions have nanorods that are either isotropic or vertically aligned to the substrate. One flower-shaped domain is seemingly composed of four linear fringes merging at the center with 90° -angles to each other. However, it could not be made the precise estimation on how the LC building blocks ($\text{LaPO}_4\text{:Eu}$ nanorods) were organized in such a peculiar domain from the 2D birefringence images, and further understanding of the structure requires an investigation using another technique allowing to measure the orientation and density of the nanorods in three-dimension. This original experiment using fluorescence confocal microscopy is demonstrated in the next section.

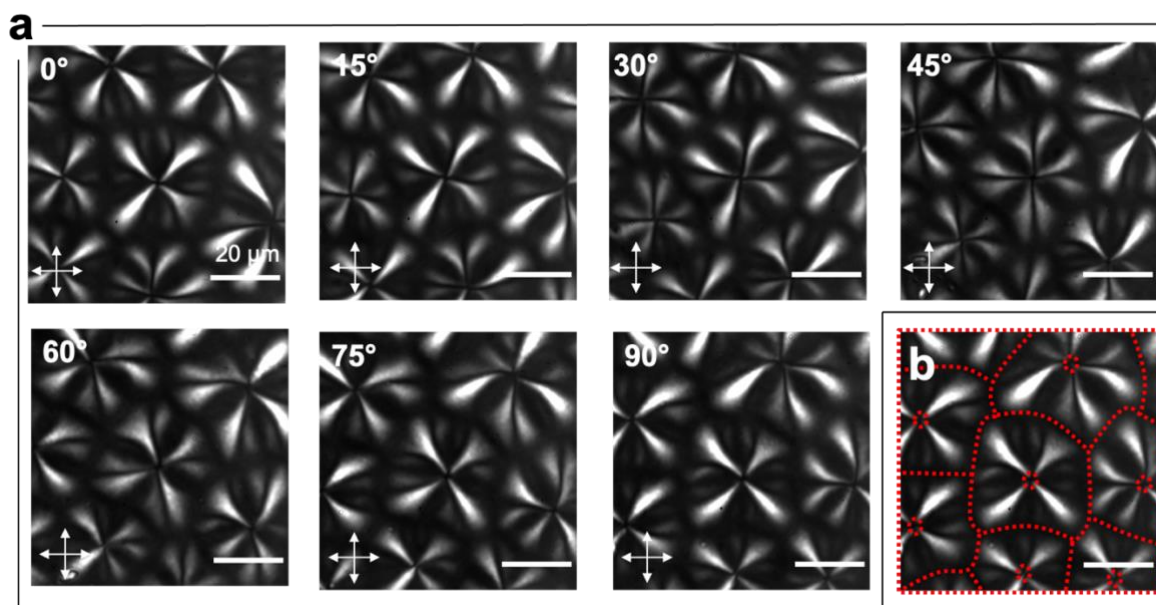


Figure 4.11. (a) Flower-shaped LC domains observed by rotating the sample in the plane between crossed polarizers. Scale bar = $20\ \mu\text{m}$. (b) Regions that show a dark image when rotating the sample are indicated as a red dashed line.

Summary of Chapter 4.1

When liquid crystal phases (LC) are confined in nanoscale geometries, the LC phase can transit to a new type of spatial LC domains. However, such LC transitions had not yet been observed in colloidal LCs. Here, we have found that the LC phases of colloidal LaPO₄:Eu nanorods confined between two hydrophilic substrates can exhibit a peculiar LC domain evolution from a typical nematic tactoid droplet to complex flower-shaped LC domains via an intermediate state with fingerprint-shaped LC domains. This new LC phenomenon can be controlled by changing the hydrophilicity of the cell surfaces or by varying the thickness of the cell spacer. A birefringence study is performed to reconstruct the structure of these LC domains induced by the confinement effect, which was however insufficient due to the limit of the birefringence pattern that is a 2D projection of the integrated signal over the sample thickness.

4.2. 3D tomography of liquid crystalline assembly of LaPO₄:Eu nanorods

4.2.1. State-of-the-art method for tomography of liquid crystalline phase

As discussed above, the confinement-induced liquid crystalline transition generates complex LC patterns that have arbitrary orientations of nematic director \vec{n} varying in three-dimension (3D). Among the non-destructive methods characterizing such LC patterns, birefringence pattern analysis is the most available technique, which however can only provide information in 2D projecting the information of 3D pattern integrated over the thickness, as discussed above. Small Angle X-ray Scattering (SAXS) analysis could offer an alternative method, which is still limited due to relatively poor spatial resolution, sensitivity, instrumental complexity and the specific requirements for the sample preparation.

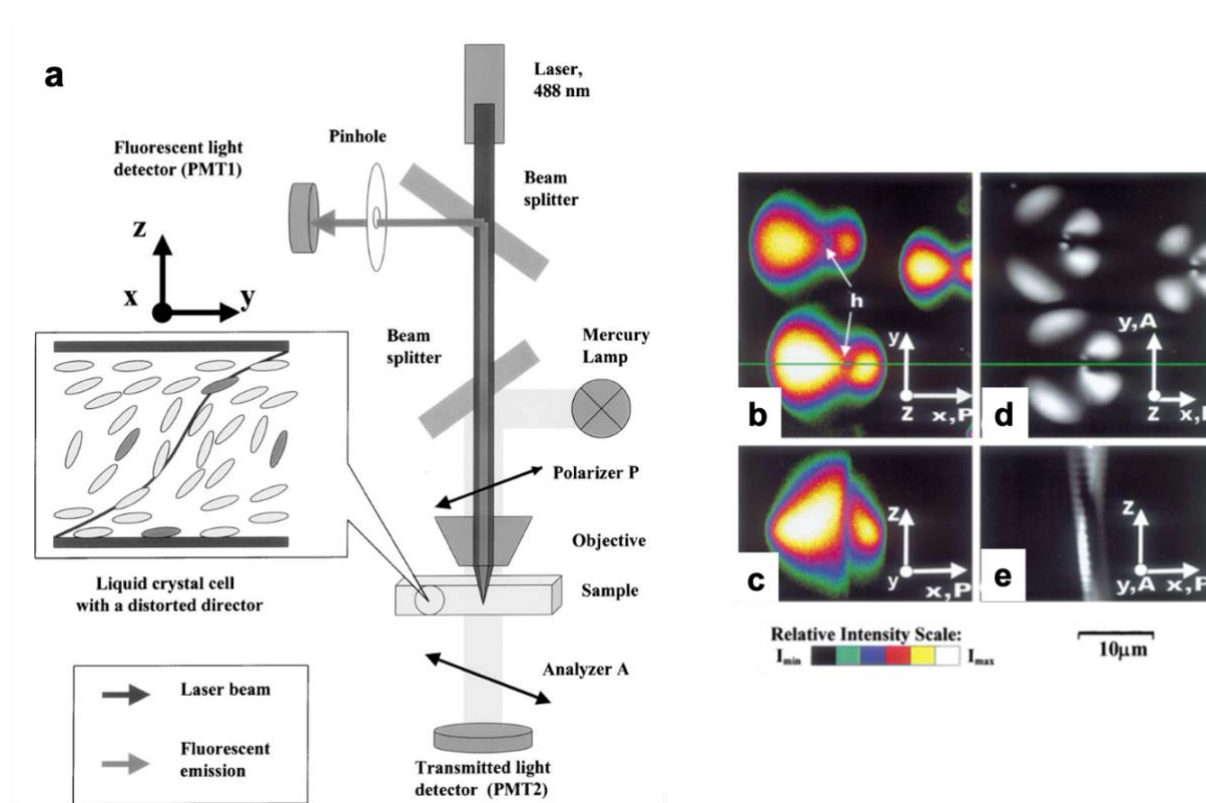


Figure 4.12. (a) Scheme of fluorescence confocal polarizing microscopy (FCPM). Images of focal conic domains (FCD) obtained by (b,c) FCPM and by (d,e) optical polarizing microscope. (b,d) horizontal cross-section of FCD. (c,e) vertical cross-section along the green lines on the image of (b,d). Images were taken from the reference.¹⁸¹

Smalyukh *et al.*, suggested a method to perform tomography of molecular LC patterns in 3D space using a fluorescence confocal polarizing microscopy.¹⁸¹ This method is based on the anisometric fluorescent dye molecules (*e.g.*, BTBP – *n,n'*-bis(2,5-di-*tert*-butylphenyl)-3,4,9,10-perylene-dicarboximide) that can align along with the nematic director \vec{n} of the LC structure (**Figure 4.12a**). These fluorescent molecules exhibit their emission intensity changing as a function of the angles of

excitation and emission polarizations, which is the maximum when the polarization angle is parallel to the axis of the dye molecule and the minimum when the polarization angle is perpendicular to the axis of the dye molecule. Therefore, when scanning the LC structure with a polarized excitation source, the intensity of the detected fluorescence signal varies as a function of the orientation of the dye molecules aligned along the \vec{n} of the LC structure. Thus, their relative emission intensity of fluorescence allows one to estimate the LC orientation and perform tomography by scanning different slices of the LC structure. For example, **Figure 4.12b-c** shows one slice of scanned fluorescence intensity of the dye molecules aligned in the focal conic domains (FCD) structure.

The limitation of this method is that it reveals only “relative” orientation changes that are roughly estimated from the global fluorescence intensity change that is not precise enough to provide the exact value of the orientation of the nematic director \vec{n} (the limitation of orientation analysis using molecular dyes was discussed in **Chapter 1**). Also, this method cannot provide information about the order parameter **S** of the LC structure despite that it is an essential feature of LC domains.

This section is dedicated to overcoming these limitations in order to understand the newly observed LC phase behavior by analyzing the polarized photoluminescence signal of rare-earth ions doped in the nanorods composing the LCs.

4.2.2. Theoretical methodology for tomography of liquid crystalline assembly

In **Chapter 1**, we have shown that the orientation (θ, φ) of individual Eu^{3+} -doped nanorods can be precisely calculated based on the peculiar characteristic of π -, σ -, and α - spectra from the observation of their polarized photoluminescence. In **Chapter 2**, based on the same principle, order parameter **S** of aligned Eu^{3+} -doped nanorods assembly with a known orientation of global alignment \vec{n} is analyzed. Liquid crystalline structure is a three-dimensional assembled structure of which both the orientation of nematic director \vec{n} (θ, φ) and the order parameter **S** are arbitrary in a different position. Therefore, three essential parameters (**S**, θ, φ) of LC structural information must be simultaneously considered in the calculation. We describe here a theoretical methodology that allows us to determine these three essential parameters (**S**, θ, φ) from the polarized photoluminescence of lanthanide ions doped in crystalline nanorods, the building blocks of LC structure investigated. Note that this is a generalized case of the method demonstrated in **Chapter 2** when the director orientation \vec{n} is unknown.

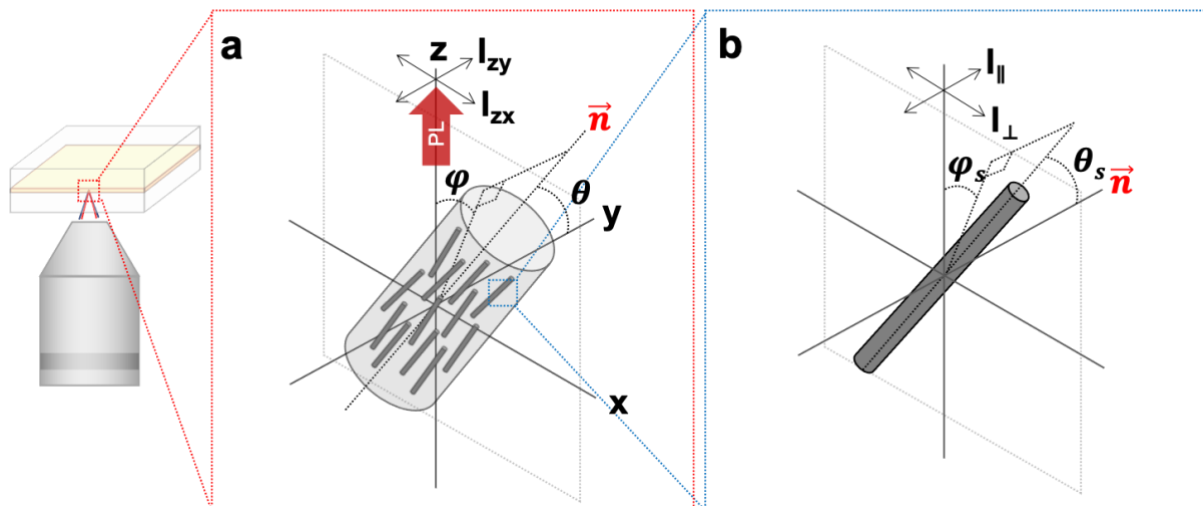


Figure 4.13. (a) Schematic illustration of nanorods assembly aligned to the nematic director \vec{n} in the focal volume of the confocal microscope. Orientation of \vec{n} have an arbitrary 3D orientation by spherical angles – polar angle θ respect to the y-axis, azimuthal angle φ on the xz-plane. (b) Schematic illustration of a single nanorod in the aligned assembly, having an orientation distribution respect to \vec{n} with spherical angles (θ_s, φ_s) .

Figure 4.13a illustrates the nanorod assembly aligned along with the nematic director \vec{n} having an arbitrary orientation in the laboratory frame by a polar angle θ with respect to the y-axis and an azimuthal angle φ on the xz-plane. The emission intensities collected at two orthogonal polarization angles, I_{zx} and I_{zy} (first and second subscripts refer to the axes of propagation and polarization respectively), have contributions of the two polarization components parallel (I_{\parallel}) and perpendicular (I_{\perp}) to nematic director \vec{n} .

For both MD and ED:

$$I_{zy}(\lambda) = I_{\parallel}(\lambda) \cdot \cos^2\theta + I_{\perp}(\lambda) \cdot \sin^2\theta \cdot \sin^2\varphi + I_{\perp}(\lambda) \cdot \sin^2\theta \cdot \cos^2\varphi \quad (4.1)$$

$$I_{zx}(\lambda) = I_{\parallel}(\lambda) \cdot \sin^2\theta \cdot \sin^2\varphi + I_{\perp}(\lambda) \cdot \cos^2\theta + I_{\perp}(\lambda) \cdot \sin^2\theta \cdot \cos^2\varphi \quad (4.2)$$

where I_{\parallel} and I_{\perp} indicate the relative intensities of two polarization components parallel and perpendicular to the nematic director \vec{n} . **Equations 4.1-2** can be simplified as:

$$I_{zy}(\lambda) = I_{\parallel}(\lambda) \cdot \cos^2\theta + I_{\perp}(\lambda) \cdot \sin^2\theta \quad (4.3)$$

$$I_{zx}(\lambda) = I_{\parallel}(\lambda) \cdot \sin^2\theta \cdot \sin^2\varphi + I_{\perp}(\lambda) \cdot (\cos^2\theta \cdot \sin^2\varphi + \cos^2\theta) \quad (4.4)$$

Two polarization components parallel (I_{\parallel}) and perpendicular (I_{\perp}) to nematic director \vec{n} in the **Equation 4.3-4** can be expressed same form with **Equations 2.7-10** discussed in **Chapter 2**.

For ED transition,

$$I_{\parallel,ED}(\lambda) = I_{\pi,ED}(\lambda) \cdot \langle \cos^2 \theta_s \rangle + I_{\sigma,ED}(\lambda) \cdot (1 - \langle \cos^2 \theta_s \rangle) \quad (4.5)$$

$$I_{\perp,ED}(\lambda) = \frac{I_{\pi,ED}(\lambda)}{2} \cdot (1 - \langle \cos^2 \theta_s \rangle) + \frac{I_{\sigma,ED}(\lambda)}{2} \cdot (1 + \langle \cos^2 \theta_s \rangle) \quad (4.6)$$

For MD transition,

$$I_{\parallel,MD}(\lambda) = \frac{I_{\sigma,MD}(\lambda)}{2} \cdot (1 - \langle \cos^2 \theta_s \rangle) + \frac{I_{\pi,MD}(\lambda)}{2} \cdot (1 + \langle \cos^2 \theta_s \rangle) \quad (4.7)$$

$$I_{\perp,MD}(\lambda) = I_{\sigma,MD}(\lambda) \cdot \langle \cos^2 \theta_s \rangle + I_{\pi,MD}(\lambda) \cdot (1 - \langle \cos^2 \theta_s \rangle) \quad (4.8)$$

where $\langle \cos^2 \theta_s \rangle$ is an average polar angle of all nanorods residing in the focal volume to nematic director \vec{n} (**Figure 4.13b**). Based on the above-expressed equations, the practical manual on how to calculate (S, θ , φ) of aligned nanorods assembly is described step by step in the following.

Step 1: Calculating $\langle \cos^2 \theta_s \rangle$

One can then rewrite $I_{zy}(\lambda)$ (**Equation 4.3**) as a function of $\langle \cos^2 \theta_s \rangle$ and $\cos^2 \theta$ by substituting I_{\parallel} , I_{\perp} with **Equations 4.5-8** separately for ED and MD transition.

For ED transition,

$$I_{zy,ED}(\lambda) = \frac{I_{\pi,ED}(\lambda)}{2} (1 - \langle \cos^2 \theta_s \rangle - \cos^2 \theta + 3\langle \cos^2 \theta_s \rangle \cdot \cos^2 \theta) + \frac{I_{\sigma,ED}(\lambda)}{2} (1 + \langle \cos^2 \theta_s \rangle + \cos^2 \theta - 3\langle \cos^2 \theta_s \rangle \cdot \cos^2 \theta) \quad (4.9)$$

For MD transition,

$$I_{zy,MD}(\lambda) = \frac{I_{\sigma,ED}(\lambda)}{2} (2\langle \cos^2 \theta_s \rangle + \cos^2 \theta - 3\langle \cos^2 \theta_s \rangle \cdot \cos^2 \theta) + \frac{I_{\pi,ED}(\lambda)}{2} (2 - 2\langle \cos^2 \theta_s \rangle - \cos^2 \theta + 3\langle \cos^2 \theta_s \rangle \cdot \cos^2 \theta) \quad (4.10)$$

The **Equations 4.9-10**, with the intensities as continuous functions of wavelength, can be rewritten with the integrated intensities for divided wavelength ranges referred to as ED1, ED2, MD1, and MD2. Area under curve ratiometry approach is discussed in **Chapter 1**.

For ED transition,

$$\begin{aligned} & \langle \cos^2 \theta_s \rangle + \cos^2 \theta - 3 \langle \cos^2 \theta_s \rangle \cdot \cos^2 \theta \\ &= -\frac{k_{zy,ED} \cdot (I_{\sigma,ED2} + I_{\pi,ED2}) - (I_{\sigma,ED1} + I_{\pi,ED1})}{k_{zy,ED} \cdot (I_{\sigma,ED2} - I_{\pi,ED2}) - (I_{\sigma,ED1} - I_{\pi,ED1})} \end{aligned} \quad (4.11)$$

where $I_{\pi,EDn}$ and $I_{\sigma,EDn}$ ($n = 1$ or 2) indicate the relative area under curve of the π and σ spectra and $k_{zy,ED}$ stand for the measured intensity ratios $I_{zy,ED1}/I_{zy,ED2}$.

For MD transition,

$$\begin{aligned} & 2 \langle \cos^2 \theta_s \rangle + \cos^2 \theta - 3 \langle \cos^2 \theta_s \rangle \cdot \cos^2 \theta \\ &= -2 \cdot \frac{k_{zy,MD} \cdot I_{\pi,MD2} - I_{\pi,MD1}}{k_{zy,MD} \cdot (I_{\sigma,MD2} - I_{\pi,MD2}) - (I_{\sigma,MD1} - I_{\pi,MD1})} \end{aligned} \quad (4.12)$$

where $I_{\pi,MDn}$ and $I_{\sigma,MDn}$ ($n = 1$ or 2) indicate the relative area under curve of the π and σ spectra and $k_{zy,MD}$ stand for the measured intensity ratios $I_{zy,MD1}/I_{zy,MD2}$.

One can obtain $\langle \cos^2 \theta_s \rangle$ by subtracting **Equation 4.12** from **Equation 4.11**, which can be rewritten as:

$$\begin{aligned} \langle \cos^2 \theta_s \rangle &= -2 \cdot \frac{k_{zy,MD} \cdot I_{\pi,MD2} - I_{\pi,MD1}}{k_{zy,MD} \cdot (I_{\sigma,MD2} - I_{\pi,MD2}) - (I_{\sigma,MD1} - I_{\pi,MD1})} \\ &+ \frac{k_{zy,ED} \cdot (I_{\sigma,ED2} + I_{\pi,ED2}) - (I_{\sigma,ED1} + I_{\pi,ED1})}{k_{zy,ED} \cdot (I_{\sigma,ED2} - I_{\pi,ED2}) - (I_{\sigma,ED1} - I_{\pi,ED1})} \end{aligned} \quad (4.13)$$

Once $\langle \cos^2 \theta_s \rangle$ is obtained, order parameter S can be calculated according to **Equation 2.1** - $S = (3 \cdot \langle \cos^2 \theta_s \rangle - 1)/2$.

One can now also calculate the integrated intensities for divided ranges (MD1, MD2, ED1 and ED2) of $I_{\parallel,MD}(\lambda)$, $I_{\perp,MD}(\lambda)$, $I_{\parallel,ED}(\lambda)$, $I_{\perp,ED}(\lambda)$ (**Equations 4.5-8**) - $I_{\parallel,MD1}$, $I_{\perp,MD1}$, $I_{\parallel,MD2}$, $I_{\perp,MD2}$, $I_{\parallel,ED1}$, $I_{\perp,ED1}$, $I_{\parallel,ED2}$, $I_{\perp,ED2}$ - which will be used for further calculation.

Step 2: Calculating $\cos^2 \theta$

Once $\langle \cos^2 \theta_s \rangle$ is obtained, $\cos^2 \theta$ can be calculated either from **Equations 4.11** or from **Equation 12**.

For ED transition,

$$\cos^2\theta = \left(\frac{1}{3\langle \cos^2\theta_s \rangle - 1} \right) \cdot \left\{ \frac{k_{zy,ED} \cdot (I_{\sigma,ED2} + I_{\pi,ED2}) - (I_{\sigma,ED1} + I_{\pi,ED1})}{k_{zy,ED} \cdot (I_{\sigma,ED2} - I_{\pi,ED2}) - (I_{\sigma,ED1} - I_{\pi,ED1})} + \langle \cos^2\theta_s \rangle \right\} \quad (4.14)$$

For MD transition,

$$\cos^2\theta = \left(\frac{2}{3\langle \cos^2\theta_s \rangle - 1} \right) \cdot \left\{ \frac{k_{zy,MD} \cdot I_{\pi,MD2} - I_{\pi,MD1}}{k_{zy,MD} \cdot (I_{\sigma,MD2} - I_{\pi,MD2}) - (I_{\sigma,MD1} - I_{\pi,MD1})} + \langle \cos^2\theta_s \rangle \right\} \quad (4.15)$$

One gets an identical value of $\cos^2\theta$ regardless of the type of transition used for the analysis, as it originates from the same equation.

Step 3: Calculating $\sin^2\varphi$

Similarly, $I_{zx}(\lambda)$ (Equations 4.4), with the intensities as continuous functions of wavelength, can be rewritten with the integrated intensities for divided wavelength ranges from which $\sin^2\varphi$ can be expressed as:

For ED transition,

$$\sin^2\varphi = \frac{k_{zx,ED} \cdot I_{\perp,ED2} - I_{\perp,ED1}}{(1 - \cos^2\theta) \cdot [(I_{\parallel,ED1} - I_{\perp,ED1}) - k_{zx,ED} \cdot (I_{\parallel,ED2} - I_{\perp,ED2})]} \quad (4.16)$$

where $I_{\parallel,EDn}$ and $I_{\perp,EDn}$ ($n = 1$ or 2) indicate the integrated intensities of $I_{\parallel,ED}(\lambda)$, $I_{\perp,ED}(\lambda)$ (Equation 4.5-6) and $k_{zx,ED}$ stand for the measured intensity ratios $I_{zx,ED1}/I_{zx,ED2}$.

For MD transition,

$$\sin^2\varphi = \frac{k_{zx,MD} \cdot I_{\perp,MD2} - I_{\perp,MD1}}{(1 - \cos^2\theta) \cdot [(I_{\parallel,MD1} - I_{\perp,MD1}) - k_{zx,MD} \cdot (I_{\parallel,MD2} - I_{\perp,MD2})]} \quad (4.17)$$

where $I_{\parallel,MDn}$ and $I_{\perp,MDn}$ ($n = 1$ or 2) indicate the integrated intensities of $I_{\parallel,MD}(\lambda)$, $I_{\perp,MD}(\lambda)$ (Equations 4.7-8) and $k_{zx,MD}$ stand for the measured intensity ratios $I_{zx,MD1}/I_{zx,MD2}$.

As $\cos^2\theta$ is already obtained, one can calculate $\sin^2\varphi$ by applying the value of integrated intensities for divided ranges of $I_{\parallel,MD}(\lambda)$, $I_{\perp,MD}(\lambda)$, $I_{\parallel,ED}(\lambda)$, $I_{\perp,ED}(\lambda)$. From the equations described above, one can obtain two values of $\sin^2\varphi$ either from MD or ED transition. In principle, these two values should be identical unless there are error sources (see the discussion about errors in ratiometric orientation analysis presented in Chapter 1.3.3). Once the orientation of nematic director $\vec{n}(\theta, \varphi)$ is calculated,

the coordinates are converted into the more intuitive angles to the observer - out-of-plane angle θ' and in-plane angle φ' with respect to the measurement plane (**Figure 4.14**). The conversion is made according to **Equations 1.11-12**.

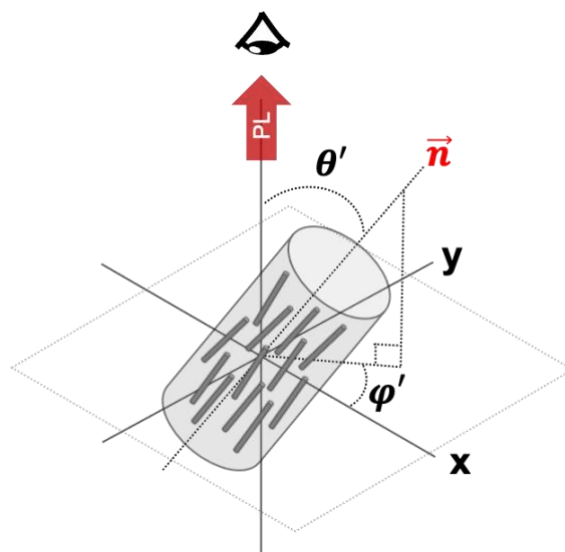


Figure 4.14. Schematic illustration of nanorods assembly aligned to the nematic director \vec{n} in the focal volume of the confocal microscope. Orientation of \vec{n} have an arbitrary 3D orientation by spherical angles – out-of-plane θ' and in-plane angle φ' on the measurement plane (xy).

Based on the above-described methodology, one can calculate the three essential parameters - order parameter S and the orientation of nematic director \vec{n} (θ , φ) – of aligned nanorods assembly. We describe in the following sections using this methodology to study the new LC domain structures. However, it is worth noting that the above-described methodology can be applied to any kind of aligned rare-earth doped nanorods assembly structure for their analysis of (S , θ , φ). Aligned nanorods assembly in a microfluidic channel by a shear force is an example shown in our previous study.⁸⁰ For the practical application of this methodology, it requires a confocal polarizing microscope to obtain the PL signal with a fine spatial resolution and the two orthogonal polarization components of polarized PL signal (I_{zx} and I_{zy}) collected from every unit volume.

4.2.3. Fluorescence confocal polarizing microscopy

Figure 4.15 shows the confocal polarizing microscopy setup developed for liquid crystal tomography. The UV excitation beam of monochromatic laser ($\lambda_{ex} = \sim 394$ nm) used for the excitation of Eu^{3+} ions doped in LaPO_4 nanorods is collimated by a collimating lens. The parallel excitation beam then meets the beam expander which adjusts the parallelism of the excitation beam, which functions as a correction for the chromatic aberration of the objective. This correction allows us to match the focal plane of the

excitation and emission beam ($\lambda_{em} = 500 \sim 700$ nm), improving the microscopy resolution. With the adjustment using the beam expander, the confocal resolution is improved more than eight times in volume and the fluorescence signal-to-noise ratio is improved more than two times. Then, the excitation beam passes through the $\lambda/4$ waveplate, which circularly polarizes the linearly-polarized excitation beam. The $\lambda/4$ waveplate is set at 45° with respect to the linear polarization axis of the laser beam. This is to minimize the overall fluctuation of the overall fluorescence intensity caused by the varying absorption cross-section of the nanorods as a function of the angles between the excitation polarization and the rod axis. The excitation beam is then reflected by a dichroic mirror and a right-angle prism mirror. We found that the metal-coated mirror should be avoided for the polarization experiment because the polarization state can be significantly affected when the beam is reflected off the metal surface. Then, the excitation beam is focused on the focal plane where the objective collects the emission beam on the same focal plane.

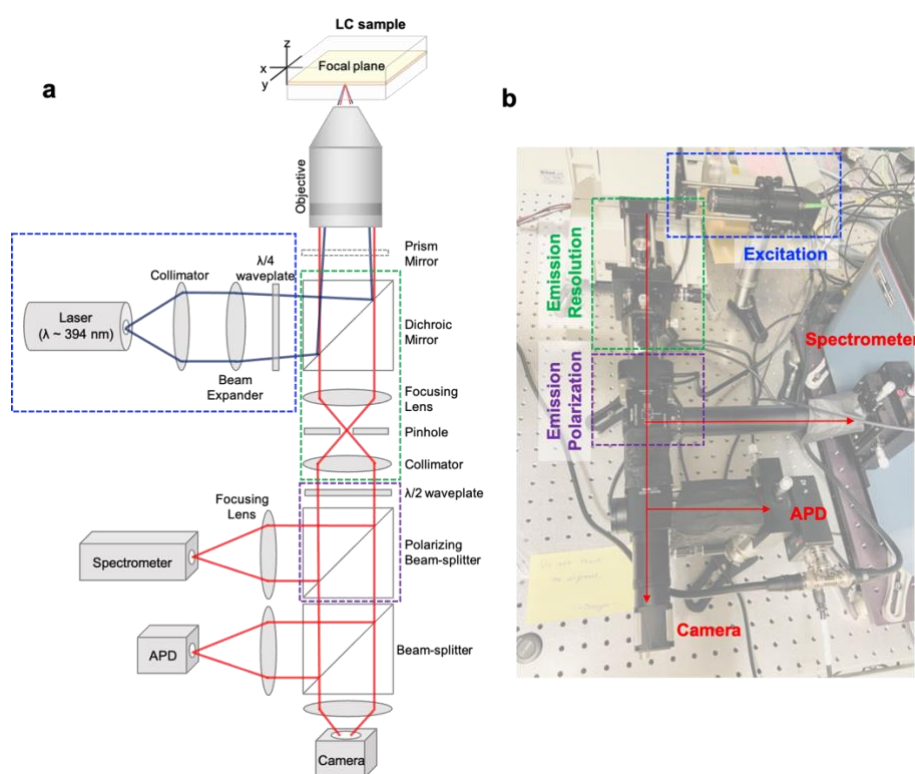


Figure 4.15. (a) Schematic illustration and (b) photograph of confocal fluorescence polarizing microscopy setup developed for liquid crystal tomography. Each section corresponding to excitation, emission-resolution and emission-polarization are marked in the dashed box.

The emission beam collected with the objective is then reflected by the right-angle prism mirror and transmits the dichroic mirror. The emission beam is then focused on the focal point where the pinhole of $15 \mu\text{m}$ is installed. Using a smaller pinhole size, the confocal resolution can be improved but there is a tradeoff with the signal-to-noise ratio. As the fluorescence intensity of lanthanide ions is relatively lower than the other phosphors (*e.g.*, organic phosphors, quantum dots) due to small absorption cross-

section and the milliseconds scale of luminescence lifetime, 15 μm was the optimum pinhole size preserving good confocal microscope resolution and the signal-to-noise ratio of collected spectra. The emission beam is then collimated, and the polarization state is rotated with a $\lambda/2$ waveplate. Afterward, the polarization state is selected by a polarizing beam-splitter that transmits p-polarization component and reflects the s-polarization component. The reflected s-polarization component is then focused and enters into the spectrophotometer. We have set a polarization setup configuring a combination of a $\lambda/2$ waveplate and polarizing beam-splitter instead of a combination of a linear polarizer. In doing so, one can make sure that the s-polarization always arrives at the spectrometer while having the possibility to select the state of polarization by rotating the $\lambda/2$ waveplate. This configuration eliminates the distortion of the line shape of the measured spectra due to the optical anisotropy of the grating inside the spectrophotometer. The transmitted p-polarization component of the emission beam is then split, focusing on the avalanche photodiode (APD) which returns the overall fluorescence intensity and the other towards a viewing camera. A photograph of the whole setup of this microscopy system is shown in **Appendix Figure 4.1**.

Spatial resolution of the confocal microscope

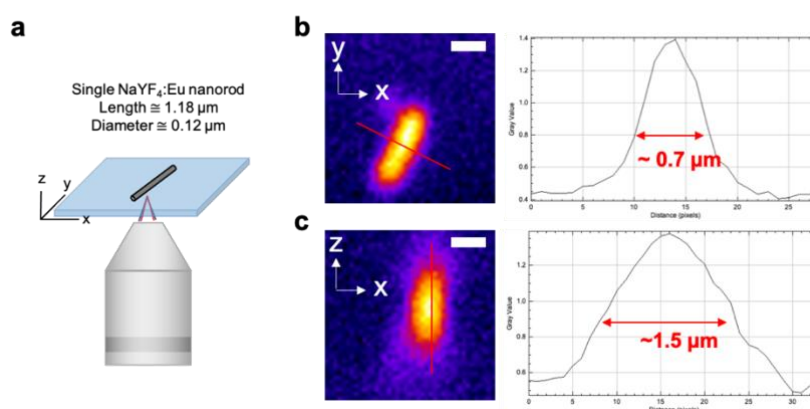


Figure 4.16. (a) Schematic illustration of single NaYF₄:Eu nanorod lying on the substrate with an objective (b,c) PL emission image obtained by scanning PL signal (from APD) synchronized with a piezoelectric stage, (b) XY slice and (c) XZ slice of a single nanorod. Scale bar = 1 μm . The Red line corresponds to the cross-section of PL intensity, shown in the right panel. The value of Full-half-width-maximum (FWHM) is written in red color.

The spatial resolution of the developed confocal microscopy is verified by scanning a PL emission of a single NaYF₄:Eu nanorod lying on the substrate (same nanorod discussed in **Chapter 1-2**). **Figure 4.16b-c** shows the collected PL emission by the APD detector synchronized with the piezo stage for different slices – xy (**Figure 4.16b**) and xz (**Figure 4.16c**) scanning. The cross-section at the diameter of a single nanorod (~120 nm) allows us to roughly estimate the spatial resolution of confocal

microscopy. The spatial resolution at the optimized condition was about $0.6\ \mu\text{m}$ for xy scanning (lateral scanning) and about $1.4\ \mu\text{m}$ for z scanning (axial scanning). The resolution is calculated by subtracting the diameter of the nanorod from the FWHM of the PL emission profile across the diameter of the nanorod (**Figure 4.16b-c**). For this test, a 100x objective with a numerical aperture (NA) of 0.9 is used. However, it should be noted that the resolution will vary greatly depending on experimental conditions such as the refractive index of the surrounding emitter, the NA of the objective, emission wavelength, and the ability to correct chromatic aberration. The theoretically estimated confocal resolution for the used excitation wavelength ($\sim 400\ \text{nm}$) and the numerical aperture (NA 0.9) is $\sim 0.3\ \mu\text{m}$ for lateral resolution and $\sim 0.8\ \mu\text{m}$ for axial resolution, which is not yet achieved.¹⁸² Further optimization is necessary to improve the spatial resolution.

4.2.4. 3D tomography of liquid crystalline nanorod assembly

Nematic tactoid droplet

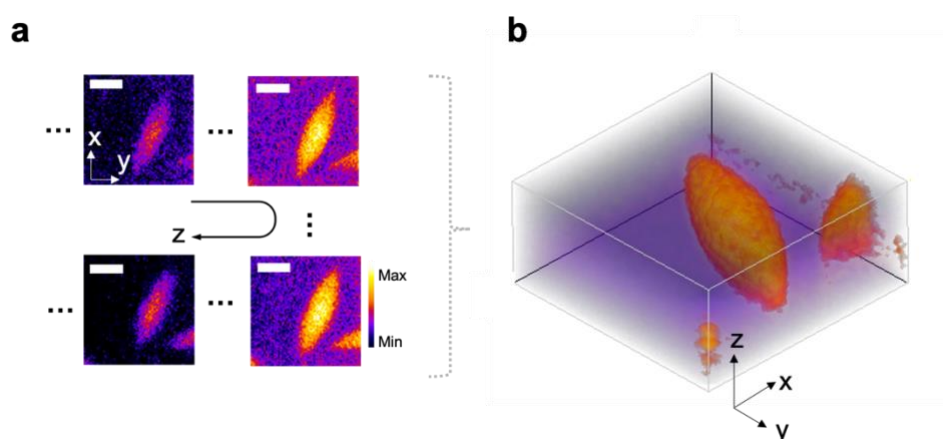


Figure 4.17. (a) Scanned PL emission of nematic tactoid droplets obtained at different Z planes. pixel size: $0.5\ \mu\text{m}$. scale bar = $10\ \mu\text{m}$. (b) Reconstructed 3D PL emission of nematic tactoid droplets.

The proposed methodology is firstly applied to the nematic tactoid droplet because its orientation structure is well understood by many other works (also illustrated in **Figure 4.9b**).¹⁴² **Figure 4.17a** shows the scanned PL image of a nematic tactoid droplet surrounded by isotropic phase, which is detected by APD synchronized with a piezo stage. Although PL is emitted both from the nematic and the isotropic phase, the phase can be distinguished because the nematic phase has a higher spatial density of nanorods than the isotropic phase. Accordingly, the measured PL intensity of the nematic phase in a given focal volume is ~ 1.5 times stronger than that of the isotropic phase. The good spatial resolution being ensured, the border between the isotropic and nematic phase appears clearly. By performing the scanning of the global PL emission intensity on XY-planes at different Z heights (**Figure**

4.17a) and putting them together, the 3D nematic LC structure can be reconstructed as shown in **Figure 4.17b**. As expected, the nematic tactoid droplet has a rugby ball shape having two poles at the end and a thicker center, having a good agreement with the discussion made in **Figure 4.9**. With these PL images collecting the global intensity of emission on a wide wavelength range, the orientation of the nanorods in the nematic tactoid cannot be calculated. The proposed methodology requires measuring the PL intensities at divided wavelength ranges (MD1, MD2, ED1, and ED2). This can be achieved by using a photodetector (*e.g.* APD) with different optical bandpass filters or using a spectrometer with a post spectral analysis. The selection of the bandpass filters for LaPO₄:Eu nanorods is described in **Appendix Figure 1.3**. The calculation of (S, θ, φ) requires measuring two polarizations (I_{zx}, I_{zy}) at four different wavelength ranges (MD1, MD2, ED1 and ED2), which means that it requires at least eight separate measurements for one scanning plane when using photodetectors. We thus chose to use a spectrometer that can cover the whole wavelength range with an automatically rotating mount to select different polarizations.

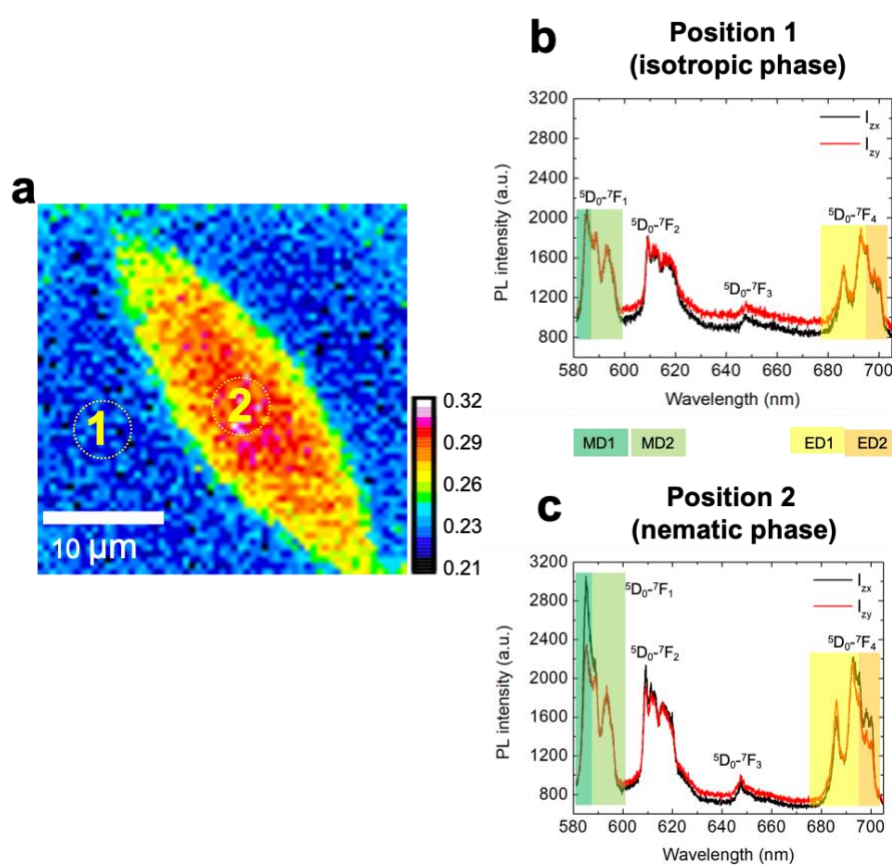


Figure 4.18. (a) Scanned PL emission of a nematic tactoid droplet of XY slice obtained at one Z height, scale bar = 10 μm. pixel size: 0.5 μm Spectrum collected at two orthogonal polarizations (I_{zx}, I_{zy}) at two different positions indicated in **Figure 4.18a** - (b) position1, isotropic phase, (c) position2, nematic phase.

Figure 4.18a shows the scanned PL emission of the nematic tactoid droplet by APD detector at one Z plane. As discussed above, the isotropic phase and nematic phase can be distinguished by their relative

PL emission intensity, which allows us to selectively measure the spectrum from an either isotropic or nematic phase. When the spectra are measured at two orthogonal polarizations in the isotropic phase (**Figure 4.18b**), it showed a negligible change in their line shape at different polarizations due to the random orientation of nanorods. Nevertheless, one can see that the background offset of spectra at two polarization states is not perfectly the same even for the isotropic phase, which may cause some errors in the analysis unless the proper background subtraction is made. The excitation laser intensity is kept low (< 20 mW) to prevent disarrangement due to local heats induced by the excitation laser when taking the reference spectra and tomographic spectra. Contrary to the isotropic phase, spectra measured in the nematic phase show distinct line shapes at different polarizations (**Figure 4.18c**). Such a difference in line shape contains the information of (S, θ, φ) in the measured focal volume of the LC structure.

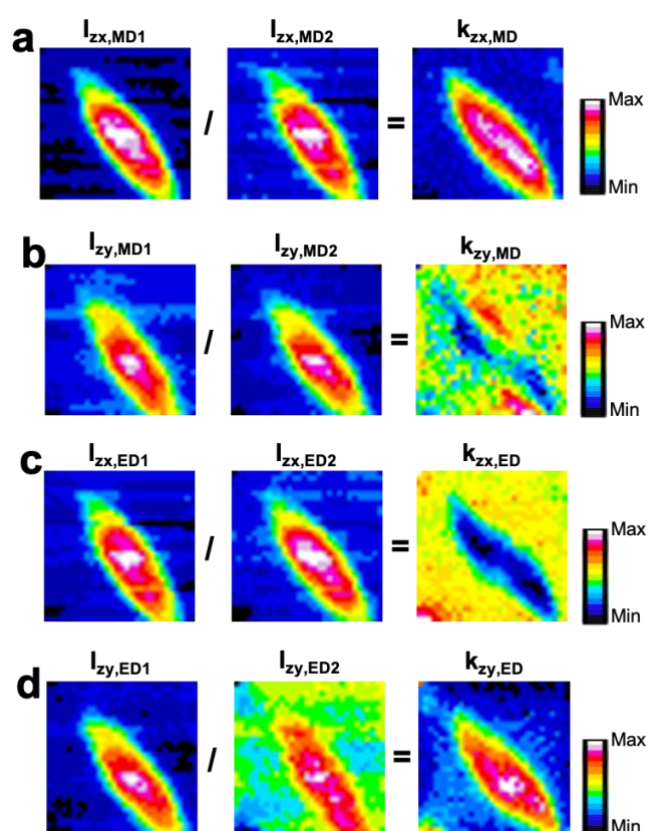


Figure 4.19. Scanned spectrum for each unit volume is used to calculate the area under curve (MD1, MD2, ED1, and ED2) and their ratio (MD1/MD2, ED1/ED2) at orthogonal polarizations (I_{zx} , I_{zy}). pixel size: $1 \mu\text{m}$ Calculated area under curve and their ratio is displayed for (a) $I_{zx,MD}$, (b) $I_{zx,ED}$, (c) $I_{zy,MD}$ and (d) $I_{zy,ED}$.

The spectra at two polarizations were automatically collected at each pixel of the 3D scanning map by synchronizing the spectrometer with the scanning piezo-stage and the polarization rotating mount. Image maps of the area under curve (MD1, MD2, ED1 and ED2) of the spectra (I_{zx} , I_{zy}) were then calculated after the background offset treatment, as shown in **Figure 4.19**. The following calculations were conducted using these 2D image maps. Unlike $\text{NaYF}_4:\text{Eu}$ nanorod considered in **Chapter 1** and

Chapter 2, for the $\text{LaPO}_4\text{:Eu}$ nanoparticles, the ${}^5\text{D}_0\text{-}{}^7\text{F}_1$ transition is used for MD emissions, and the ${}^5\text{D}_0\text{-}{}^7\text{F}_4$ transition is used for ED emissions. This is because the ${}^5\text{D}_0\text{-}{}^7\text{F}_4$ transition showed the highest DOP among other ED transitions available in one spectrogram (e.g., ${}^5\text{D}_0\text{-}{}^7\text{F}_2$ and ${}^5\text{D}_0\text{-}{}^7\text{F}_3$ transitions).^{2,66} (see the highlight in **Figure 4.18b-c** for the wavelength range used for the area under curve). The area under the curve ratio calculated by dividing the area under the curve (MD1/MD2 and ED1/ED2) for orthogonal polarizations (I_{xz} , I_{zy}) is used for the subsequent calculation of (S, θ, φ) (**Figure 4.19**). The calculation (S, θ, φ) requires a reference spectrum (I_π , I_σ) obtained under the same experimental conditions (e.g., refractive index, objective, grating of the spectrometer, same batch of nanoparticles, etc.) where the experimental data are obtained.

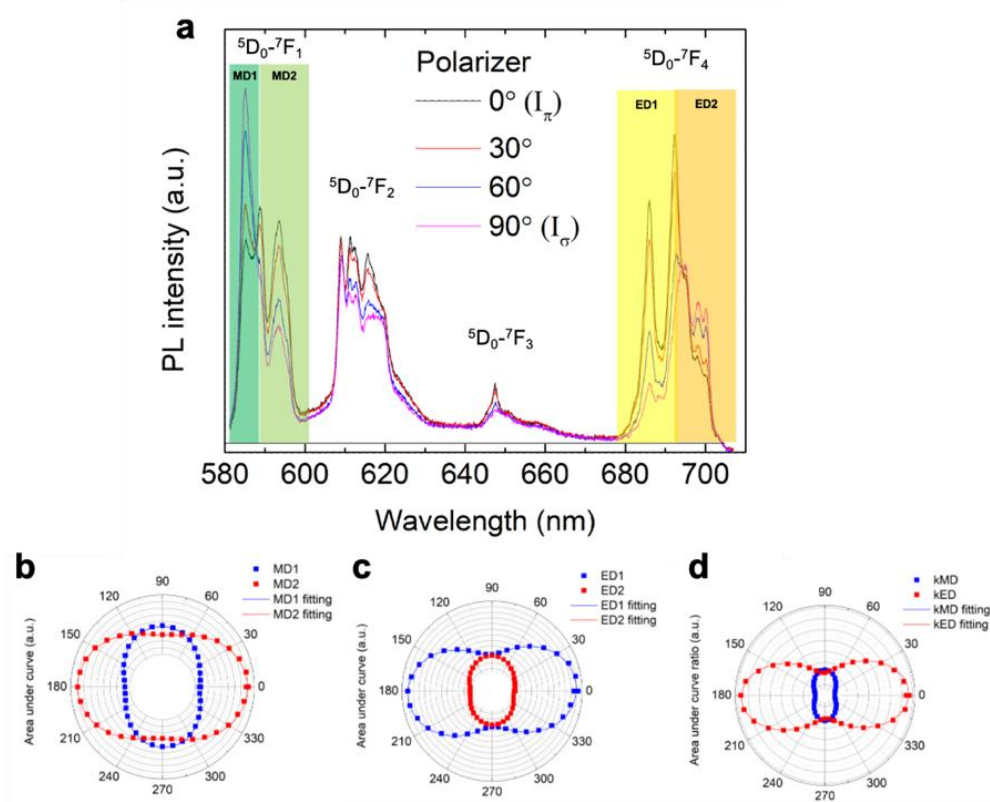


Figure 4.20. Reference spectrum of $\text{LaPO}_4\text{:Eu}$ nanorods obtained at the center of nematic tactoid droplet. (a) Spectra with a rotating polarizer. Area under curve of (b) MD1 and MD2 wavelength range and (c) ED1 and ED2 wavelength range for spectra with a rotating polarizer. (d) Area under curve ratio of MD1/MD2 and ED1/ED2.

Here, the reference spectrum is obtained at the center of the nematic tactoid droplet where the alignment of nanorods is expected to be almost perfect ($0.8 < S < 1$). It is essential to find a nematic tactoid droplet with the orientation director parallel to the substrate for collecting the reference spectra. It is interesting to note that the reference spectra can be also obtained from the aligned thin film⁷⁵, nematic LC phase⁶⁹, and the single nanorod⁸⁰. In the case of the single nanorods, the reference spectra will be the most perfect in terms of DOP, but there is a tradeoff with the S/N ratio as the emission intensity of a single nanorod

is very small. In the case of the nematic sample, getting reference spectra at a different position is necessary to find a position that shows the perfect alignment where S is close to 1, thus showing the highest DOP. In the case of aligned thin film, it is interesting as there would be no wobbling of nanorods by thermal effects. However, it has a different optical environment surrounding the emitting nanorods, such as the refractive index and close interface with the substrate, which may cause some errors in the analysis.

Figure 4.20 presents the reference spectra measured at the center of the nematic tactoid droplet parallel to the substrate, showing a clear line shape change with a rotating polarizer. Reference spectra - I_π and I_σ - are measured parallel (noted 0°) and perpendicular (noted 90°) to the main axis of a spindle-shaped nematic tactoid droplet, respectively. Using the same wavelength ranges (MD1, MD2, ED1 and ED2) with experimental spectrum map (**Figure 4.18b-c**), the reference intensities - $I_{\pi,MD1}$, $I_{\pi,MD2}$, $I_{\pi,ED1}$, $I_{\pi,ED2}$, and $I_{\sigma,MD1}$, $I_{\sigma,MD2}$, $I_{\sigma,ED1}$, $I_{\sigma,ED2}$ - can be calculated. **Figure 4.20b-d** shows the polar diagram of area under curve and their ratio of the reference spectra. The calculated degree of polarization (DOP) of area under curve for MD1, MD2, ED1 and ED2 wavelength ranges is -0.23, 0.24, 0.40 and -0.22. The DOP of the area under curve ratio for MD1/MD2 and ED1/ED2 is -0.45 and 0.57. Better accuracy is expected when ED emission is used as an analysis as it showed a higher DOP.

As the spectrum map of $k_{zx,MD}$, $k_{zx,ED}$, $k_{zy,MD}$ and $k_{zy,ED}$ (**Figure 4.19**) and the reference intensities ($I_{\pi,MD1}$, $I_{\pi,MD2}$, $I_{\pi,ED1}$, $I_{\pi,ED2}$, and $I_{\sigma,MD1}$, $I_{\sigma,MD2}$, $I_{\sigma,ED1}$, $I_{\sigma,ED2}$) (**Figure 4.20**) are obtained, $\langle \cos^2 \theta_s \rangle$ - an average polar angle of all nanorods residing in the focal volume to nematic director \vec{n} - can be firstly calculated using **Equation 4.13** for each pixel. Once $\langle \cos^2 \theta_s \rangle$ is calculated, order parameter $S = (3 \cdot \langle \cos^2 \theta_s \rangle - 1) / 2$ can be calculated, as shown in **Figure 4.21a**. The calculated value of order parameter S appears higher (~ 0.20) for the areas near the nematic tactoid droplet and lower (~ 0) for the areas far from the tactoid nematic droplet. The non-zero S very close to the surface of the nematic tactoid droplet may be due to the capillary nematization effect. However, the calculated order parameter S fluctuates from 0 and 0.20 in the isotropic phase, even far from the nematic droplets. As the expected value for the randomly oriented isotropic phase is 0, the fluctuation seems to be mainly due to an insufficient spatial resolution. Thus, there were calculation errors due to signal fluctuation from pixel to pixel. Further optimization is necessary for improving the resolution. In the nematic phase, the calculated order parameter S was between 0.40 and 0.70 and appeared to gradually decrease from the center of the tactoid to the isotropic-nematic interface. Such a tendency of gradual change in S is necessary to reduce the energy of strong director distortions at the isotropic and nematic interface.¹⁸³ Or, it can also be simply an artifact caused by the insufficient spatial resolution of the current optical setup. The “absolute” value of the order parameter S remains unchecked for their accuracy at this state because it requires comparison with the theoretical study adapted to the nanorod system studied. Based on the calculated order parameter S map, the isotropic phase areas where the calculated value of order

parameter S is between 0 and 0.20 are excluded for further calculation of orientation of nematic director \vec{n} . It is interesting to note that one would get a specific value of director orientation even for areas where S is very low. Still, the resulting value has no physical meaning.

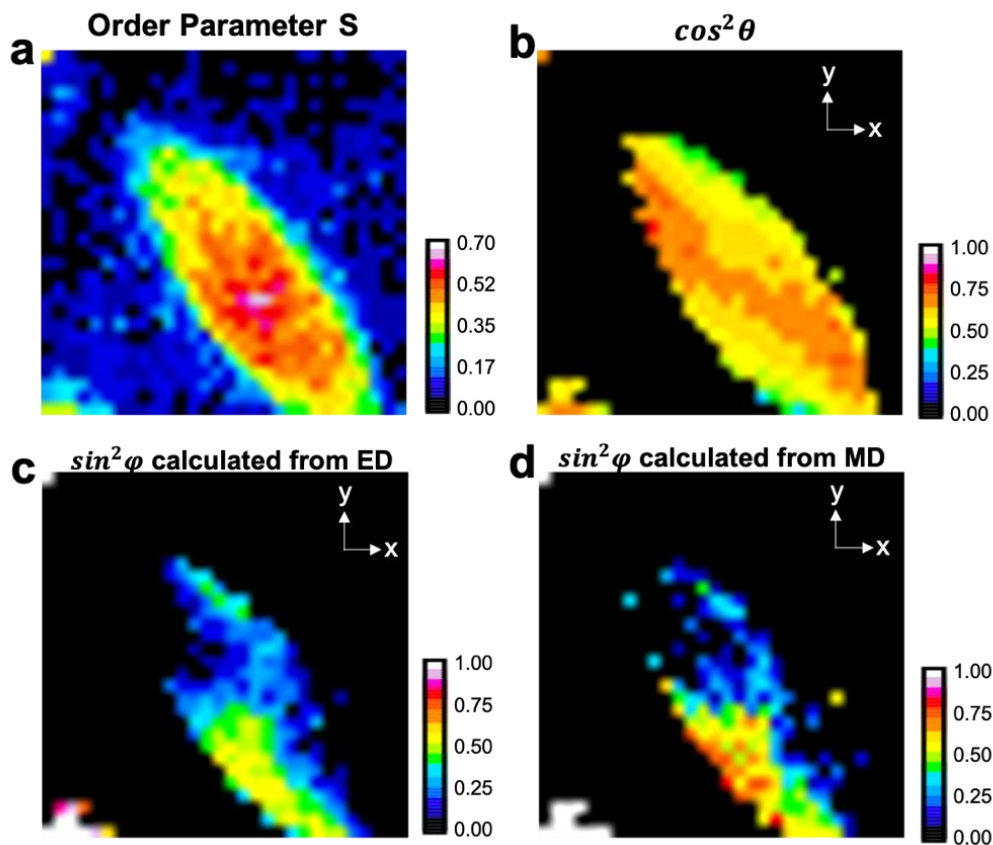


Figure 4.21. Orientation-tomography of the nematic tactoid droplet at one Z height. (a) Calculated order parameter S . Calculated orientation of nematic director \vec{n} : (b) $\cos^2\theta$, (c) $\sin^2\varphi$ from ED emission and (d) $\sin^2\varphi$ from MD emission. pixel size: 1 μm

Then, $\cos^2\theta$ – the polar angle of orientation of nematic director \vec{n} with respect to the y-axis – is calculated using either $k_{zy,MD}$ (MD1/MD2 of I_{zy} , **Figure 4.19b**) based on **Equation 4.15** or $k_{zy,ED}$ (ED1/ED2 of I_{zy} , **Figure 4.19d**) based on **Equation 4.14**. Calculated $\cos^2\theta$ from two images and equations shows the identical result (**Figure 4.21b**). Finally, $\sin^2\varphi$ – the azimuthal angle of orientation of nematic director \vec{n} on the xz-plane – can be calculated from two k-images. $k_{zx,ED}$ (ED1/ED2 of I_{zx}) image shown in **Figure 4.19c** can be used for the calculation based on **Equation 4.16** or $k_{zx,MD}$ (MD1/MD2 of I_{zx}) image shown in **Figure 4.19a** can be used for the calculation based on **Equation 4.17**. Calculated $\sin^2\varphi$ from ED emission ($k_{zx,ED}$) and MD emission ($k_{zx,MD}$) is shown in **Figure 4.21c** and **Figure 4.21d**, respectively. These two images show a similar trend in the resulting values, but the absolute values are not identical for each pixel, indicating that there are error sources in the analysis. Such calculated ($\cos^2\theta$, $\sin^2\varphi$) is then converted into a more intuitive orientation set (θ' , φ'), using

Equation 1.11-12. MATLAB code used for the LC tomography analysis is shown in **Appendix Table 4.1**.

Figure 4.22a and **Figure 4.22c** show the out-of-plane angle θ' of the orientation of the nematic director \vec{n} on xy plane calculated from MD or ED emissions, respectively. The two calculated out-of-plane angle θ' show the tendency where the out-of-plane angle θ' is higher (close to 80°) at the center of the tactoid and lower (close to 60°) at the outer part of the tactoid, meaning that the nanorods at the center of the tactoid are oriented almost parallel to the substrate and progressively more inclined at the outer part of the tactoid. Verification of the absolute value of the resulting values requires comparison with the scanned PL emission image at XZ slice. **Figure 4.22b** and **Figure 4.22d** show the in-plane angle φ' of the orientation of the nematic director \vec{n} calculated from MD or ED emissions, respectively. The two calculated in-plane angle φ' show the symmetrical orientation distribution from the central axis of the nematic tactoid droplet.

Figure 4.23a and **Figure 4.23b** show the visualization of the calculated results (shown in **Figure 4.22**) where the angle of the line is displayed based on the in-plane angle φ' and the length of the line is based on the out-of-plane angle θ' . From this visualized map, it can be understood that the orientation of the nematic director \vec{n} is tangential to the isotropic-nematic interface, which have a good agreement with the typical bi-polar nematic tactoid discussed in **Figure 4.9**. However, it should be noted that the results from MD emissions and ED emissions are similar but not identical in their values, implying that there are error sources. Various error sources in the ratiometric analysis are discussed in **Chapter 1.3.3**. As discussed in **Figure 4.20**, since the DOP of ED1/ED2 is higher than that of MD1/MD2, the calculated result of ED emissions seems to be more correct than the one from MD emissions. It is also interesting to note that some parts where the in-plane angle φ' is expected to close to 0° and 90° have lost their precision of the analysis. The analysis has more errors when the nanorod are oriented parallel or perpendicular to the polarizer or the substrate (*i.e.*, θ' and φ' are 0° or 90°), as discussed in **Chapter 1.3.3**. Further experiments are necessary to ensure the accuracy of the calculated result. Repeating the same analysis at different Z heights of the structure allows the complete tomography of LC structure, which remains as a future study at this state.

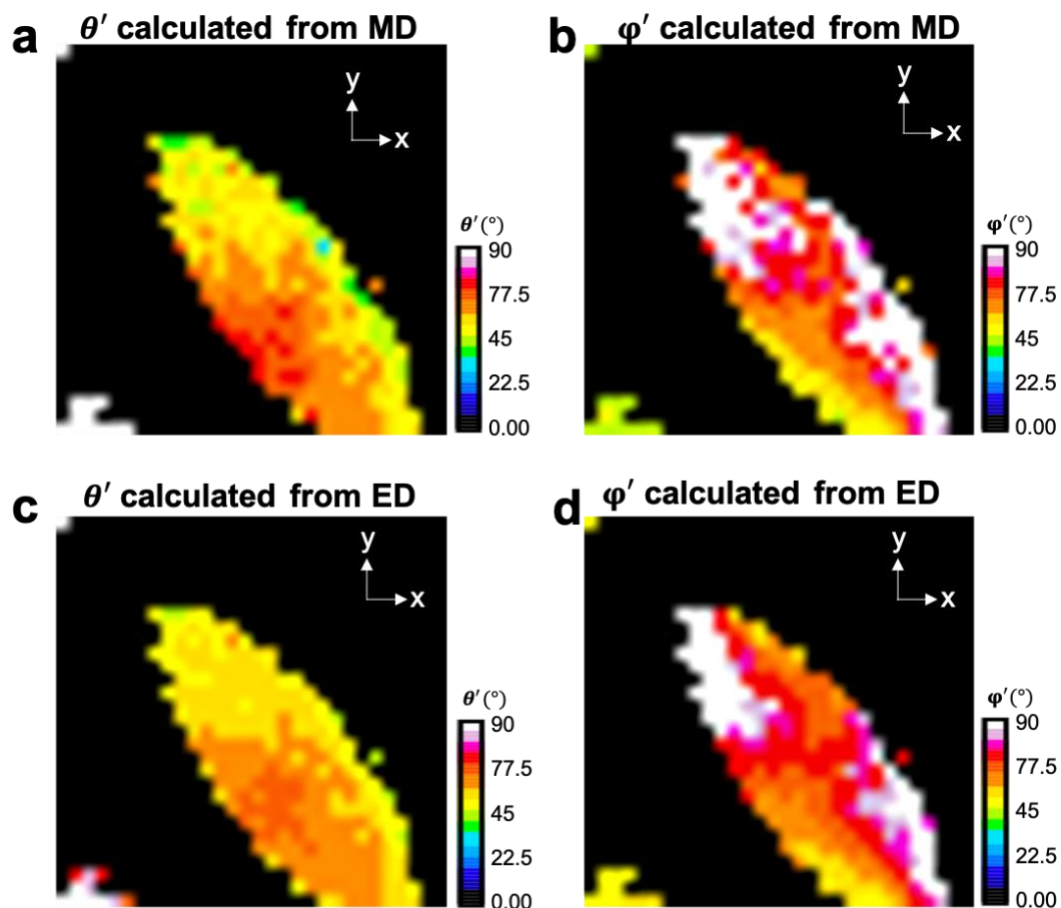


Figure 4.22. Orientation-tomography of nematic tactoid droplet at one Z height. Calculated orientation of nematic director \vec{n} : (a,c) out-of-plane angle θ' , (b,d) in-plane angle φ' . The orientation is calculated either (a-b) from MD emission or (c-d) from ED emission.

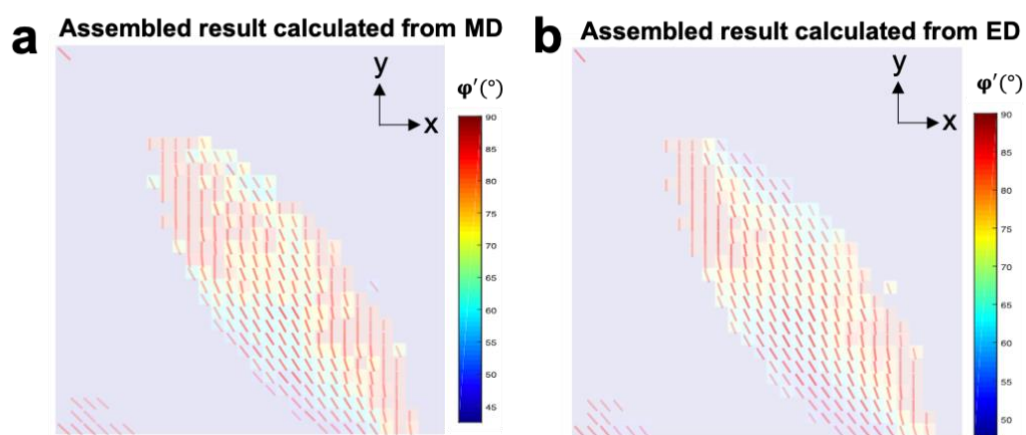


Figure 4.23. Visualized nanorod orientation based on the calculated result shown in **Figure 4.22**. The orientation is calculated either (a) from MD emission or (b) from ED emission.

Flower-shaped nematic LC domain

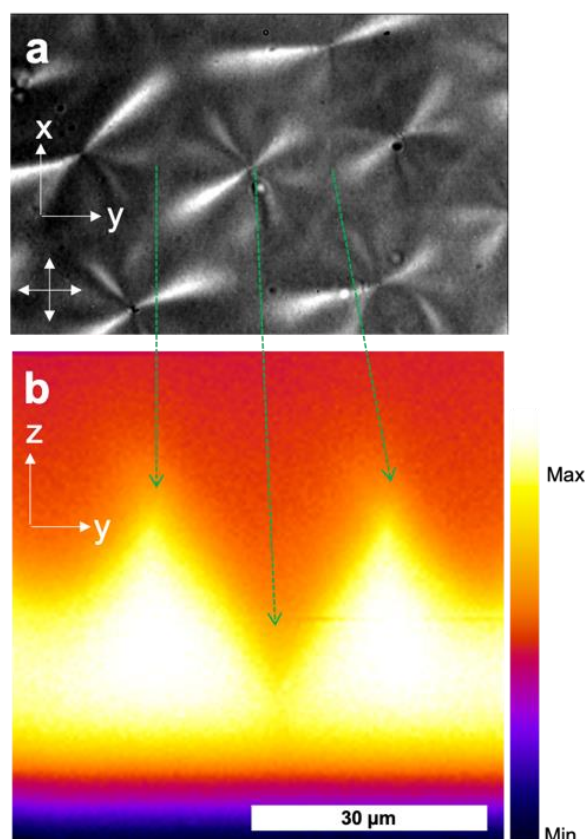


Figure 4.24. (a) Birefringence image of flower-shaped nematic LC domain (xy plane). (b) PL emissions scanned by APD at yz-plane.

The above-described methodology is also applied to the flower-shaped LC domain, the final structure of colloidal LC evolution in the confined geometry. Tomographic mapping of other LC domains (*e.g.*, fingerprint-like LC domain - **Figure 4.10** and intermediate state of LC evolution – **Figure 4.7**) remains as a future work at this state. **Figure 4.24a** shows the birefringence image of the flower-shaped LC domain observed between crossed polarizers. Compared to the nematic tactoid droplet, it is more challenging to define the isotropic and nematic interface from the birefringence image due to their complex structure. We firstly scanned the PL intensity of the LC structure using the APD detector at the YZ slices and found a very interesting vertical arrangement of isotropic and nematic phases and their interface changing its height dramatically inside the confinement gap between the top and bottom substrates. The center and border of the flower-shaped domain correspond to crater and hill, configuring a mountain-like morphology of the interface (**Figure 4.24b**). The most interesting point is that the mountain-like interface has a very sharp pointing edge (singularity). From the birefringence images (**Figure 4.11**), the nanorods at these centers and the border of the flower-shaped domain were estimated to be either isotropic or vertically aligned. Regarding that the dense nematic phase continuously covers the bottom layer inside the cell, it seems that the nanorods in the nematic part are vertically aligned at

these points and lines. When the flower-shaped LC domain is viewed by white light illumination without the crossed polarizers (**Figure 4.25a**), the center of the structure appeared as the brightest point and the border as the darkest point. **Figure 4.25c** shows the PL intensity scanned by the APD detector at different Z heights. The 3D nematic pattern reconstructed by assembling images obtained at different Z height confirmed the mountain-like isotropic-nematic interface, as shown in **Figure 4.25d**.

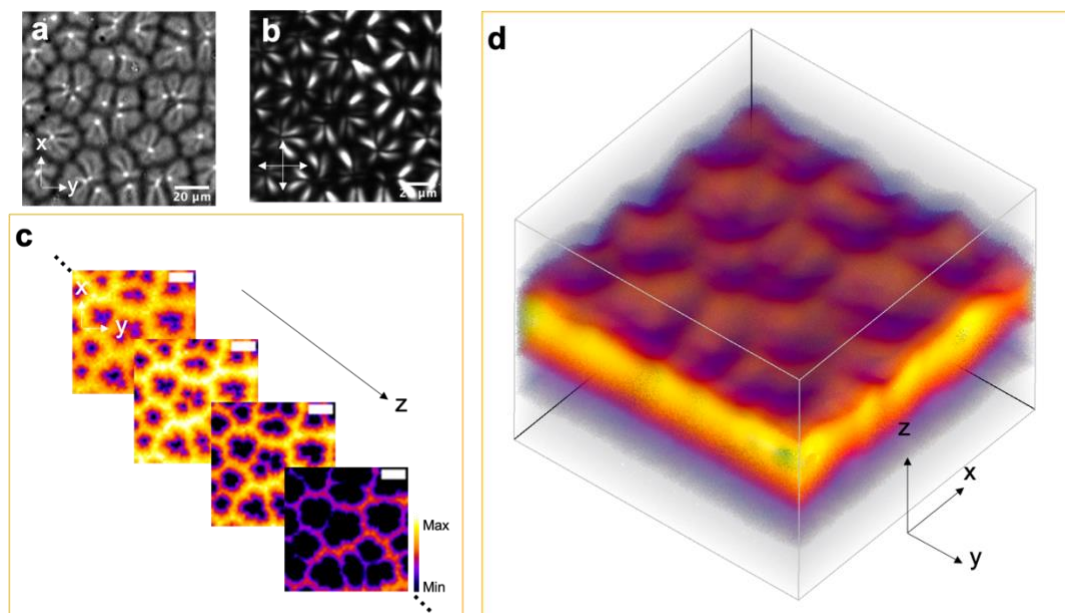


Figure 4.25. CCD captured flower-like nematic LC patterns (**a**) by white-light source illumination and (**b**) between crossed polarizers. (**c**) Scanned PL emission of flower-like nematic LC pattern obtained at different Z height. Scale bar = 20 μm. (**d**) Reconstructed 3D PL emission of flower-like LC nematic pattern based on the images shown in **Figure 4.25c**.

Before applying the proposed tomography method, we investigated the polarization behavior of PL collected from the structure near the bottom and the top substrates (**Figure 4.26b-c**). The spectra collected with a rotating polarizer near the top and bottom substrate showed almost perfectly isotropic polarization showing no spectral line shape changes for different analyzer angles. Although both spectra showed an isotropic behavior, the spectra collected near the top substrate shows a line shape of a mixture of I_{π} and I_{α} , indicating that the nanorods are randomly oriented (isotropic phase). In contrast, the spectra collected near the bottom substrate shows a purely a configuration (I_{α}) where the MD emission exhibits π configuration and the ED emission exhibits σ configuration, indicating that the nanorods are oriented vertically near the bottom substrate.

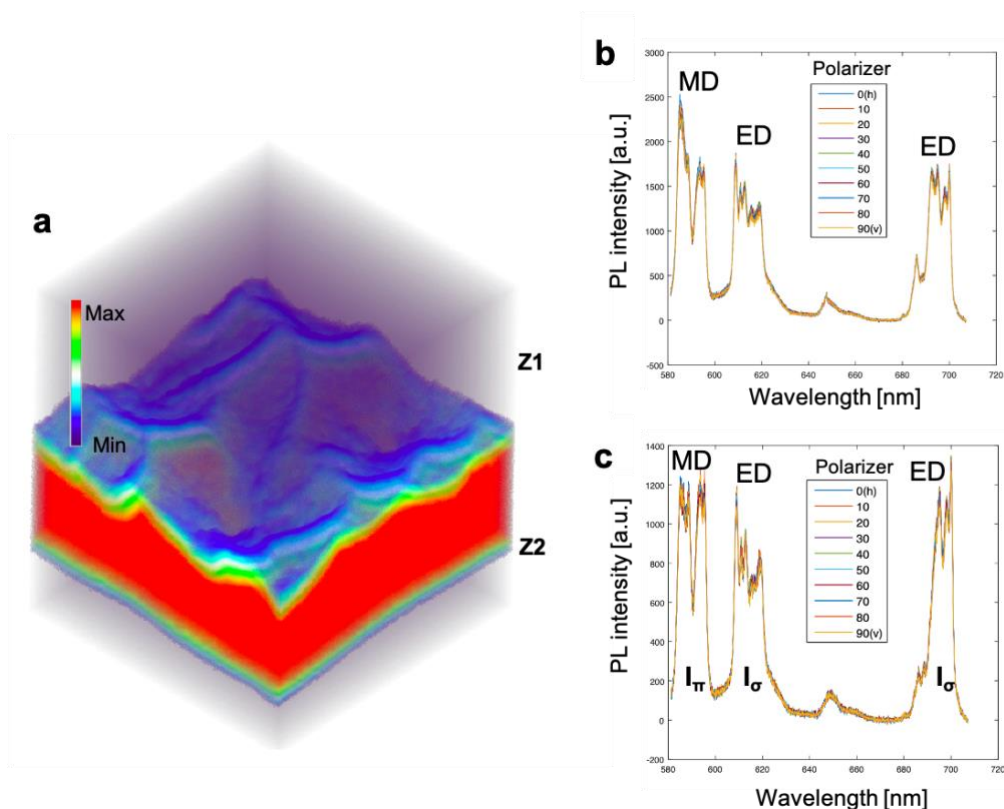


Figure 4.26. (a) Reconstructed 3D structure of PL emission of flower-like nematic LC pattern. (b-c) Polarized spectra obtained at different Z height (Z1 and Z2, indicated in **Figure 4.26a**) with a rotating polarizer.

Based on the above observation, a hypothetical scenario on the LC evolution in confined geometry can be made (**Figure 4.27**). First, small nematic tactoid droplets having a lateral arrangement of nanorods are formed in the isotropic medium (**Figure 4.27a**). The small tactoid droplets merge with adjacent tactoids growing the domain size. Due to the gravity, the nematic tactoid domains slowly settle at the bottom side of the cell gap, and the isotropic phase floats on the top (**Figure 4.27b**). The nematic domains start to fill the bottom surface lining the bottom layer with nanorods parallel to the substrate. The surface state of the ends of the nanorods in the nematic domains is preferentially attracted to the hydrophilic surface of the substrate. Then, the nanorods slowly rotate to align vertically to the substrate to decrease the interfacial surface energy (**Figure 4.27c**). The initially vertically rotated nanorods from randomly distributed anchoring points generating strong distortion stress with the nanorods around with lateral arrangement in the nematic domain (**Figure 4.27c**). With this distortion stress and the rod-end-to-substrate attraction as driving forces, the anchoring points (point defects initially) propagate in lateral and vertical directions, completely deforming the tactoid structure into layered linear defects (**Figure 4.3**). At the top of the new nematic domain interfacing with the isotropic phase, the vertical nanorods rearrange to minimize the interfacial energy, configuring an arrangement similar to the spindle-shaped outer line of the original tactoid droplets (**Figure 4.27d**). As the whole bottom area of the cell is filled

with a continuous nematic phase, it finally stabilizes into chains of a mountain-like isotropic-nematic interface (**Figure 4.24b**), configuring the flower-shaped LC domain in the global view.

Palermo *et al.*, showed that vertical arrangement of LCs building block could be observed with organic LCs where the LC molecules are adsorbed vertically on the substrate.¹⁷³ Their simulation result suggested that isotropic attractive-repulsive surface potential energy between the substrate and the molecules are the key parameters to determine the anchoring of the molecules to the substrate, which seems to be a similar situation in the current case of colloidal LCs composed of the LaPO₄:Eu nanorods on the hydrophilic surface. We attribute the preferential anchoring of the rod-end with the hydrophilic surface to the anisotropic surface chemistry of the basal and prismatic planes of the hexagonal LaPO₄:Eu crystal. For its qualitative analysis, the AFM scanning potential technique would be interesting for mapping the surface potential of the nanorod and the substrate, which may validate the above-proposed hypothetical scenario.

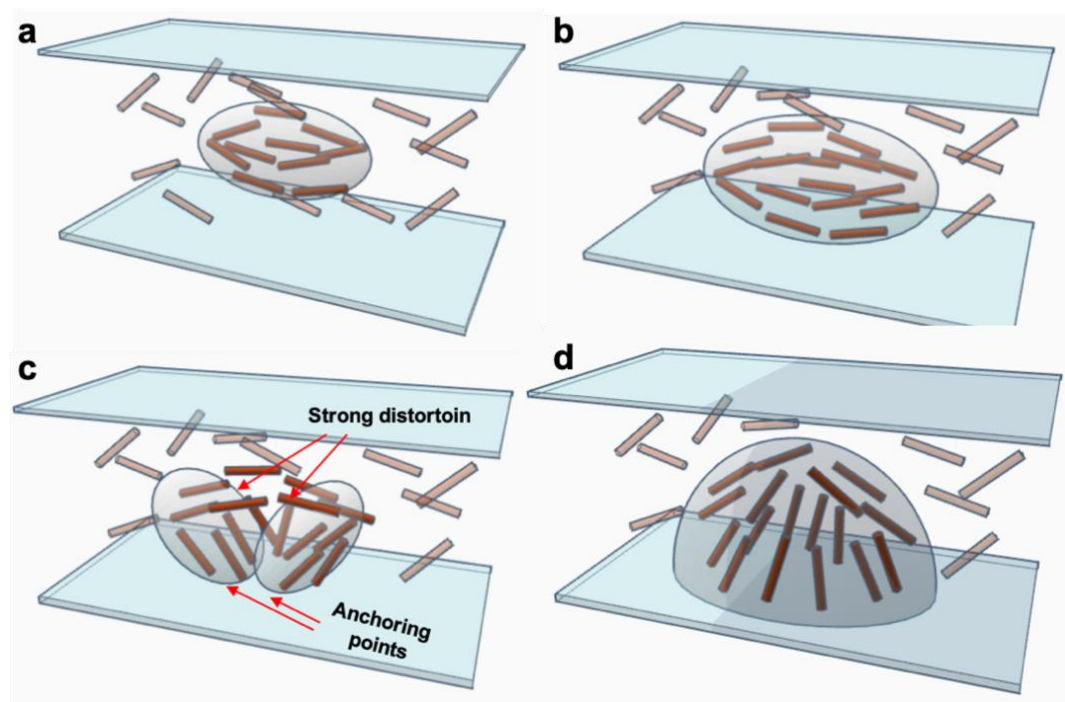


Figure 4.27. Schematic illustration of the estimated mechanism of LC evolution from nematic tactoid droplet to flower-shaped LC domain.

Afterward, we applied the tomography methodology to the flower-like LC pattern, which will allow us to compare the estimated orientation profile of nanorods in the LC domain. **Figure 4.28a** shows a close-up birefringence image of one flower-shaped domain where a tomography was performed. We have chosen a relatively large flower-shaped domain (size $\sim 50 \mu\text{m}$) for better imaging of the local structure inside with the spatial resolution of the optical setup. **Figure 4.28c** shows a map of the calculated order parameter S where the isotropic phase ($S < 0.2$) is shown as dark. The calculated S image shows only

one wing because the height of the other wings is lower than the studied Z height. The calculated order parameter S shows the tendency where the S is higher at the center of the wing (~ 0.6) and gradually decreases towards the outer part of the wing (~ 0.3). This tendency seems similar to the nematic tactoid droplet but should be checked if there were an artifact caused by insufficient spatial resolution. In the 2D projected image (**Figure 4.28d**), the calculated in-plane angle φ' seems to have a tangential orientation distribution on the lateral side of the wing (near the isotropic-nematic interface) (**Figure 4.28d** and **Figure 4.29**).

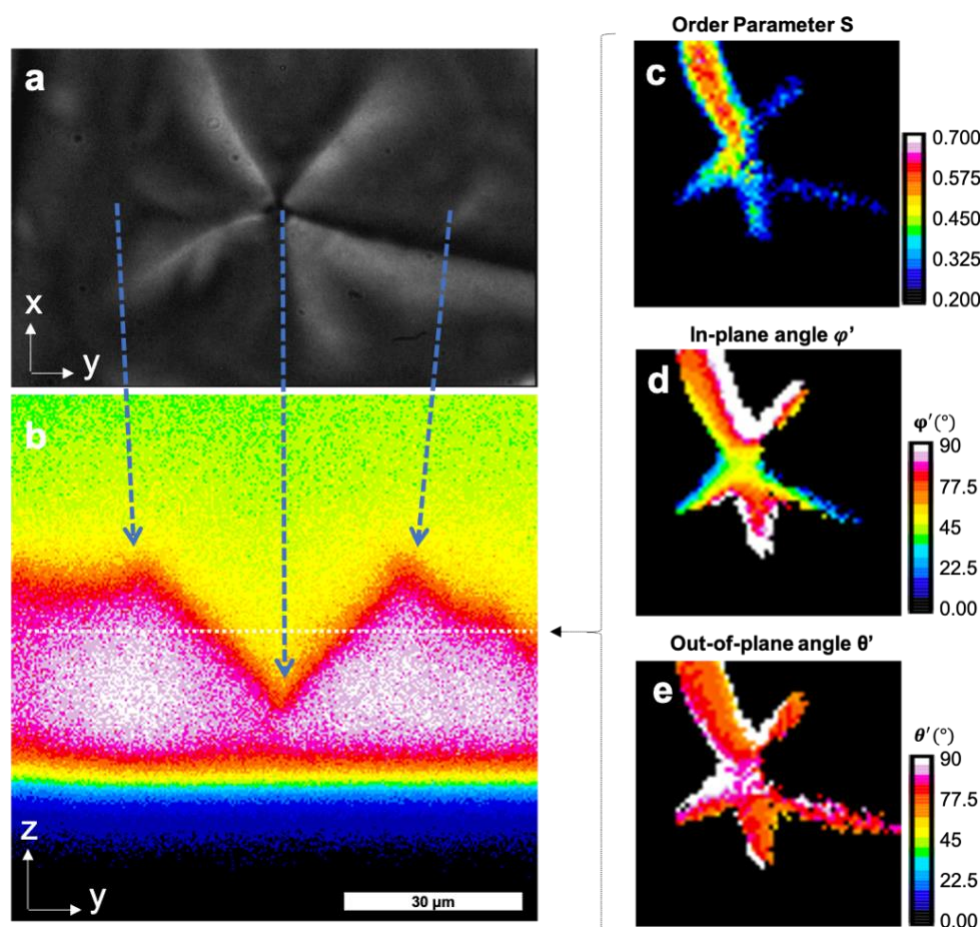


Figure 4.28. (a) Birefringence image of flower-like nematic LC pattern. (b) PL emissions scanned by APD at yz -plane. Orientation-tomography of flower-like nematic LC pattern at one Z plane. (c) order parameter S and the orientation of nematic director \vec{n} : (d) in-plane angle φ' and (e) out-of-plane angle θ' (f) visualized rod based on the calculated result.

According to the orientation map, there exists an abrupt change in the orientation of the nematic director \vec{n} both in the out-of-plane angle θ' (**Figure 4.28e**) and the in-plane angle φ' (**Figure 4.28d**) along the midline of the wing. These midlines of the wings thus seem to be linear defects and the centers of the flower-shaped domains (craters) seem to be point defects, but it is not clear at the current state with limited measurement resolution. The calculated out-of-plane angle θ' at the wing midline was close to 90° , meaning that the nanorods are oriented parallel to the substrate, which is not a good agreement

with the discussion made in **Figure 4.27** and the result from polarization response shown in **Figure 4.26**. Thus, there seem to exist many errors in the current state of the analysis for the case of flower-like nematic LC patterns. Especially, the size of the flower-shaped domain is relatively small and has complex Isotropic-Nematic boundaries in a small volume, which may cause the error due to the insufficient spatial resolution of the current state of our microscopy setup. Also, as the orientation of the nematic director \vec{n} is estimated to have a vertical alignment, the bigger error is estimated due to the intrinsically higher error range for this orientation (**Chapter 1.3.3**). Therefore, further improvement in the spatial resolution by optimizing the optical setting is necessary to increase the accuracy of the analysis of the fine structure of the new LC domains having an abrupt change of the orientation of nanorods. For this case having a complex nanorod orientation, a 3D reconstruction map of multiple scans at different Z heights seems to be mandatory to precisely estimate the nanorod orientation, which remains as a future work at this state.

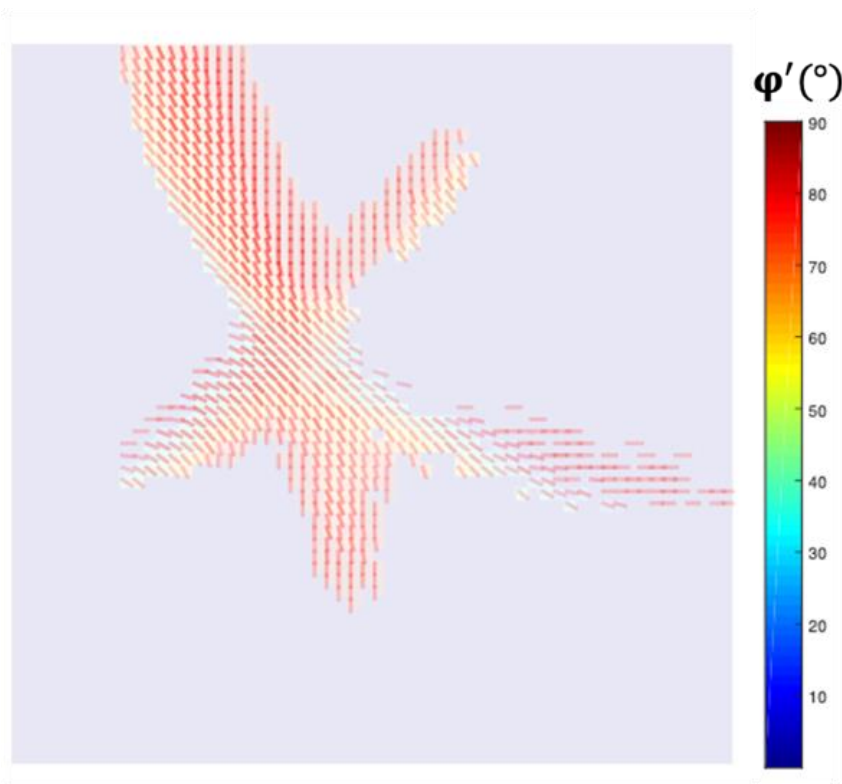


Figure 4.29. Visualized nanorod orientation based on the calculated result shown in **Figure 4.28**.

Summary of Chapter 4.2

A methodology for tomographic mapping of the orientation of the nematic director and the order parameter of the nanorod assembly aligned in 3D space is developed. The method is based on the mutually different polarization nature of multiple emission dipoles of different types of dipoles (MD, ED) inherent in the lanthanide emission, as discussed throughout this thesis study. Fluorescence polarization confocal microscopy is designed and configured to scan a PL signal of an aligned nanorod assembly with good resolution. The previously prepared confinement-induced LC domains are studied as a proof-of-concept to demonstrate the developed methodology. We found that in the case of nematic tactoid droplets, the structural information obtained from the developed spectroscopic tomography has a good agreement with the birefringence study. However, the tomographic performance was insufficient in the case of complex LC structures such as flower-shaped LC domain due to insufficient spatial resolution of the current state of the microscopy system. Investigation of the polarization response of flower-shaped LC domains revealed that the bottom lining of LC domains has vertical adsorption to the substrate. Accordingly, a hypothetical scenario of LC evolution in confined geometry could be proposed and now requires validation by studying the structure using an improved microscopy system.

4.3. Conclusion

In this chapter, we have proposed a methodology allowing the calculation of not a relative but an exact value of order parameter S and the orientation of nematic director $\vec{n}(\theta, \varphi)$ of the three-dimensional liquid crystalline nanorods assembly. The methodology is based on the unique polarization behavior of lanthanide emission dipoles doped in nanorods, a building block of the LC structure. Such methodology is experimentally demonstrated for nematic tactoid droplets by using a newly developed fluorescence confocal polarizing microscope. As the methodology offers the possibility to calculate (S, θ, φ) in three-dimensional space, many interesting target applications can be proposed, such as a twisting helical structure.

We have also shown a rich phenomenology of the liquid crystal (LC) transition of the colloidal LC suspension when confined between two hard walls. Confined LC showed a transition from a typical spindle-shaped tactoid nematic droplet to a complex flower-shaped LC structure whose fate of the final LC structure is controllable by the spacer thickness and surface property of the confined cell. Especially, a flower-shaped LC domain is discovered for the first time and has never been reported elsewhere. This particular LC domain seems to be formed by the vertically adsorbed nanorods to the substrate and by being rearranged to minimize the interfacial energy between the isotropic and nematic domain. We performed a tomographic mapping to this LC domain, which seems however have many error sources in the analysis due to insufficient spatial resolution, which remains as a future work for the further optimization. The improved resolution will provide better angular accuracy at the focal volume where order parameter S and the orientation of the nematic director vary. Improving the resolution is possible using a higher wavelength excitation laser ($\lambda \sim 464$ nm) instead of a UV-laser ($\lambda \sim 394$ nm) as it would have less chromatic aberration with the emission beams ($\lambda = 500\sim 700$ nm). However, if a 464 nm laser is used as an excitation beam, the signal-to-noise ratio of spectra would be lower, degrading the accuracy of the spectroscopic analysis. Therefore, there is a tradeoff and requires optimization through the experiments. It is also important to note that the spatial resolution obtained in the specific experimental condition (*e.g.*, objective numerical aperture, the refractive index of dispersing medium) cannot be considered as a general resolution of the microscopy system. A special effort should be made to find the best-suited microscopy condition for different samples. For a complete tomography of three-dimensional structure with a better resolution, scanning at a smaller step size is also necessary. One may scan the spectrum every 500 nm for the $50\ \mu\text{m} \times 50\ \mu\text{m} \times 50\ \mu\text{m}$ of the structure for each x, y , and z -axis. This means that 2M spectra ($1\text{M} \times 2$ (two polarization)) are needed for studying one LC structure. If it takes 1 second to collect one spectrum, it takes around 12 days. Therefore, it is necessary to find the shortest exposure time to collect one spectrum while maintaining a good signal-to-noise ratio. Although this is not the scope of this manuscript, reducing the electronic delay time required to communicate between the spectrophotometer and the piezo stage for synchronization is also necessary.

It is important to note that a method for discrimination of the mirror angle (θ' , $-\theta'$ and φ' , $-\varphi'$) should be developed for the samples having a varying order parameter S . The method for discriminating mirror angle is discussed based on the established boundary condition for the case of single nanorod in **Figure 1.23**. For the sample having a varying order parameter S , the reference polar diagram should be simulated as a function of order parameter S to define the boundary condition as a function of the order parameter S . We have applied the proposed methodology to the liquid crystalline structures as a proof-of-concept in this study. However, any other type of aligned nanorods assembly can benefit from the discussed method to analyze their orientation of alignment and the degree of alignment.

Conclusion and Prospects

This thesis study presents the original idea of using the photoluminescence of rare-earth ions doped in the crystalline nanorods as an orientation indicating probe. The proposed method employing multiple optical dipoles of different nature - magnetic and electric dipole - inherent in lanthanide ions have allowed to spectroscopically analyze the probe's spatial orientation in three-dimension using a single spectrogram. We have proven the simple yet powerful analytic method by applying the concept to calculate the orientation of NaYF₄:Eu single nanorod, the order parameter of electrically aligned NaYF₄:Eu nanorods assembly, and to perform the tomography of a liquid crystalline structure composed of LaPO₄:Eu nanorods.

We highlight that the analytic methodology described in this thesis study is not limited to the characterization of the demonstrated specific system but should be considered as a new "tool" for understanding the orientation-related dynamics of a various system in different fields (*e.g.*, optical trapping^{25, 73, 184}, microfluidic application⁸⁰, dynamics of bio-molecule^{17, 185}, self-assembly of nanomaterial¹⁸⁶, liquid crystal¹⁸¹). The most significant advantage of the proposed methodology over the other analytic methods is the ability to do the analysis on a single measurement plane and single emission spectrum, which significantly reduces the time required for the experiment and simplifies the optical micro-spectroscopy setup. This advantage must be emphasized because it would allow other researchers or engineers to easily and quickly implement the proposed methodology in their research environment.

We also highlight that any probe material with different dopants, composition, and structure exhibiting simultaneous ED and MD transitions can be used for the proposed methodology, not limited to NaYF₄:Eu and LaPO₄:Eu nanorod used in this thesis study. There are already many materials that could instantly benefit from the proposed method, such as lanthanide up-conversion particle⁷³, organometallic lanthanide chelate, to mention a few. Common non-lanthanide molecular fluorescent dyes cannot use the proposed methodology as they usually exhibit a single emission dipole. However, it would be possible to engineer the molecular structure by combining multiple dyes with distinctly fixed dipole axes to incorporate multiple dipoles in one molecule. Such molecular dyes would allow doing spectroscopic analysis as we proposed in this thesis study.

It is important to note that there exist several intrinsic drawbacks of the proposed methodology to overcome. The first is the low excitation cross-section of the lanthanide-doped crystalline phosphors, which lowers the S/N noise ratio, degrading the precision of analysis. And the second is the generally long fluorescence lifetime of the lanthanide emission, limiting the temporal resolution for the analysis.

Therefore, it is interesting to develop fundamental solutions for increasing the efficiency of luminescence, for example, by co-doping with sensitizing lanthanides or by plasmonic enhancement.¹⁸⁷

Finally, we would like to highlight the fundamental interest in the potential role of charges in apolar media to prepare enriched colloidal LCs stabilized by electrostatic and steric repulsion. Also, regarding the newly observed LC structures such as flower-shaped domains, it should be noted that inorganic colloidal LCs can exhibit both fundamentally and technically interesting novel LC phenomena originating from the combination of surface interaction, particle shape, composition promising for making unprecedented functional optical devices.

* List of publication issued during this thesis work

Journal Articles

J. Kim, R. Chaçon, Z. Wang, E. Larquet, K. Lahlil, A. Leray, G. Colas des Francs, J. Kim, T. Gacoin, “Measuring 3D orientation of nanocrystals via polarized luminescence of rare-earth dopants”, *Nat. Commun.*, 12, 1943 (2021)

J. Kim, K. Lahlil, T. Gacoin, J. Kim, “Measuring the order parameter of vertically aligned nanorods assembly”, *Nanoscale.*, 13, 1630-7637 (2021)

J. Kim, (author list to be completed upon the submission), “Liquid crystalline behavior of charged nanorods in apolar media”, *to be submitted* (2021)

Z. Wang, **J. Kim**, L. Magermans, F. Corbella, I. Florea, E. Larquet, J. Kim, T. Gacoin, “Development of monazite LaPO₄:Eu³⁺ nanorods for high-resolution orientation tracking”, *to be submitted* (2021)

A. Kumar, **J. Kim**, K. Lahlil, G. Julie, S. N. Chormaic, J. -W. Kim, T. Gacoin, J. Fick, “Optical trapping and orientation-resolved spectroscopy of europium-doped nanorods”, *J. Phys. Photonics.*, 2, 025007 (2020)

R. Chaçon, A. Leray, **J. Kim**, S. Mathew, A. Bouhelier, J.-W. Kim, T. Gacoin, G. Colas des Francs, "Measuring the magnetic dipole transition of single nanorods by spectroscopy and Fourier microscopy", *Phys. Rev. Applied.*, 14, 054010 (2020)

Conference (as a presenter)

J. Kim, Z. Wang, E. Larquet, K. Lahlil, J.-W. Kim, T. Gacoin, “Three-dimensional orientation analysis of Eu-doped crystalline single nanorod using purely spectroscopic method”, *MRS spring-fall joint meeting, virtual* (2020) – oral presentation

J. Kim, K. Lahlil, J.-W. Kim, T. Gacoin, “Liquid Crystalline behavior of LaPO₄ Nanorods in Apolar Solvent”, *MRS spring-fall joint meeting, virtual* (2020) – oral presentation

J. Kim, K. Lahlil, J.-W. Kim, T. Gacoin, “Visualizing the orientation of the LaPO₄:Eu nanorods in 3D dimension”, *Journee de l'ED interface, Palaiseau, France* (2018) – poster presentation, awarded as a best poster

Experimental details

Hydrothermal synthesis of NaYF₄:Eu nanorod (Chapter 1-2)

NaYF₄ nanorods with 5% Eu-doping were hydrothermally synthesized following the procedure demonstrated in the reference.⁵⁶⁻⁵⁸ The experimental condition is optimized previously in the group.³ Firstly, 45 mmol (1.8 g) of NaOH dissolved in 6 mL of water were mixed with 15 mL of ethanol (EtOH) and 30 mL of oleic acid (OA) under stirring. To the resulting mixture were selectively added 0.95 mmol (288 mg) of Y(Cl)₃·6H₂O, 0.05 mmol (18 mg) of Eu(Cl)₃·6H₂O and 10.2 mmol (377mg) of NH₄F dissolved in 4 mL of water. The solution was then transferred into an autoclave and heated at 200°C for 24 h under stirring. The resulting nanoparticles were washed with water and ethanol several times, vacuum-dried, and collected as a white powder.

Surface-functionalization of NaYF₄:Eu nanorod (Chapter 1-2)

Surface functionalization by ligand exchange was performed to ensure good dispersion in polar solvents by the process adapted from the reference.¹⁰⁵ The experimental condition is optimized previously in the group.³ 20 mg of NaYF₄:Eu particles with native oleic acid (OA) ligands were mixed with 2 mL of aqueous citrate solution (0.2 M), and the mixture was sonicated and centrifuged. Another 2mL of aqueous citrate solution is used to redisperse pellets. The same cycle was repeated three times to fully exchange OA with citrate. As the step is repeated, nanoparticles are easily dispersed under mild sonication. Finally, the residual OA ligand in the solution was removed by washing with EtOH and water. The resultant citrate-functionalized nanorods were well dispersed in water or ethylene glycol.

Nanoparticle characterizations and optical spectroscopy (Chapter 1-2)

High-resolution transmission electron microscopy (HR-TEM) was performed using JEOL JEM-2010F. Scanning electron microscopy (SEM) was performed using Hitachi S4800. Photoluminescence (PL) spectra of NaYF₄:Eu single nanorods were obtained using an upright polarizing optical microscope (Olympus BX 51WI, objective: magnification = 100x, NA = 0.9). A fiber-coupled monochromatic excitation laser (OXXIUS, $\lambda_{\text{center}} = 394$ nm, FWHM = 0.7 nm) was used as an excitation source matching with the ⁷F₀→⁵L₆ transition of Eu³⁺. PL signals were collected with a fiber-coupled spectrometer (SpectraPro-300i, Princeton Instrument equipped with LN/CCD-1100-PP camera) or with a CCD

camera (Discovery plus DTA DX 1600E SN) PL signals of aligned nanorods under electric field were obtained also using the same optical setup with lower magnification (objective: 20x, NA = 0.45). The series of PL spectra with continuous analyzer angles were collected using an inverted microscope (Nikon Eclipse Ti) and two objectives: A Nikon CFI S Plan Fluor (Magnification = 40x, NA = 0.6) and a Nikon CFI APO TIRF (Magnification = 60x, NA = 1.49). The optical setup is equipped with a polarizer-mounted rotation stage (Newport, PR50CC), a piezoelectric stage (Mad Labs City, Model Nano-LP100), a spectrometer (Andor Shamrock 303i, Andor Newton 920 CCD camera) and a silicon avalanche photodiode (APD, Perkin Elmer, SPCM-AQRH-15). The scanned nanorod image was obtained using the synchronized APD and piezoelectric stage.

Data treatment (Chapter 1-2, 4)

Baselines of all the photoluminescence spectra were taken as a flat line with averaged intensity between 600 nm and 608 nm where Eu^{3+} luminescence is not present (**Figure 1.18c**). Reference spectra used for the orientation calculation are normalized, as shown in **Appendix Figure 1.4**. For the $\text{NaYF}_4:\text{Eu}$ nanorod, spectral fitting analysis was conducted on the wavelength ranges of 587.33 nm ~ 601.65 nm (MD) and 607.05 nm ~ 623.87 nm (ED). Area under curve ratiometry analysis was conducted on the four wavelength ranges of 587.75 nm ~ 592.85 nm (MD1), 592.85 nm ~ 598.5 nm (MD2), 610.00 nm ~ 617.75 nm (ED1), and 617.75 nm ~ 622.50 nm (ED2). For the $\text{LaPO}_4:\text{Eu}$ nanorod, area under curve ratiometry analysis was conducted on the four wavelength ranges of 587.75 nm ~ 592.85 nm (MD1), 592.85 nm ~ 598.5 nm (MD2), 610.00 nm ~ 617.75 nm (ED1), and 617.75 nm ~ 622.50 nm (ED2).

As the wavelength can be slightly shifted depending on the optical system, these wavelength ranges should be adapted for each experiment. The polar diagrams (**Figure 1.22a,b**) were corrected to compensate for the polarization-dependent beam distortion by optical parts. Detailed correction method using unpolarized white light background source is shown in the **Appendix Figure 1.5**. Matlab code used for the single rod orientation analysis is shown in **Appendix Table 1.5**.

Electro-optical switching (Chapter 2)

For measuring the PL spectra in the π , σ , and α configurations, nanorods were aligned using electro-optical (E/O) cells. For the in-plane alignment (π and σ configurations), an in-plane switching cell was made with gold thin-film electrodes deposited with a parallel gap (width ~ 150 μm) and a 60 μm -thick spacer. 20 μL of nanorods dispersion in ethylene glycol was dropped at the center and covered with a glass coverslip. An AC electric field (1 kHz, 0.47 V/ μm) was applied to fully align the nanorods

between the gap. For the homeotropic alignment (α configuration), a commercial homeotropic E/O cell (Instec, Inc.) was also used with an AC electric field (500 kHz, 0.25 V/ μm).

Preparation of LaPO₄:Eu nanorods suspension in ethylene glycol (Chapter 3-4)

Bare LaPO₄ nanorods, with 20% Eu doping, were solvothermal synthesized and dispersed in ethylene glycol by the following method. Aqueous precursor solutions of (NH₄)₂HPO₄ (50 mM), La(NO₃)₃·6H₂O (40 mM), Eu(NO₃)₃·xH₂O (10 mM) were cooled down to 0 °C and mixed, resulting in the precipitation of seed particles. Milky solution of seed particles was then heated in the sealed glass tube at 170 °C for 3 hours. Particles are collected by centrifugation and re-dispersed in acidic water (pH2 adjusted with HNO₃) and dialyzed in the same acidic water for more than two days. The purified aqueous dispersion was then transferred into ethylene glycol (EG) by distillation using a rotary pump.

Surface modification of LaPO₄:Eu nanorods using n-decyl phosphonic acid (n-DPA) (Chapter 3)

In a typical experiment, 10 mL each of LaPO₄:Eu nanorod in EG (0.03 vol%) and n-DPA dissolved in chloroform (quarter equivalent to mole number of the particle) were taken into the vial, and the biphasic mixture was stirred slowly overnight at room temperature. Nanorods relocate from EG to chloroform by the alkyl chain of n-DPA molecule on the particle surface. Functionalized nanorods in chloroform were then afterward collected by centrifugation and washed with chloroform two times. Washed nanorods are re-dispersed in chloroform with controlled excess of n-DPA ligand molecules. Suspension with higher nanorod concentration was prepared by using a bigger solvent volume (100 mL for EG and chloroform), keeping a same nanorod and n-DPA ligand concentration. Surface functionalization for bigger solvent volume takes a longer time (~3 days) than a typical experiment.

Nanoparticle Characterizations (Chapter 3)

The hydrodynamic size of nanorods is measured by dynamic light scattering (DLS). Photoluminescence of LaPO₄:Eu was measured under the excitation by a monochromatic laser (OXXIUS, $\lambda = \sim 394$ nm, FWHM = ~ 0.7 nm). SEM sample is prepared by spin-coating bare LaPO₄:Eu nanorods dispersion in EG onto the UV-ozone treated glass substrate. For the spin-coating of functionalized LaPO₄:Eu@n-DPA apolar suspension, the glass substrate is pre-treated by dipping and sonicating the substrate in chloroform to enhance hydrophobic wetting, minimizing aggregation mediated by solvent evaporation. Fourier transform infrared spectroscopy (FTIR) is performed by transmission mode. Around two μL of

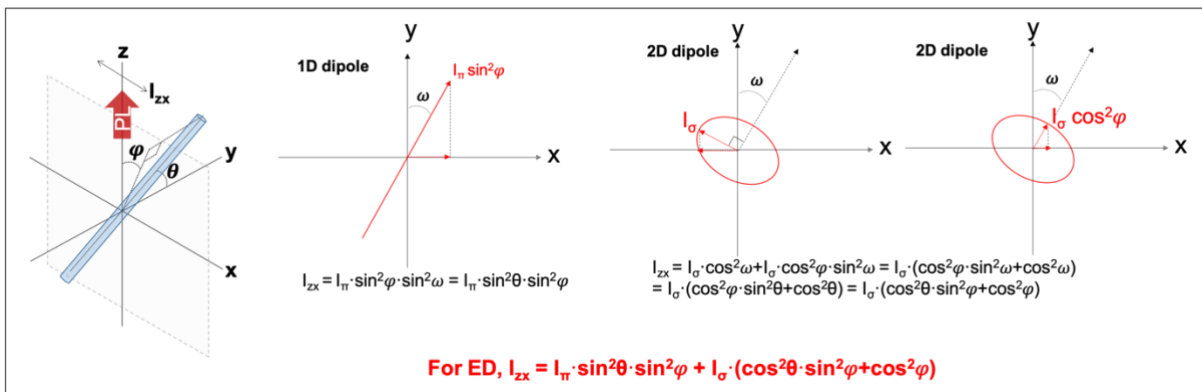
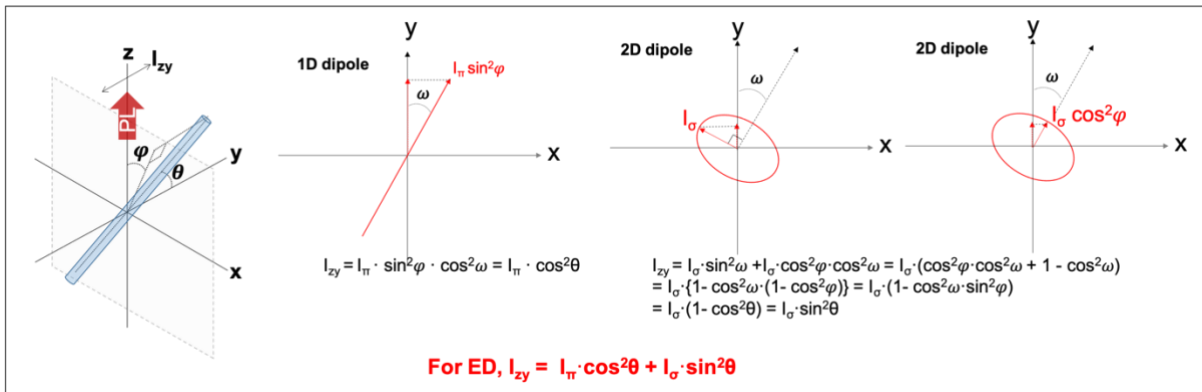
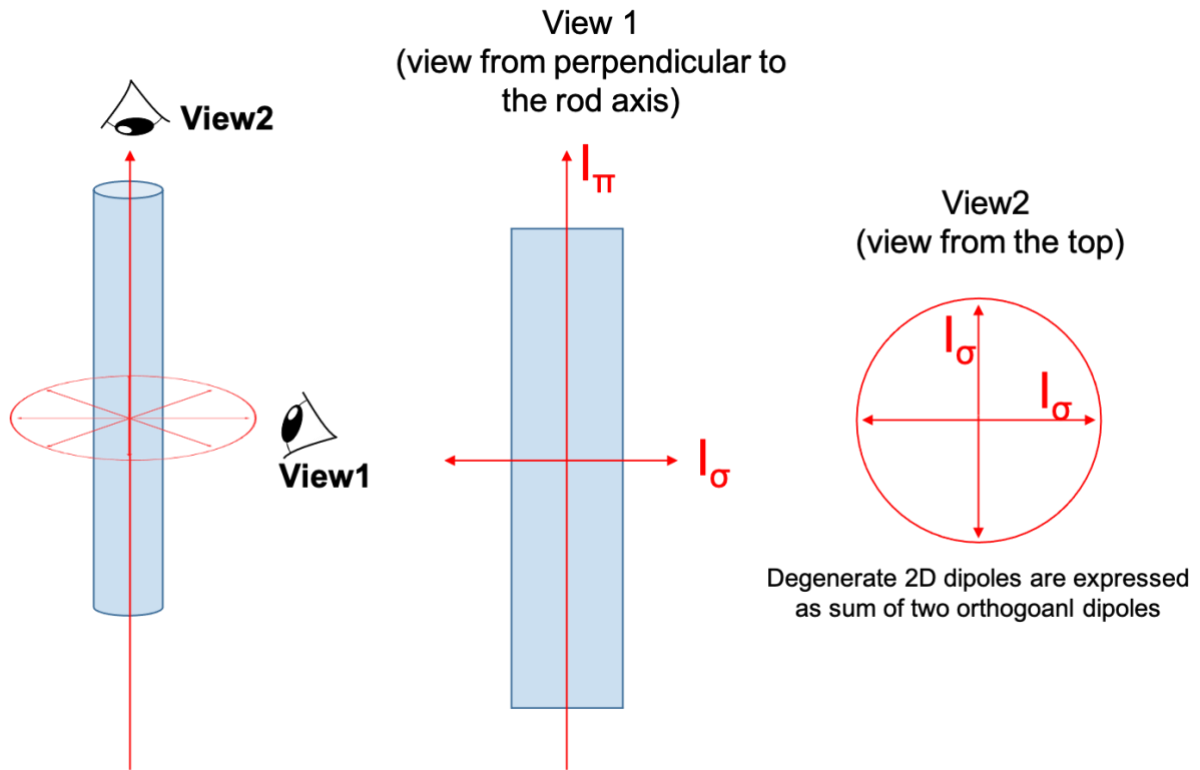
LaPO₄:Eu@n-DPA LC suspension is inserted into electro-optical cell of 6.8 μm thickness by capillary force and observed between crossed polarizers using Olympus BX51 microscope combined with a CCD camera (Discovery plus DTA DX 1600E SN). LaPO₄:Eu@n-DPA LC suspension is inserted into 100 μm flat optical capillary by mild centrifugation.

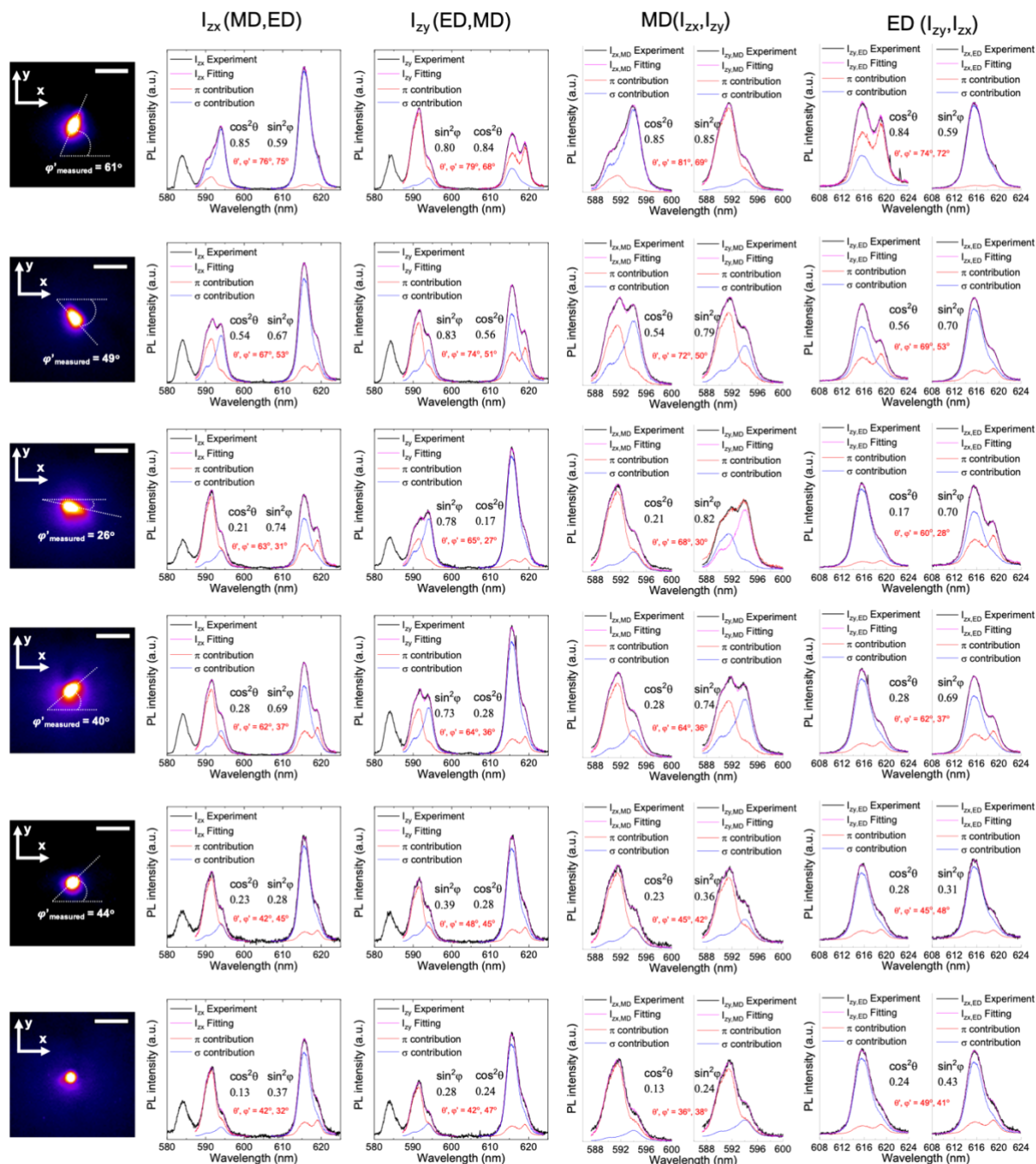
Appendix

Appendix Table 1.1. Comparison of pre-existing orientation analysis method with the proposed method.

Technique	Fluorescence polarization microscopy using multiple dipoles (this work) ^{25, 26, 80}	Fluorescence polarization microscopy using a single dipole ^{11-20, 30, 32-35}	Back-focal plane imaging / defocusing imaging ^{42-46, 188, 189}	Non-linear microscopy ^{21-24, 190}	Plasmonic imaging ¹⁹¹⁻¹⁹⁹
Probe Material	Rare-earth-doped nanocrystal	Molecular phosphor / Quantum rod	Molecular phosphor / Quantum rod	Molecular or nanocrystal host of non-linear luminescence: two-photon fluorescence (TPF), second harmonic generation (SHG), etc.	Plasmonic nanoparticle
Analysis	Simultaneous consideration of polarization behaviors of multiple emission dipoles	Polarization behavior of a single emission dipole	Intensity distribution of emission dipole + Image analysis	Polarization behaviors of multiple non-linear processes	Polarization behavior of plasmonic light interaction
Pros	<ul style="list-style-type: none"> - Possible to measure 3D orientation angles with a single acquisition - One measurement plane - Robust to probe polydispersity and global intensity fluctuation (ratiometric analysis) - No photobleaching or blinking - Wide range of phosphors can be used 	<ul style="list-style-type: none"> - Fast dynamics with molecular phosphors - Wide range of phosphors can be used 	<ul style="list-style-type: none"> - Possible to measure 3D orientation angles with a single acquisition - One measurement plane - Fast dynamics with molecular phosphors - Wide range of phosphors can be used 	<ul style="list-style-type: none"> - Possible to measure 3D orientation angles with a single acquisition - One measurement plane. - Probe-free measurement possible 	<ul style="list-style-type: none"> - One measurement plane - Fast optical process - No photobleaching or blinking
Cons	<ul style="list-style-type: none"> - Relatively low temporal resolution due to low excitation cross-section and long decay time of lanthanide emission 	<ul style="list-style-type: none"> - Complicated optical setup for multiple excitation angles and measurement planes - Requires full scanning of polarization angles to measure 3D orientation angles - Sensitive to photobleaching, blinking - Sensitive to probe polydispersity 	<ul style="list-style-type: none"> - Requires model-dependent image analysis - Sensitive to photobleaching, blinking, or scattering - Very sensitive to focusing 	<ul style="list-style-type: none"> - Sensitive to external environment (optical index, temperature, etc) - Complicated optical setup for non-linear microscopy - Very sensitive to excitation condition 	<ul style="list-style-type: none"> - Requires model-dependent image analysis for 3D orientation - Very sensitive to polydispersity - Sensitive to other sources of absorption and scattering

Appendix Note 1.1. Deriving Equation 1.4 and Equation 1.6 (in the case of electric dipole)





Appendix Figure 1.1. Spectral fitting orientation analysis of 6 different NaYF₄:Eu nanorods randomly oriented in polymer film. First column displays a photograph of the photoluminescence (PL) of a single nanorod captured by the CCD camera (scale bar: 2 μ m). Spectral fitting analysis using a polarized PL spectrum of I_{zx} (second column), I_{zy} (third column) where both MD and ED emissions are used for the orientation analysis. Spectral fitting analysis using a single dipole emission of MD (fourth column) and ED (fifth column) where two orthogonal polarizations (I_{zx}, I_{zy}) are used for the orientation analysis. The calculated values of the trigonometric functions of (θ, φ) and the absolute values of (θ', φ') are presented in the figure.

Appendix Table 1.2-4 presents full dataset of analyzed orientation of randomly selected NaYF₄:Eu nanorods. All the calculated/measured values are rounded up. “N/A” indicates nanorods that in-plane angle ϕ' was not obvious to measure from CCD captured image due to very low ellipticity (oriented close to vertical to the substrate or smaller in size than the resolution of CCD camera). “Error” indicates nanorods that calculated $\cos^2\theta$ or/and $\sin^2\phi$ is out of sinusoidal function range (0-1), thus conversion to (θ', ϕ') could not be made. The origin of the error is discussed in the main text. **Appendix Table 1.4** shows the statistics of analyzed orientation pre presented in **Appendix Table 1.2-3**. Nanorods shown as “N/A” or “Error” is not included in error calculation.

Appendix Table 1.2. Calculated values of the trigonometric functions of (θ, ϕ) and the absolute values of (θ', ϕ') of NaYF₄:Eu nanorods randomly oriented 3D in polymer film. Orientation is analyzed using spectral fitting analysis and area under curve ratiometry (AUCR). Calculated in-plane angle ϕ' is compared with measured ϕ' on the elliptical shape of CCD captured nanorod image (data not shown). Out-of-plane angle (θ') remains incomparable. Results shown here is denoted as “3D sample” in **Appendix Table 1.4**.

Rod number	Method	Polarization	Dipole	$\cos^2\theta_{cal}$	$\sin^2\phi_{cal}$	$\theta'_{cal}(^\circ)$	$\phi'_{cal}(^\circ)$	$\phi'_{measured}(^\circ)$	Error on ϕ' ($^\circ$)
1	Spectral Fitting	Izx	MD,ED	0.48	0.64	64	50	48	2
		Izy	MD,ED	0.50	0.87	75	47		1
		Izx,Izy	MD	0.48	0.71	69	52		4
		Izx,Izy	ED	0.50	0.68	66	51		3
	AUCR	Izx	MD,ED	0.48	0.64	64	50		2
		Izy	MD,ED	0.53	0.92	79	48		0
		Izx,Izy	MD	0.48	0.84	73	46		2
		Izx,Izy	ED	0.53	0.70	68	52		4
2	Spectral Fitting	Izx	MD,ED	0.54	0.55	63	56	52	4
		Izy	MD,ED	0.53	0.70	68	52		0
		Izx,Izy	MD	0.54	0.71	69	52		0
		Izx,Izy	ED	0.53	0.53	62	56		4
	AUCR	Izx	MD,ED	0.54	0.51	62	57		5
		Izy	MD,ED	0.53	0.71	68	51		1
		Izx,Izy	MD	0.54	0.73	70	52		0
		Izx,Izy	ED	0.53	0.49	61	56		4
3	Spectral Fitting	Izx	MD,ED	0.77	0.75	76	65	N/A	
		Izy	MD,ED	0.67	0.67	71	60		
		Izx,Izy	MD	0.77	0.96	84	61		
		Izx,Izy	ED	0.67	0.52	66	63		
	AUCR	Izx	MD,ED	0.77	0.67	74	66		
		Izy	MD,ED	0.64	0.64	69	59		
		Izx,Izy	MD	0.77	0.99	87	61		
		Izx,Izy	ED	0.64	0.43	63	64		
4	Spectral Fitting	Izx	MD,ED	0.37	0.18	44	61	57	4
		Izy	MD,ED	0.32	0.14	40	61		4
		Izx,Izy	MD	0.37	0.15	43	63		6
		Izx,Izy	ED	0.32	0.17	41	59		2
	AUCR	Izx	MD,ED	0.37	0.16	43	63		6
		Izy	MD,ED	0.30	0.15	39	59		2
		Izx,Izy	MD	0.37	0.17	44	62		5
		Izx,Izy	ED	0.30	0.14	39	60		3
5	Spectral Fitting	Izx	MD,ED	0.58	0.34	58	63	57	6
		Izy	MD,ED	0.45	0.43	56	54		3
		Izx,Izy	MD	0.58	0.56	65	57		0
		Izx,Izy	ED	0.45	0.26	50	60		3
	AUCR	Izx	MD,ED	0.57	0.26	56	66		9
		Izy	MD,ED	0.39	0.40	53	52		5
		Izx,Izy	MD	0.57	0.57	65	57		0

6	Spectral Fitting	Izx,Izy	ED	0.39	0.18	45	62	34	5
		Izx	MD,ED	0.31	0.72	64	38		4
		Izy	MD,ED	0.30	0.63	59	39		5
		Izx,Izy	MD	0.31	0.64	60	40		6
	AUCR	Izx,Izy	ED	0.30	0.71	63	38		4
		Izx	MD,ED	0.31	0.69	62	39		5
		Izy	MD,ED	0.19	0.55	53	33		1
		Izx,Izy	MD	0.31	0.65	60	40		6
7	Spectral Fitting	Izx,Izy	ED	0.19	0.59	55	32	38	2
		Izx	MD,ED	0.34	0.80	69	39		1
		Izy	MD,ED	0.31	0.86	72	36		2
		Izx,Izy	MD	0.34	0.89	75	37		1
	AUCR	Izx,Izy	ED	0.31	0.77	67	37		1
		Izx	MD,ED	0.34	0.79	68	39		1
		Izy	MD,ED	0.30	0.85	71	35		3
		Izx,Izy	MD	0.34	0.90	75	37		1
8	Spectral Fitting	Izx,Izy	ED	0.30	0.74	65	37	47	1
		Izx	MD,ED	0.16	0.22	36	43		4
		Izy	MD,ED	0.20	0.18	36	49		2
		Izx,Izy	MD	0.16	0.17	34	47		0
	AUCR	Izx,Izy	ED	0.20	0.23	38	46		1
		Izx	MD,ED	0.17	0.21	36	44		3
		Izy	MD,ED	0.20	0.18	36	49		2
		Izx,Izy	MD	0.17	0.18	34	47		0
9	Spectral Fitting	Izx,Izy	ED	0.20	0.22	38	47	N/A	0
		Izx	MD,ED	0.08	0.69	58	20		
		Izy	MD,ED	0.06	0.74	60	16		
		Izx,Izy	MD	0.08	0.76	62	19		
	AUCR	Izx,Izy	ED	0.06	0.68	57	17		
		Izx	MD,ED	0.10	0.70	59	21		
		Izy	MD,ED	0.05	0.73	60	15		
		Izx,Izy	MD	0.10	0.77	63	20		
10	Spectral Fitting	Izx,Izy	ED	0.05	0.66	56	16	39	0
		Izx	MD,ED	0.30	0.53	55	42		3
		Izy	MD,ED	0.31	0.60	58	41		2
		Izx,Izy	MD	0.30	0.59	58	40		1
	AUCR	Izx,Izy	ED	0.31	0.54	56	42		3
		Izx	MD,ED	0.31	0.53	55	43		4
		Izy	MD,ED	0.29	0.61	58	40		1
		Izx,Izy	MD	0.31	0.62	60	41		2
11	Spectral Fitting	Izx,Izy	ED	0.29	0.51	54	42	N/A	3
		Izx	MD,ED	0.36	0.11	41	66		
		Izy	MD,ED	0.36	0.18	43	60		
		Izx,Izy	MD	0.36	0.18	43	60		
	AUCR	Izx,Izy	ED	0.36	0.11	41	66		
		Izx	MD,ED	0.36	0.11	41	66		
		Izy	MD,ED	0.37	0.19	44	60		
		Izx,Izy	MD	0.36	0.19	44	60		
12	Spectral Fitting	Izx,Izy	ED	0.37	0.11	41	67	44	0
		Izx	MD,ED	0.23	0.28	42	45		1
		Izy	MD,ED	0.28	0.39	48	45		1
		Izx,Izy	MD	0.23	0.36	45	42		2
	AUCR	Izx,Izy	ED	0.28	0.31	45	48		4
		Izx	MD,ED	0.24	0.29	43	46		2
		Izy	MD,ED	0.29	0.39	49	45		1
		Izx,Izy	MD	0.24	0.37	46	43		1
13	Spectral Fitting	Izx,Izy	ED	0.29	0.31	46	49	44	5
		Izx	MD,ED	0.45	0.47	57	53		9
		Izy	MD,ED	0.40	0.60	61	47		3
		Izx,Izy	MD	0.45	0.65	64	48		4
	AUCR	Izx,Izy	ED	0.40	0.43	54	51		7
		Izx	MD,ED	0.46	0.46	57	54		10
		Izy	MD,ED	0.40	0.60	61	46		2
		Izx,Izy	MD	0.46	0.67	65	48		4
14	Spectral Fitting	Izx,Izy	ED	0.40	0.41	53	52	42	8
		Izx	MD,ED	0.48	0.79	71	47		5
		Izy	MD,ED	0.48	0.93	79	45		3
		Izx,Izy	MD	0.48	0.94	80	45		3
	AUCR	Izx,Izy	ED	0.48	0.79	70	47		5
		Izx	MD,ED	0.49	0.77	70	48		6
		Izy	MD,ED	0.48	0.94	80	45		3

		Izx,Izy	MD	0.49	0.96	82	45		3
		Izx,Izy	ED	0.48	0.76	69	48		6
15	Spectral Fitting	Izx	MD,ED	0.28	0.69	62	37	40	3
		Izy	MD,ED	0.28	0.73	64	36		4
		Izx,Izy	MD	0.28	0.74	64	36		4
		Izx,Izy	ED	0.28	0.69	62	37		3
	AUCR	Izx	MD,ED	0.30	0.70	63	38		2
		Izy	MD,ED	0.27	0.73	64	36		4
		Izx,Izy	MD	0.30	0.75	65	37		3
		Izx,Izy	ED	0.27	0.68	61	37		3
16	Spectral Fitting	Izx	MD,ED	0.85	0.59	76	72	61	11
		Izy	MD,ED	0.84	0.80	79	68		7
		Izx,Izy	MD	0.85	0.85	81	69		8
		Izx,Izy	ED	0.84	0.56	74	72		11
	AUCR	Izx	MD,ED	0.85	0.53	75	73		12
		Izy	MD,ED	0.84	0.88	82	68		7
		Izx,Izy	MD	0.85	0.93	84	68		7
		Izx,Izy	ED	0.84	0.50	74	73		12
17	Spectral Fitting	Izx	MD,ED	0.71	Error			N/A	Error
		Izy	MD,ED	0.65	0.21	58	71		N/A
		Izx,Izy	MD	0.71	0.26	62	72		Error
		Izx,Izy	ED	0.65	Error				Error
	AUCR	Izx	MD,ED	0.71	Error				N/A
		Izy	MD,ED	0.66	0.27	60	70		N/A
		Izx,Izy	MD	0.71	0.32	64	70		Error
		Izx,Izy	ED	0.66	Error				Error
18	Spectral Fitting	Izx	MD,ED	0.54	0.67	67	53	49	4
		Izy	MD,ED	0.56	0.83	74	51		2
		Izx,Izy	MD	0.54	0.79	72	50		1
		Izx,Izy	ED	0.56	0.70	68	53		4
	AUCR	Izx	MD,ED	0.54	0.67	67	53		4
		Izy	MD,ED	0.56	0.85	75	51		1
		Izx,Izy	MD	0.54	0.82	73	50		1
		Izx,Izy	ED	0.56	0.69	68	54		5
19	Spectral Fitting	Izx	MD,ED	0.34	0.50	55	45	41	4
		Izy	MD,ED	0.37	0.68	63	43		2
		Izx,Izy	MD	0.34	0.66	62	42		1
		Izx,Izy	ED	0.37	0.53	57	47		6
	AUCR	Izx	MD,ED	0.36	0.52	56	46		5
		Izy	MD,ED	0.37	0.70	64	42		1
		Izx,Izy	MD	0.36	0.69	64	42		1
		Izx,Izy	ED	0.37	0.53	57	46		5
20	Spectral Fitting	Izx	MD,ED	0.13	0.37	42	32	N/A	
		Izy	MD,ED	0.24	0.28	42	47		
		Izx,Izy	MD	0.13	0.24	36	38		
		Izx,Izy	ED	0.24	0.43	49	41		
	AUCR	Izx	MD,ED	0.14	0.42	45	32		
		Izy	MD,ED	0.28	0.30	45	49		
		Izx,Izy	MD	0.14	0.25	37	39		
		Izx,Izy	ED	0.28	0.50	53	42		
21	Spectral Fitting	Izx	MD,ED	0.33	0.45	53	46	N/A	
		Izy	MD,ED	0.34	0.48	54	46		
		Izx,Izy	MD	0.33	0.47	54	45		
		Izx,Izy	ED	0.34	0.46	53	47		
	AUCR	Izx	MD,ED	0.34	0.49	55	46		
		Izy	MD,ED	0.36	0.52	56	46		
		Izx,Izy	MD	0.34	0.50	55	45		
		Izx,Izy	ED	0.36	0.51	56	47		
22	Spectral Fitting	Izx	MD,ED	0.43	0.28	50	58	N/A	
		Izy	MD,ED	0.45	0.22	49	63		
		Izx,Izy	MD	0.43	0.21	48	62		
		Izx,Izy	ED	0.45	0.30	52	59		
	AUCR	Izx	MD,ED	0.44	0.30	51	58		
		Izy	MD,ED	0.47	0.25	51	62		
		Izx,Izy	MD	0.44	0.24	49	61		
		Izx,Izy	ED	0.47	0.32	53	59		
23	Spectral Fitting	Izx	MD,ED	0.21	0.74	63	31	26	5
		Izy	MD,ED	0.17	0.78	65	27		1
		Izx,Izy	MD	0.21	0.82	68	30		4
		Izx,Izy	ED	0.17	0.70	60	28		2
	AUCR	Izx	MD,ED	0.23	0.74	63	32		6

		Izy	MD,ED	0.17	0.78	65	27		1
		Izx,Izy	MD	0.23	0.84	69	31		5
		Izx,Izy	ED	0.17	0.69	59	28		2
24	Spectral Fitting	Izx	MD,ED	0.28	0.48	52	42	19	23
		Izy	MD,ED	0.27	0.55	55	39		20
		Izx,Izy	MD	0.28	0.56	56	40		21
		Izx,Izy	ED	0.27	0.47	51	41		22
	AUCR	Izx	MD,ED	0.29	0.47	52	43		24
		Izy	MD,ED	0.26	0.53	54	39		20
		Izx,Izy	MD	0.29	0.56	56	41		22
		Izx,Izy	ED	0.26	0.45	50	42		23
25	Spectral Fitting	Izx	MD,ED	0.29	0.72	64	37	43	6
		Izy	MD,ED	0.23	0.76	64	32		11
		Izx,Izy	MD	0.29	0.83	70	35		8
		Izx,Izy	ED	0.23	0.66	59	34		9
	AUCR	Izx	MD,ED	0.31	0.74	65	38		5
		Izy	MD,ED	0.22	0.76	64	31		12
		Izx,Izy	MD	0.31	0.86	72	36		7
		Izx,Izy	ED	0.22	0.65	59	34		9
26	Spectral Fitting	Izx	MD,ED	0.33	0.76	66	39	41	2
		Izy	MD,ED	0.26	0.80	67	33		8
		Izx,Izy	MD	0.33	0.88	73	37		4
		Izx,Izy	ED	0.26	0.69	61	35		6
	AUCR	Izx	MD,ED	0.34	0.74	66	40		1
		Izy	MD,ED	0.24	0.77	65	33		8
		Izx,Izy	MD	0.34	0.89	74	38		3
		Izx,Izy	ED	0.24	0.64	59	35		6
27	Spectral Fitting	Izx	MD,ED	0.47	0.22	50	63	N/A	
		Izy	MD,ED	0.50	0.11	48	72		
		Izx,Izy	MD	0.47	0.10	46	71		
		Izx,Izy	ED	0.50	0.23	52	64		
	AUCR	Izx	MD,ED	0.47	0.14	47	68		
		Izy	MD,ED	0.48	0.12	48	70		
		Izx,Izy	MD	0.47	0.12	47	70		
		Izx,Izy	ED	0.48	0.14	48	68		
28	Spectral Fitting	Izx	MD,ED	0.48	0.33	54	59	54	5
		Izy	MD,ED	0.40	0.41	54	52		2
		Izx,Izy	MD	0.48	0.47	58	54		0
		Izx,Izy	ED	0.40	0.29	49	57		3
	AUCR	Izx	MD,ED	0.48	0.27	52	61		8
		Izy	MD,ED	0.39	0.42	53	51		2
		Izx,Izy	MD	0.48	0.49	59	54		0
		Izx,Izy	ED	0.39	0.23	47	59		5
29	Spectral Fitting	Izx	MD,ED	0.30	0.35	48	48	N/A	
		Izy	MD,ED	0.33	0.37	49	49		
		Izx,Izy	MD	0.30	0.35	48	48		
		Izx,Izy	ED	0.33	0.37	50	49		
	AUCR	Izx	MD,ED	0.30	0.34	47	49		
		Izy	MD,ED	0.33	0.37	49	49		
		Izx,Izy	MD	0.30	0.36	48	48		
		Izx,Izy	ED	0.33	0.35	49	50		
30	Spectral Fitting	Izx	MD,ED	0.58	0.26	56	67	N/A	
		Izy	MD,ED	0.55	0.33	57	62		
		Izx,Izy	MD	0.58	0.36	59	63		
		Izx,Izy	ED	0.55	0.24	54	66		
	AUCR	Izx	MD,ED	0.58	0.27	56	66		
		Izy	MD,ED	0.54	0.35	57	61		
		Izx,Izy	MD	0.58	0.39	60	62		
		Izx,Izy	ED	0.54	0.24	54	65		
31	Spectral Fitting	Izx	MD,ED	0.37	Error			37	Error
		Izy	MD,ED	0.43					
		Izx,Izy	MD	0.37					
		Izx,Izy	ED	0.43					
	AUCR	Izx	MD,ED	0.37	0.95	80	38		1
		Izy	MD,ED	0.44	Error				Error
		Izx,Izy	MD	0.37					
		Izx,Izy	ED	0.44					
32	Spectral Fitting	Izx	MD,ED	0.26	0.08	34	65	N/A	
		Izy	MD,ED	0.26	0.11	36	60		
		Izx,Izy	MD	0.26	0.11	36	60		
		Izx,Izy	ED	0.26	0.08	34	65		

33	AUCR	Izx	MD,ED	0.26	0.04	32	71	N/A	
		Izy	MD,ED	0.23	0.12	35	58		
		Izx,Izy	MD	0.26	0.12	36	59		
		Izx,Izy	ED	0.23	0.04	31	70		
	Spectral Fitting	Izx	MD,ED	0.68	0.08	57	79		
		Izy	MD,ED	0.51	0.15	50	69		
		Izx,Izy	MD	0.68	0.23	60	72		
		Izx,Izy	ED	0.51	0.05	47	78		
		AUCR	Izx	MD,ED	0.67	0.00	55		88
			Izy	MD,ED	0.49	0.16	49		68
			Izx,Izy	MD	0.67	0.24	60		71
			Izx,Izy	ED	0.49	0.00	45		87

Appendix Table 1.3. Calculated values of the trigonometric functions of (θ , φ) and the absolute values of (θ' , φ') of NaYF₄:Eu nanorods lying on the substrate. Orientation is analyzed using spectral fitting analysis and area under curve ratiometry (AUCR). Calculated in-plane angle φ' is compared with measured φ' on the elliptical shape of CCD captured nanorod image (data not shown). Calculate out-of-plane angle θ' is compared with known $\theta' = 90^\circ$. Results shown here is denoted as “2D sample” in **Appendix Table 1.4.**

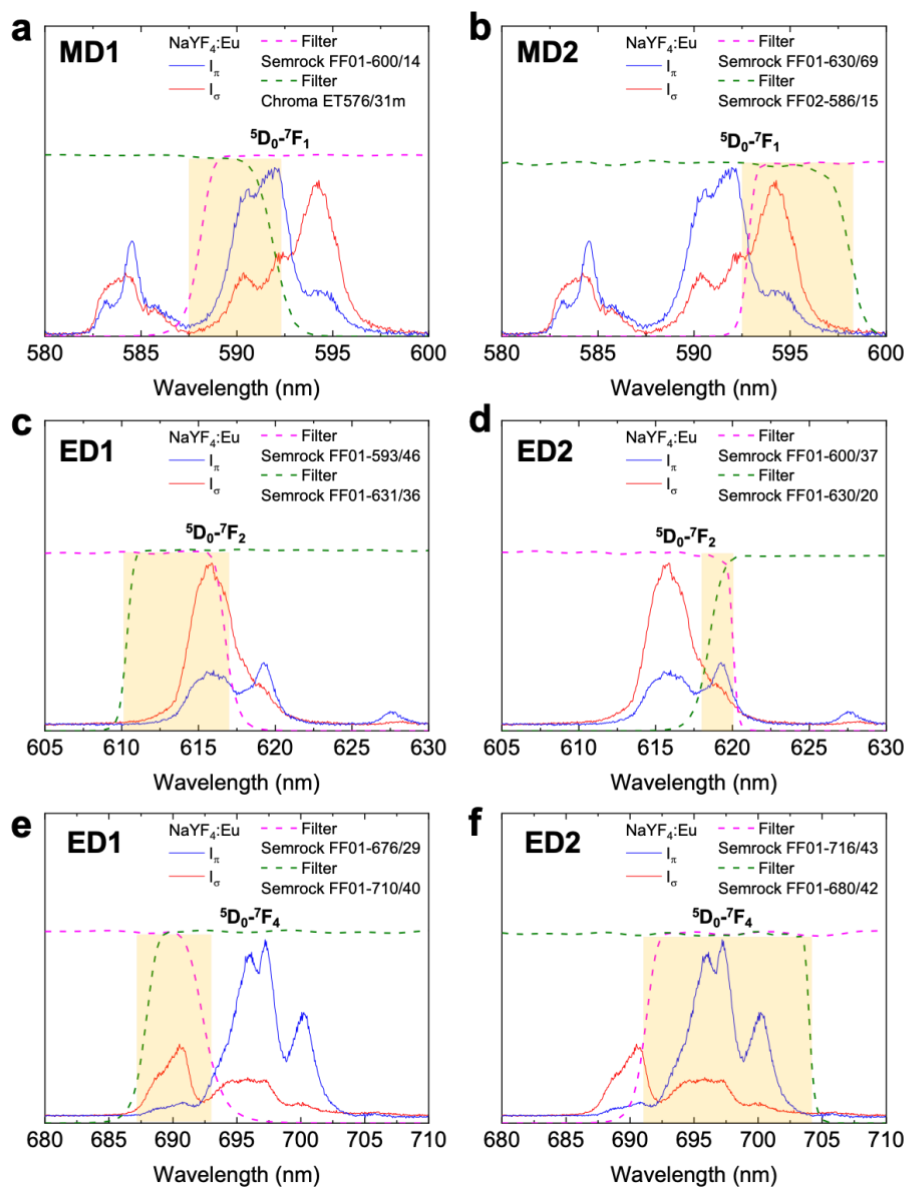
Rod number	Method	Polarization	Dipole	$\cos^2\theta_{cal}$	$\sin^2\varphi_{cal}$	$\theta'_{cal}(^\circ)$	$\varphi'_{cal}(^\circ)$	Error on $\theta'(^\circ)$	$\varphi'_{measured}(^\circ)$	Error on $\varphi'(^\circ)$	
1	Spectral Fitting	Izx	MD,ED	0.08	0.97	81	17	9	16	1	
		Izy	MD,ED	0.05	0.95	77	14	13		2	
		Izx,Izy	MD	0.08	0.97	81	17	9		1	
		Izx,Izy	ED	0.05	0.94	77	14	13		3	
	AUCR	Izx	MD,ED	0.09	0.97	81	18	9		2	
		Izy	MD,ED	0.02	0.93	74	7	16		8	
		Izx,Izy	MD	0.09	Error			Error			
		Izx,Izy	ED	0.02	0.90	71	8	19		8	
2	Spectral Fitting	Izx	MD,ED	0.58	0.97	83	50	7	54	4	
		Izy	MD,ED	0.66	Error			Error			
		Izx,Izy	MD	0.58	0.92	80	51	10		3	
		Izx,Izy	ED	0.66	Error			Error			
	AUCR	Izx	MD,ED	0.59	0.93	80	51	10		2	
		Izy	MD,ED	0.65	Error			Error			
		Izx,Izy	MD	0.59	0.97	84	51	6		3	
		Izx,Izy	ED	0.65	Error			Error			
3	Spectral Fitting	Izx	MD,ED	0.21	1.00	89	27	1	27	0	
		Izy	MD,ED	0.19	0.94	78	27	12		0	
		Izx,Izy	MD	0.21	0.97	80	28	10		1	
		Izx,Izy	ED	0.19	0.98	82	26	8		1	
	AUCR	Izx	MD,ED	0.22	1.00	89	28	1		1	
		Izy	MD,ED	0.13	0.89	72	22	18		5	
		Izx,Izy	MD	0.22	0.99	86	28	4		1	
		Izx,Izy	ED	0.13	0.90	73	22	17		5	
4	Spectral Fitting	Izx	MD,ED	0.05	1.00	87	13	3	8	5	
		Izy	MD,ED	0.03	0.96	78	10	12		2	
		Izx,Izy	MD	0.05	0.98	82	13	8		5	
		Izx,Izy	ED	0.03	0.98	81	10	9		2	
	AUCR	Izx	MD,ED	0.06	Error			Error			
		Izy	MD,ED	0.00	0.94	75	4	15		4	
		Izx,Izy	MD	0.06	0.99	86	14	4		6	
		Izx,Izy	ED	0.00	0.94	76	4	14		4	
5	Spectral Fitting	Izx	MD,ED	0.15	0.99	84	23	6	27	4	
		Izy	MD,ED	0.15	1.00	87	22	3		5	
		Izx,Izy	MD	0.15	Error			Error			
		Izx,Izy	ED	0.15	0.98	83	23	7		4	
	AUCR	Izx	MD,ED	0.17	1.00	88	24	2		3	
		Izy	MD,ED	0.10	0.96	79	19	11		8	
		Izx,Izy	MD	0.17	Error			Error			
		Izx,Izy	ED	0.10	0.92	74	19	16		8	
6	Spectral Fitting	Izx	MD,ED	0.29	Error			Error			
		Izy	MD,ED	0.42	Error			Error			
		Izx,Izy	MD	0.29	0.97	80	33	10	1		
		Izx,Izy	ED	0.42	Error			Error			

	AUCR	Izx	MD,ED	0.30	Error				Error
		Izy	MD,ED	0.41					
		Izx,Izy	MD	0.30	1.00	89	33	1	
		Izx,Izy	ED	0.41	Error				
7	Spectral Fitting	Izx	MD,ED	0.80	0.82	79	65	11	69
		Izy	MD,ED	0.83	Error				
		Izx,Izy	MD	0.80	0.86	80	65	10	
		Izx,Izy	ED	0.83	0.98	87	66	3	
	AUCR	Izx	MD,ED	0.82	0.78	78	67	12	
		Izy	MD,ED	0.83	Error				
		Izx,Izy	MD	0.82					
		Izx,Izy	ED	0.83	0.83	80	67	10	
8	Spectral Fitting	Izx	MD,ED	0.16	0.94	78	24	12	29
		Izy	MD,ED	0.20	0.94	78	27	12	
		Izx,Izy	MD	0.16	0.90	73	25	17	
		Izx,Izy	ED	0.20	0.99	86	27	4	
	AUCR	Izx	MD,ED	0.17	0.95	78	25	12	
		Izy	MD,ED	0.17	0.90	74	26	16	
		Izx,Izy	MD	0.17	0.90	73	25	17	
		Izx,Izy	ED	0.17	0.95	79	25	11	
9	Spectral Fitting	Izx	MD,ED	0.01	0.96	78	7	12	4
		Izy	MD,ED		Error				
		Izx,Izy	MD	0.01	0.94	76	7	14	
		Izx,Izy	ED		Error				
	AUCR	Izx	MD,ED	0.03	0.97	81	9	9	
		Izy	MD,ED		Error				
		Izx,Izy	MD	0.03	0.95	77	10	13	
		Izx,Izy	ED		Error				
10	Spectral Fitting	Izx	MD,ED	0.08	Error				14
		Izy	MD,ED	0.11					
		Izx,Izy	MD	0.08	0.99	85	17	5	
		Izx,Izy	ED	0.11	Error				
	AUCR	Izx	MD,ED	0.09	Error				
		Izy	MD,ED	0.12					
		Izx,Izy	MD	0.09					
		Izx,Izy	ED	0.12					
11	Spectral Fitting	Izx	MD,ED	0.54	Error				45
		Izy	MD,ED	0.70					
		Izx,Izy	MD	0.54					
		Izx,Izy	ED	0.70					
	AUCR	Izx	MD,ED	0.56	Error				
		Izy	MD,ED	0.72					
		Izx,Izy	MD	0.56					
		Izx,Izy	ED	0.72					
12	Spectral Fitting	Izx	MD,ED	0.51	Error				44
		Izy	MD,ED	0.69					
		Izx,Izy	MD	0.51					
		Izx,Izy	ED	0.69					
	AUCR	Izx	MD,ED	0.53	Error				
		Izy	MD,ED	0.72					
		Izx,Izy	MD	0.53					
		Izx,Izy	ED	0.72					
13	Spectral Fitting	Izx	MD,ED	0.17	0.94	77	25	13	24
		Izy	MD,ED	0.23	0.95	79	30	11	
		Izx,Izy	MD	0.17	0.87	71	26	19	
		Izx,Izy	ED	0.23	Error				
	AUCR	Izx	MD,ED	0.17	0.93	76	25	14	
		Izy	MD,ED	0.22	0.94	77	29	13	
		Izx,Izy	MD	0.17	0.88	71	26	19	
		Izx,Izy	ED	0.22	0.99	85	28	5	
14	Spectral Fitting	Izx	MD,ED	0.72	0.54	69	66	21	62
		Izy	MD,ED	0.76	0.87	80	62	10	
		Izx,Izy	MD	0.72	0.76	75	62	15	
		Izx,Izy	ED	0.76	0.62	72	66	18	
	AUCR	Izx	MD,ED	0.72	0.44	66	67	24	
		Izy	MD,ED	0.75	0.85	79	62	11	
		Izx,Izy	MD	0.72	0.75	75	61	15	
		Izx,Izy	ED	0.75	0.49	69	68	21	
15	Spectral Fitting	Izx	MD,ED	0.00	0.90	72	4	18	11
		Izy	MD,ED	0.05	0.91	73	14	17	
		Izx,Izy	MD	0.00	0.87	69	4	21	

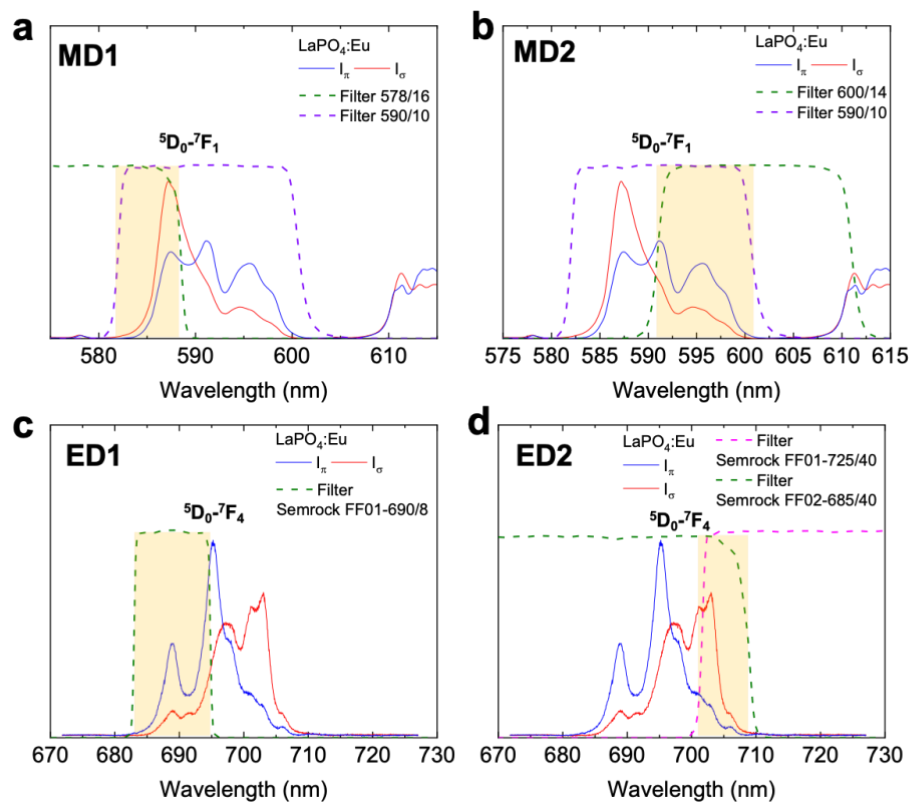
	AUCR	Izx,Izy	ED	0.05	0.95	77	13	13		2			
		Izx	MD,ED	0.02	0.91	73	8	17		3			
		Izy	MD,ED	0.04	0.90	72	12	18		1			
		Izx,Izy	MD	0.02	0.88	70	8	20		3			
		Izx,Izy	ED	0.04	0.93	75	12	15		1			
16	Spectral Fitting	Izx	MD,ED	0.53	0.71	68	52	22	52	0			
		Izy	MD,ED	0.61	0.72	71	56	19		4			
		Izx,Izy	MD	0.53	0.60	64	54	26		2			
		Izx,Izy	ED	0.61	0.86	76	54	14		2			
		Izx	MD,ED	0.52	0.64	66	53	24		1			
	AUCR	Izy	MD,ED	0.59	0.68	69	55	21		3			
		Izx,Izy	MD	0.52	0.59	64	54	26		2			
		Izx,Izy	ED	0.59	0.75	71	54	19		2			
		17	Spectral Fitting	Izx	MD,ED	0.13	0.87	70		23	20	32	9
				Izy	MD,ED	0.22	0.84	69		30	21		2
Izx,Izy	MD			0.13	0.76	63	24	27	8				
Izx,Izy	ED			0.22	0.96	79	28	11	4				
Izx	MD,ED			0.14	0.85	69	23	21	9				
AUCR	Izy	MD,ED	0.20	0.81	67	29	23	3					
	Izx,Izy	MD	0.14	0.75	63	25	27	7					
	Izx,Izy	ED	0.20	0.91	74	27	16	5					
	18	Spectral Fitting	Izx	MD,ED	0.41	0.85	73	42	17	43	1		
			Izy	MD,ED	0.50	0.93	79	46	11		3		
Izx,Izy			MD	0.41	0.79	69	43	21	0				
Izx,Izy			ED	0.50	Error				Error				
Izx			MD,ED	0.41	0.82	71	43	19	0				
AUCR	Izy	MD,ED	0.49	0.91	77	46	13	3					
	Izx,Izy	MD	0.41	0.79	69	43	21	0					
	Izx,Izy	ED	0.49	0.94	80	45	10	2					
	19	Spectral Fitting	Izx	MD,ED	0.74	0.74	75	63	15	60	3		
			Izy	MD,ED	0.81	0.89	82	65	8		5		
Izx,Izy			MD	0.74	0.66	73	64	17	4				
Izx,Izy			ED	0.81	Error				Error				
Izx			MD,ED	0.74	0.71	74	64	16	4				
AUCR	Izy	MD,ED	0.81	0.94	84	65	6	5					
	Izx,Izy	MD	0.74	0.70	74	64	16	4					
	Izx,Izy	ED	0.81	0.96	85	65	5	5					
	20	Spectral Fitting	Izx	MD,ED	0.82	Error				Error			
			Izy	MD,ED	0.92	Error				Error			
Izx,Izy			MD	0.82	0.42	71	73	19	6				
Izx,Izy			ED	0.92	Error				Error				
Izx			MD,ED	0.82	Error				Error				
AUCR	Izy	MD,ED	0.92	0.95	86	74	4	6					
	Izx,Izy	MD	0.82	0.44	71	73	19	6					
	Izx,Izy	ED	0.92	Error				Error					
	21	Spectral Fitting	Izx	MD,ED	0.87	Error				Error			
			Izy	MD,ED	0.92	0.00	74	89	16	3			
Izx,Izy			MD	0.87	0.00	69	89	21	3				
Izx,Izy			ED	0.92	Error				Error				
Izx			MD,ED	0.86	Error				Error				
AUCR	Izy	MD,ED	0.92	0.11	75	84	15	2					
	Izx,Izy	MD	0.86	0.06	69	84	21	2					
	Izx,Izy	ED	0.92	Error				Error					

Appendix Table 1.4. Statistics of analyzed orientation presented in **Appendix Table 1.2-3.**

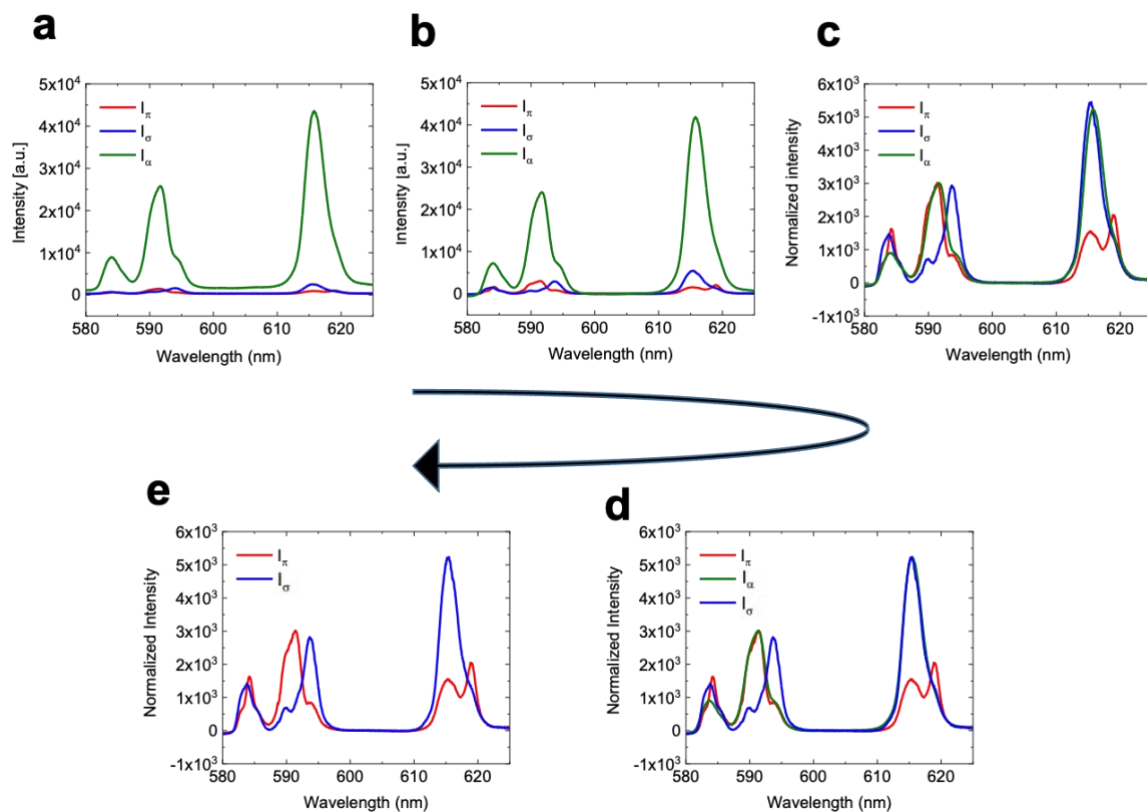
Sample type	Method	Angle	Total measurements counts	“N/A” counts	“Error” counts	Counted for Statistics	Mean absolute errors(°)
3D	Spectral fitting	φ'	132	46	6	80	4.6
	AUCR	φ'	132	46	5	81	4.8
2D	Spectral fitting	θ'	84	0	29	55	13.1
		φ'	84	0	29	55	3.2
	AUCR	θ'	84	0	27	57	14.3
		φ'	84	0	27	57	3.6
Sample type	Method	Angle	The deviation in angle values (θ' , φ') (°) calculated by the different polarization (I _{xz} and I _{zy} using both MD and ED) and by the different dipole transition (MD and ED using both I _{xz} and I _{zy})				
3D	Spectral fitting	θ'	3.2				
		φ'	2.3				
	AUCR	θ'	4.5				
		φ'	2.4				
2D	Spectral fitting	θ'	1.6				
		φ'	4.0				
	AUCR	θ'	2.0				
		φ'	5.0				



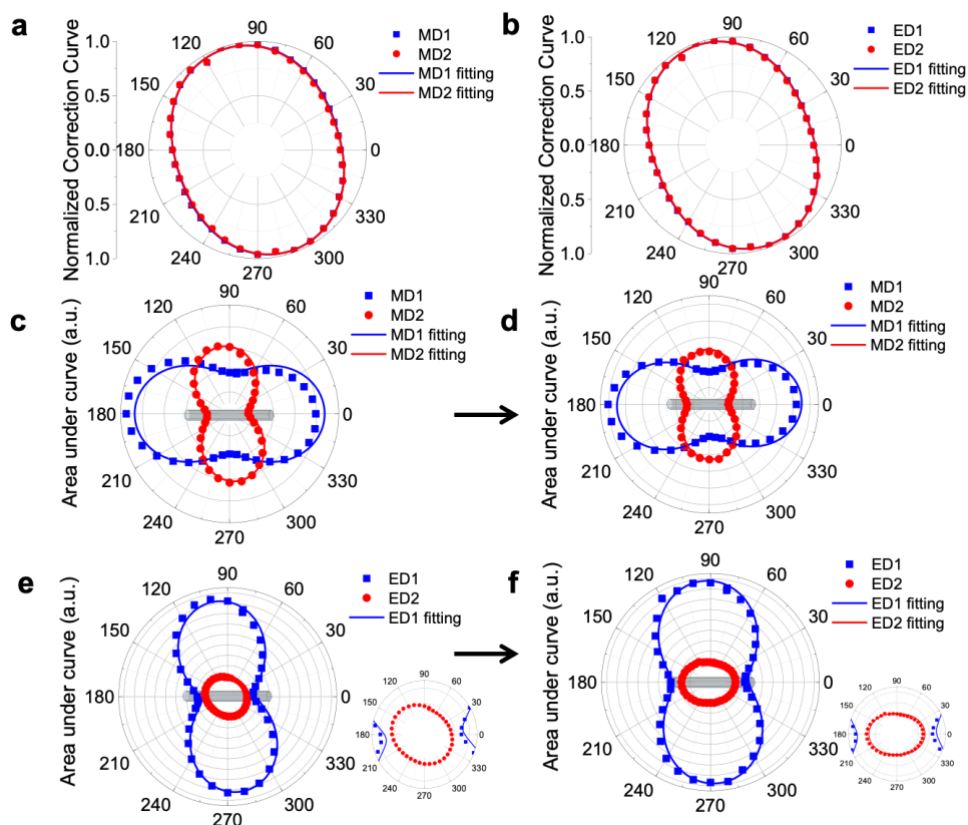
Appendix Figure 1.2. Selected optical filter for area under curve ratiometry using NaYF₄:Eu nanoparticles. Transmission of selected optical filters were plotted with NaYF₄:Eu reference signals (I_π and I_σ) for different transition levels : **(a,b)** MD1 and MD2 for ⁵D₀-⁷F₁ transition level, **(c,d)** ED1 and ED2 for ⁵D₀-⁷F₂ transition level and **(e,f)** ED1 and ED2 for ⁵D₀-⁷F₄ transition level.



Appendix Figure 1.3. Selected optical filter for area under curve ratiometry using LaPO₄:Eu nanoparticles. Transmission of selected optical filters were plotted with LaPO₄:Eu reference signals (I_π and I_σ) for different transition levels : **(a,b)** MD1 and MD2 for ⁵D₀-⁷F₁ transition level, **(c,d)** ED1 and ED2 for ⁵D₀-⁷F₄ transition level.



Appendix Figure 1.4. Normalization process for the reference spectra. **(a)** Raw spectrum of π , σ and α signal, showing a big difference in their global intensity. **(b)** Baseline subtracted spectrum of π , σ and α signal. Average intensity value of wavelength where Eu luminescence is not present is subtracted for each spectrum. **(c)** Normalized α signal to π signal **(d)** Normalized σ signal to α signal **(e)** Intensity corrected reference spectrum used for orientation analysis.



Appendix Figure 1.5. (a,b) Polar diagram of normalized area under curve of unpolarized white light background source spectra within selected wavelength ranges (**Figure 1.13b**) for (a) MD1 and MD2, (b) ED1 and ED2. Polar diagrams of selected wavelength ranges for (c,d) MD1 and MD2, (e,f) ED1 and ED2 of NaYF₄:Eu polarized photoluminescence spectra (c,e) before and (d,f) after white light correction. Correction was made for each analyzer angle as: $I_{\text{corrected}} = I_{\text{raw}} / I_{\text{white-source}}$.

The incident ray to the dielectric surface retards when they are reflected or/and transmitted. Similarly, most of optical pass- and band- filters and mirrors hold different magnitude of transmittance and reflectance depending on the polarization state of incoming wave, which induce the detected signal different with intrinsic polarization emission. Even though the white light background source is unpolarized, the polar diagrams (**Appendix Figure 1.5a,b**) observed shows obvious ellipsoid due to reason mentioned above. In an ideal case of unpolarized light, the polar diagram should show a perfect circle. This polarization dependency result in distorted polar diagram neither parallel nor orthogonal to the rod c-axis (**Appendix Figure 1.5c,e**). By applying white light background as a compensator ($I_{\text{corrected}} = I_{\text{raw}} / I_{\text{white-source}}$), intrinsic polarization behavior can be obtained (**Appendix Figure 1.5d,f**).

Appendix Table 1.5. Matlab code for single rod orientation analysis

```

% Data read
data_raw=xlsread('dataset.xlsx');

% Raw data import
W=data_raw(:,1); pi=data_raw(:,2); sigma=data_raw(:,3); Izy=data_raw(:,4); Izx=data_raw(:,5);

% Reference spectra data import
pi_MD=pi(258:525,1); sigma_MD=sigma(258:525,1); pi_ED=pi(627:949,1); sigma_ED=sigma(627:949,1);

% Experimental data import
Izy_MD=Izy(258:525,1); Izx_MD=Izx(258:525,1); Izy_ED=Izy(627:949,1); Izx_ED=Izx(627:949,1);

% AUCR data import

% AUCR reference
I_pi_MD1 = trapz(W(266:360,1),pi(266:360,1)); I_pi_MD2 = trapz(W(361:466,1),pi(361:466,1));
I_pi_ED1 = trapz(W(683:831,1),pi(683:831,1)); I_pi_ED2 = trapz(W(832:922,1),pi(832:922,1));
I_sigma_MD1 = trapz(W(266:360,1),sigma(266:360,1)); I_sigma_MD2 = trapz(W(361:466,1),sigma(361:466,1));
I_sigma_ED1 = trapz(W(683:831,1),sigma(683:831,1)); I_sigma_ED2 = trapz(W(832:922,1),sigma(832:922,1));

% AUCR data
I_Izx_MD1 = trapz(W(266:360,1),Izx(266:360,1)); I_Izx_MD2 = trapz(W(361:466,1),Izx(361:466,1));
I_Izx_ED1 = trapz(W(683:831,1),Izx(683:831,1)); I_Izx_ED2 = trapz(W(832:922,1),Izx(832:922,1));
I_Izy_MD1 = trapz(W(266:360,1),Izy(266:360,1)); I_Izy_MD2 = trapz(W(361:466,1),Izy(361:466,1));
I_Izy_ED1 = trapz(W(683:831,1),Izy(683:831,1)); I_Izy_ED2 = trapz(W(832:922,1),Izy(832:922,1));

k_Izx_MD = I_Izx_MD1/I_Izx_MD2; k_Izx_ED = I_Izx_ED1/I_Izx_ED2;
k_Izy_MD = I_Izy_MD1/I_Izy_MD2; k_Izy_ED = I_Izy_ED1/I_Izy_ED2

% Spectral Fitting_Izx
% x=sigma / y=pi / a=cos2theta / b=sin2phi / c= global intensity
fit_Izx_MD = fitype('c*(x*a+y*(1-a))', 'independent', {'x', 'y'}, 'dependent', 'z');
[fitresult_Izx_MD,gof_Izx_MD] = fit( [sigma_MD, pi_MD], Izx_MD, fit_Izx_MD);
coefficient_Izx_MD = coeffvalues(fitresult_Izx_MD);

for i=258:525
fit_curve_Izx_MD(i,1)=coefficient_Izx_MD(1,2)*(sigma(i,1)*coefficient_Izx_MD(1,1)+pi(i,1)*(1-coefficient_Izx_MD(1,1)));
end

for i=258:525
fit_curve_Izx_MD_pi(i,1)=coefficient_Izx_MD(1,2)*(pi(i,1)*(1-coefficient_Izx_MD(1,1)));
end

for i=258:525
fit_curve_Izx_MD_sigma(i,1)=coefficient_Izx_MD(1,2)*(sigma(i,1)*coefficient_Izx_MD(1,1));
end

```

```

% x=sigma / y=pi / a=cos2theta / b=sin2phi / c= global intensity

fit_Izx_ED = fittype('c*(y*(1-a)*b+x*(a*b+(1-b)))','independent',{'x','y'},'dependent','z','problem','a');

[fitresult_Izx_ED,gof_Izy_MD] = fit( [sigma_ED, pi_ED], Izx_ED, ft_Izx_ED, 'problem',coefficient_Izx_MD(1,1));

coefficient_Izx_ED=coeffvalues(fitresult_Izx_ED);

for i=627:949

fit_curve_Izx_ED(i,1)=coefficient_Izx_ED(1,2)*(pi(i,1))*(1-
coefficient_Izx_MD(1,1))*coefficient_Izx_ED(1,1)+sigma(i,1)*(coefficient_Izx_MD(1,1)*coefficient_Izx_ED(1,1)+(1-
coefficient_Izx_ED(1,1)));

end

for i=627:949

fit_curve_Izx_ED_pi(i,1)=coefficient_Izx_ED(1,2)*pi(i,1)*((1-coefficient_Izx_MD(1,1))*coefficient_Izx_ED(1,1));

end

for i=627:949

fit_curve_Izx_ED_sigma(i,1)=coefficient_Izx_ED(1,2)*(sigma(i,1))*(coefficient_Izx_MD(1,1)*coefficient_Izx_ED(1,1)+(1-
coefficient_Izx_ED(1,1)));

end

% AUCR_Izx

cos2theta_Izx = (k_Izx_MD*I_pi_MD2-I_pi_MD1)/(k_Izx_MD*(I_pi_MD2-I_sigma_MD2)-(I_pi_MD1-I_sigma_MD1));

sin2phi_Izx = (k_Izx_ED*I_sigma_ED2-I_sigma_ED1)/((1-cos2theta_Izx)*((I_pi_ED1-I_sigma_ED1)-k_Izx_ED*(I_pi_ED2-
I_sigma_ED2)))

% Spectral Fitting Izy

% x=sigma / y=pi / a=cos2theta / b=sin2phi / c= global intensity

fit_Izy_ED = fittype('c*(y*a+x*(1-a))','independent',{'x','y'},'dependent','z');

[fitresult_Izy_ED,gof_Izy_ED] = fit ( [sigma_ED, pi_ED], Izy_ED, ft_Izy_ED);

coefficient_Izy_ED = coeffvalues(fitresult_Izy_ED);

for i=627:949

fit_curve_Izy_ED(i,1)=coefficient_Izy_ED(1,2)*(pi(i,1))*coefficient_Izy_ED(1,1)+sigma(i,1)*(1-coefficient_Izy_ED(1,1));

end

for i=627:949

fit_curve_Izy_ED_pi(i,1)=coefficient_Izy_ED(1,2)*(pi(i,1))*coefficient_Izy_ED(1,1);

end

for i=627:949

fit_curve_Izy_ED_sigma(i,1)=coefficient_Izy_ED(1,2)*(sigma(i,1))*(1-coefficient_Izy_ED(1,1));

end

% x=sigma / y=pi / a=cos2theta / b=sin2phi / c= global intensity

fit_Izy_MD = fittype('c*(x*(1-a)*b+y*(a*b+(1-b)))','independent',{'x','y'},'dependent','z','problem','a');

[fitresult_Izy_MD,gof_Izy_MD] = fit( [sigma_MD, pi_MD], Izy_MD, ft_Izy_MD, 'problem',coefficient_Izy_ED(1,1));

```

```

coefficient_Izy_MD=coeffvalues(fitresult_Izy_MD);

for i=258:525

    fit_curve_Izy_MD(i,1)=coefficient_Izy_MD(1,2)*(sigma(i,1)*(1-
coefficient_Izy_ED(1,1))*coefficient_Izy_MD(1,1)+pi(i,1)*(coefficient_Izy_ED(1,1)*coefficient_Izy_MD(1,1)+(1-
coefficient_Izy_MD(1,1))));

end

for i=258:525

    fit_curve_Izy_MD_pi(i,1)=coefficient_Izy_MD(1,2)*(pi(i,1)*(coefficient_Izy_ED(1,1)*coefficient_Izy_MD(1,1)+(1-
coefficient_Izy_MD(1,1))));

end

for i=258:525

    fit_curve_Izy_MD_sigma(i,1)=coefficient_Izy_MD(1,2)*(sigma(i,1)*(1-coefficient_Izy_ED(1,1))*coefficient_Izy_MD(1,1));

end

% AUCR_Izy

cos2theta_Izy = (k_Izy_ED*I_sigma_ED2-I_sigma_ED1)/(k_Izy_ED*(I_sigma_ED2-I_pi_ED2)-(I_sigma_ED1-I_pi_ED1));

sin2phi_Izy = (k_Izy_MD*I_pi_MD2-I_pi_MD1)/((1-cos2theta_Izy)*((I_sigma_MD1-I_pi_MD1)-k_Izy_MD*(I_sigma_MD2-
I_pi_MD2)));

% Conversion (theta,phi) --> (theta',phi')

theta_Izx_fit=radtodeg(acos(sqrt(coefficient_Izx_MD(1,1))));

phi_Izx_fit=radtodeg(asin(sqrt(coefficient_Izx_ED(1,1))));

theta_prime_Izx_fit=radtodeg(acos(sin(degtorad(theta_Izx_fit))*cos(degtorad(phi_Izx_fit))));

phi_prime_Izx_fit=radtodeg(asin(cos(degtorad(theta_Izx_fit))/sqrt(1-
sin(degtorad(theta_Izx_fit))^2*cos(degtorad(phi_Izx_fit))^2)));

theta_Izx_AUCR=radtodeg(acos(sqrt(cos2theta_Izx)));

phi_Izx_AUCR=radtodeg(asin(sqrt(sin2phi_Izx)));

theta_prime_Izx_AUCR=radtodeg(acos(sin(degtorad(theta_Izx_AUCR))*cos(degtorad(phi_Izx_AUCR))));

phi_prime_Izx_AUCR=radtodeg(asin(cos(degtorad(theta_Izx_AUCR))/sqrt(1-
sin(degtorad(theta_Izx_AUCR))^2*cos(degtorad(phi_Izx_AUCR))^2)));

theta_Izy_fit=radtodeg(acos(sqrt(coefficient_Izy_ED(1,1))));

phi_Izy_fit=radtodeg(asin(sqrt(coefficient_Izy_MD(1,1))));

theta_prime_Izy_fit=radtodeg(acos(sin(degtorad(theta_Izy_fit))*cos(degtorad(phi_Izy_fit))));

phi_prime_Izy_fit=radtodeg(asin(cos(degtorad(theta_Izy_fit))/sqrt(1-
sin(degtorad(theta_Izy_fit))^2*cos(degtorad(phi_Izy_fit))^2)));

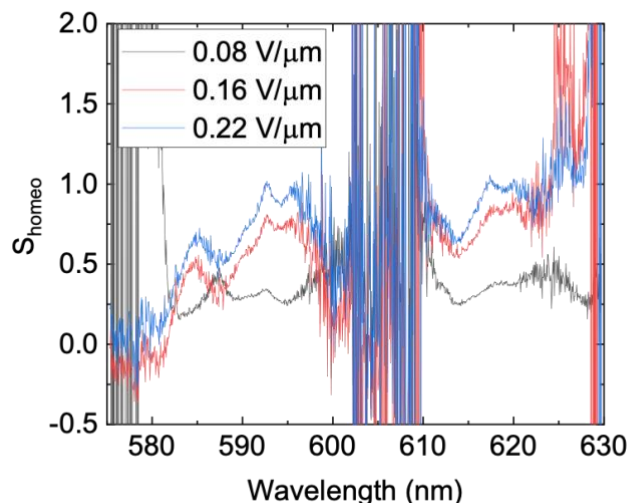
theta_Izy_AUCR=radtodeg(acos(sqrt(cos2theta_Izy)));

phi_Izy_AUCR=radtodeg(asin(sqrt(sin2phi_Izy)));

theta_prime_Izy_AUCR=radtodeg(acos(sin(degtorad(theta_Izy_AUCR))*cos(degtorad(phi_Izy_AUCR))));

phi_prime_Izy_AUCR=radtodeg(asin(cos(degtorad(theta_Izy_AUCR))/sqrt(1-
sin(degtorad(theta_Izy_AUCR))^2*cos(degtorad(phi_Izy_AUCR))^2)));

```

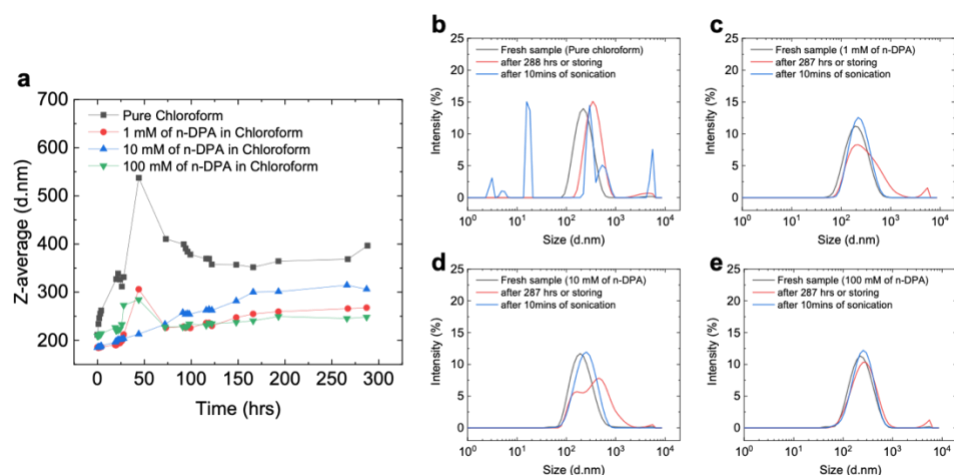


Appendix Figure 2.1. Calculated S_{homeo} as a function of wavelength for the orientation-controlled NaYF₄:Eu nanorods under the external electric field (0.08, 0.16 and 0.22 V/μm).

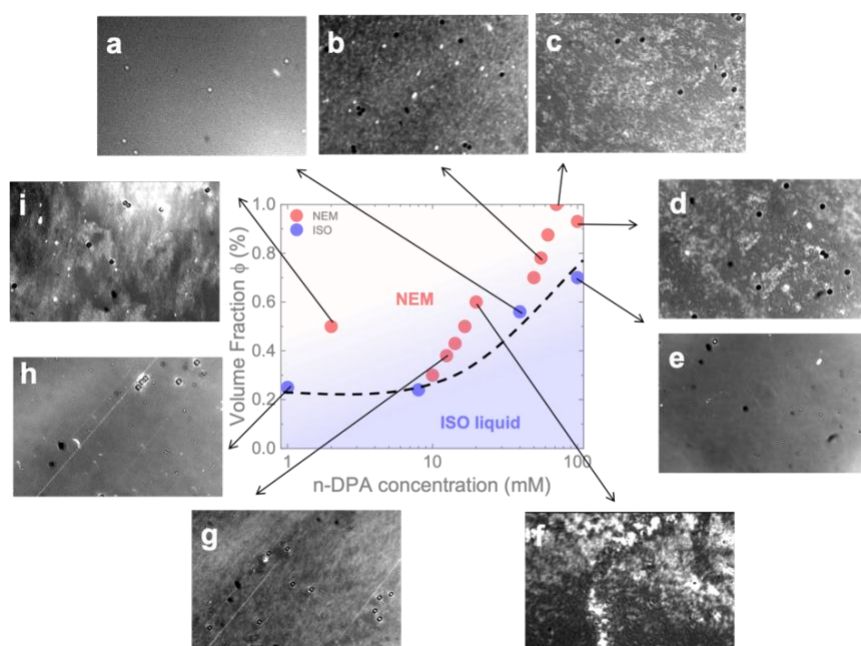
In the main text, spectral fitting analysis is performed to calculate S_{homeo} using **Equation 2.15**. Instead of spectral fitting analysis, S_{homeo} can also be calculated as a function of wavelength according to equation $S_{\text{homeo}} = (I_{\pi+\sigma} + I_{\alpha}) / (I_{\pi+\sigma} - 2 \cdot (I_{\alpha} - I_z))$, as shown in **Appendix Figure 2.1**. The averaged value of calculated S_{homeo} in wavelength of interest (5D_0 - 7F_1 and 5D_0 - 7F_2 transition lines) was 0.36 for 0.08 V/μm, 0.70 for 0.16 V/μm is 0.70, and 0.82 for 0.22 V/μm. These values are slightly lower than the value calculated from spectral fitting analysis (obtained S_{homeo} for 0.08 V/μm is 0.40, for 0.16 V/μm is 0.76 and for 0.22 V/μm is 0.88). In principle, both methods should give an identical result. However, the precision appears to be more degraded for wavelength-dependent calculation as it can be more influenced by non-perfect baseline treatment and noise, *etc.*

Appendix Table 2.1. Determined polar angle θ of crystal's orientation by polarized signal and unpolarized signal. Image: CCD camera captured PL emission of the nanorod (scale bar: 2 μm).

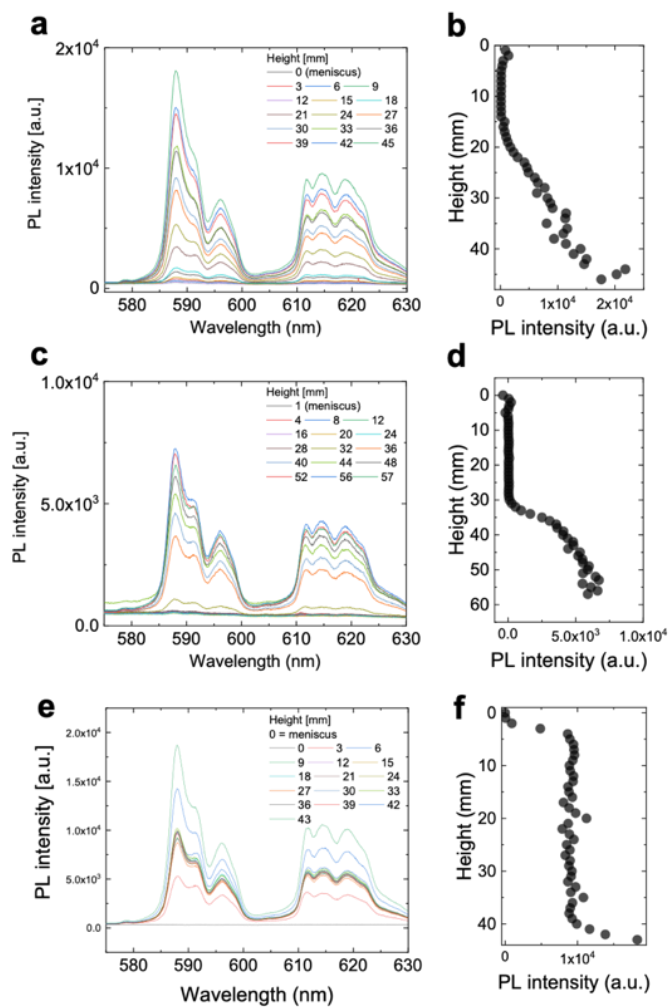
PL emission image							
Calculated out-of-plane angle (°)	Polarization	I_{zx}	76	67	63	62	42
		I_{zy}	80	74	65	64	42
	No polarization		72	68	65	63	37



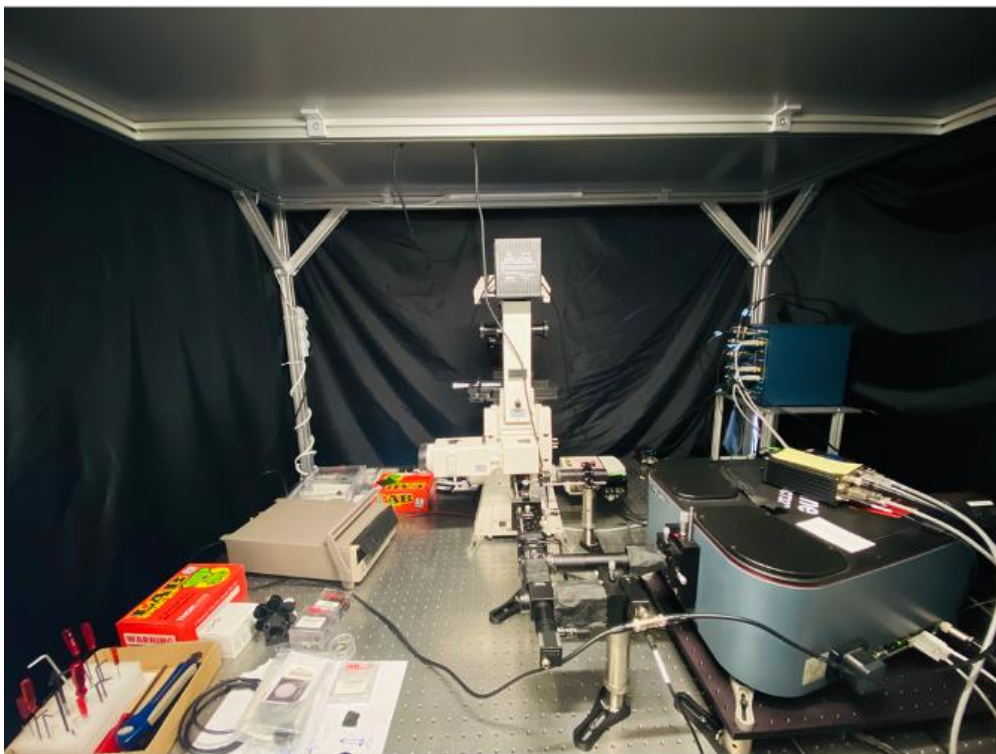
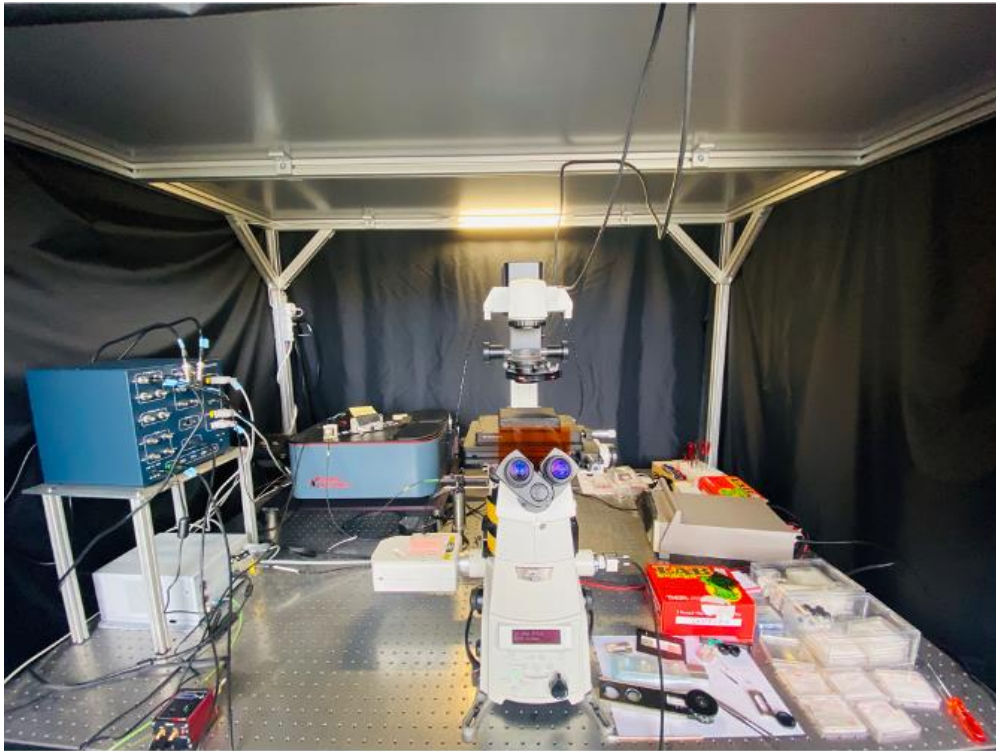
Appendix Figure 3.1. (a) Z-average size of surface-functionalized $\text{LaPO}_4:\text{Eu}$ nanorods dispersed in pure chloroform or with an excess of 1, 10 and 100 mM of n-DPA ligand molecules in chloroform. (b-e) Intensity profile as a function of hydrodynamic size of $\text{LaPO}_4:\text{Eu}$ nanorods dispersed in (b) pure chloroform or with an excess of (c) 1, (d) 10 and (e) 100 mM of n-DPA ligand molecules, measured in fresh state, after ~ 287 hours of storing and after ~ 10 mins of sonication after aging.



Appendix Figure 3.2. Optical texture observed between crossed polarizer of surface-functionalized $\text{LaPO}_4:\text{Eu}@n\text{-DPA}$ nanorod suspension in chloroform as a function of volume fraction (Φ , vol%) and excess n-DPA ligand concentration (mM). (a) $\Phi = 0.56$ vol% / n-DPA = 40.0 mM, (b) $\Phi = 0.78$ vol% / n-DPA = 56.0 mM, (c) $\Phi = 1.00$ vol% / n-DPA = 71.4 mM, (d) $\Phi = 0.93$ vol% / n-DPA = 100.0 mM, (e) $\Phi = 0.70$ vol% / n-DPA = 100.0 mM, (f) $\Phi = 0.60$ vol% / n-DPA = 20.0 mM, (g) $\Phi = 0.38$ vol% / n-DPA = 12.5 mM, (h) $\Phi = 0.25$ vol% / n-DPA = 1.0 mM, (i) $\Phi = 0.50$ vol% / n-DPA = 2.0 mM,



Appendix Figure 3.3. (a,c,e) Emission spectra of Eu³⁺ dopant measured along the height of the capillary. (b,d,f) PL intensity of the peak at ~589 nm along the height of the capillary. (a,b) $\Phi = 0.5$ vol% / n-DPA = 2.0 mM, (c,d) $\Phi = 0.6$ vol% / n-DPA = 20.0 mM, (e,f) $\Phi = 1.4$ vol% / n-DPA = 100.0 mM



Appendix Figure 4.1. Photograph of developed fluorescence polarizing confocal microscope

Appendix Table 4.1. Matlab code for liquid crystal tomography

```

% Polarized Spectrum load

datapol15_raw=csvread('227.csv',2,0); datapol60_raw=csvread('317.csv',2,0);

W=datapol15_raw(:,1);

datapol15=cell(1,2500); datapol60=cell(1,2500);

for i=1:2500

    datapol15{i}=datapol15_raw(:,i+1);    datapol60{i}=datapol60_raw(:,i+1);

end

%Data offset subtract

I_pol15_subtract=cell(1,2500); I_pol60_subtract=cell(1,2500); I_pol15=cell(1,2500); I_pol60=cell(1,2500);

for i=1:2500

    I_pol15_subtract{i}=mean(datapol15{i}(707:730,1));    I_pol60_subtract{i}=mean(datapol60{i}(707:730,1));

    I_pol15{i}=datapol15{i}-I_pol15_subtract{i};    I_pol60{i}=datapol60{i}-I_pol60_subtract{i};

end

%Data analyze

I_MD1_pol15=cell(1,2500); I_MD2_pol15=cell(1,2500); I_ED1_pol15=cell(1,2500); I_ED2_pol15=cell(1,2500);

I_MD1_pol60=cell(1,2500); I_MD2_pol60=cell(1,2500); I_ED1_pol60=cell(1,2500); I_ED2_pol60=cell(1,2500);

I_kMD_pol15=cell(1,2500); I_kED_pol15=cell(1,2500); I_kMD_pol60=cell(1,2500); I_kED_pol60=cell(1,2500);

for i=1:2500

    I_MD1_pol15{i}=trapz(W(33:110),I_pol15{i}(33:110,1));    I_MD2_pol15{i}=trapz(W(111:200),I_pol15{i}(111:200,1));

    I_ED1_pol15{i}=trapz(W(774:918),I_pol15{i}(774:918,1));    I_ED2_pol15{i}=trapz(W(919:1021),I_pol15{i}(919:1021,1));

    I_MD1_pol60{i}=trapz(W(33:110),I_pol60{i}(33:110,1));    I_MD2_pol60{i}=trapz(W(111:200),I_pol60{i}(111:200,1));

    I_ED1_pol60{i}=trapz(W(774:918),I_pol60{i}(774:918,1));    I_ED2_pol60{i}=trapz(W(919:1021),I_pol60{i}(919:1021,1));

    I_kMD_pol15{i}=I_MD1_pol15{i}/I_MD2_pol15{i};    I_kED_pol15{i}=I_ED1_pol15{i}/I_ED2_pol15{i};

    I_kMD_pol60{i}=I_MD1_pol60{i}/I_MD2_pol60{i};    I_kED_pol60{i}=I_ED1_pol60{i}/I_ED2_pol60{i};

end

%Reference spectrum

data_pi=csvread('pi.dat'); data_sigma=csvread('sigma.dat');pi_raw=data_pi(:,2); sigma_raw=data_sigma(:,2);

pi=pi_raw-mean(pi_raw(707:730,1)); sigma=sigma_raw-mean(sigma_raw(707:730,1));

pi_MD1=trapz(W(33:110),pi(33:110,1));pi_MD2=trapz(W(111:200),pi(111:200,1));pi_ED1=trapz(W(774:918),pi(774:918,1));pi_
ED2=trapz(W(919:1021),pi(919:1021,1));

sigma_MD1=trapz(W(33:110),sigma(33:110,1));sigma_MD2=trapz(W(111:200),sigma(111:200,1));sigma_ED1=trapz(W(774:918
),sigma(774:918,1));sigma_ED2=trapz(W(919:1021),sigma(919:1021,1));

% Tomography Calculation

cos2theta_bracket=cell(1,2500);    cos2theta_ED=cell(1,2500);    cos2theta_MD=cell(1,2500);    sin2phi=cell(1,250);
sin2phi_MD=cell(1,250); sin2phi_ED=cell(1,2500);

I_parallel_MD1=cell(1,2500);I_parallel_MD2=cell(1,2500);I_parallel_ED1=cell(1,2500);I_parallel_ED2=cell(1,2500);

```

```

S=cell(1,2500); theta=cell(1,2500); phi=cell(1,2500); theta_prime=cell(1,2500); phi_prime=cell(1,2500);

I_perpendicular_MD1=cell(1,2500);I_perpendicular_MD2=cell(1,2500);I_perpendicular_ED1=cell(1,2500);I_perpendicular_ED2
=cell(1,2500);

for i=1:2500

    cos2theta_bracket{i}=-2*((I_kMD_pol60{i}*pi_MD2-pi_MD1)/(I_kMD_pol60{i}*(sigma_MD2-pi_MD2)-(sigma_MD1-
pi_MD1)))+(I_kED_pol60{i}*(sigma_ED2+pi_ED2)-(sigma_ED1+pi_ED1))/(I_kED_pol60{i}*(sigma_ED2-pi_ED2)-
(sigma_ED1-pi_ED1)));

    S{i}=(3*cos2theta_bracket{i}-1)/2;

    cos2theta_{i}=(cos2theta_bracket{i}+(I_kED_pol60{i}*(sigma_ED2+pi_ED2)-
(sigma_ED1+pi_ED1))/(I_kED_pol60{i}*(sigma_ED2-pi_ED2)-(sigma_ED1-pi_ED1)))/(3*cos2theta_bracket{i}-1);

    cos2theta_MD{i}=2*(cos2theta_bracket{i}+(I_kMD_pol60{i}*pi_MD2-pi_MD1)/(I_kMD_pol60{i}*(sigma_MD2-pi_MD2)-
(sigma_MD1-pi_MD1)))/(3*cos2theta_bracket{i}-1);

    cos2theta_ED{i}=(cos2theta_bracket{i}+(I_kED_pol60{i}*(sigma_ED2+pi_ED2)-
(sigma_ED1+pi_ED1))/(I_kED_pol60{i}*(sigma_ED2-pi_ED2)-(sigma_ED1-pi_ED1)))/(3*cos2theta_bracket{i}-1);

    % cos2theta can be calculated from MD and ED, but these two are same

    I_parallel_MD1{i} = (sigma_MD1*(1-cos2theta_bracket{i})/2)+(pi_MD1*(1+cos2theta_bracket{i})/2);
    I_parallel_MD2{i} = (sigma_MD2*(1-cos2theta_bracket{i})/2)+(pi_MD2*(1+cos2theta_bracket{i})/2);
    I_parallel_ED1{i} = (pi_ED1*cos2theta_bracket{i})+(sigma_ED1*(1-cos2theta_bracket{i}));
    I_parallel_ED2{i} = (pi_ED2*cos2theta_bracket{i})+(sigma_ED2*(1-cos2theta_bracket{i}));
    I_perpendicular_MD1{i} = (sigma_MD1*cos2theta_bracket{i})+(pi_MD1*(1-cos2theta_bracket{i}));
    I_perpendicular_MD2{i} = (sigma_MD2*cos2theta_bracket{i})+(pi_MD2*(1-cos2theta_bracket{i}));
    I_perpendicular_ED1{i} = (pi_ED1*(1-cos2theta_bracket{i})/2)+(sigma_ED1*(1+cos2theta_bracket{i})/2);
    I_perpendicular_ED2{i} = (pi_ED2*(1-cos2theta_bracket{i})/2)+(sigma_ED2*(1+cos2theta_bracket{i})/2);

    sin2phi_ED{i}=(I_kED_pol15{i}*I_perpendicular_ED2{i}-I_perpendicular_ED1{i})/((1-cos2theta_{i})*((I_parallel_ED1{i}-
I_perpendicular_ED1{i})-I_kED_pol15{i}*(I_parallel_ED2{i}-I_perpendicular_ED2{i})));

    sin2phi_MD{i}=(I_kMD_pol15{i}*I_perpendicular_MD2{i}-I_perpendicular_MD1{i})/((1-
cos2theta_{i})*((I_parallel_MD1{i}-I_perpendicular_MD1{i})-I_kMD_pol15{i}*(I_parallel_MD2{i}-I_perpendicular_MD2{i})));

    % sin2phi can be calculated from MD and ED, these are not same

    theta_{i}=radtodeg(acos(sqrt(cos2theta_{i})));

    phi_ED{i}=radtodeg(asin(sqrt(sin2phi_ED{i})));

    phi_MD{i}=radtodeg(asin(sqrt(sin2phi_MD{i})));

    theta_prime_MD{i}=radtodeg(acos(sin(degtorad(theta_{i}))*cos(degtorad(phi_MD{i})))));

    theta_prime_ED{i}=radtodeg(acos(sin(degtorad(theta_{i}))*cos(degtorad(phi_ED{i})))));

    phi_prime_MD{i}=radtodeg(asin(cos(degtorad(theta_{i}))/sqrt(1-sin(degtorad(theta_{i}))^2*cos(degtorad(phi_MD{i}))^2)));

    phi_prime_ED{i}=radtodeg(asin(cos(degtorad(theta_{i}))/sqrt(1-sin(degtorad(theta_{i}))^2*cos(degtorad(phi_ED{i}))^2)));

end

%Data reshape
I_MD1_Matrix_pol15=cell(50,50); I_MD2_Matrix_pol15=cell(50,50);
I_ED1_Matrix_pol15=cell(50,50); I_ED2_Matrix_pol15=cell(50,50);
I_MD1_Matrix_pol60=cell(50,50); I_MD2_Matrix_pol60=cell(50,50);

```

```

I_ED1_Matrix_pol60=cell(50,50); I_ED2_Matrix_pol60=cell(50,50);

I_kMD_Matrix_pol15=cell(50,50); I_kED_Matrix_pol15=cell(50,50);

I_kMD_Matrix_pol60=cell(50,50); I_kED_Matrix_pol60=cell(50,50);

S_Matrix=cell(50,50); cos2theta_Matrix=cell(50,50);

sin2phi_MD_Matrix=cell(50,50); sin2phi_ED_Matrix=cell(50,50);

theta_prime_MD_Matrix=cell(50,50); theta_prime_ED_Matrix=cell(50,50);

phi_prime_MD_Matrix=cell(50,50); phi_prime_ED_Matrix=cell(50,50);

for i=1:50

    for j=0:49

        I_MD1_Matrix_pol15{j+1,i}=I_MD1_pol15{1,i+50*j};    I_MD2_Matrix_pol15{j+1,i}=I_MD2_pol15{1,i+50*j};
        I_ED1_Matrix_pol15{j+1,i}=I_ED1_pol15{1,i+50*j};    I_ED2_Matrix_pol15{j+1,i}=I_ED2_pol15{1,i+50*j};
        I_MD1_Matrix_pol60{j+1,i}=I_MD1_pol60{1,i+50*j};    I_MD2_Matrix_pol60{j+1,i}=I_MD2_pol60{1,i+50*j};
        I_ED1_Matrix_pol60{j+1,i}=I_ED1_pol60{1,i+50*j};    I_ED2_Matrix_pol60{j+1,i}=I_ED2_pol60{1,i+50*j};
        I_kMD_Matrix_pol15{j+1,i}=I_kMD_pol15{1,i+50*j};    I_kED_Matrix_pol15{j+1,i}=I_kED_pol15{1,i+50*j};
        I_kMD_Matrix_pol60{j+1,i}=I_kMD_pol60{1,i+50*j};    I_kED_Matrix_pol60{j+1,i}=I_kED_pol60{1,i+50*j};
        S_Matrix{j+1,i}=S{1,i+50*j};    cos2theta_Matrix{j+1,i}=cos2theta{1,i+50*j};
        sin2phi_MD_Matrix{j+1,i}=sin2phi_MD{1,i+50*j};    sin2phi_ED_Matrix{j+1,i}=sin2phi_ED{1,i+50*j};
        theta_prime_MD_Matrix{j+1,i}=theta_prime_MD{1,i+50*j};
        theta_prime_ED_Matrix{j+1,i}=theta_prime_ED{1,i+50*j};
        phi_prime_MD_Matrix{j+1,i}=phi_prime_MD{1,i+50*j};
        phi_prime_ED_Matrix{j+1,i}=phi_prime_ED{1,i+50*j};
    end
end

S_data=cell2mat(S_Matrix)'; cos2theta_data=cell2mat(cos2theta_Matrix)';

sin2phi_MD_data=cell2mat(sin2phi_MD_Matrix)'; sin2phi_ED_data=cell2mat(sin2phi_ED_Matrix)';

theta_prime_MD_data=cell2mat(theta_prime_MD_Matrix)'; theta_prime_ED_data=cell2mat(theta_prime_ED_Matrix)';

phi_prime_MD_data=cell2mat(phi_prime_MD_Matrix)'; phi_prime_ED_data=cell2mat(phi_prime_ED_Matrix)';

% Masking based on order parameter

mask_Matrix=cell(50,50);

S_data_cell=num2cell(S_data);

for i=1:50

    for j=1:50

        if S_data_cell{i,j} < 0.2

            mask_Matrix{i,j}=NaN;

        else

```

```

    mask_Matrix{i,j}=1;

    end

    end

end

mask=cell2mat(mask_Matrix); S_data=cell2mat(S_Matrix).!*mask;

cos2theta_data=cell2mat(cos2theta_Matrix).!*mask; sin2phi_MD_data=cell2mat(sin2phi_MD_Matrix).!*mask;

sin2phi_ED_data=cell2mat(sin2phi_ED_Matrix).!*mask; theta_prime_MD_data=cell2mat(theta_prime_MD_Matrix).!*mask;

theta_prime_ED_data=cell2mat(theta_prime_ED_Matrix).!*mask; hi_prime_MD_data=cell2mat(phi_prime_MD_Matrix).!*mask;

phi_prime_ED_data=cell2mat(phi_prime_ED_Matrix).!*mask;

% Rod visualization

figure;

h=imshow(phi_prime_MD_data,'InitialMagnification','fit','DisplayRange',[ ],'Colormap','jet'); hold on

set(h,'AlphaData',0.1);

colorbar; hold off

[Grid_x,Grid_y]=meshgrid(1:1:50,1:1:50);

Data_x = cos(deg2rad(phi_prime_MD_data)).*sin(deg2rad(theta_prime_MD_data));

Data_y = sin(deg2rad(phi_prime_MD_data)).*sin(deg2rad(theta_prime_MD_data));

x=Data_x+Grid_x; y=Data_y+Grid_y;

alpha=zeros(50,50);

for i=1:50

    for j=1:50

        X_temp=[x(i,j)-0.25;Grid_x(i,j)-0.25]; Y_temp=[y(i,j)-0.25;Grid_y(i,j)-0.25];

        p(i,j)=line(X_temp,Y_temp,'Color','r','LineWidth',2);

        if isnan(S_data(i,j))

            alpha(i,j)=0;

        elseif S_data(i,j)>1

            alpha(i,j)=1;

        else

            alpha(i,j)=S_data(i,j);

        end

        p(i,j).Color(4)=alpha(i,j);

    end

end

end

```

References

1. Kim, J. Elaboration, optical properties, and applications of colloidal suspensions of LaPO₄ nanorods. Thèse de l'École polytechnique, 2013.
2. Chaudan, E. Développement de nanoémetteurs polarisés pour leur application comme sondes d'orientation. Thèse de l'Université Paris-Saclay, 2018.
3. Thiriet, M. Nanobâtonnets de NaYF₄ à upconversion: synthèse, dispersion colloïdale et propriétés électro-optiques. Thèse de l'Université Paris-Saclay, 2016.
4. Huang, B.; Bates, M.; Zhuang, X., Super-Resolution Fluorescence Microscopy. *Annual Review of Biochemistry* **2009**, *78* (1), 993-1016.
5. Yildiz, A.; Forkey, J. N.; McKinney, S. A.; Ha, T.; Goldman, Y. E.; Selvin, P. R., Myosin V Walks Hand-Over-Hand: Single Fluorophore Imaging with 1.5-nm Localization. *Science* **2003**, *300* (5628), 2061-2065.
6. Weiss, S., Measuring conformational dynamics of biomolecules by single molecule fluorescence spectroscopy. *Nature Structural Biology* **2000**, *7* (9), 724-729.
7. Zhang, X.; Xiao, Y.; Qian, X., A Ratiometric Fluorescent Probe Based on FRET for Imaging Hg²⁺ Ions in Living Cells. *Angewandte Chemie International Edition* **2008**, *47* (42), 8025-8029.
8. Saha, K.; Agasti, S. S.; Kim, C.; Li, X.; Rotello, V. M., Gold Nanoparticles in Chemical and Biological Sensing. *Chemical Reviews* **2012**, *112* (5), 2739-2779.
9. Mayer, K. M.; Lee, S.; Liao, H.; Rostro, B. C.; Fuentes, A.; Scully, P. T.; Nehl, C. L.; Hafner, J. H., A Label-Free Immunoassay Based Upon Localized Surface Plasmon Resonance of Gold Nanorods. *ACS Nano* **2008**, *2* (4), 687-692.
10. Anker, J. N.; Hall, W. P.; Lyandres, O.; Shah, N. C.; Zhao, J.; Van Duyne, R. P., Biosensing with plasmonic nanosensors. *Nature Materials* **2008**, *7* (6), 442-453.
11. Sosa, H.; Peterman, E. J. G.; Moerner, W. E.; Goldstein, L. S. B., ADP-induced rocking of the kinesin motor domain revealed by single-molecule fluorescence polarization microscopy. *Nature Structural Biology* **2001**, *8* (6), 540-544.
12. Adachi, K.; Yasuda, R.; Noji, H.; Itoh, H.; Harada, Y.; Yoshida, M.; Kinosita, K., Stepping rotation of F1-ATPase visualized through angle-resolved single-fluorophore imaging. *Proceedings of the National Academy of Sciences* **2000**, *97* (13), 7243-7247.
13. Ha, T.; Laurence, T. A.; Chemla, D. S.; Weiss, S., Polarization Spectroscopy of Single Fluorescent Molecules. *The Journal of Physical Chemistry B* **1999**, *103* (33), 6839-6850.
14. Backer, A. S.; Lee, M. Y.; Moerner, W. E., Enhanced DNA imaging using super-resolution microscopy and simultaneous single-molecule orientation measurements. *Optica* **2016**, *3* (6), 659-666.
15. Valades Cruz, C. A.; Shaban, H. A.; Kress, A.; Bertaux, N.; Monneret, S.; Mavrikis, M.; Savatier, J.; Brasselet, S., Quantitative nanoscale imaging of orientational order in biological filaments by polarized superresolution microscopy. *Proceedings of the National Academy of Sciences* **2016**, *113* (7), E820-E828.
16. Lethiec, C.; Laverdant, J.; Vallon, H.; Javaux, C.; Dubertret, B.; Frigerio, J.-M.; Schwob, C.; Coolen, L.; Maître, A., Measurement of Three-Dimensional Dipole Orientation of a Single Fluorescent Nanoemitter by Emission Polarization Analysis. *Physical Review X* **2014**, *4* (2), 021037.
17. Ohmachi, M.; Komori, Y.; Iwane, A. H.; Fujii, F.; Jin, T.; Yanagida, T., Fluorescence microscopy for simultaneous observation of 3D orientation and movement and its application to quantum rod-tagged myosin V. *Proceedings of the National Academy of Sciences* **2012**, *109* (14), 5294-5298.
18. Early, K. T.; McCarthy, K. D.; Odoi, M. Y.; Sudeep, P. K.; Emrick, T.; Barnes, M. D., Linear Dipole Behavior in Single CdSe-Oligo(phenylene vinylene) Nanostructures. *ACS Nano* **2009**, *3* (2), 453-461.
19. Chung, I.; Shimizu, K. T.; Bawendi, M. G., Room temperature measurements of the 3D orientation of single CdSe quantum dots using polarization microscopy. *Proceedings of the National Academy of Sciences* **2003**, *100* (2), 405-408.
20. Empedocles, S. A.; Neuhauser, R.; Bawendi, M. G., Three-dimensional orientation measurements of symmetric single chromophores using polarization microscopy. *Nature* **1999**, *399* (6732), 126-130.
21. Brasselet, S.; Le Floch, V.; Treussart, F.; Roch, J.-F.; Zyss, J.; Botzung-Appert, E.; Ibanez, A., In Situ Diagnostics of the Crystalline Nature of Single Organic Nanocrystals by Nonlinear Microscopy. *Physical Review Letters* **2004**, *92* (20), 207401.
22. Winters, D. G.; Smith, D. R.; Schlup, P.; Bartels, R. A., Measurement of orientation and susceptibility ratios using a polarization-resolved second-harmonic generation holographic microscope. *Biomed. Opt. Express* **2012**, *3* (9), 2004-2011.
23. Tiaho, F.; Recher, G.; Rouède, D., Estimation of helical angles of myosin and collagen by second harmonic generation imaging microscopy. *Opt. Express* **2007**, *15* (19), 12286-12295.

24. Stoller, P.; Reiser, K. M.; Celliers, P. M.; Rubenchik, A. M., Polarization-Modulated Second Harmonic Generation in Collagen. *Biophysical Journal* **2002**, *82* (6), 3330-3342.
25. Rodríguez-Sevilla, P.; Labrador-Páez, L.; Wawrzyńczyk, D.; Nyk, M.; Samoć, M.; Kar, A. K.; Mackenzie, M. D.; Paterson, L.; Jaque, D.; Haro-González, P., Determining the 3D orientation of optically trapped upconverting nanorods by in situ single-particle polarized spectroscopy. *Nanoscale* **2016**, *8* (1), 300-308.
26. Green, K. K.; Wirth, J.; Lim, S. F., Nanoplasmonic Upconverting Nanoparticles as Orientation Sensors for Single Particle Microscopy. *Scientific Reports* **2017**, *7* (1), 762.
27. Royer, C. A., Probing Protein Folding and Conformational Transitions with Fluorescence. *Chemical Reviews* **2006**, *106* (5), 1769-1784.
28. O'Neill, M.; Kelly, S. M., Ordered Materials for Organic Electronics and Photonics. *Advanced Materials* **2011**, *23* (5), 566-584.
29. Mohraz, A.; Solomon, M. J., Direct Visualization of Colloidal Rod Assembly by Confocal Microscopy. *Langmuir* **2005**, *21* (12), 5298-5306.
30. Rosenberg, S. A.; Quinlan, M. E.; Forkey, J. N.; Goldman, Y. E., Rotational Motions of Macromolecules by Single-Molecule Fluorescence Microscopy. *Accounts of Chemical Research* **2005**, *38* (7), 583-593.
31. Shroder, D. Y.; Lippert, L. G.; Goldman, Y. E., Single molecule optical measurements of orientation and rotations of biological macromolecules. *Methods and Applications in Fluorescence* **2016**, *4* (4), 042004.
32. Forkey, J. N.; Quinlan, M. E.; Alexander Shaw, M.; Corrie, J. E. T.; Goldman, Y. E., Three-dimensional structural dynamics of myosin V by single-molecule fluorescence polarization. *Nature* **2003**, *422* (6930), 399-404.
33. Yamamoto, J.; Oura, M.; Yamashita, T.; Miki, S.; Jin, T.; Haraguchi, T.; Hiraoka, Y.; Terai, H.; Kinjo, M., Rotational diffusion measurements using polarization-dependent fluorescence correlation spectroscopy based on superconducting nanowire single-photon detector. *Opt. Express* **2015**, *23* (25), 32633-32642.
34. Tsay, J. M.; Doose, S.; Weiss, S., Rotational and Translational Diffusion of Peptide-Coated CdSe/CdS/ZnS Nanorods Studied by Fluorescence Correlation Spectroscopy. *Journal of the American Chemical Society* **2006**, *128* (5), 1639-1647.
35. Sezgin, E.; Schneider, F.; Galiani, S.; Urbančič, I.; Waithe, D.; Lagerholm, B. C.; Eggeling, C., Measuring nanoscale diffusion dynamics in cellular membranes with super-resolution STED-FCS. *Nature Protocols* **2019**, *14* (4), 1054-1083.
36. Eggeling, C.; Widengren, J.; Rigler, R.; Seidel, C. A. M., Photobleaching of Fluorescent Dyes under Conditions Used for Single-Molecule Detection: Evidence of Two-Step Photolysis. *Analytical Chemistry* **1998**, *70* (13), 2651-2659.
37. Song, L.; Hennink, E. J.; Young, I. T.; Tanke, H. J., Photobleaching kinetics of fluorescein in quantitative fluorescence microscopy. *Biophysical Journal* **1995**, *68* (6), 2588-2600.
38. Shimizu, K. T.; Neuhauser, R. G.; Leatherdale, C. A.; Empedocles, S. A.; Woo, W. K.; Bawendi, M. G., Blinking statistics in single semiconductor nanocrystal quantum dots. *Physical Review B* **2001**, *63* (20), 205316.
39. Galland, C.; Ghosh, Y.; Steinbrück, A.; Sykora, M.; Hollingsworth, J. A.; Klimov, V. I.; Htoon, H., Two types of luminescence blinking revealed by spectroelectrochemistry of single quantum dots. *Nature* **2011**, *479* (7372), 203-207.
40. Hoogenboom, J. P.; Hernando, J.; van Dijk, E. M. H. P.; van Hulst, N. F.; García-Parajó, M. F., Power-Law Blinking in the Fluorescence of Single Organic Molecules. *ChemPhysChem* **2007**, *8* (6), 823-833.
41. Chen, H.-Y.; Yang, Y.-C.; Lin, H.-W.; Chang, S.-C.; Gwo, S., Polarized photoluminescence from single GaN nanorods: Effects of optical confinement. *Opt. Express* **2008**, *16* (17), 13465-13475.
42. Lieb, M. A.; Zavislan, J. M.; Novotny, L., Single-molecule orientations determined by direct emission pattern imaging. *J. Opt. Soc. Am. B* **2004**, *21* (6), 1210-1215.
43. Patra, D.; Gregor, I.; Enderlein, J., Image Analysis of Defocused Single-Molecule Images for Three-Dimensional Molecule Orientation Studies. *The Journal of Physical Chemistry A* **2004**, *108* (33), 6836-6841.
44. Li, T.; Li, Q.; Xu, Y.; Chen, X.-J.; Dai, Q.-F.; Liu, H.; Lan, S.; Tie, S.; Wu, L.-J., Three-Dimensional Orientation Sensors by Defocused Imaging of Gold Nanorods through an Ordinary Wide-Field Microscope. *ACS Nano* **2012**, *6* (2), 1268-1277.
45. Lethiec, C.; Pisanello, F.; Carbone, L.; Bramati, A.; Coolen, L.; Maître, A., Polarimetry-based analysis of dipolar transitions of single colloidal CdSe/CdS dot-in-rods. *New Journal of Physics* **2014**, *16* (9), 093014.
46. Böhmer, M.; Enderlein, J., Orientation imaging of single molecules by wide-field epifluorescence microscopy. *J. Opt. Soc. Am. B* **2003**, *20* (3), 554-559.

47. Lukosz, W., Light emission by multipole sources in thin layers. I. Radiation patterns of electric and magnetic dipoles. *J. Opt. Soc. Am.* **1981**, 71 (6), 744-754.
48. Bünzli, J.-C. G.; Eliseeva, S. V., Basics of Lanthanide Photophysics. In *Lanthanide Luminescence: Photophysical, Analytical and Biological Aspects*, Hänninen, P.; Härmä, H., Eds. Springer Berlin Heidelberg: Berlin, Heidelberg, 2011; pp 1-45.
49. Brecher, C.; Samelson, H.; Lempicki, A.; Riley, R.; Peters, T., Polarized Spectra and Crystal-Field Parameters of Eu³⁺ in YVO₄. *Physical Review* **1967**, 155 (2), 178-187.
50. Yang, D.; Peng, Z.; Zhan, Q.; Huang, X.; Peng, X.; Guo, X.; Dong, G.; Qiu, J., Anisotropic Excitation Polarization Response from a Single White Light-Emitting β -NaYF₄:Yb³⁺,Pr³⁺ Microcrystal. *Small* **2019**, 15 (43), 1904298.
51. Li, Z.; Zhang, Y.; Jiang, S., Multicolor Core/Shell-Structured Upconversion Fluorescent Nanoparticles. *Advanced Materials* **2008**, 20 (24), 4765-4769.
52. Zhou, J.; Chen, G.; Wu, E.; Bi, G.; Wu, B.; Teng, Y.; Zhou, S.; Qiu, J., Ultrasensitive Polarized Up-Conversion of Tm³⁺-Yb³⁺ Doped β -NaYF₄ Single Nanorod. *Nano Letters* **2013**, 13 (5), 2241-2246.
53. Yi, G.; Lu, H.; Zhao, S.; Ge, Y.; Yang, W.; Chen, D.; Guo, L.-H., Synthesis, Characterization, and Biological Application of Size-Controlled Nanocrystalline NaYF₄:Yb,Er Infrared-to-Visible Up-Conversion Phosphors. *Nano Letters* **2004**, 4 (11), 2191-2196.
54. Zhou, S.; Deng, K.; Wei, X.; Jiang, G.; Duan, C.; Chen, Y.; Yin, M., Upconversion luminescence of NaYF₄: Yb³⁺, Er³⁺ for temperature sensing. *Optics Communications* **2013**, 291, 138-142.
55. Vetrone, F.; Naccache, R.; Zamarrón, A.; Juarranz de la Fuente, A.; Sanz-Rodríguez, F.; Martínez Maestro, L.; Martín Rodríguez, E.; Jaque, D.; García Solé, J.; Capobianco, J. A., Temperature Sensing Using Fluorescent Nanothermometers. *ACS Nano* **2010**, 4 (6), 3254-3258.
56. Wang, F.; Han, Y.; Lim, C. S.; Lu, Y.; Wang, J.; Xu, J.; Chen, H.; Zhang, C.; Hong, M.; Liu, X., Simultaneous phase and size control of upconversion nanocrystals through lanthanide doping. *Nature* **2010**, 463, 1061.
57. Wang, L.; Li, Y., Na(Y_{1.5}Na_{0.5})F₆ Single-Crystal Nanorods as Multicolor Luminescent Materials. *Nano Letters* **2006**, 6 (8), 1645-1649.
58. Wang, X.; Zhuang, J.; Peng, Q.; Li, Y., A general strategy for nanocrystal synthesis. *Nature* **2005**, 437 (7055), 121-124.
59. Binnemans, K., Interpretation of europium(III) spectra. *Coordination Chemistry Reviews* **2015**, 295, 1-45.
60. Powell, R. C., *Symmetry, Group Theory, and the Physical Properties of Crystals*. Springer-Verlag New York: 2010; Vol. 824.
61. Atkins, P. W.; Child, M. S.; Phillips, C. S. G., *Tables for group theory*. Oxford University Press Oxford: 1970; Vol. 6.
62. Tu, D.; Liu, Y.; Zhu, H.; Li, R.; Liu, L.; Chen, X., Breakdown of Crystallographic Site Symmetry in Lanthanide-Doped NaYF₄ Crystals. *Angewandte Chemie International Edition* **2013**, 52 (4), 1128-1133.
63. Gao, D.; Zheng, H.; Zhang, X.; Fu, Z.; Zhang, Z.; Tian, Y.; Cui, M., Efficient fluorescence emission and photon conversion of LaOF:Eu³⁺ nanocrystals. *Applied Physics Letters* **2011**, 98 (1), 011907.
64. Sayre, E. V.; Freed, S., Spectra and Quantum States of the Europium Ion in Crystals. II. Fluorescence and Absorption Spectra of Single Crystals of Europium Ethylsulfate Nonahydrate. *The Journal of Chemical Physics* **1956**, 24 (6), 1213-1219.
65. Görrler-Walrand, C.; Hendrickx, I.; Fluyt, L.; Gos, M. P.; D'Olieslager, J.; Blasse, G., Optical spectra and crystal-field analysis of europium double nitrates. *The Journal of Chemical Physics* **1992**, 96 (8), 5650-5658.
66. Chaudan, E.; Kim, J.; Tusseau-Nenez, S.; Goldner, P.; Malta, O. L.; Peretti, J.; Gacoin, T., Polarized Luminescence of Anisotropic LaPO₄:Eu Nanocrystal Polymorphs. *Journal of the American Chemical Society* **2018**, 140 (30), 9512-9517.
67. Chacon, R.; Leray, A.; Kim, J.; Lahlil, K.; Mathew, S.; Bouhelier, A.; Kim, J.-W.; Gacoin, T.; Colas des Francs, G., Measuring the Magnetic Dipole Transition of Single Nanorods by Spectroscopy and Fourier Microscopy. *Physical Review Applied* **2020**, 14 (5), 054010.
68. Kim, J.; Martinelli, L.; Lahlil, K.; Boilot, J.-P.; Gacoin, T.; Peretti, J., Optimized combination of intrinsic and form birefringence in oriented LaPO₄ nanorod assemblies. *Applied Physics Letters* **2014**, 105 (6), 061102.
69. Kim, J.; de la Cotte, A.; Deloncle, R.; Archambeau, S.; Biver, C.; Cano, J.-P.; Lahlil, K.; Boilot, J.-P.; Grelet, E.; Gacoin, T., LaPO₄ Mineral Liquid Crystalline Suspensions with Outstanding Colloidal Stability for Electro-Optical Applications. *Advanced Functional Materials* **2012**, 22 (23), 4949-4956.
70. Hänninen, P.; Härmä, H., *Lanthanide luminescence: photophysical, analytical and biological aspects*. Springer Science & Business Media: 2011; Vol. 7.

71. Labrador-Páez, L.; Pedroni, M.; Speghini, A.; García-Solé, J.; Haro-González, P.; Jaque, D., Reliability of rare-earth-doped infrared luminescent nanothermometers. *Nanoscale* **2018**, *10* (47), 22319-22328.
72. Shen, Y.; Lifante, J.; Fernández, N.; Jaque, D.; Ximendes, E., In Vivo Spectral Distortions of Infrared Luminescent Nanothermometers Compromise Their Reliability. *ACS Nano* **2020**, *14* (4), 4122-4133.
73. Rodríguez-Sevilla, P.; Zhang, Y.; de Sousa, N.; Marqués, M. I.; Sanz-Rodríguez, F.; Jaque, D.; Liu, X.; Haro-González, P., Optical Torques on Upconverting Particles for Intracellular Microrheometry. *Nano Letters* **2016**, *16* (12), 8005-8014.
74. Maier, S. A., *Plasmonics: fundamentals and applications*. Springer Science & Business Media: 2007.
75. Kim, J.; Peretti, J.; Lahlil, K.; Boilot, J.-P.; Gacoin, T., Optically Anisotropic Thin Films by Shear-Oriented Assembly of Colloidal Nanorods. *Advanced Materials* **2013**, *25* (24), 3295-3300.
76. Morozovska, A. N.; Eliseev, E. A.; Glinchuk, M. D., Ferroelectricity enhancement in confined nanorods: Direct variational method. *Physical Review B* **2006**, *73* (21), 214106.
77. Batra, K.; Sinha, N.; Goel, S.; Yadav, H.; Joseph, A. J.; Kumar, B., Enhanced dielectric, ferroelectric and piezoelectric performance of Nd-ZnO nanorods and their application in flexible piezoelectric nanogenerator. *Journal of Alloys and Compounds* **2018**, *767*, 1003-1011.
78. Wu, J.-J.; Liu, S.-C.; Yang, M.-H., Room-temperature ferromagnetism in well-aligned Zn_{1-x}CoxO nanorods. *Applied Physics Letters* **2004**, *85* (6), 1027-1029.
79. Ip, K.; Frazier, R. M.; Heo, Y. W.; Norton, D. P.; Abernathy, C. R.; Pearson, S. J.; Kelly, J.; Rairigh, R.; Hebard, A. F.; Zavada, J. M.; Wilson, R. G., Ferromagnetism in Mn- and Co-implanted ZnO nanorods. *Journal of Vacuum Science & Technology B: Microelectronics and Nanometer Structures Processing, Measurement, and Phenomena* **2003**, *21* (4), 1476-1481.
80. Kim, J.; Michelin, S.; Hilbers, M.; Martinelli, L.; Chaudan, E.; Amselem, G.; Fradet, E.; Boilot, J.-P.; Brouwer, A. M.; Baroud, C. N.; Peretti, J.; Gacoin, T., Monitoring the orientation of rare-earth-doped nanorods for flow shear tomography. *Nature Nanotechnology* **2017**, *12*, 914.
81. Park, S.; Mundoor, H.; Fleury, B.; Davidson, P.; van de Lagemaat, J.; Smalyukh, I. I., Liquid Crystalline Order and Electric Switching of Upconversion Luminescence in Colloidal Nanorod Suspensions. *Advanced Optical Materials* **2019**, *7* (9), 1900041.
82. Xie, Y.; Li, Y.; Wei, G.; Liu, Q.; Mundoor, H.; Chen, Z.; Smalyukh, I. I., Liquid crystal self-assembly of upconversion nanorods enriched by depletion forces for mesostructured material preparation. *Nanoscale* **2018**, *10* (9), 4218-4227.
83. Baker, J. L.; Widmer-Cooper, A.; Toney, M. F.; Geissler, P. L.; Alivisatos, A. P., Device-Scale Perpendicular Alignment of Colloidal Nanorods. *Nano Letters* **2010**, *10* (1), 195-201.
84. Zanella, M.; Gomes, R.; Povia, M.; Giannini, C.; Zhang, Y.; Riskin, A.; Van Bael, M.; Hens, Z.; Manna, L., Self-Assembled Multilayers of Vertically Aligned Semiconductor Nanorods on Device-Scale Areas. *Advanced Materials* **2011**, *23* (19), 2205-2209.
85. Ahmed, S.; Ryan, K. M., Self-Assembly of Vertically Aligned Nanorod Supercrystals Using Highly Oriented Pyrolytic Graphite. *Nano Letters* **2007**, *7* (8), 2480-2485.
86. Hamon, C.; Postic, M.; Mazari, E.; Bizien, T.; Dupuis, C.; Even-Hernandez, P.; Jimenez, A.; Courbin, L.; Gosse, C.; Artzner, F.; Marchi-Artzner, V., Three-Dimensional Self-Assembling of Gold Nanorods with Controlled Macroscopic Shape and Local Smectic B Order. *ACS Nano* **2012**, *6* (5), 4137-4146.
87. Hu, H.; Pauly, M.; Felix, O.; Decher, G., Spray-assisted alignment of Layer-by-Layer assembled silver nanowires: a general approach for the preparation of highly anisotropic nano-composite films. *Nanoscale* **2017**, *9* (3), 1307-1314.
88. Börzsönyi, T.; Szabó, B.; Törös, G.; Wegner, S.; Török, J.; Somfai, E.; Bien, T.; Stannarius, R., Orientational Order and Alignment of Elongated Particles Induced by Shear. *Physical Review Letters* **2012**, *108* (22), 228302.
89. Ryan, K. M.; Mastroianni, A.; Stancil, K. A.; Liu, H.; Alivisatos, A. P., Electric-Field-Assisted Assembly of Perpendicularly Oriented Nanorod Superlattices. *Nano Letters* **2006**, *6* (7), 1479-1482.
90. Hu, Z.; Fischbein, M. D.; Querner, C.; Drndić, M., Electric-Field-Driven Accumulation and Alignment of CdSe and CdTe Nanorods in Nanoscale Devices. *Nano Letters* **2006**, *6* (11), 2585-2591.
91. de la Cotte, A.; Merzeau, P.; Kim, J. W.; Lahlil, K.; Boilot, J.-P.; Gacoin, T.; Grelet, E., Electric field induced birefringence in non-aqueous dispersions of mineral nanorods. *Soft Matter* **2015**, *11* (33), 6595-6603.
92. Lemaire, B. J.; Davidson, P.; Ferré, J.; Jamet, J. P.; Panine, P.; Dozov, I.; Jolivet, J. P., Outstanding Magnetic Properties of Nematic Suspensions of Goethite (alpha-FeOOH) Nanorods. *Physical Review Letters* **2002**, *88* (12), 125507.
93. Wang, M.; Gao, C.; He, L.; Lu, Q.; Zhang, J.; Tang, C.; Zorba, S.; Yin, Y., Magnetic Tuning of Plasmonic Excitation of Gold Nanorods. *Journal of the American Chemical Society* **2013**, *135* (41), 15302-15305.

94. van der Beek, D.; Petukhov, A. V.; Davidson, P.; Ferré, J.; Jamet, J. P.; Wensink, H. H.; Vroege, G. J.; Bras, W.; Lekkerkerker, H. N. W., Magnetic-field-induced orientational order in the isotropic phase of hard colloidal platelets. *Physical Review E* **2006**, *73* (4), 041402.
95. Twersky, V., Form and intrinsic birefringence*. *J. Opt. Soc. Am.* **1975**, *65* (3), 239-245.
96. Oldenbourg, R.; Ruiz, T., Birefringence of macromolecules. Wiener's theory revisited, with applications to DNA and tobacco mosaic virus. *Biophysical Journal* **1989**, *56* (1), 195-205.
97. Bragg, W. L.; Pippard, A. B., The form birefringence of macromolecules. *Acta Crystallographica* **1953**, *6* (11-12), 865-867.
98. Connolly, J.; Duijneveldt, J. S. v.; Klein, S.; Pizzey, C.; Richardson, R. M., Manipulation of modified clay particles in a nematic solvent by a magnetic field. *Journal of Physics: Condensed Matter* **2007**, *19* (15), 156103.
99. Murata, K.-i.; Tanaka, H., Microscopic identification of the order parameter governing liquid-liquid transition in a molecular liquid. *Proceedings of the National Academy of Sciences* **2015**, *112* (19), 5956-5961.
100. Ahmed, W.; Kooij, E. S.; van Silfhout, A.; Poelsema, B., Quantitative Analysis of Gold Nanorod Alignment after Electric Field-Assisted Deposition. *Nano Letters* **2009**, *9* (11), 3786-3794.
101. Baiyasi, R.; Gallagher, M. J.; McCarthy, L. A.; Searles, E. K.; Zhang, Q.; Link, S.; Landes, C. F., Quantitative Analysis of Nanorod Aggregation and Morphology from Scanning Electron Micrographs Using SEMseg. *The Journal of Physical Chemistry A* **2020**, *124* (25), 5262-5270.
102. Liu, K.; Zhao, N.; Kumacheva, E., Self-assembly of inorganic nanorods. *Chemical Society Reviews* **2011**, *40* (2), 656-671.
103. Kumar, R.; Nyk, M.; Ohulchanskyy, T. Y.; Flask, C. A.; Prasad, P. N., Combined Optical and MR Bioimaging Using Rare Earth Ion Doped NaYF₄ Nanocrystals. *Advanced Functional Materials* **2009**, *19* (6), 853-859.
104. Krämer, K. W.; Biner, D.; Frei, G.; Güdel, H. U.; Hehlen, M. P.; Lüthi, S. R., Hexagonal Sodium Yttrium Fluoride Based Green and Blue Emitting Upconversion Phosphors. *Chemistry of Materials* **2004**, *16* (7), 1244-1251.
105. Cao, T.; Yang, T.; Gao, Y.; Yang, Y.; Hu, H.; Li, F., Water-soluble NaYF₄:Yb/Er upconversion nanophosphors: Synthesis, characteristics and application in bioimaging. *Inorganic Chemistry Communications* **2010**, *13* (3), 392-394.
106. Kim, J.; Chacon, R.; Wang, Z.; Larquet, E.; Lahlil, K.; Leray, A.; Colas des Francs, G.; Kim, J.; Gacoin, T., Measuring 3D Orientation of Nanocrystals via Polarized Luminescence of Rare-Earth Dopants. *Nature Communications* **2020**, *Under Review*.
107. Fan, Z.; Razavi, H.; Do, J.-w.; Moriwaki, A.; Ergen, O.; Chueh, Y.-L.; Leu, P. W.; Ho, J. C.; Takahashi, T.; Reichertz, L. A.; Neale, S.; Yu, K.; Wu, M.; Ager, J. W.; Javey, A., Three-dimensional nanopillar-array photovoltaics on low-cost and flexible substrates. *Nature Materials* **2009**, *8* (8), 648-653.
108. Law, M.; Greene, L. E.; Johnson, J. C.; Saykally, R.; Yang, P., Nanowire dye-sensitized solar cells. *Nature Materials* **2005**, *4* (6), 455-459.
109. Varghese, O. K.; Paulose, M.; Grimes, C. A., Long vertically aligned titania nanotubes on transparent conducting oxide for highly efficient solar cells. *Nature Nanotechnology* **2009**, *4* (9), 592-597.
110. Li, Y.; Takata, T.; Cha, D.; Takanabe, K.; Minegishi, T.; Kubota, J.; Domen, K., Vertically Aligned Ta₃N₅ Nanorod Arrays for Solar-Driven Photoelectrochemical Water Splitting. *Advanced Materials* **2013**, *25* (1), 125-131.
111. Wang, J. X.; Sun, X. W.; Yang, Y.; Huang, H.; Lee, Y. C.; Tan, O. K.; Vayssieres, L., Hydrothermally grown oriented ZnO nanorod arrays for gas sensing applications. *Nanotechnology* **2006**, *17* (19), 4995-4998.
112. Peng, B.; Li, G.; Li, D.; Dodson, S.; Zhang, Q.; Zhang, J.; Lee, Y. H.; Demir, H. V.; Yi Ling, X.; Xiong, Q., Vertically Aligned Gold Nanorod Monolayer on Arbitrary Substrates: Self-Assembly and Femtomolar Detection of Food Contaminants. *ACS Nano* **2013**, *7* (7), 5993-6000.
113. Liao, Q.; Mu, C.; Xu, D.-S.; Ai, X.-C.; Yao, J.-N.; Zhang, J.-P., Gold Nanorod Arrays with Good Reproducibility for High-Performance Surface-Enhanced Raman Scattering. *Langmuir* **2009**, *25* (8), 4708-4714.
114. Greeneltch, N. G.; Blaber, M. G.; Schatz, G. C.; Van Duyne, R. P., Plasmon-Sampled Surface-Enhanced Raman Excitation Spectroscopy on Silver Immobilized Nanorod Assemblies and Optimization for Near Infrared ($\lambda_{ex} = 1064$ nm) Studies. *The Journal of Physical Chemistry C* **2013**, *117* (6), 2554-2558.
115. Kumar, S.; Sahare, P. D.; Kumar, S., Optimization of the CVD parameters for ZnO nanorods growth: Its photoluminescence and field emission properties. *Materials Research Bulletin* **2018**, *105*, 237-245.
116. Cerf, R.; Scheraga, H. A., Flow Birefringence in Solutions of Macromolecules. *Chemical Reviews* **1952**, *51* (2), 185-261.
117. Atkins, P.; De Paula, J., *Physical chemistry for the life sciences*. W.H. Freeman and Company, New York: 2011.
118. Chang, R., *Physical chemistry for the biosciences*. University Science Books, California: 2005.

119. Matter, F.; Luna, A. L.; Niederberger, M., From colloidal dispersions to aerogels: How to master nanoparticle gelation. *Nano Today* **2020**, *30*, 100827.
120. Parsegian, V. A., *Van der Waals forces: a handbook for biologists, chemists, engineers, and physicists*. Cambridge University Press: 2005.
121. Hamaker, H. C., The London—van der Waals attraction between spherical particles. *Physica* **1937**, *4* (10), 1058-1072.
122. Israelachvili, J. N., *Intermolecular and surface forces*. Academic press: 2011.
123. Verwey, E. J. W., Theory of the Stability of Lyophobic Colloids. *The Journal of Physical and Colloid Chemistry* **1947**, *51* (3), 631-636.
124. Zoicher, H., Über freiwillige Strukturbildung in Solen. (Eine neue Art anisotrop flüssiger Medien.). *Zeitschrift für anorganische und allgemeine Chemie* **1925**, *147* (1), 91-110.
125. Dessombz, A.; Chiche, D.; Davidson, P.; Panine, P.; Chanéac, C.; Jolivet, J.-P., Design of Liquid-Crystalline Aqueous Suspensions of Rutile Nanorods: Evidence of Anisotropic Photocatalytic Properties. *Journal of the American Chemical Society* **2007**, *129* (18), 5904-5909.
126. Gabriel, J.-C. P.; Davidson, P., Mineral liquid crystals from self-assembly of anisotropic nanosystems. In *Colloid Chemistry I*, Springer: 2003; pp 119-172.
127. Lemaire, B. J.; Davidson, P.; Ferré, J.; Jamet, J. P.; Petermann, D.; Panine, P.; Dozov, I.; Jolivet, J. P., Physical properties of aqueous suspensions of goethite (α -FeOOH) nanorods. *Eur. Phys. J. E* **2004**, *13* (3), 291-308.
128. Vroege, G. J.; Thies-Weesie, D. M. E.; Petukhov, A. V.; Lemaire, B. J.; Davidson, P., Smectic Liquid-Crystalline Order in Suspensions of Highly Polydisperse Goethite Nanorods. *Advanced Materials* **2006**, *18* (19), 2565-2568.
129. Xu, Z.; Gao, C., Aqueous Liquid Crystals of Graphene Oxide. *ACS Nano* **2011**, *5* (4), 2908-2915.
130. Li, L.-s.; Walda, J.; Manna, L.; Alivisatos, A. P., Semiconductor Nanorod Liquid Crystals. *Nano Letters* **2002**, *2* (6), 557-560.
131. Oster, G., TWO-PHASE FORMATION IN SOLUTIONS OF TOBACCO MOSAIC VIRUS AND THE PROBLEM OF LONG-RANGE FORCES. *Journal of General Physiology* **1950**, *33* (5), 445-473.
132. Fraden, S.; Maret, G.; Caspar, D. L. D.; Meyer, R. B., Isotropic-nematic phase transition and angular correlations in isotropic suspensions of tobacco mosaic virus. *Physical Review Letters* **1989**, *63* (19), 2068-2071.
133. Davidson, P.; Batail, P.; Gabriel, J. C. P.; Livage, J.; Sanchez, C.; Bourgaux, C., Mineral liquid crystalline polymers. *Progress in Polymer Science* **1997**, *22* (5), 913-936.
134. Michot, L. J.; Bihannic, I.; Maddi, S.; Funari, S. S.; Baravian, C.; Levitz, P.; Davidson, P., Liquid-crystalline aqueous clay suspensions. *Proceedings of the National Academy of Sciences* **2006**, *103* (44), 16101-16104.
135. Onsager, L., THE EFFECTS OF SHAPE ON THE INTERACTION OF COLLOIDAL PARTICLES. *Annals of the New York Academy of Sciences* **1949**, *51* (4), 627-659.
136. Espinosa, C. E.; Guo, Q.; Singh, V.; Behrens, S. H., Particle Charging and Charge Screening in Nonpolar Dispersions with Nonionic Surfactants. *Langmuir* **2010**, *26* (22), 16941-16948.
137. Crocker, J. C.; Grier, D. G., When Like Charges Attract: The Effects of Geometrical Confinement on Long-Range Colloidal Interactions. *Physical Review Letters* **1996**, *77* (9), 1897-1900.
138. Sainis, S. K.; Germain, V.; Mejean, C. O.; Dufresne, E. R., Electrostatic Interactions of Colloidal Particles in Nonpolar Solvents: Role of Surface Chemistry and Charge Control Agents. *Langmuir* **2008**, *24* (4), 1160-1164.
139. Dong, X.; Al-Jumaily, A.; Escobar, I. C., Investigation of the Use of a Bio-Derived Solvent for Non-Solvent-Induced Phase Separation (NIPS) Fabrication of Polysulfone Membranes. *Membranes* **2018**, *8* (2), 23.
140. Wang, Z. L., Structural Analysis of Self-Assembling Nanocrystal Superlattices. *Advanced Materials* **1998**, *10* (1), 13-30.
141. Murray, C. B.; Kagan, C. R.; Bawendi, M. G., Self-Organization of CdSe Nanocrystallites into Three-Dimensional Quantum Dot Superlattices. *Science* **1995**, *270* (5240), 1335-1338.
142. Kaznacheev, A. V.; Bogdanov, M. M.; Taraskin, S. A., The nature of prolate shape of tactoids in lyotropic inorganic liquid crystals. *Journal of Experimental and Theoretical Physics* **2002**, *95* (1), 57-63.
143. Yang, J.; Lee, J. Y.; Ying, J. Y., Phase transfer and its applications in nanotechnology. *Chemical Society Reviews* **2011**, *40* (3), 1672-1696.
144. Kumar, A.; Mandale, A. B.; Sastry, M., Phase Transfer of Aqueous CdS Nanoparticles by Coordination with Octadecanethiol Molecules Present in Nonpolar Organic Solvents. *Langmuir* **2000**, *16* (24), 9299-9302.
145. Queffelec, C.; Petit, M.; Janvier, P.; Knight, D. A.; Bujoli, B., Surface Modification Using Phosphonic Acids and Esters. *Chemical Reviews* **2012**, *112* (7), 3777-3807.

146. Koole, R.; Schapotschnikow, P.; de Mello Donegá, C.; Vlugt, T. J. H.; Meijerink, A., Time-Dependent Photoluminescence Spectroscopy as a Tool to Measure the Ligand Exchange Kinetics on a Quantum Dot Surface. *ACS Nano* **2008**, *2* (8), 1703-1714.
147. Phan, T.-A.; Perrin, F.-X.; Nguyen-Dinh, L., Synthesis and characterization of decyl phosphonic acid, applications in emulsion polymerization and anti-corrosion coating. *Korean Journal of Chemical Engineering* **2018**, *35* (6), 1365-1372.
148. Fadeev, A. Y.; Helmy, R.; Marcinko, S., Self-Assembled Monolayers of Organosilicon Hydrides Supported on Titanium, Zirconium, and Hafnium Dioxides. *Langmuir* **2002**, *18* (20), 7521-7529.
149. Coppel, Y.; Spataro, G.; Pagès, C.; Chaudret, B.; Maisonnat, A.; Kahn, M. L., Full Characterization of Colloidal Solutions of Long-Alkyl-Chain-Amine-Stabilized ZnO Nanoparticles by NMR Spectroscopy: Surface State, Equilibria, and Affinity. *Chemistry – A European Journal* **2012**, *18* (17), 5384-5393.
150. Puech, N.; Grelet, E.; Poulin, P.; Blanc, C.; van der Schoot, P., Nematic droplets in aqueous dispersions of carbon nanotubes. *Physical Review E* **2010**, *82* (2), 020702.
151. Morrison, I. D., Electrical charges in nonaqueous media. *Colloids and Surfaces A: Physicochemical and Engineering Aspects* **1993**, *71* (1), 1-37.
152. Kemp, R.; Sanchez, R.; Mutch, K. J.; Bartlett, P., Nanoparticle Charge Control in Nonpolar Liquids: Insights from Small-Angle Neutron Scattering and Microelectrophoresis. *Langmuir* **2010**, *26* (10), 6967-6976.
153. Wang, Z.-W.; Li, G.-Z.; Guan, D.-R.; Yi, X.-Z.; Lou, A.-J., The Surface Potential of a Spherical Colloid Particle: Functional Theoretical Approach. *Journal of Colloid and Interface Science* **2002**, *246* (2), 302-308.
154. Sader, J. E., Accurate Analytic Formulae for the Far Field Effective Potential and Surface Charge Density of a Uniformly Charged Sphere. *Journal of Colloid and Interface Science* **1997**, *188* (2), 508-510.
155. Bruggen, M. P. B. v.; Kooij, F. M. v. d.; Lekkerkerker, H. N. W., Liquid crystal phase transitions in dispersions of rod-like colloidal particles. *Journal of Physics: Condensed Matter* **1996**, *8* (47), 9451-9456.
156. Hsu, M. F.; Dufresne, E. R.; Weitz, D. A., Charge Stabilization in Nonpolar Solvents. *Langmuir* **2005**, *21* (11), 4881-4887.
157. Roberts, G. S.; Sanchez, R.; Kemp, R.; Wood, T.; Bartlett, P., Electrostatic Charging of Nonpolar Colloids by Reverse Micelles. *Langmuir* **2008**, *24* (13), 6530-6541.
158. Guo, Q.; Singh, V.; Behrens, S. H., Electric Charging in Nonpolar Liquids Because of Nonionizable Surfactants. *Langmuir* **2010**, *26* (5), 3203-3207.
159. Smith, P. G.; Patel, M. N.; Kim, J.; Milner, T. E.; Johnston, K. P., Effect of Surface Hydrophilicity on Charging Mechanism of Colloids in Low-Permittivity Solvents. *The Journal of Physical Chemistry C* **2007**, *111* (2), 840-848.
160. Poovarodom, S.; Berg, J. C., Effect of particle and surfactant acid–base properties on charging of colloids in apolar media. *Journal of Colloid and Interface Science* **2010**, *346* (2), 370-377.
161. Schulz, E. P.; Piñeiro, Á.; Rodriguez, J. L.; Minardi, R. M.; Frechero, M.; Schulz, P. C., Intermediate Structures for Higher Level Arrangements: Catching Disk-Like Micelles in Decane Phosphonic Acid Aqueous Solutions. *The Journal of Physical Chemistry B* **2013**, *117* (20), 6231-6240.
162. Asakura, S.; Oosawa, F., Interaction between particles suspended in solutions of macromolecules. *Journal of Polymer Science* **1958**, *33* (126), 183-192.
163. Buitenhuis, J.; Donselaar, L. N.; Buining, P. A.; Stroobants, A.; Lekkerkerker, H. N. W., Phase Separation of Mixtures of Colloidal Boehmite Rods and Flexible Polymer. *Journal of Colloid and Interface Science* **1995**, *175* (1), 46-56.
164. Dogic, Z.; Purdy, K. R.; Grelet, E.; Adams, M.; Fraden, S., Isotropic-nematic phase transition in suspensions of filamentous virus and the neutral polymer Dextran. *Physical Review E* **2004**, *69* (5), 051702.
165. Baranov, D.; Fiore, A.; van Huis, M.; Giannini, C.; Falqui, A.; Lafont, U.; Zandbergen, H.; Zanella, M.; Cingolani, R.; Manna, L., Assembly of Colloidal Semiconductor Nanorods in Solution by Depletion Attraction. *Nano Letters* **2010**, *10* (2), 743-749.
166. Royall, C. P.; Roij, R. v.; Blaaderen, A. v., Extended sedimentation profiles in charged colloids: the gravitational length, entropy, and electrostatics. *Journal of Physics: Condensed Matter* **2005**, *17* (15), 2315-2326.
167. Raşa, M.; Philipse, A. P., Evidence for a macroscopic electric field in the sedimentation profiles of charged colloids. *Nature* **2004**, *429* (6994), 857-860.
168. Philipse, A. P.; Koenderink, G. H., Sedimentation–diffusion profiles and layered sedimentation of charged colloids at low ionic strength. *Advances in Colloid and Interface Science* **2003**, *100-102*, 613-639.
169. Mourad, M. C. D.; Byelov, D. V.; Petukhov, A. V.; Matthijs de Winter, D. A.; Verkleij, A. J.; Lekkerkerker, H. N. W., Sol–Gel Transitions and Liquid Crystal Phase Transitions in Concentrated Aqueous Suspensions of Colloidal Gibbsite Platelets. *The Journal of Physical Chemistry B* **2009**, *113* (34), 11604-11613.
170. Philipse, A. P.; Wierenga, A. M., On the Density and Structure Formation in Gels and Clusters of Colloidal Rods and Fibers. *Langmuir* **1998**, *14* (1), 49-54.

171. Nyström, G.; Arcari, M.; Mezzenga, R., Confinement-induced liquid crystalline transitions in amyloid fibril cholesteric tactoids. *Nature Nanotechnology* **2018**, *13* (4), 330-336.
172. Jeong, J.; Kim, M. W., Confinement-Induced Transition of Topological Defects in Smectic Liquid Crystals: From a Point to a Line and Pearls. *Physical Review Letters* **2012**, *108* (20), 207802.
173. Palermo, V.; Biscarini, F.; Zannoni, C., Abrupt orientational changes for liquid crystals adsorbed on a graphite surface. *Physical Review E* **1998**, *57* (3), R2519-R2522.
174. de las Heras, D.; Velasco, E.; Mederos, L., Capillary Smectization and Layering in a Confined Liquid Crystal. *Physical Review Letters* **2005**, *94* (1), 017801.
175. Crawford, G. P.; Ondris-Crawford, R.; Žumer, S.; Doane, J. W., Anchoring and orientational wetting transitions of confined liquid crystals. *Physical Review Letters* **1993**, *70* (12), 1838-1841.
176. Rodríguez-Ponce, I.; Romero-Enrique, J. M.; Velasco, E.; Mederos, L.; Rull, L. F., Interplay between Anchoring and Wetting at a Nematic-Substrate Interface. *Physical Review Letters* **1999**, *82* (13), 2697-2700.
177. Rodríguez-Ponce, I.; Romero-Enrique, J. M.; Velasco, E.; Mederos, L.; Rull, L. F., Anchoring and nematic-isotropic transitions in a confined nematic phase. *Journal of Physics: Condensed Matter* **2000**, *12* (8A), A363-A367.
178. Heras, D. d. l.; Martínez-Ratón, Y.; Velasco, E., Phase transitions in nanoconfined binary mixtures of highly oriented colloidal rods. *Physical Chemistry Chemical Physics* **2010**, *12* (36), 10831-10841.
179. Tasaltin, N.; Sanli, D.; Jonáš, A.; Kiraz, A.; Erkey, C., Preparation and characterization of superhydrophobic surfaces based on hexamethyldisilazane-modified nanoporous alumina. *Nanoscale Research Letters* **2011**, *6* (1), 487.
180. Jamali, V.; Biggers, E. G.; van der Schoot, P.; Pasquali, M., Line Tension of Twist-Free Carbon Nanotube Lyotropic Liquid Crystal Microdroplets on Solid Surfaces. *Langmuir* **2017**, *33* (36), 9115-9121.
181. Smalyukh, I. I.; Shiyankovskii, S. V.; Lavrentovich, O. D., Three-dimensional imaging of orientational order by fluorescence confocal polarizing microscopy. *Chemical Physics Letters* **2001**, *336* (1), 88-96.
182. Cole, R. W.; Jinadasa, T.; Brown, C. M., Measuring and interpreting point spread functions to determine confocal microscope resolution and ensure quality control. *Nature Protocols* **2011**, *6* (12), 1929-1941.
183. Kim, Y.-K.; Shiyankovskii, S. V.; Lavrentovich, O. D., Morphogenesis of defects and tactoids during isotropic-nematic phase transition in self-assembled lyotropic chromonic liquid crystals. *Journal of Physics: Condensed Matter* **2013**, *25* (40), 404202.
184. Mor, F. M.; Sienkiewicz, A.; Forró, L.; Jeney, S., Upconversion Particle as a Local Luminescent Brownian Probe: A Photonic Force Microscopy Study. *ACS Photonics* **2014**, *1* (12), 1251-1257.
185. Pierrat, S.; Hartinger, E.; Faiss, S.; Janshoff, A.; Sönnichsen, C., Rotational Dynamics of Laterally Frozen Nanoparticles Specifically Attached to Biomembranes. *The Journal of Physical Chemistry C* **2009**, *113* (26), 11179-11183.
186. Chakrabarty, A.; Raffy, G.; Maity, M.; Gartzia-Rivero, L.; Marre, S.; Aymonier, C.; Maitra, U.; Del Guerso, A., Nanofiber-Directed Anisotropic Self-Assembly of CdSe-CdS Quantum Rods for Linearly Polarized Light Emission Evidenced by Quantum Rod Orientation Microscopy. *Small* **2018**, *14* (37), 1802311.
187. Han, S.; Deng, R.; Xie, X.; Liu, X., Enhancing Luminescence in Lanthanide-Doped Upconversion Nanoparticles. *Angewandte Chemie International Edition* **2014**, *53* (44), 11702-11715.
188. Toprak, E.; Enderlein, J.; Syed, S.; McKinney, S. A.; Petschek, R. G.; Ha, T.; Goldman, Y. E.; Selvin, P. R., Defocused orientation and position imaging (DOPI) of myosin V. *Proceedings of the National Academy of Sciences* **2006**, *103* (17), 6495-6499.
189. Dedecker, P.; Muls, B.; Deres, A.; Uji-i, H.; Hotta, J.-i.; Sliwa, M.; Soumillion, J.-P.; Müllen, K.; Enderlein, J.; Hofkens, J., Defocused Wide-field Imaging Unravels Structural and Temporal Heterogeneity in Complex Systems. *Advanced Materials* **2009**, *21* (10-11), 1079-1090.
190. Mayer, L.; Slablab, A.; Dantelle, G.; Jacques, V.; Lepagnol-Bestel, A.-M.; Perruchas, S.; Spinicelli, P.; Thomas, A.; Chauvat, D.; Simonneau, M.; Gacoin, T.; Roch, J.-F., Single KTP nanocrystals as second-harmonic generation biolabels in cortical neurons. *Nanoscale* **2013**, *5* (18), 8466-8471.
191. Xiao, L.; Yeung, E. S., Optical Imaging of Individual Plasmonic Nanoparticles in Biological Samples. *Annual Review of Analytical Chemistry* **2014**, *7* (1), 89-111.
192. Chang, W.-S.; Ha, J. W.; Slaughter, L. S.; Link, S., Plasmonic nanorod absorbers as orientation sensors. *Proceedings of the National Academy of Sciences* **2010**, *107* (7), 2781-2786.
193. Ha, J. W.; Marchuk, K.; Fang, N., Focused Orientation and Position Imaging (FOPI) of Single Anisotropic Plasmonic Nanoparticles by Total Internal Reflection Scattering Microscopy. *Nano Letters* **2012**, *12* (8), 4282-4288.
194. Xiao, L.; Ha, J. W.; Wei, L.; Wang, G.; Fang, N., Determining the Full Three-Dimensional Orientation of Single Anisotropic Nanoparticles by Differential Interference Contrast Microscopy. *Angewandte Chemie International Edition* **2012**, *51* (31), 7734-7738.

195. Ha, J. W.; Sun, W.; Stender, A. S.; Fang, N., Dual-Wavelength Detection of Rotational Diffusion of Single Anisotropic Nanocarriers on Live Cell Membranes. *The Journal of Physical Chemistry C* **2012**, *116* (4), 2766-2771.
196. Marchuk, K.; Ha, J. W.; Fang, N., Three-Dimensional High-Resolution Rotational Tracking with Superlocalization Reveals Conformations of Surface-Bound Anisotropic Nanoparticles. *Nano Letters* **2013**, *13* (3), 1245-1250.
197. Wang, G.; Sun, W.; Luo, Y.; Fang, N., Resolving Rotational Motions of Nano-objects in Engineered Environments and Live Cells with Gold Nanorods and Differential Interference Contrast Microscopy. *Journal of the American Chemical Society* **2010**, *132* (46), 16417-16422.
198. Xiao, L.; Qiao, Y.; He, Y.; Yeung, E. S., Imaging Translational and Rotational Diffusion of Single Anisotropic Nanoparticles with Planar Illumination Microscopy. *Journal of the American Chemical Society* **2011**, *133* (27), 10638-10645.
199. Wackenhut, F.; Failla, A. V.; Züchner, T.; Steiner, M.; Meixner, A. J., Three-dimensional photoluminescence mapping and emission anisotropy of single gold nanorods. *Applied Physics Letters* **2012**, *100* (26), 263102.

Titre : Analyse d'orientation et comportement des cristaux liquides de nanobâtonnet dopés aux lanthanides

Mots clés : anisotropie, lanthanides, polarisation, luminescence, science colloïdale, auto-assemblage

Résumé : Les nanocristaux luminescents ont fait l'objet de nombreux travaux en vue de leurs applications dans de nombreux domaines tels que les dispositifs d'affichage ou comme marqueurs biologiques. Parmi eux, les nanocristaux dopés aux ions lanthanides présentent des caractéristiques d'émission très spécifiques associées à des transitions soit dipolaires magnétiques (MD), soit dipolaires électriques (ED). Le premier objectif de cette thèse était de développer une méthodologie pour la détermination de l'orientation 3D des nanocristaux en tirant parti des caractéristiques uniques de polarisation des transitions MD et ED. À titre d'exemple, des nanobâtonnets de NaYF₄:Eu ont été synthétisés, fonctionnalisés en surface et orientés aléatoirement dans un film de polymère rigide. La détermination avec une grande précision de l'orientation 3D des nanorods est démontrée à l'aide d'un spectrogramme unique de la photoluminescence polarisée. Une deuxième partie est consacrée à la détermination du degré d'orientation (paramètre d'ordre) par rapport à la direction d'alignement global de nanobâtonnets colloïdaux NaYF₄:Eu alignés par un champ électrique dans une cellule électro-optique.

Le deuxième objectif de cette thèse était d'étudier le comportement cristal liquide des nanocristaux anisotropes. Des nanobâtonnets de LaPO₄:Eu ont été synthétisés, stabilisés avec un ligand de surface et dispersés dans un milieu apolaire où le comportement cristal liquide (CL) a été mis en évidence. Ce phénomène a été comparé au comportement CL précédemment rapporté des mêmes nanobâtonnets dispersés en milieu polaire. Dans une seconde partie, le comportement CL a été étudié dans le cas où le système est confiné entre deux parois. La dispersion confinée a montré une évolution originale de sa structure menant à l'observation de domaines CL en forme de fleur. Une cartographie tomographique 3D de l'orientation et du paramètre d'ordre a été réalisée sur la base de la photoluminescence polarisée des ions lanthanides dopés. Ceci fournit un premier exemple d'application de la technique pour la caractérisation d'assemblages auto-organisés, ouvrant la voie à des applications encore plus complexes comme le suivi de la dynamique rotationnelle de nano-objets.

Title : Orientation analysis and liquid crystalline behavior of lanthanide-doped nanorods

Keywords : anisotropy, lanthanides, polarization, luminescence, colloidal science, self-assembly

Abstract : Luminescent nanocrystals have been of great interest for their use for many applications such as display devices or biological markers. Among them, nanocrystals doped with lanthanide ions exhibit particular emission features associated with magnetic (MD) or electric dipole (ED) transitions. The first objective of this thesis was to develop a methodology for the determination of the 3D orientation of nanocrystals by taking advantage of the unique polarization features of MD and ED transitions. As a case example, NaYF₄:Eu nanorods were synthesized, surface-functionalized, and randomly oriented within a rigid polymer film. The possible determination of the 3D orientation of the nanorods with high accuracy is demonstrated using a single-shot spectrogram of the polarized photoluminescence. A second part is devoted to determining the degree of orientation (order parameter) with respect to the global alignment direction of colloidal NaYF₄:Eu nanorods aligned under an electric field in an electro-optical cell.

The second objective of this thesis was to investigate the colloidal liquid crystal behavior of anisotropic nanocrystals. LaPO₄:Eu nanorods were synthesized, stabilized with a surface ligand, and dispersed in an apolar medium where its liquid crystalline (LC) behavior was evidenced. This phenomenon was compared to the previously reported LC behavior of the same nanorods dispersed in polar media. In the second part, the LCs behavior was investigated when the system is confined between two walls. The confined LC showed an unprecedented LC evolution leading to the observation of flower-shaped LC domains. A 3D tomographic mapping of the orientation and order parameter was performed based on the polarized photoluminescence of doped lanthanide ions. This thesis study provides the first example of applying the new spectroscopic orientation analysis technique for the characterization of nanoparticle self-assemblies, opening a way toward even more challenging applications such as the rotational dynamic tracking of nano-objects.